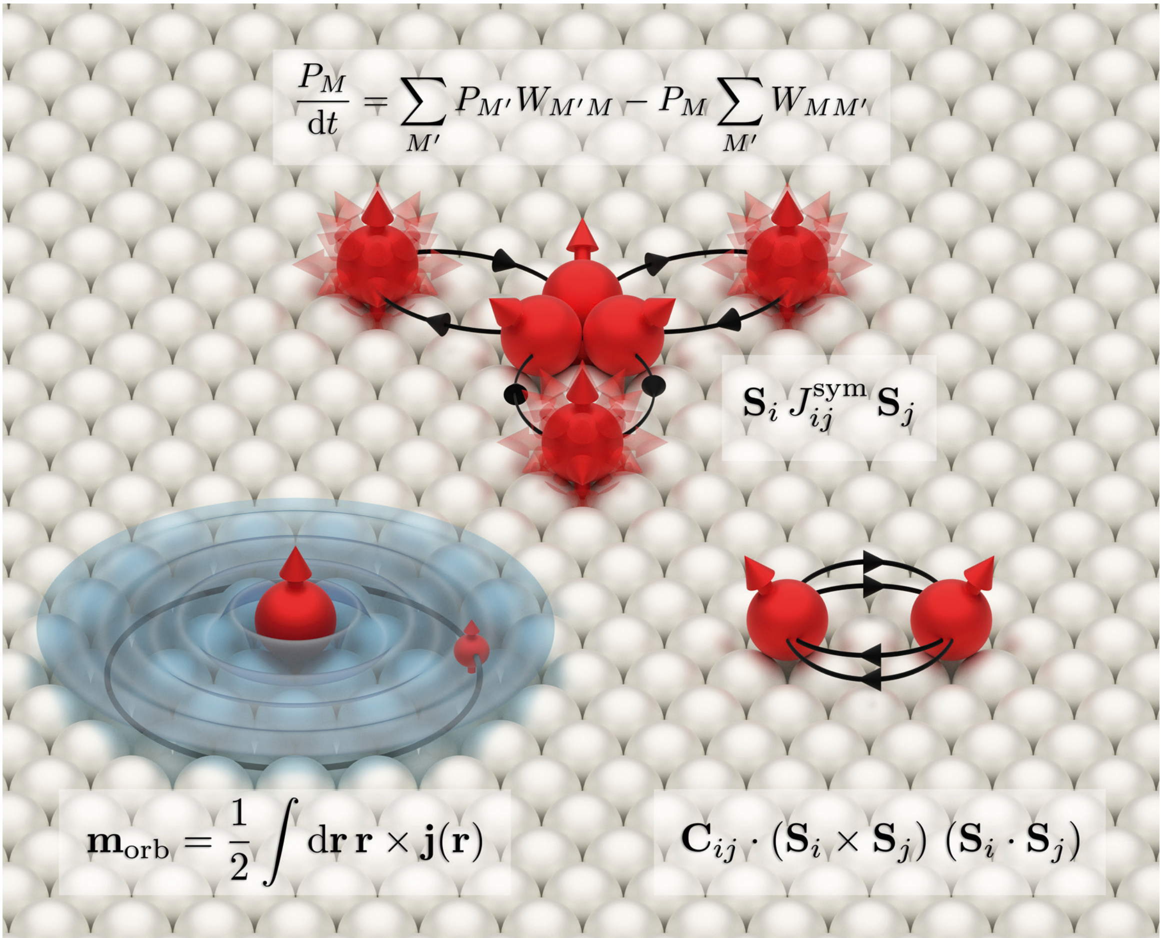

Complex magnetism of nanostructures on surfaces: from orbital magnetism to spin excitations

Sascha Brinker

Schlüsseltechnologien / Key Technologies
Band / Volume 228
ISBN 978-3-95806-525-3

Mitglied der Helmholtz-Gemeinschaft

JÜLICH
Forschungszentrum

Schriften des Forschungszentrums Jülich
Reihe Schlüsseltechnologien / Key Technologies Band / Volume 228

Forschungszentrum Jülich GmbH
Peter Grünberg Institut (PGI)
Quanten-Theorie der Materialien (PGI-1/IAS-1)

Complex magnetism of nanostructures on surfaces: from orbital magnetism to spin excitations

Sascha Brinker

Schriften des Forschungszentrums Jülich
Reihe Schlüsseltechnologien / Key Technologies Band / Volume 228

ISSN 1866-1807 ISBN 978-3-95806-525-3

Bibliografische Information der Deutschen Nationalbibliothek.
Die Deutsche Nationalbibliothek verzeichnet diese Publikation in der
Deutschen Nationalbibliografie; detaillierte Bibliografische Daten
sind im Internet über http://dnb.d-nb.de abrufbar.

Herausgeber und Vertrieb: Forschungszentrum Jülich GmbH
Zentralbibliothek, Verlag
52425 Jülich
Tel.: +49 2461 61-5368
Fax: +49 2461 61-6103
zb-publikation@fz-juelich.de
www.fz-juelich.de/zb

Umschlaggestaltung: Grafische Medien, Forschungszentrum Jülich GmbH

Druck: Grafische Medien, Forschungszentrum Jülich GmbH

Schriften des Forschungszentrums Jülich
Reihe Schlüsseltechnologien / Key Technologies, Band / Volume 228

D 82 (Diss. RWTH Aachen University, 2020)

ISSN 1866-1807
ISBN 978-3-95806-525-3

Vollständig frei verfügbar über das Publikationsportal des Forschungszentrums Jülich (JuSER)
unter www.fz-juelich.de/zb/openaccess.

Kurzfassung

Magnetische Nanostrukturen auf Oberflächen sind vielversprechende Bausteine zukünftiger Spintronik-Geräte, da sie die ultimative Grenze der Miniaturisierung darstellen. In dieser Arbeit wird eine Kombination aus Dichtefunktionaltheorie und modellbasierten Studien verwendet, um magnetische Nanostrukturen auf Oberflächen in Bezug auf grundlegende theoretische Eigenschaften und in Bezug auf Experimente in der Rastertunnelmikroskopie zu untersuchen. Neue Eigenschaften werden in dieser Klasse von Systemen durch verschiedene methodische Entwicklungen enthüllt – von einer neuen Perspektive auf den Bahnmagnetismus bis hin zu den statischen und dynamischen Eigenschaften komplexer nicht-kollinearer magnetischer Zustände.

Erstens betrachten wir das magnetische Bahnmoment in magnetischen Nanostrukturen auf Oberflächen und finden eine neue Komponente - das interatomare Bahnmoment. Eine systematische Analyse deckt seinen eindeutigen physikalischen Ursprung, seine nicht zu vernachlässigende Stärke und seine besonders große Reichweite in realistischen Systemen wie Adatomen auf der Pt(111)-Oberfläche auf. Unsere Ergebnisse zeigen eindeutig die Bedeutung und das Potential dieses neuen Beitrags zum Bahnmagnetismus.

Zweitens untersuchen wir magnetische Austauschwechselwirkungen in magnetischen Nanostrukturen, die über die üblichen bilinearen Austauschwechselwirkungen hinausgehen. Besonderes Augenmerk wird auf Wechselwirkungen höherer Ordnung gelegt, deren mikroskopischer Ursprung mit Hilfe einer modellbasierten Studie geklärt wird. Mit Hilfe der prototypischen Testsysteme magnetischer Dimere finden wir eine neue chirale Paarwechselwirkung, die chirale biquadratische Wechselwirkung, die das biquadratische Äquivalent zur bekannten Dzyaloshinskii-Moriya-Wechselwirkung ist, und untersuchen ihre Auswirkungen nicht nur auf endliche Nanostrukturen, sondern auch auf ausgedehnte Systeme.

Drittens konzentrieren wir uns auf die Spin-Dynamik und die Dämpfung in nicht-kollinearen Strukturen, indem wir die Abhängigkeiten des Gilbert-Dämpfungstensors von der Nicht-Kollinearität in einer atomistischen Form mit einer Kombination aus einer modellbasierten Studie und First-Principles-Berechnungen untersuchen. Wir zeigen, wie isotrope und chirale Abhängigkeiten in einem an das Anderson Modell angelehnte Modell und in realistischen Systemen, wie magnetischen Dimeren auf der Au(111)-Oberfläche, auftreten. Diese Ergebnisse haben das Potential das Gebiet der atomistischen Spin-Dynamik zu einer ausgefeilteren Beschreibung der Dämpfungsmechanismen zu führen.

Viertens untersuchen wir die magnetische Stabilität von Nanostrukturen, die eine der Schlüsselkomponenten für zukünftige Datenspeicher ist. Der Einfluss von magnetischen Austauschwechselwirkungen zwischen Nanostrukturen auf die magnetische Stabilität, wie sie in Telegraphen-Rausch-Tunnelmikroskopie-Experimenten untersucht wird, wird am Beispiel eines magnetischen Trimers und eines magnetischen Adatoms analysiert. Wir finden drei Regime, die jeweils durch eine unterschiedliche magnetische Austauschwechselwirkung hervorgerufen werden, und zeigen, wie dieses Wissen zur Verbesserung der magnetischen Stabilität genutzt werden kann.

Zuletzt analysieren wir das komplexe Zusammenspiel von Magnetismus, Spin-Bahn-Kopplung und Supraleitung in magnetischen Ketten auf einem supraleitenden Substrat, wobei ein besonderer Schwerpunkt auf der Entstehung von Grenzzuständen liegt. Wir klären den rätselhaften magnetischen Grundzustand von Fe-Ketten auf dem Re(0001)-Substrat auf und zeigen, wie Randeffekte durch die Terminierung mit nicht-magnetischen Co-Ketten minimiert werden können. Unsere Ergebnisse liefern wichtige Hinweise auf die Art der Grenzzustände, die in den Fe-Ketten auf Re(0001) zu finden sind, und unterstützen ihre Identifizierung als Majorana-Zustände.

Abstract

Magnetic nanostructures on surfaces are promising building blocks of future spintronics devices, as they represent the ultimate limit in miniaturization. In this thesis, a combination of density functional theory and model-based studies is used to investigate magnetic nanostructures on surfaces with respect to fundamental theoretical properties and in relation to scanning tunneling microscopy experiments. Novel properties are unveiled in this class of systems by several methodological developments, from a new perspective on the orbital magnetism to the static and dynamic properties of complex non-collinear magnetic states.

Firstly, we shed light on the orbital magnetic moment in magnetic nanostructures on surfaces and find a new component – the inter-atomic orbital moment. A systematic analysis uncovers its distinct physical origin, its non-negligible strength, and its particular long range in realistic systems like adatoms deposited on the Pt(111) surface. Our results show unambiguously the importance and the potential of this new contribution to the orbital magnetism.

Secondly, we investigate magnetic exchange interactions in magnetic nanostructures going beyond the common bilinear exchange interactions. Special focus is given to higher-order interactions whose microscopic origin is clarified using a model-based study. Using the prototypical test systems of magnetic dimers we find a new chiral pair interaction, the chiral biquadratic interaction, which is the biquadratic equivalent to the well-known Dzyaloshinskii-Moriya interaction, and investigate its properties and its implications not only for finite nanostructures but also for extended systems.

Thirdly, we focus on the spin dynamics and the damping in non-collinear magnetic structures by investigating the dependencies of the Gilbert damping tensor on the non-collinearity in an atomistic form using a combination of a model-based study and first-principles calculations. We show how isotropic and chiral dependencies evolve from an Anderson-like model and in realistic systems like magnetic dimers on the Au(111) surface. These results have the potential to drive the field of atomistic spin dynamics to a more sophisticated description of the damping mechanisms.

Fourthly, we investigate the magnetic stability of nanostructures, which is one of the key ingredients on the road towards future data storage devices. The impact of magnetic exchange interactions between nanostructures on the magnetic stability as probed in telegraph noise scanning tunneling microscopy experiments is analyzed by using the example of a magnetic trimer and a magnetic adatom. We find three regimes each driven by a distinct magnetic exchange interaction and show how this knowledge can be used to engineer the magnetic stability.

Lastly, we analyze the complex interplay of magnetism, spin-orbit coupling and superconductivity in magnetic chains on a superconducting substrate with a special focus on the emergence of boundary states. We shed light on the puzzling magnetic ground state of Fe chains on the Re(0001) substrate and show how boundary effects can be minimized by termination with non-magnetic Co chains. Our results provide vital clues on the nature of the boundary states found in Fe chains on Re(0001), and support their identification as Majorana states.

Contents

1

Introduction

Digitization (the digital encoding of information) has revolutionized every aspect of modern life by generating copious amounts of information that can be used to understand and improve our personal lives, societies and our environment. This vast amount of data not only has to be stored but also processed efficiently, an aspect that casts a dark shadow on the revolution promised by information technology. Recent studies have estimated that the traffic to and from data centers has increased from $60\,\mathrm{PB}$ in 1997 to $1.1\,\mathrm{ZB}$ in 2017 and that in 2030 up to $7\,\%$ of the worldwide power consumption will be solely used for data centers [1, 2]. Facing global problems related to climate change, it is the responsibility of societies to not only rethink the usage of consumer electronics, but also to improve data storage and processing technologies.

In the last 50 years, technological advances in commercially-used devices have been mainly driven by ever-shrinking electronic circuit elements, such as the transistor. The transistor operates based on properties controlled by the electron's charge, and its miniaturization is approaching fundamental physical limits, as illustrated by the recent slowdown in Moore's law [3]. A major source of concern is the increase in power consumption associated with faster or smaller transistors, due to the increased energy dissipation by Joule heating. A promising alternative for improved future information technology is to rely instead on the electron's spin, which is the founding principle of the field of spintronics. Spin-based devices have the potential to be energy-efficient, either by non-volatile storage of information bits or by energy-efficient bit transfer, while remaining functional when miniaturized, thus overcoming the limitations of charge-based devices. The discovery of the giant magnetoresistance (GMR) by Grünberg *et al.* [4] and Fert *et al.* [5] and the related tunnel magnetoresistance (TMR) [6–8] is nowadays seen as the major breakthrough of spintronics, for which Grünberg and Fert were awarded the Nobel prize in 2007. The key finding is that the electric resistance of a magnetic tunnel junction depends on the relative magnetic orientation of two ferromagnetic layers, which are separated by an insulator. In most of nowadays magnetic hard disk drives a single bit of information is encoded in the orientation of ferromagnetic domains, which can be read based on the GMR or TMR effect.

In real materials, the electron's spin can be present both as a mobile degree of freedom (of the conduction electrons) or as a localized one (of the magnetic moments carried by each atom). The latter are the ones exploited in the described hard disk drive technology, where the magnetic moments of many adjacent atoms align parallel to each other in a ferromagnetic order, and the magnetic bits are defined by regions of opposite orientation of the magnetization (ferromagnetic domains). Other types of magnetic order have recently attracted a lot of interest, as they present advantages over ferromagnets. Antiferromagnetic materials, where the magnetic moments of adjacent atoms are antiparallel instead of parallel, have much faster spin dynamics and are insensitive to potentially destabilizing external magnetic fields, and it was experimentally demonstrated that lower electric currents are needed for the manipulation of the magnetic state [9]. Even more complex magnetic textures have shown promise for future spintronic devices. Localized twists of the orientation of the magnetic moments in a ferromagnet with a non-trivial winding number, such as skyrmions [10], bobbers [11] and even hopfions [12], are themselves mobile and so can act as magnetic bit carriers. These have been conceptualized into racetrack-like devices [13, 14], generalizing the original idea based on ferromagnetic domain walls [15].

In order to increase processing speeds and decrease their power consumption, all of the currently-proposed spintronic devices require to be miniaturized while remaining functional. Depending on the type of functionality, different minimal number of atoms may be involved. For data storage devices, the ultimate goal is the usage of single magnetic atoms or small magnetic clusters that encode a single bit of information. These device elements could also be used for information processing if they could be switching controllably and in a fast way between different states, in response to appropriate stimuli. Apart from fabrication and other technological challenges, miniaturization poses different physical questions which have to be answered by fundamental experimental and theoretical research. Some of these key questions are: Can we rely on the physics known from bulk systems to understand the behavior of nanoscale systems, or do quantum effects, like the quantization of spin or quantum fluctuations, become important? What are the fundamental limits of miniaturization for functional devices and what obstacles must be overcome? How can prototypical miniaturized systems be accessed experimentally and how can they be described theoretically?

The visualization and manipulation of systems at the nanoscale was made possible by the invention of scanning tunneling microscopy (STM) by Rohrer and Binning in 1982 [16–18], which were awarded the Nobel prize in 1986 (together with Ernst Ruska). The STM can reach atomic resolution, therefore giving experimental access to nanostructures down to a single atom. While in the first application the STM was used purely as an visualization tool for objects at the nanoscale, it quickly evolved into a tool for the manipulation of these systems. In 1990, Eigler and Schweizer demonstrated for the first time how man-made nanostructures can be built atom-by-atom using lateral atom manipulation [19]. The same year saw the invention of the spin-polarized STM (SP-STM) [20], which is based on the TMR effect, opening the door to the study of magnetic properties a single atom at a time. For instance, it allowed the investigation of magnetic textures, such as the observation of an antiferromagnetic ground state in a Mn layer deposited on the W(110) surface [21], which had been theoretically predicted [22], or with the detection of nanoskyrmions in an Fe monolayer deposited on the Ir(111) surface [23].

Going one step further, atom-resolved electronic properties can be accessed using scanning tunneling spectroscopy (STS). Voltage sweeps at a fixed spatial position lead to variations in the current between the STM tip and the probed surface, which can be related to the local density of electronic states of the surface [24, 25]. If the applied voltages are large enough, the energy carried by each tunneling electron can also cause excitations in the probed system, which is the foundation of inelastic scanning tunneling spectroscopy (ISTS). ISTS can thus be used to learn about the dynamical electronic and magnetic properties of systems at the nanoscale, which are the central interest of this thesis. Knowledge of these properties are also crucial for the field of information technology, since encoding and processing information are highly dynamical processes. Applications of the ISTS range from the vibrational spectrum of molecules [26] to the spin excitation spectrum of magnetic nanostructures [27]. The spin excitation spectrum of various magnetic nanostructures was investigated using the ISTS technique, ranging from large magnetic molecule [28] and magnetic nanostructures composed out of multiple atoms [29, 30] down to single atoms [27, 31–34]. Spin excitations are addressed in Chapter 5 with a special focus on non-collinear structures.

Now that it is clear that prototypical nanostructures composed of a few atoms can be controllably assembled and interrogated experimentally, we turn to the key question towards the realization of miniaturized data storage devices: What is their magnetic stability, that is, for how long does the magnetic state remain unchanged? The SP-STM enables a direct access to the magnetic stability of a nanostructure via pump-probe or telegraph noise experiments. In pump-probe STM experiments, a pump pulse of strong current excites the nanostructure and is followed by weak probe pulses to detect the magnetic state as function of the time [35]. In telegraph-noise STM experiments, the fluctuations of the magnetic moments are constantly measured as function of time via the STM tip, which is also permanently interacting with the nanostructure through the tunneling current. Due to the TMR effect, the tunneling conductance depends on the magnetic state of the nanostructure, and a lifetime can be defined as the average time the nanostructure stays in a certain state, i.e. its magnetic moment points in a certain direction. The telegraph noise technique was used to prove that the size of the nanostructures which are magnetically stable are a 5-atom Fe cluster on the Cu(111) surface [34], an Fe trimer on the Pt(111) surface [30], down to the ultimate goal of a stable single atom in the form of a Ho adatom on a thin MgO film [36]. Essential to magnetic stability is the magnetic anisotropy energy, which describes the energy barrier preventing the magnetic moment from rotating away from its equilibrium orientation, and how it is related to the local symmetry [37]. Lowering the spatial symmetry of a nanostructure enables new transition channels based on for example in-plane anisotropies, which can drastically affect the stability of a nanostructure. Surprisingly, little is known about the impact of other magnetic interactions on the magnetic stability, either for strong interactions, which dominate in compact clusters, or for weak long-ranged interactions, which are relevant if two or more clusters are placed on the same surface. It is often assumed that increasing the total spin moment should generally increase the stability of a magnetic nanostructure. However, one key result of this thesis is that symmetry is also of crucial importance for the stability of coupled interacting nanostructures, and enlarging a nanostructure will not always increase its magnetic stability [38], as discussed in Chapter 6.

One remaining question is, why is achieving magnetic stability for single atoms, the ultimate goal for miniaturization, so difficult? First of all, the formation of a magnetic moment in zero dimensions is favoured compared to higher dimensions, since often the Stoner criterion is easier to fulfill when the coordination number of the atom is lowered. However, quantum effects like zero-point fluctuations and classical ones such as thermal fluctuations prevent most single magnetic atoms from having a stable magnetic ground state. Both effects can be countered by a suitable magnetic anisotropy energy, which can be engineered by changing the chemical environment of the atom [39, 40] or by building nanostructures assembled out of multiple atoms [30, 34, 41]. Even though it is expected that the magnetic anisotropy energy should increase with reduced dimensionality, in the last decades surprisingly large magnetic anisotropy energies were found for single atoms, ranging from the giant anisotropy of single Co adatom deposited on the Pt(111) surface [42] to different $3d$ transition metal adatoms on the insulating MgO substrate [43, 44].

The sometimes very complex experimental situations can be clarified and informed by resorting to theoretical studies. In the last decades, first-principles methods based on density functional theory (DFT) became the main workhorse for the quantitative prediction of material-specific properties. At the heart of condensed matter physics lies the complexity of the interacting many-body problem. Based on the seminal works of Hohenberg and Kohn [45] and Kohn and Sham [46] (for which Walter Kohn was awarded the Nobel prize in chemistry in 1998), DFT sidesteps this complexity by introducing a solvable non-interacting problem, hiding the difficulties in the exchange-correlation functional. Although the exact functional is unknown, very successful approximations to it have been and are still being devised. This in turn explains the success of DFT in many different fields of physics, describing the electronic properties of bulk materials, thin films, molecules, or nanostructures on surfaces [47]. A practical difficulty faced by DFT methods using periodic boundary conditions is how to describe nanostructures on surfaces with a supercell approximation. However, especially for long-ranged effects it is desirable to avoid the interactions between the periodic replica of a nanostructure. The work presented in this thesis avoids these difficulties by employing the so-called Korringa-Kohn-Rostoker (KKR) Green function method [48] in a real-space formulation, which defines an embedding scheme perfectly suited to investigate nanostructures deposited on surfaces. Another strength of the KKR method is the ease of accessing critical material-specific parameters, the magnetic exchange interactions between atoms, which can be used in an atomistic spin model such as the Heisenberg model [49]. The Heisenberg model is the ancestor of many other more specific models with many applications to problems in magnetism: calculation of the magnetic ground state and of the magnetic ordering temperature, and simulation of spin dynamics, in combination with the Landau-Lifshitz-Gilbert equation [50, 51], to name just a few examples. These spin models are essential to describe the magnetic stability of nanostructures.

Magnetic exchange interactions are not only important for the understanding of magnetic stability, but even more so concerning the formation of complex magnetic textures, which may rely on the subtle interplay of different types of interactions. While the conventional antiferromagnetic Heisenberg exchange interaction can lead to frustration and non-collinear magnetic ground states [52, 53], nanoskyrmions are mainly stabilized by the chiral Dzyaloshinkii-Moriya interaction (DMI) [54, 55], which emerges in inversion-symmetry-broken systems with large spin-orbit coupling. Chirality is a geometrical property favouring a certain handedness, left- or right-handed, which in terms of a magnetic interaction means that a certain sense of rotation of the magnetic texture is favoured. The DMI is not only relevant for the formation of magnetic skyrmions, but also for spin spirals, domain walls and magnetic bobbers. Using SP-STM, chiral magnetic order based on the DMI can even be mapped atom-by-atom [56]. In addition to the well-studied Heisenberg interaction and the DMI, which are bilinear in the spin moments, higher-order interactions that involve four or more spin moments are also known, and can sometimes be the deciding factor concerning the magnetic ground state structure [23, 52, 57, 58]. In Chapter 4, we investigate the physical origin of general higher-order interactions from a microscopic model and apply the gained knowledge to small nanostructures on surfaces. While most studies focused on isotropic higher-order interactions, we put special emphasis on chiral higher-order interactions [59] which are recently attracting a lot of attention [60, 61]. As chiral interactions are important for non-collinear magnetic structures, chiral higher-order interactions might help to explain the so-far not understood magnetic ground state of MnGe [61]. Another kind of magnetic interaction which might play a role in future devices are those that couple even well-separated nanostructures [62, 63]. These long-ranged interactions are mediated by the Friedel oscillations [64] of the surface electron density created by each nanostructure [65, 66].

The importance of the interaction with the surface electrons is also seen in the dependence of the magnetic and electronic properties of an adatom on its environment, as the same adatom can behave completely differently on different surfaces or on different positions on the same surface. An illustrative example is the magnetic anisotropy energy of a single Fe atom on the Pt(111) surface, which was found to change drastically by moving the adatom between similar surface sites [67], and is collectively determined by a large number of substrate atoms [68]. The induced magnetism plays a key role not only for the magnetic anisotropy energy, but also for magnetic interactions, and especially long-ranged magnetic interactions. Palladium and platinum are known as nearly-ferromagnetic metals responding strongly to magnetic atoms via their large spin susceptibility. A famous example are the giant moments induced by $3d$ transition metal atoms in Pd [69–71]. In addition to its large spin polarizability, Pt shows a significant spin-orbit coupling, which opens new possibilities ranging from chiral interactions [63] to orbital magnetism.

Most experimental and theoretical attention has been given to the spin magnetism. However, the orbital degrees of freedom also contribute to the total magnetic moment yet remain mostly unexplored. Pioneering theoretical studies enabled the discovery of novel aspects, e.g. magnetic order which is solely based on the orbital degrees of freedom like the orbital ferromagnetism found in systems exhibiting no net spin moment [72, 73], or even no spin magnetism at all [74]. While the spin moment can be seen as an essentially local quantity arising from the electronic spin density, the orbital moment stems from circulating ground state electronic charge currents, a quantum-mechanical counterpart of classical electrodynamics [75], $\boldsymbol{m}_{\mathrm{o}} = \frac{1}{2}\int \mathrm{d}\boldsymbol{r}\, \boldsymbol{r}\times\boldsymbol{j}(\boldsymbol{r})$. In the atomic approximation, only the current swirling around each atom is considered in the calculation of the orbital magnetic moment, which circumvents the need to handle the position operator $\boldsymbol{r}$ for periodic (bulk) systems. These difficulties were lifted with the modern theory of orbital magnetization [76], unveiling significant differences with the atomic approximation [72]. Magnetic nanostructures on surfaces belong to an intermediate class of systems. Their properties are not local, due to the long-range substrate polarization effects, and so the atomic approximation to the orbital magnetic moments might not hold. They also break translational symmetry, thus the modern approach using Berry phases in reciprocal space cannot be straightforwardly employed. A successful way forward is to evaluate the classical formula without restricting the charge current to its atomic swirling part, building upon initial developments reported in my Master thesis [77], which are extended and discussed in Chapter 3.

A completely different paradigm for future technologies is based on quantum instead of classical computation. As in the problem of data storage, where stability of the magnetic state is of utmost importance, for quantum computing it is the stability of the quantum-mechanical bits (qubits) which is paramount. Here the usage of quantum states which are especially robust against environmental disturbances, such as topologically non-trivial Majorana states, is a promising way forward [78, 79]. Theories have predicted that Majorana bound states can emerge in finite magnetic chains with either a helical magnetic structure or strong spin-orbit coupling, which are proximity-coupled to a superconductor [80–82]. While experiments have found signatures for such boundary states [83, 84], it is a priori unclear if these boundary states are Majorana states of if they are Yu-Shiba-Rusinov (YSR) states [85, 86]. The YSR states, which in contrast to the Majorana states are topologically trivial, can also emerge in magnetic chains which are proximity-coupled to a superconductor and due to possible boundary effects present in the magnetic structure of the chains they could be localized at the boundaries. Distinguishing these trivial YSR-states from non-trivial Majorana states is (so far) experimentally impossible, which is why theoretical investigations based on first-principles calculations are needed. First-principles calculations can answer questions concerning the magnetic and electronic properties, and provide information for tight-binding models, which are the current state of the art to treat superconductivity. This approach is followed in Chapter 7 where boundary states in magnetic chains on the Re(0001) substrate are studied.

In this thesis, a combination of first-principles methods and models is used to investigate diverse phenomena in magnetic nanostructures deposited on surfaces. The topics range from the description of fundamental magnetic phenomena, like the orbital magnetic moment, higher-order magnetic exchange interactions, and spin dynamics in non-collinear magnetic structures, to the prediction of magnetic lifetimes and boundary states, which directly show their relevance for the interpretation of experiments. The thesis is structured as follows:

In Chapter 2, the theoretical and computational framework, which is used throughout this thesis, is introduced. The basic concepts of DFT and of the KKR formalism are discussed and the method developments needed for parts of this thesis are explained. In particular, the calculation scheme of ground state charge currents, their relation to the orbital magnetic moment, and the implementation of non-collinear magnetic fields in the used KKR codes are discussed. The magnetic fields are the basis for magnetic constraining fields which can be used to map first-principles calculations to a generalized Heisenberg model and quantify higher-order magnetic exchange interactions. Apart from the static ground state DFT, dynamical spin excitations are introduced in the framework of time-dependent DFT and linear response.

The first fundamental topic tackled in this thesis is the magnetism induced by magnetic nanostructures to non-magnetic surfaces, presented in Chapter 3. Special focus is given to the orbital contribution to the induced magnetic moment. Using the ground state charge currents, first we demonstrate how our newly developed computational scheme can describe giant real space clusters containing up to 3000 atoms and extract the new long-ranged contribution to the orbital moment – the inter-atomic orbital moment. In a comprehensive analysis, we study the impacts of the spin polarizability and of spin-orbit coupling on the different contributions to the induced magnetism by investigating several $3d$ transition metal adatoms deposited on several late $4d$ and $5d$ transition metal surfaces. We shed light on the physical origins of the induced magnetic moments and show the relevance of the new inter-atomic orbital moment. We also propose an experimental probing technique based on magnetic stray fields, which might allow an experimental access to the magnitude and the range of the induced magnetism in general.

In Chapter 4, magnetic exchange interactions are investigated using a combination of a microscopic model and first-principles calculations. Based on the ideas of Levy and Fert [87, 88], the microscopic system is separated in magnetic sites and sites hosting spin-orbit coupling. Using systematic expansions, we show how magnetic exchange interactions, and especially those of higher-order nature, emerge from the microscopic model. Special focus is given to chiral interactions arising from spin-orbit coupling. We find a new chiral higher-order pair interaction – the chiral biquadratic interaction. We investigate its symmetry properties using the microscopic model and its relevance in realistic systems using first-principles calculations of magnetic dimers deposited on different heavy metal substrates. Apart from its relevance, we find it to have non-trivial implications not only for magnetic dimers but also for extended systems like a nanoskyrmion lattice.

Spin dynamics in non-collinear systems are discussed in Chapter 5. Apart from the magnetic exchange interactions the so-called Gilbert damping tensor is a crucial ingredient for the descriptions of spin dynamics based on the Landau-Lifshitz-Gilbert model. Using a comprehensive model-based study we shed light on the atomistic form of the Gilbert damping tensor, both with and without spin-orbit coupling. Using first-principles studies of magnetic dimers deposited on the Au(111) surface, the non-trivial impact of non-collinearities on the Gilbert damping tensor is analysed. We show that the Gilbert damping can be systematically expanded in terms of isotropic and chiral multi-site terms. Our results can be used to generalize the LLG model for complex non-collinear structures.

In Chapter 6, long-ranged interactions between nanostructures and their impact on the magnetic stability as measured in a telegraph noise experiment are discussed. In collaboration with the experimental group of Dr. Jens Wiebe from the University of Hamburg, we investigate the dependence of the magnetic stability in a trimer-adatom complex on the distance between the adatom and the trimer. Using a model based on a master equation approach and parameters obtained mainly from first principles, we show how the magnetic stability can be separated into three regimes depending on the coupling between the trimer and the adatom. In the first regime, where the trimer and the adatom are only weakly coupled, we show how the adatom can be used as a sensor for the magnetic state of the unprobed trimer, which enhances the magnetic stability of the trimer by orders of magnitude, since there is no direct interaction between the STM tip and the trimer. In the second regime, the intermediate-coupling regime, we show how the DMI generally destabilizes the adatom-trimer complex. In the last regime, the weak-coupling regime, the often-neglected symmetric anisotropic exchange interaction (or compass anisotropy) is found to destabilize the adatom-trimer complex, which can be used to engineer magnetic stability. We show that by using a symmetric placement of additional adatoms the influence of this interaction can be minimized and the lifetime of a magnetic state can be enhanced by orders of magnitude.

In Chapter 7, bound states in magnetic chains on the superconducting Re surface are discussed. This chapter is also resulting from a collaboration with the group of Dr. Jens Wiebe. In a first step based on first-principles calculations, we investigate the magnetic structure of a 20-atomic Fe chain and of the same chain with five Co atoms attached to one or both sites. On the one hand, we show how a complex interplay of antiferromagnetic interactions leads to the experimentally observed spin structure and on the other hand, how the non-magnetic Co influences the electronic and magnetic properties of the Fe chain. Based on first-principles calculations, we set up an effective tight-binding model for the magnetic chains incorporating the effects of the Re substrate and treating the proximity-induced superconductivity as a parameter. Using this tight-binding model, we show how Co provides an orbitally-smooth but non-magnetic extension of the Fe chain, thus reducing boundary effects. We find that boundary states within the superconducting energy gap emerge in the Fe chain, and are only slightly affected by the additional Co placed on either side of the Fe chain, providing a strong indication towards the nature of these states being topologically non-trivial Majorana states and not simply YSR states.

The last chapter concludes the results and gives a brief outlook of future research directions.

2

Density functional theory

In this chapter the theoretical framework of the thesis is set. The main workhorse lies in the density functional theory (DFT), which allows for an efficient solution of the many-body *problem. The particular framework used to solve the DFT equations is the Korringa-Kohn-Rostoker Green function method, which is introduced in this chapter. Apart from static properties, dynamical properties are introduced using linear response theory in the spirit of time-dependent DFT with its main application to the magnetic susceptibility. In addition to a recap of known concepts, the chapter gives also an overview of code and method developments, which were needed for several results of this thesis, namely ground state charge currents and the related stray fields, general non-collinear magnetic fields, magnetic torques, and magnetic constraining fields. This chapter is intended to introduce briefly the basic concepts needed to understand the remaining chapters of the thesis. It should not be seen as a comprehensive introduction to neither DFT nor the KKR formalism. Introductions to DFT can be found in standard textbooks, e.g. [47, 89, 90], or lecture notes, e.g. [91]. A detailed introduction to the KKR formalism can be found in the textbook Ref. [92] or in the PhD thesis of Drittler [93] and Bauer [94].*

2.1. The basics of density functional theory

Crystals being composed of periodic arrangements of nuclei and electrons involve several types of interactions. The three main mechanisms are the interactions among electrons, the interactions of electrons with nuclei and the interactions of nuclei with themselves. All of those give rise to the many-body problem, which is at the heart of every theory in condensed matter physics. The solution of the stationary Schrödinger equation,

$$\mathcal{H}\Psi = E\Psi \quad , \tag{2.1}$$

where $\mathcal{H}$ is a general hamiltonian and Ψ a (spin-dependent) many-body wavefunction, gives access to every observable in quantum physics. However, due to the exponential complexity of the many-body problem the solution of the Schrödinger equation is not feasible for a realistic solid. A first simplification is the Born-Oppenheimer approximation, which decouples the electronic degrees of freedom from the motion of the nuclei. The Hamiltonian describing the many-body problem simplifies to

$$\mathcal{H} = \sum_i \left(-\boldsymbol{\nabla}_i^2 + V_{\text{ext}}(\boldsymbol{r}_i) + \mu_{\text{B}}\, \boldsymbol{\sigma} \cdot \boldsymbol{B}_{\text{ext}}(\boldsymbol{r}_i) \right) + \sum_{i \neq j} \frac{1}{|\boldsymbol{r}_i - \boldsymbol{r}_j|} \quad , \tag{2.2}$$

where $-\boldsymbol{\nabla}_i^2$ describes the kinetic energy of the electrons, $V_{\text{ext}}(\boldsymbol{r}_i)$ is an external field including the interaction of the electrons with the nuclei, μ_{B} is the Bohr magneton, $\boldsymbol{\sigma}$ is the vector of Pauli matrices, $\boldsymbol{B}_{\text{ext}}(\boldsymbol{r}_i)$ is an external magnetic field, $\frac{1}{|\boldsymbol{r}_i - \boldsymbol{r}_j|}$ describes the Coulomb interactions among the electrons, and Rydberg atomic units were used (see Appendix A). One of the most powerful techniques to solve the many-body problem is density functional theory (DFT). The essence of DFT was set by Hohenberg and Kohn [45] and Kohn and Sham [46] with their ground-breaking theorems. The fundamental concept of Hohenberg and Kohn is that every observable can be determined via the ground-state charge density $n(\boldsymbol{r})$ without knowledge of the wavefunction, which was later on generalized for spin-dependent systems using the ground-state spin density $\boldsymbol{m}(\boldsymbol{r})$ in addition [95]. For non-degenerate ground states the Hohenberg Kohn theorems state that (i) there is a one-to-one correspondence between the many-body wavefunction Ψ and the densities $\{n(\boldsymbol{r}), \boldsymbol{m}(\boldsymbol{r})\}$, (ii) there exists an energy functional $E[n, \boldsymbol{m}]$, which is minimized only for the ground-state densities $\{n_0(\boldsymbol{r}), \boldsymbol{m}_0(\boldsymbol{r})\}$, and (iii) there exists an universal energy functional $F[n, \boldsymbol{m}]$ containing the kinetic energy and the electron-electron interaction, which depends only on the interaction between the electrons and not on the underlying lattice. The idea of Kohn and Sham was to replace the system of interacting particles by an auxiliary system of non-interacting particles. The main essence is that there exist a unique potential $V_{\text{xc}}(\boldsymbol{r})$ and a unique magnetic field $\boldsymbol{B}_{\text{xc}}(\boldsymbol{r})$ such that the system of non-interacting particles,

$$\left[-\boldsymbol{\nabla}^2 + V_{\text{ext}}(\boldsymbol{r}) + V_{\text{H}}(\boldsymbol{r}) + V_{\text{xc}}(\boldsymbol{r}) + \mu_{\text{B}}\boldsymbol{\sigma} \cdot (\boldsymbol{B}_{\text{ext}}(\boldsymbol{r}) + \boldsymbol{B}_{\text{xc}}(\boldsymbol{r}))\right] \phi_i(\boldsymbol{r}) = E_i \phi_i(\boldsymbol{r}) \quad , \tag{2.3}$$

with the single-particle wavefunction $\phi_i(\boldsymbol{r})$ and single-particle energy E_i, has exactly the same ground-state densities,

$$n(\boldsymbol{r}) = \sum_{i=1}^{N} |\phi_i(\boldsymbol{r})|^2 \quad \text{, and} \quad \boldsymbol{m}(\boldsymbol{r}) = -\mu_{\text{B}} \sum_{i=1}^{N} \phi_i^{\dagger}(\boldsymbol{r}) \boldsymbol{\sigma} \phi_i(\boldsymbol{r}) \quad , \tag{2.4}$$

as the corresponding real system of N interacting particles. Eq. (2.3) is the so-called Kohn-Sham equation, which is a set of (coupled) differential equations. The exchange-correlation potentials rise from an exchange-correlation (xc) energy functional via a variational principle, $V_{\text{xc}} = \frac{\delta E_{\text{xc}}[n,\boldsymbol{m}]}{\delta n(\boldsymbol{r})}\Big|_{GS}$ and $\boldsymbol{B}_{\text{xc}} = -\frac{\delta E_{\text{xc}}[n,\boldsymbol{m}]}{\delta \boldsymbol{m}(\boldsymbol{r})}\Big|_{GS}$. It accounts for all electron-electron interactions, which go beyond the Hartree approximation described by the Hartree potential $V_{\text{H}}(\boldsymbol{r}) = 2\int \mathrm{d}^3 r' \frac{n(\boldsymbol{r})}{|\boldsymbol{r}-\boldsymbol{r}'|}$. Even though the Kohn-Sham equations yield an exact relation between the interacting and the non-interacting system, the precise form of the exchange-correlation energy is not known and can only be approximated for a few physical systems. The most used approximation is the local (spin) density approximation (LSDA), which is based on the homogeneous electron gas for which the exchange energy is known analytically and the correlation energy can be obtained using for example Quantum Monte Carlo methods [96]. The parametrization of the correlation energy, which is used throughout this thesis is given by Vosko, Wilk and Nusair [97]. The key essence of LSDA is that the exchange-correlation energy is approximated locally by the corresponding energy of a homogeneous electron gas with charge density $n(\boldsymbol{r})$ and spin density $\boldsymbol{m}(\boldsymbol{r})$. As a consequence, the exchange correlation magnetic field in LSDA is always collinear to the spin density $\boldsymbol{m}(\boldsymbol{r})$. One of the main strengths of the LSDA is the underlying real physical system. Even though the homogeneous electron gas deviates drastically from a realistic solid with inhomogeneities, the local density approximation yields good results for many physical systems, which is related to certain sum rules which are satisfied by the homogeneous electron gas [98, 99]. For highly inhomogeneous and complex materials other more sophisticated exchange-correlation functionals were invented. A prominent representative is the class of generalized gradient approximations (GGA), which include non-local contributions depending on the gradient of the electron density in addition to the local dependence on the electron density in LDA. In solid state physics the most widely used GGA functional was invented by Perdew, Burke and Ernzerhof (PBE) [100]. Depending on the specific ground-state property and the material class being addressed, several specialised functionals were invented, e.g. a more recent version of the PBE functional (PBEsol) [101] yields improved atomic geometries for many systems.

2.1.1. Relativistic corrections

The classical hamiltonian discussed in relation to eq. (2.2) does not include relativistic effects. In general, instead of the non-relativistic Schrödinger equation the Dirac equation can be utilized to account for relativistic effects. The main difference of the latter to the former equation is that the wavefunction becomes four dimensional including a so-called smaller and bigger component in addition to the two spin components. However, using perturbation theory for the non-relativistic limit in linear order the Dirac equation gives rise to a perturbed hamiltonian, which can be used to treat relativistic effects in the usual Schrödinger equation as shown in standard text books, e.g. Ref. [102], or in Ref. [77]. In total, there are four new terms rising from the perturbation – a relativistic correction to the kinetic energy and the Darwin term, which are typically combined in the so-called scalar relativistic approximation, an interaction with a time-dependent magnetic field, which is irrelevant for static problems, and the spin-orbit coupling (SOC). The spin-orbit coupling giving rise to many important phenomena in the field of spintronics has the form

$$\mathcal{H}_{\mathsf{SOC}} = -\frac{\mu_{\mathsf{B}}}{c^2}\boldsymbol{\sigma}\cdot(\boldsymbol{E}\times\boldsymbol{p}) \quad , \tag{2.5}$$

where c is the speed of light, $\boldsymbol{E} = -\boldsymbol{\nabla}V$ is the electric field generated by the potential $V(\boldsymbol{r})$, and $\boldsymbol{p}$ is the momentum associated to the motion of the electrons. It couples the spin of the electron, described by the Pauli matrices $\boldsymbol{\sigma}$, to the momentum of the electrons via the electric field. For a single atom in the stationary case it can be further simplified yielding,

$$\mathcal{H}_{\mathsf{SOC}} = \frac{1}{c^2}\frac{1}{r}\frac{\mathrm{d}V}{\mathrm{d}r}\boldsymbol{\sigma}\cdot\boldsymbol{L} = \lambda_{\mathsf{SOC}}\,\boldsymbol{\sigma}\cdot\boldsymbol{L} \quad , \tag{2.6}$$

where V is the radial potential of the nucleus, $\boldsymbol{L} = \boldsymbol{r}\times\boldsymbol{p}$ is the angular momentum, and λ_{SOC} is the spin-orbit coupling strength. This form immediately shows the coupling between the spin degrees of freedom of the electrons associated to the Pauli vectors and the orbital degrees of freedom of the electrons associated to the angular momentum. The spin-orbit coupling can be added to the Kohn-Sham equation, eq. (2.3), as part of the external magnetic field resulting in a coupling of the two spin channels.

With the Kohn-Sham equation, we introduced in this section the on practical grounds most relevant DFT equation. However, we did not explain how to solve this fundamental equation. Different techniques were developed in the past ranging from plane wave methods [47] to for example the linearized augmented plane wave (LAPW) method [103]. In this thesis, the Korringa-Kohn-Rostoker Green function method [48], which is explained in the following, is used.

2.2. Korringa-Kohn-Rostoker Green function method

The Korringa-Kohn-Rostoker (KKR) method is based on multiple scattering theory and goes back to the seminal works of Korringa [104] and Kohn and Rostoker [105]. In the end of the last century, the KKR method was intensively used due to its computational advantages compared to plane wave methods. With the increase of computational resources and the decrease of computational costs for many calculations plane wave methods are ahead nowadays, which is also related to the theoretical complexity of the KKR method. However, in this thesis a perfect class of systems for which the KKR method shows its full strength and beauty is discussed – namely magnetic nanostructures deposited on surfaces. As will be shown in next sections, the main strength of the KKR method lies in an efficient embedding technique, which allows for a treatment of nanostructures deposited on extended surfaces directly in real space. This not only allows for a more efficient treatment of this class of systems compared to a supercell approach needed in conventional plane wave codes, but also enables the discovery of long-range effects, like e.g. the non-local orbital moment discussed in the chapter 3 or the interaction between different nanostructures discussed in chapter 6. The KKR method is based on a Green function approach which is the starting point of the following discussion.

2.2.1. The Green function formalism

The stationary single particle Green function is defined as the resolvent of the single particle hamiltonian,

$$G(E + \mathrm{i}\eta) = (E + \mathrm{i}\eta - \mathcal{H})^{-1} \quad , \tag{2.7}$$

where E is the energy, and η gives rise to a small imaginary component avoiding the poles at the real axis attributed to the real eigenenergies of the hamiltonian $\mathcal{H}$. Note that the defined Green function is different from the Green functions commonly used in the quantum many-body theory. In the eigenenergy basis of the hamiltonian the Green function can be written as,

$$G(E + \mathrm{i}\eta) = \sum_n \frac{|n\rangle\langle n|}{E - E_n + \mathrm{i}\eta} \quad \Rightarrow \quad G(\boldsymbol{r}, \boldsymbol{r}'; E + \mathrm{i}\eta) = \sum_n \frac{\psi_n(\boldsymbol{r})\psi_n^*(\boldsymbol{r}')}{E - E_n + \mathrm{i}\eta} \quad . \tag{2.8}$$

For $\eta \to 0^+/0^-$ the Green function is called retarded or advanced, respectively, where the naming originates from the time dependence of the Fourier transformed Green function. The Green function itself contains, similarly to the wavefunction, all the physical information of the system. In particular, the expectation value of every physical observable A can be calculated using the Green function,

$$\langle A \rangle = \sum_n f(E_n) \langle n|A|n\rangle \tag{2.9}$$

$$= -\frac{1}{\pi} \mathrm{Im}\,\mathrm{Tr} \int^{E_\mathrm{F}} \mathrm{d}E \, A \, G(E) \quad , \tag{2.10}$$

where we worked at zero temperature, and $f(E)$ is the Fermi-Dirac distribution function being one up to the Fermi level E_F and zero otherwise. For an application to DFT the two main quantities are the charge and magnetization density, which are connected to the operators σ_0 (two-dimensional unit matrix) and $\boldsymbol{\sigma}$, respectively, and can be calculated according to eq. (2.10).

Another strength of a Green function approach lies in the application of perturbation theory. Consider a potential $\Delta V(\boldsymbol{r})$ perturbing the hamiltonian $\mathcal{H}_0$ with the associated wave function

$\Psi_0(\boldsymbol{r}, E)$. The Lippmann-Schwinger equation gives a recursive solution for the wave function of the full system, $\mathcal{H} = \mathcal{H}_0 + \Delta V$, using the Green function of the unperturbed system $G_0(\boldsymbol{r}, \boldsymbol{r}'; E)$,

$$\Psi(\boldsymbol{r}, E) = \Psi_0(\boldsymbol{r}, E) + \int \mathrm{d}\boldsymbol{r}'\, G_0(\boldsymbol{r}, \boldsymbol{r}'; E)\Delta V(\boldsymbol{r}')\Psi(\boldsymbol{r}', E) \quad . \tag{2.11}$$

An even more powerful approach from the perturbative perspective is the Dyson equation, which connects the full Green function $G(E)$ to the Green function of the unperturbed system,

Dyson equation

$$G(E) = G_0(E) + G_0(E)\,\Delta V\, G(E) = G_0(E) + G(E)\,\Delta V\, G_0(E) \quad . \tag{2.12}$$

Both the Dyson equation and the Lippmann-Schwinger equation allow for an iterative solution including arbitrary orders of ΔV, yielding for example for the Dyson equation

$$G(E) = G_0(E) + G_0(E)\,\Delta V\, G_0(E) + G_0(E)\,\Delta V\, G_0(E)\Delta V\, G_0(E) + \ldots \quad . \tag{2.13}$$

Another useful concept is the transition matrix (t-matrix) approach,

$$G(E) = G_0(E) + G_0(E)\,\Delta t\, G_0(E) \quad , \tag{2.14}$$

with

$$\Delta t = \Delta V + \Delta V\, G_0(E)\,\Delta t \quad , \tag{2.15}$$

where the recursive part of the Dyson equation was transferred to the perturbation of the potential.

2.2.2. The fundamentals of KKR

The KKR method is a real space approach utilizing the Green function discussed in the previous section. One of its distinctive features compared to plane wave codes is the underlying geometrical construction. The space is divided into cells, which contain either a single atom or vacuum, using a so-called Voronoi construction. The Voronoi construction for a triagonal lattice is illustrated in Fig. 2.1. The Voronoi cells themselves fill the entire space. However, within KKR there are two different approaches for treating the geometry – the atomic sphere approximation (ASA), which approximates each cell by a sphere containing a spherically-symmetric potential and therefore neglects any inter-cell region, and the full potential method which makes no shape approximations of the potential and describes correctly the interstitial region between the atoms. In this thesis, both approaches are used, but since the full potential approach needs a more general treatment, the following discussion focus on the full potential approach and the resulting simplifications for the ASA are explained later.

Due to the cell construction the spatial coordinates of the KKR Green function are centered around the corresponding sites i and j at $\boldsymbol{R}_i$ and $\boldsymbol{R}_j$, respectively,

$$G(\boldsymbol{X}, \boldsymbol{X}'; E) = G(\boldsymbol{r} + \boldsymbol{R}_i, \boldsymbol{r}' + \boldsymbol{R}_j; E) = G_{ij}(\boldsymbol{r}, \boldsymbol{r}'; E) \quad , \tag{2.16}$$

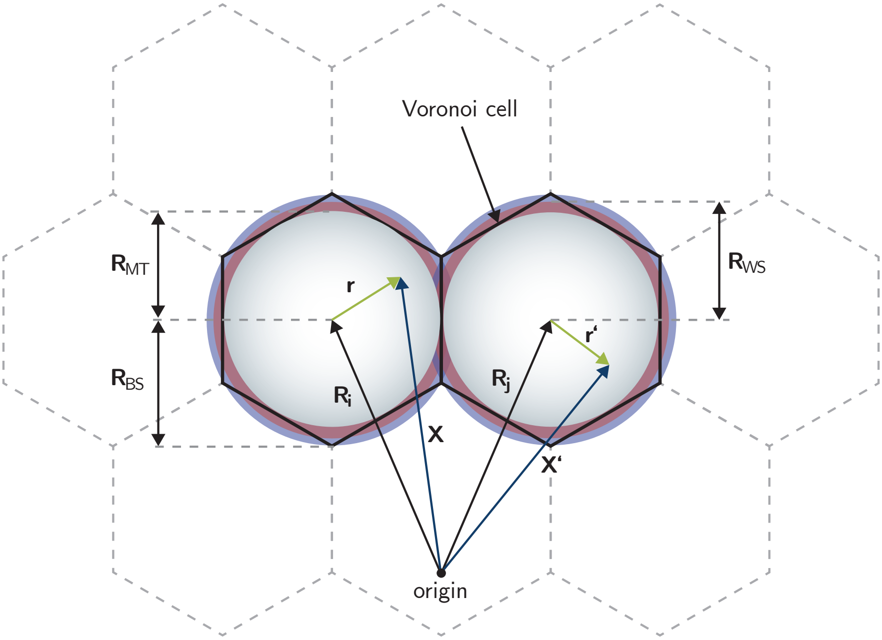

Figure 2.1.: Illustration of the Voronoi construction for an hexagonal lattice. The Voronoi cell of site i is centered at $\boldsymbol{R}_i$ defining a local frame $\boldsymbol{X} = \boldsymbol{r} + \boldsymbol{R}_i$. Each cell has an associated muffin tin radius R_{MT}, which is defined by the largest sphere fitting completely inside the Wigner-Seitz cell, a Wigner-Seitz radius R_{WS}, which defines a sphere having the same volume as the Wigner-Seitz cell, and the radius of the bounding sphere R_{BS}, which is the smallest sphere enclosing the full Wigner-Seitz cell.

as illustrated in Fig. 2.1. Using this separation, the Green function can be split into an on-site contribution and a structural contribution accounting for the multiple scattering,

$$G_{ij}(\boldsymbol{r}, \boldsymbol{r}'; E) = G_i^{\text{on-site}}(\boldsymbol{r}, \boldsymbol{r}'; E)\, \delta_{ij} + G_{ij}^{\text{str}}(\boldsymbol{r}, \boldsymbol{r}'; E) \quad . \tag{2.17}$$

Due to the Voronoi construction the potential of a site i is only defined within the volume $\mathcal{V}_i$ of the corresponding cell

$$V_i(\boldsymbol{r}) = \begin{cases} V_i(\boldsymbol{r}) & , \quad \text{if } \boldsymbol{r} \in \mathcal{V}_i \\ 0 & , \quad \text{else} \end{cases} \quad , \tag{2.18}$$

which gives rise to the definition of the so-called shape function $\Theta_i(\boldsymbol{r})$,

$$\Theta_i(\boldsymbol{r}) = \begin{cases} 1 & , \quad \text{if } \boldsymbol{r} \in \mathcal{V}_i \\ 0 & , \quad \text{else} \end{cases} \quad . \tag{2.19}$$

The potential of each site i is treated in the local frames (see Fig. 2.1) and is expanded in real spherical harmonics,

$$V_i(\boldsymbol{r})\Theta_i(\boldsymbol{r}) = \sum_L V_L(r) Y_L(\hat{r}) \quad , \tag{2.20}$$

where $L = (\ell, m)$ is the combined angular index, $r = |\boldsymbol{r}|$ is the absolute distance, and $\hat{r} = \boldsymbol{r}/r$ is the unit direction. Note that, in the entire thesis instead of complex spherical harmonics real spherical harmonics are used. In this convention, $V_L(r)$ is convoluted with the shape function,

$$V_L(r) = \sum_{L'L''} C^L_{L'L''} V^0_L(r') \Theta_{L''}(r) \quad , \tag{2.21}$$

where the Gaunt coefficient $C^L_{L'L''}$ is defined as

$$C^L_{L'L''} = \int \mathrm{d}\hat{r}\, Y_L(\hat{r}) Y_{L'}(\hat{r}) Y_{L''}(\hat{r}) \quad , \tag{2.22}$$

$V^0_L(r)$ is the expansion of the potential in spherical harmonics without taking any spatial constraint into account and $\Theta_L(r)$ is the expansion coefficient of the shape function. In full potential, the radial argument r is defined up to the radius of the bounding sphere, which is the smallest sphere enclosing the full Wigner-Seitz cell as illustrated in Fig. 2.1.

In the following, the Green function formalism is utilized to solve the Schrödinger equation starting from the free electron gas. Throughout this discussion the Green function, as well as the potential V, have to be understood as 2×2 matrices allowing for the most general treatment including the spin degree of freedom.

Potential free Green function

The Green function and the wave function of the free electron gas can be written as

$$g(\boldsymbol{r}, \boldsymbol{r}'; E) = -\frac{1}{4\pi} \frac{e^{\mathrm{i}\sqrt{E}|\boldsymbol{r}-\boldsymbol{r}'|}}{|\boldsymbol{r}-\boldsymbol{r}'|} \quad \text{and} \quad \Psi^0_{\boldsymbol{k}}(\boldsymbol{r}) = e^{\mathrm{i}\boldsymbol{k}\cdot\boldsymbol{r}} \quad , \tag{2.23}$$

with $\boldsymbol{k} = \hat{k}\sqrt{E}$. Using spherical Bessel and Hankel functions, $j_\ell(r)$ and $h_\ell(r)$, respectively, the Green function of the free electron gas can be expanded in terms of spherical harmonics,

$$g(\boldsymbol{r}, \boldsymbol{r}'; E) = \sum_L Y_L(\hat{r}) g_\ell(r, r'; E) Y_L(\hat{r}') \quad \text{with} \quad g_\ell(r, r'; E) = -\mathrm{i}\sqrt{E}\, j_\ell(\sqrt{E}\, r_<) h_\ell(\sqrt{E}\, r_>) \quad , \tag{2.24}$$

where $r_{</>}$ = min/max$\{r, r'\}$ were used. The Hankel function is irregular in the limit of $r \to 0$, while the Bessel function is regular in the same limit. The Green function fulfills the translational invariance of the free electron gas depending only on the relative distance $|\boldsymbol{r} - \boldsymbol{r}'|$. The wavefunction of the free electron gas can be expressed in terms of a Bessel function,

$$\Psi^0_{\boldsymbol{k}}(\boldsymbol{r}) = e^{\mathrm{i}\boldsymbol{k}\cdot\boldsymbol{r}} = \sum_L 4\pi\, \mathrm{i}^\ell\, Y_L(\hat{k}) j_\ell(\sqrt{E}\, r) Y_L(\hat{r}) \quad . \tag{2.25}$$

On-site solution of the Schrödinger equation

According to the wavefunction of the free electron gas, eq. (2.25), an ansatz for the wavefunction of the full system is

$$\Psi_{\boldsymbol{k}}(\boldsymbol{r}) = \sum_L 4\pi\, \mathrm{i}^\ell\, Y_L(\hat{k}) R^L(\boldsymbol{r};E) \quad , \tag{2.26}$$

where $R^L(\boldsymbol{r};E)$ is the so-called regular solution of the Schrödinger equation, which in a basis of spherical harmonics can be written as,

$$R^L(\boldsymbol{r};E) = \sum_{L'} \frac{1}{r} R^L_{L'}(r;E) Y_{L'}(\hat{r}) \quad , \tag{2.27}$$

depending in general on an angular index L denoting the partial wave component of the original free-electron plane wave, and another index L', which is sued to describe the spatial shape that the partial wave adopts upon scattering by a non-spherical potential. Inserting eqs. (2.25), (2.26), and (2.27) into eq. (2.11), we obtain a set of coupled radial Lippmann-Schwinger equations,

$$R^{L'}_L(r;E) = r j_\ell(\sqrt{E}r)\,\delta_{LL'} + \int \mathrm{d}r'\, g_\ell(r,r';E) \sum_{L''} V_{LL''}(r')\, R^{L'}_{L''}(r';E) \quad , \tag{2.28}$$

where matrix elements of the non-spherical potential with two spherical harmonics were used,

$$V(\boldsymbol{r}) = \sum_{LL'} Y_L(\hat{r}) V_{LL'}(r) Y_{L'}(\hat{r}) \quad \text{with} \quad V_{LL'}(r) = \sum_{L''} C^{L''}_{LL'} V_{L''}(r) \quad . \tag{2.29}$$

In addition to the regular solution, a couple of other basis functions are needed for the construction of the on-site Green function. The first one is the irregular solution based on the Hankel functions, which will be called $S^{L'}_L(r;E)$. Furthermore, the Schrödinger equation being a set of coupled second-order linear differential equations allows for right and left solutions if the potential is non-diagonal in spin space (see Ref. [94] for details). The right solutions were discussed above, while the left solutions are called $\overline{R}^{L'}_L$ and $\overline{S}^{L'}_L$ for the regular and irregular solution, respectively, which are 2 dimensional row vectors in spin space. The radial wave functions can be obtained from

$$S^{L'}_L(r;E) = r h_\ell(\sqrt{E}r)\,\beta^{L'}_L + \int \mathrm{d}r'\, g_\ell(r,r';E) \sum_{L''} V_{LL''}(r')\, S^{L'}_{L''}(r';E) \quad , \tag{2.30}$$

$$\overline{R}^{L'}_L(r;E) = r j_\ell(\sqrt{E}r)\,\delta_{LL'} + \int \mathrm{d}r' \sum_{L''} \overline{R}^{L'}_{L''}(r';E)\, V_{L''L}(r')\, g_\ell(r',r;E) \quad , \tag{2.31}$$

$$\overline{S}^{L'}_L(r;E) = \overline{\beta}^{L'}_L\, r h_\ell(\sqrt{E}r) + \int \mathrm{d}r' \sum_{L''} \overline{S}^{L'}_{L''}(r';E)\, V_{L''L}(r')\, g_\ell(r',r;E) \quad , \tag{2.32}$$

with

$$\beta^{L'}_L = \delta_{LL'} - \sqrt{E} \int \mathrm{d}r'\, r j_\ell(\sqrt{E}r') \sum_{L''} V_{LL''}(r')\, S^{L'}_{L''}(r';E) \quad , \tag{2.33}$$

$$\overline{\beta}_L^{L'} = \delta_{LL'} - \sqrt{E} \int \mathrm{d}r' \sum_{L''} \overline{S}_{L''}^{L'}(r';E)\, V_{L''L}(r')\, r j_\ell(\sqrt{E}r') \quad . \tag{2.34}$$

The on-site Green function can be obtained using the right and left solutions via (see e.g. [94]),

$$G_{LL'}^{\text{on-site}}(\boldsymbol{r},\boldsymbol{r}';E) = -\mathrm{i}\sqrt{E} \sum_{L''} \begin{cases} R_L^{L''}(r;E)\overline{S}_{L'}^{L''}(r';E) & , \quad \text{if} \quad r' > r \\ S_L^{L''}(r;E)\overline{R}_{L'}^{L''}(r';E) & , \quad \text{if} \quad r > r' \end{cases} \quad . \tag{2.35}$$

Multiple scattering theory

The second crucial ingredient to the full KKR Green function is the structural part, which takes apart from all the multiple scatterings also geometrical details into account. Starting again from the free electron gas the Green function between the two different sites i and j can be expanded as

$$g(\boldsymbol{r}+\boldsymbol{R}_i,\boldsymbol{r}'+\boldsymbol{R}_j;E) = \sum_{LL'} Y_L(\hat{r}) j_\ell(\sqrt{E}r)\, g_{LL'}^{ij}(E)\, j_{\ell'}(\sqrt{E}r') Y_{L'}(\hat{r}') \quad , \tag{2.36}$$

where the coefficient $g_{LL'}^{ij}(E)$ can be derived from a theorem for the transformation of Hankel functions,

$$g_{LL'}^{ij}(E) = -(1-\delta_{ij}) 4\pi\, \mathrm{i}\, \sqrt{E} \sum_{L''} \mathrm{i}^{\ell-\ell'+\ell''} C_{LL'}^{L''}\, h_{\ell''}(\sqrt{E}\,|\boldsymbol{R}_i - \boldsymbol{R}_j|)\, Y_{L''}\Big(\frac{\boldsymbol{R}_i - \boldsymbol{R}_j}{|\boldsymbol{R}_i - \boldsymbol{R}_j|}\Big) \quad . \tag{2.37}$$

Using a proper ansatz for the total Green function of the system,

$$G_{ij}(\boldsymbol{r},\boldsymbol{r}';E) = G_i^{\text{on-site}}(\boldsymbol{r},\boldsymbol{r}';E)\,\delta_{ij} + \sum_{LL'} R_L^i(\boldsymbol{r};E)\, G_{LL'}^{ij}(E)\, \overline{R}_{L'}^j(\boldsymbol{r}';E) \tag{2.38}$$

and the Dyson equation from eq. (2.12) the following Dyson-like equation for the structural part of the Green function can be proven (see e.g. [94]),

$$G_{LL'}^{ij}(E) = g_{LL'}^{ij}(E) + \sum_k g_{LL''}^{ik}(E)\, t_{L''L'''}^k(E)\, G_{L'''L'}^{kj}(E) \quad , \tag{2.39}$$

where $t_{LL'}^k(E) = \int \mathrm{d}\boldsymbol{r}\, r j_\ell(\sqrt{E}r)\, V^k(\boldsymbol{r})\, R_{L'}^k(\boldsymbol{r};E)$ describes the scattering at the potential of site k. Thus, successively iterating the Dyson equation like shown in eq. 2.13 describes free waves being scattered at different potentials corresponding to different sites, which is the essence of multiple scattering theory.

Embedding scheme

The embedding scheme in KKR is used to modulate a host system in real space by either changing the chemical nature of an existing atom or deposit an atom on a host surface. The host system, e.g. a two dimensional extended surface, is described by the host hamiltonian $\mathcal{H}_{\text{host}}$ and assumed to be solved using the KKR formalism described above implicating that the host Green function (on-site and structural part) are known. The main idea of the embedding is

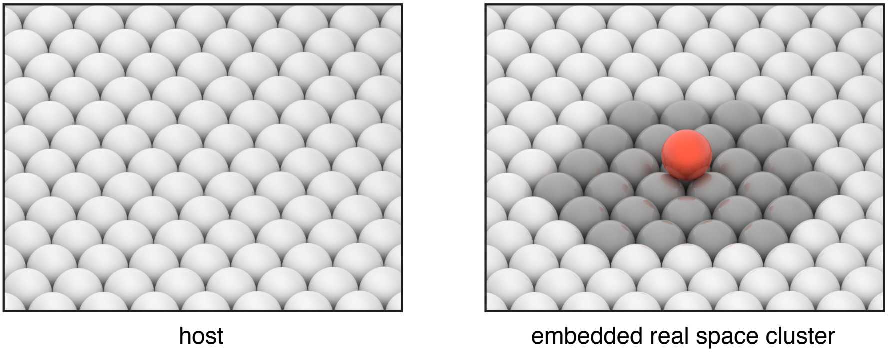

Figure 2.2.: Illustration of the embedding scheme. The host (light grey spheres) is the reference system used for a real space embedding (dark grey spheres) of a perturbation ΔV as discussed in relation to eq. (2.40).

to treat the embedded structure as a local impurity, which can be described by a perturbation ΔV with a finite spatial range, which can be ensured using the method of repulsive potential [48]. The Dyson equation can be utilized to obtain the full Green function in real space,

$$G = G_{\text{host}} + G_{\text{host}}\,\Delta V\,G = G_{\text{host}} + G_{\text{host}}\,\Delta V\,G_{\text{host}} + G_{\text{host}}\,\Delta V\,G_{\text{host}}\,\Delta V\,G_{\text{host}} + \dots \quad , \tag{2.40}$$

where the perturbations act as scattering centers at the impurities. The embedding scheme is illustrated in Figure 2.2.

The rigid spin approximation

The spin-dependent potential in the local KKR codes is treated in the so-called rigid spin approximation, which is illustrated in Figure 2.3. Within each Voronoi cell the magnetization is assumed to be collinear pointing in the direction of the magnetic moment, which is defined by the spatial integral of the spin density, eq. (2.4), over the volume of site i,

$$\boldsymbol{m}_i = \int_{\mathcal{V}_i} \mathrm{d}\boldsymbol{r}\,\boldsymbol{m}(\boldsymbol{r}) \quad . \tag{2.41}$$

This results in an exchange-correlation magnetic field of the form,

$$\boldsymbol{B}_i^{\text{xc}}(\boldsymbol{r}) = B_i^{\text{xc}}(r)\,\boldsymbol{e}_i \quad , \tag{2.42}$$

where $\boldsymbol{e}_i = \boldsymbol{m}_i/|\boldsymbol{m}_i|$ is the direction of the magnetic moment of site i. Note that the on-site and the multiple scattering solutions treat the magnetization with the full non-sphericity and the rigid spin approximation is only used for the input potential.

Atomic sphere approximation compared to full potential

The previously discussed KKR formalism applies to the full potential treatment of the atomic potentials and related geometries. In the often used atomic sphere approximation the actual shape of the Voronoi cells is neglected and every atom is considered to be spherical.

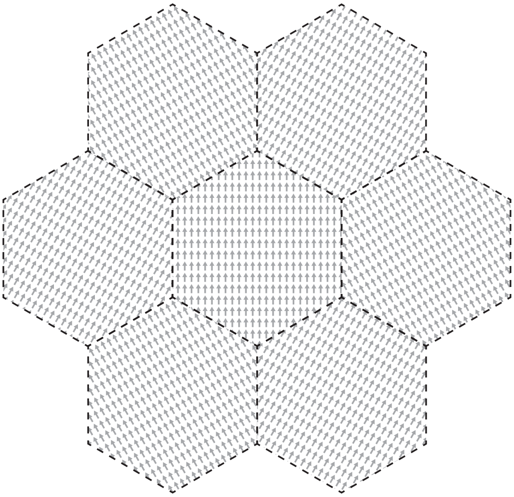

Figure 2.3.: Illustration of the rigid spin approximation. The arrows indicate the magnetization, which is assumed collinear within each Voronoi cell.

This implies that the potential does not have any non-spherical contribution, which in turn implies $V_{LL'}(r) = \delta_{LL'}\delta_{L0}V(r)$. Most of the previously discussed equations simplify drastically, e.g. the radial Lippmann-Schwinger equation, eq. (2.28), couples only radial wavefunction of the same angular shape, which only depend on ℓ, and the scatterings described in eq. (2.39) are isotropic.

However, note that the theoretical and computational simplification of the ASA come at the cost of numerical accuracy. For some quantities a treatment in full potential taking all non-sphericities into account is crucial. Well-known examples are magnetic exchange interactions and magnetic anisotropies (see chapters 4 and 6). On the other hand, some properties require further reductions of the computational costs. An example is the magnetic susceptibility, for which a projection scheme simplifying the radial basis of the KKR formalism is introduced in the next section.

The projection scheme

Since the KKR radial basis functions are explicitly energy-dependent (see e.g. eq. (2.28)), the general Green function becomes in the ASA a $n \times n$ matrix with $n = \#\text{atom} \times (\ell_{\text{max}} + 1)^2 \times \#\text{spins} \times \#\text{energies}$. In a typical calculation of transition elements the angular momentum cut-off is set to $\ell_{\text{max}} = 3$. For the energy integration needed to calculate the expectation value of any observable (see eq. 2.10), complex analysis is used to replace the real axis integration by an energy contour in the complex plane [106], which typically contains around 30 energy points. The Dyson equation requires an inversion of the Green function, which has the numerical complexity $\mathcal{O}(n^3)$. Since the number of atoms as well as the spin is fixed, only the angular momentum cut-off and the energy-dependence of the basis can be used to simplify the numerical complexity of the problem.

The idea of the projection scheme is to transfer the energy dependence to the Green function matrix element and to replace the energy dependent radial basis set by a smaller radial basis set described by $\phi_{i\ell b}(r)$ with $b = \{1, 2, \ldots\}$. The projection scheme is described in Ref. [107]. In total the Green function in the projection basis can be written as,

$$G_{ij}(\boldsymbol{r}, \boldsymbol{r}'; E) = \sum_{\substack{Lbs \\ L'b's'}} Y_L(\hat{r})\phi_{i\ell b}(r)\, G_{iLbs;jL'b's'}(E)\, \phi_{j\ell' b'}(r')Y_{L'}(\hat{r}') \quad . \tag{2.43}$$

The projected basis is constructed from the regular radial basis functions evaluated at a set of energy points $\{E_b\}$ within the range of valence states,

$$\overline{\phi}_{i\ell b}(r) = \frac{R^i_\ell(r; E_b)}{\sqrt{\int \mathrm{d}r'\, r'^2 (R^i_\ell(r'; E_b))^2}} \quad . \tag{2.44}$$

From the constructed basis set the overlap matrix is calculated,

$$\mathcal{O}^{i\ell}_{bb'} = \int \mathrm{d}r\, r^2 \overline{\phi}_{i\ell b}(r)\overline{\phi}_{i\ell b'}(r) \quad , \tag{2.45}$$

which is used to construct the basis $\phi_{i\ell b}(r)$ from linear combinations corresponding to the eigenvectors of the overlap matrix. Typically only two basis functions corresponding to the two largest eigenvalues are kept, which results in a drastic computational simplification and is quite similar in structure to the linear muffin-tin orbital method [108].

2.2.3. KKR code familiy

In Jülich different KKR codes incorporating the different aspects presented in the previous section are developed [109]. The KKRhost code solves the KKR equations for extended systems, like bulk or two-dimensional slabs. It gives access to all important ground-state properties including magnetic properties and it can be seen as the initial step of any real space calculation, since it sets the foundation of the real space embedding using the Dyson equation by giving access to the reference Green functions. The real space embedding is done in the KKRimp code, which can be used to describe local perturbations. The perturbations can be either additional atoms deposited on a surface (adatoms), or a change of the chemical nature of a host atom (inatom). Both, the host and the impurity code, can use full-potential as well as ASA, can add SOC to the scalar relativistic approximation, can treat non-collinear magnetism, and can be used to extract magnetic exchange parameters.

In addition to the main workhorses presented above, the KKRsusc code being an add-on of the KKRimp code incorporates the ideas of a projection basis. It allows for a more efficient treatment of all previously mentioned properties. Its main purpose, however, is the calculation of the magnetic susceptibility, which will be presented in section 2.3.

2.2.4. Code developments

For the several different effects discussed in this thesis, different code developments were necessary, which are described in the following.

Ground-state currents

The development of the calculation scheme for ground-state charge and spin currents was part of my Master thesis [77]. Since it is needed for the calculation of the non-local orbital moment in Chapter 3, it will be discussed here. Before we start with the actual discussion of the ground-state currents within the KKR formalism, a brief reminder of the origin of ground-state currents is given in the following.

Continuity equation

Starting from a general static single-particle hamiltonian in an external magnetic field,

$$\mathcal{H} = (\boldsymbol{p} - e\boldsymbol{A}(\boldsymbol{r}))^2 - \mu_{\mathrm{B}}\boldsymbol{\sigma}\cdot\boldsymbol{B}(\boldsymbol{r}) + V(\boldsymbol{r}) \quad , \tag{2.46}$$

a continuity equation for the particle density, $n(\boldsymbol{r},t) = \Psi^\dagger(\boldsymbol{r},t)\Psi(\boldsymbol{r},t)$, can be derived using the time-dependent Schrödinger equation,

$$\begin{aligned} \partial_t n(\boldsymbol{r},t) &= \Psi^\dagger(\boldsymbol{r},t)\left(\partial_t\Psi(\boldsymbol{r},t)\right) + \left(\partial_t\Psi^\dagger(\boldsymbol{r},t)\right)\Psi(\boldsymbol{r},t) \\ &= -\mathrm{i}\Psi^\dagger(\boldsymbol{r},t)\left(\mathcal{H}(\boldsymbol{r})\Psi(\boldsymbol{r},t)\right) + \mathrm{i}\left(\mathcal{H}(\boldsymbol{r})\Psi(\boldsymbol{r},t)\right)^\dagger\Psi(\boldsymbol{r},t) \\ &= \boldsymbol{\nabla}\cdot\boldsymbol{j}(\boldsymbol{r},t) \quad . \end{aligned} \tag{2.47}$$

The continuity equation describes the time-dependent change of the particle density due to a source or a sink of particles related to the particle current $\boldsymbol{j}(\boldsymbol{r},t)$. In the ground state the particle density has to be steady resulting in a divergence free particle current. The current is defined by

$$\begin{aligned} \boldsymbol{\nabla}\cdot\boldsymbol{j}(\boldsymbol{r},t) &= -\mathrm{i}\left[\Psi^\dagger(\boldsymbol{r},t)\left((\boldsymbol{p}-e\boldsymbol{A}(\boldsymbol{r}))^2\Psi(\boldsymbol{r},t)\right) - \left((\boldsymbol{p}-e\boldsymbol{A}(\boldsymbol{r}))^2\Psi(\boldsymbol{r},t)\right)^\dagger\Psi(\boldsymbol{r},t)\right] \\ &= \boldsymbol{\nabla}\cdot\left\{\left[\Psi^\dagger(\boldsymbol{r},t)\,\overrightarrow{\boldsymbol{p}}\,\Psi(\boldsymbol{r},t) - \Psi^\dagger(\boldsymbol{r},t)\,\overleftarrow{\boldsymbol{p}}\,\Psi(\boldsymbol{r},t)\right] - e\boldsymbol{A}(\boldsymbol{r})\Psi^\dagger(\boldsymbol{r},t)\Psi(\boldsymbol{r},t)\right\} \quad , \end{aligned} \tag{2.48}$$

where the notation $(\boldsymbol{p}\Psi)^\dagger = -\Psi^\dagger\overleftarrow{\boldsymbol{p}}$ was used, indicating that the action of the momentum operator in real space, $\boldsymbol{p} = -i\boldsymbol{\nabla}$, is to the left side of the operator. The first part of eq. (2.48) is the so-called paramagnetic current, which can be represented by the current operator,

$$\boldsymbol{j}_{\text{para}} = -\mathrm{i}\left(\overrightarrow{\boldsymbol{\nabla}} - \overleftarrow{\boldsymbol{\nabla}}\right) \quad , \tag{2.49}$$

while the second part is the diamagnetic current related to an external magnetic field and its corresponding vector potential,

$$\boldsymbol{j}_{\text{dia}}(\boldsymbol{r}) = -e\boldsymbol{A}(\boldsymbol{r})\,\boldsymbol{n}(\boldsymbol{r}) \tag{2.50}$$

Both the Zeeman term as well as the external potential do not contribute to the divergence of the current. However, it can be shown that the Zeeman term yields a finite divergence-free contribution to the ground state current [110],

$$\boldsymbol{j}_{\text{Zeeman}}(\boldsymbol{r}) = \boldsymbol{\nabla}\times\boldsymbol{m}(\boldsymbol{r}) \quad , \tag{2.51}$$

where $\boldsymbol{m}(\boldsymbol{r})$ is the magnetization density. Another source of ground-state currents is the spin-orbit coupling, which by using the form eq. (2.5) for the hamiltonian yields,

$$\boldsymbol{j}_{\mathsf{SOC}}(\boldsymbol{r}) = \frac{1}{c^2}\,\boldsymbol{m}(\boldsymbol{r}) \times \boldsymbol{E}(\boldsymbol{r}) \quad . \tag{2.52}$$

However, this contribution was shown to be negligible [77] and is not discussed in this thesis. The SOC itself is important for the ground-state currents to emerge since it lifts the orbital degeneracy and therefore is the main driving mechanism for finite paramagnetic ground-state currents. Another driving mechanism is an emergent magnetic field in non-collinear magnetic structures [111].
In the remaining thesis, the term charge current will be used synonymously for the paramagnetic contribution to the charge current.

The paramagnetic current of atom i can be evaluated according to eq. (2.10),

$$\boldsymbol{j}_i(\boldsymbol{r}) = -\mathrm{i} \lim_{\boldsymbol{r}'\to\boldsymbol{r}} \left(\boldsymbol{\nabla}_{\boldsymbol{r}} - \boldsymbol{\nabla}_{\boldsymbol{r}'}\right) \mathrm{Tr}\, \boldsymbol{\sigma}_0\, \rho_{ii}(\boldsymbol{r}, \boldsymbol{r}'; E) \quad , \tag{2.53}$$

where we used the density matrix defined as,

$$\rho_{ij}(\boldsymbol{r}, \boldsymbol{r}') = -\frac{1}{\pi} \int^{E_{\mathsf{F}}} \mathrm{d}E \; \mathrm{Im}\, G_{ij}(\boldsymbol{r}, \boldsymbol{r}'; E) \quad . \tag{2.54}$$

The groundstate currents are calculated in the ASA using the projection scheme and were implemented in the KKRsusc code. Therefore, the density matrix is given in the following basis,

$$\rho_{ij}(\boldsymbol{r}, \boldsymbol{r}') = \sum_{\substack{Lbs \\ L'b's'}} Y_L(\hat{r}) \phi_{i\ell b}(r)\, \rho_{iLbs;jL'b's'}\, \phi_{j\ell'b'}(r') Y_{L'}(\hat{r}') \quad . \tag{2.55}$$

The main operation to calculate the current is the action of the gradient on the KKR projection basis. In a brute force approach, the gradient could be calculated on a regular 3-dimensional grid, which, however, would neither be computationally efficient nor accurate. Here we use an elegant approach utilizing the angular momentum operator arriving at an analytical formula for the spherical degree of freedom in combination with a derivative on the radial mesh. Using the definition of the angular momentum operator in real space, $\boldsymbol{L} = -\mathrm{i}\, \boldsymbol{r} \times \boldsymbol{\nabla}$, and the identity

$$\boldsymbol{a} \times (\boldsymbol{b} \times \boldsymbol{c}) = \boldsymbol{b}\,(\boldsymbol{a} \cdot \boldsymbol{c}) - \boldsymbol{c}\,(\boldsymbol{a} \cdot \boldsymbol{b}) \quad , \tag{2.56}$$

yields,

$$\boldsymbol{r} \times \boldsymbol{L} = -\mathrm{i}\, \boldsymbol{r}(\boldsymbol{r} \cdot \boldsymbol{\nabla}) + \mathrm{i} r^2 \boldsymbol{\nabla} \quad \Rightarrow \quad \boldsymbol{\nabla} = \hat{r}\, \partial_r - \mathrm{i}\, \frac{1}{r}\, \hat{r} \times \boldsymbol{L} \quad . \tag{2.57}$$

The action of the angular momentum operator on the spherical harmonics basis is analytically known and can be expressed in terms of the angular momentum matrix elements $L_{\ell,mm'}$,

$$\boldsymbol{\nabla} Y_{\ell m}(\hat{r}) = -\mathrm{i}\, \frac{1}{r}\, \hat{r} \times \sum_{m'} L_{\ell,mm'}\, Y_{\ell m'}(\hat{r}) \quad . \tag{2.58}$$

The spatial angular dependence in the unit vector, $\hat{r}$, can be expressed in spherical harmonics with $\ell = 1$ by writing,

$$\hat{r} = \sqrt{\frac{4\pi}{3}} \left(Y_{(\ell,m)_x}(\hat{r}),\ Y_{(\ell,m)_y}(\hat{r}),\ Y_{(\ell,m)_z}(\hat{r}) \right) \quad , \tag{2.59}$$

with $(\ell, m)_x = (1, 1)$, $(\ell, m)_y = (1, -1)$, and $(\ell, m)_z = (1, 0)$. Combining the spherical harmonics in eq. (2.58) and taking the radial basis into account the derivative with respect to $\alpha = \{x, y, z\}$ can be written as,

$$\partial_\alpha\, \phi_{i\ell b}(r) Y_{\ell m}(\hat{r}) = \sqrt{\frac{4\pi}{3}} \sum_{\ell' m'} \left[C^{\ell' m'}_{\ell m,(\ell m)_\alpha} \frac{\mathrm{d}\phi_{i\ell b}(r)}{\mathrm{d}r} - \mathrm{i}\, \frac{\phi_{i\ell b}(r)}{r} \sum_{m''} \epsilon_{\alpha\beta\gamma} C^{\ell' m'}_{\ell m'',(\ell m)_\beta} L^\gamma_{\ell, m m''} \right] Y_{\ell' m'}(\hat{r}) \quad . \tag{2.60}$$

Combining eqs. (2.53) with (2.55) and (2.60) allows for an efficient and elegant calculation of the ground-state current of atom i, $\boldsymbol{j}_i(\boldsymbol{r})$, within the KKR basis yielding the current in a basis of spherical harmonics,

$$\boldsymbol{j}_i(\boldsymbol{r}) = \sum_{\ell m} \boldsymbol{j}_i^{\ell m}(r) Y_{\ell m}(\hat{r}) \quad . \tag{2.61}$$

With this small recap the necessary theoretical and numerical developments of my Master thesis were discussed. The following developments are all part of this PhD thesis.

Magnetic stray fields

Following classical electrodynamics any electrical current gives rise to a magnetic field (see any standard textbook on classical electrodynamics, e.g. [75]). Starting from the Biot-Savart law the vector potential, $\boldsymbol{A}(\boldsymbol{r})$, is related to a finite current distribution in the volume $\mathcal{V}$ by,

$$\boldsymbol{A}(\boldsymbol{r}) = \frac{\mu_0}{4\pi} \int_{\mathcal{V}} \mathrm{d}\boldsymbol{r}'\, \frac{\boldsymbol{j}(\boldsymbol{r}')}{|\boldsymbol{r} - \boldsymbol{r}'|} \quad , \tag{2.62}$$

where the Coulomb gauge, $\boldsymbol{\nabla} \cdot \boldsymbol{A} = 0$, was used. For $\boldsymbol{r} > \boldsymbol{r}'$ the denominator can be expanded using a multipole expansion,

$$\frac{1}{|\boldsymbol{r} - \boldsymbol{r}'|} = \frac{1}{r} + \frac{\boldsymbol{r} \cdot \boldsymbol{r}'}{r^3} + \frac{3(\boldsymbol{r} \cdot \boldsymbol{r}')^2 - r'^2 r^2}{2r^5} + \ldots \quad . \tag{2.63}$$

The first term gives rise to the so-called monopole contribution,

$$\boldsymbol{A}^{(0)}(\boldsymbol{r}) = \frac{\mu_0}{4\pi} \frac{1}{r} \int_{\mathcal{V}} \mathrm{d}\boldsymbol{r}'\, \boldsymbol{j}(\boldsymbol{r}') \quad . \tag{2.64}$$

For a finite bound current, which vanishes outside the volume $\mathcal{V}$ and on its surface $\partial\mathcal{V}$, the monopole term vanishes, since the continuity equation, $\boldsymbol{\nabla} \cdot \boldsymbol{j} = 0$, prohibits any sources and sinks of current, which results in no finite net current, $\int \mathrm{d}\boldsymbol{r}\, \boldsymbol{j}(\boldsymbol{r}) = 0$. However, if the space is split into various non-overlapping cells, $\mathcal{V} = \{\mathcal{V}_1, \mathcal{V}_2, \ldots\}$, similarly to the geometry within KKR, the current does not need to be bound within each cell but only within the entire volume.

As a consequence finite monopole contributions can appear. Working in the local frame of cell i, $\boldsymbol{r}' \rightarrow \boldsymbol{r}' + \boldsymbol{R}_i$, and expanding in the small local vector $\boldsymbol{r}'$ the multipole expansion, eq. (2.63), with the proper replacements is valid for all $\boldsymbol{r} - \boldsymbol{R}_i > \boldsymbol{r}'$. The total vector potential from all cells can be written as,

$$\begin{aligned}\boldsymbol{A}(\boldsymbol{r}) = \frac{\mu_0}{4\pi}\sum_i \int_{\mathcal{V}_i} \mathrm{d}\boldsymbol{r}'\, \boldsymbol{j}^i(\boldsymbol{r}') \Bigg[& \frac{1}{|\boldsymbol{r}-\boldsymbol{R_i}|} + \frac{\boldsymbol{r}'\cdot(\boldsymbol{r}-\boldsymbol{R}_i)}{|\boldsymbol{r}-\boldsymbol{R_i}|^3} \\ & + \frac{3(\boldsymbol{r}'\cdot(\boldsymbol{r}-\boldsymbol{R}_i))^2 - r'^2|\boldsymbol{r}-\boldsymbol{R_i}|^2}{2|\boldsymbol{r}-\boldsymbol{R_i}|^5} + \dots \Bigg] \quad . \end{aligned} \tag{2.65}$$

The magnetic field $\boldsymbol{B}(\boldsymbol{r})$ is defined by the curl of the vector potential yielding

$$\begin{aligned}\boldsymbol{B}(\boldsymbol{r}) = \boldsymbol{\nabla}\times\boldsymbol{A}(\boldsymbol{r}) = \frac{\mu_0}{4\pi}\sum_i \epsilon_{abc}\hat{e}_c \Bigg\{ & \mathcal{M}^i_a \frac{r_b - R^i_b}{|\boldsymbol{r}-\boldsymbol{R}_i|^3} + \mathcal{D}^i_{ad}\frac{3(r_d - R^i_d)}{|\boldsymbol{r}-\boldsymbol{R}_i|^5}(r_b - R^i_b) - \mathcal{D}^i_{ab}\frac{1}{|\boldsymbol{r}-\boldsymbol{R}_i|^3} \\ & -\mathcal{Q}^i_{abd}\frac{3(r_d - R^i_d)}{|\boldsymbol{r}-\boldsymbol{R}_i|^5} + \mathcal{Q}^i_{ade}\frac{15(r_d - R^i_d)(r_e - R^i_e)}{2|\boldsymbol{r}-\boldsymbol{R}_i|^7}(r_b - R^i_b) - \mathcal{Q}^i_{add}\frac{3}{2|\boldsymbol{r}-\boldsymbol{R}_i|^5}(r_b - R^i_b)\Bigg\} \quad , \end{aligned} \tag{2.66}$$

where the monopole contribution $\mathcal{M}$ is defined as,

$$\mathcal{M}^i_a = \int_{\mathcal{V}_i} \mathrm{d}\boldsymbol{r}\, j_a(\boldsymbol{r}) \quad , \tag{2.67}$$

which is the net current flowing through cell i, the dipole tensor $\mathcal{D}$ is defined as,

$$\mathcal{D}^i_{ab} = \int_{\mathcal{V}_i} \mathrm{d}\boldsymbol{r}\, j_a(\boldsymbol{r})\, r_b \quad , \tag{2.68}$$

and the quadrupole tensor $\mathcal{Q}$ is defined as,

$$\mathcal{Q}^i_{abc} = \int_{\mathcal{V}_i} \mathrm{d}\boldsymbol{r}\, j_a(\boldsymbol{r})\, r_b\, r_c \quad . \tag{2.69}$$

For a finite current distribution (no monopole contribution) the identity, $\int \mathrm{d}\boldsymbol{r}\, r_\alpha\, j_\beta(\boldsymbol{r}) = -\int \mathrm{d}\boldsymbol{r}\, r_\beta\, j_\alpha(\boldsymbol{r})$, can be derived [112], which after a few lines of algebra yields the well-known form for the magnetic field of a single dipole,

$$\boldsymbol{B}(\boldsymbol{r}) = \frac{\mu_0}{4\pi}\left[\frac{3(\boldsymbol{r}\cdot\boldsymbol{m})\,\boldsymbol{r}}{r^5} - \frac{\boldsymbol{m}}{r^3}\right] \quad , \tag{2.70}$$

where the dipole moment $\boldsymbol{m}$ is defined via the current by,

$$\boldsymbol{m} = \frac{1}{2}\int \mathrm{d}\boldsymbol{r}\, \boldsymbol{r}\times\boldsymbol{j}(\boldsymbol{r}) \quad , \tag{2.71}$$

and the quadrupole contribution was neglected. In the far-field, where $|\boldsymbol{r}| \gg |\boldsymbol{R}_j|$ with $\boldsymbol{R}_j$ being the maximal range of a finite current distribution, eq. (2.66) approaches the magnetic field of a single dipole, eq. (2.70).

Applications of ground-state currents and magnetic stray fields will be discussed in Chapter 3 in more detail.

Non-collinear magnetic fields

An important feature of any first-principles code treating magnetism is an external magnetic field. In its former version the KKRimp code was able to treat non-collinearity, but magnetic fields could only be applied collinearly to the magnetic moments. A part of this work is the generalization to arbitrary magnetic fields.

For the sake of simplicity, assume a homogeneous spin-only magnetic field within a cell,

$$\boldsymbol{B}(\boldsymbol{r}) = \boldsymbol{B}_0 = \boldsymbol{B}_0\sqrt{4\pi}Y_0(\hat{r}) \quad . \tag{2.72}$$

The magnetic field is only defined within the cell, which can be obtained using a convolution with the shape functions of the cell,

$$\boldsymbol{B}_L(r) = \Theta_L(r)\boldsymbol{B}_0 \quad , \tag{2.73}$$

yielding the non-spherical dependence solely from the shape function. Similarly to the potential the shape functions (and magnetic fields) need to be expanded in a double spherical harmonics basis,

$$\Theta_{LL'}(r) = \sum_{L''} C_{LL'}^{L''}\Theta_{L''}(r) \quad . \tag{2.74}$$

Explicitly writing the spin dependence of the potential is,

$$V_{LL'}(r) = \begin{pmatrix} V_{LL'}^{\downarrow\downarrow}(r) & V_{LL'}^{\downarrow\uparrow}(r) \\ V_{LL'}^{\uparrow\downarrow}(r) & V_{LL'}^{\uparrow\uparrow}(r) \end{pmatrix} \quad , \tag{2.75}$$

using the $\{\downarrow,\uparrow\}$ basis similarly to the KKR codes, which yields for the magnetic field

$$B_{LL'}(r) = \begin{pmatrix} -B_z & B_x + iB_y \\ B_x - iB_y & B_z \end{pmatrix}\Theta_{LL'}(r) \quad . \tag{2.76}$$

The magnetic field in this form can be added to the potential. It opens new possibilities ranging from the treatment of non-collinear structures in external magnetic fields to the stabilization of arbitrary non-collinear configurations using constraining fields [113–115] and the extraction of magnetic exchange interactions using magnetic torques [59, 116]. The torques and constraining fields will be discussed in the following.

Magnetic torques

For any magnetic configuration, which is not the ground state configuration of the particular system, a magnetic torque is exerted on the magnetic moment. The torque acting on the magnetic moment j can be calculated via the derivative of the energy with respect to the direction of the magnetic moment, $\hat{e}_j$, which is similar to the definition of a force but using the spherical magnetic degrees of freedom. In the Kohn-Sham framework, the corresponding energy is the so-called band energy, which is the sum of all occupied single particle eigenstates. Using the Green function formalism in the rigid spin approximation and eq. (2.10) it can be written as,

$$\epsilon_{\text{band}} = -\frac{1}{\pi}\text{Im Tr}\int^{E_{\text{F}}} \mathrm{d}E\,(E - E_{\text{F}})\sum_i \int_{\mathcal{V}_i} \mathrm{d}\boldsymbol{r}\; G_{ii}(\boldsymbol{r},\boldsymbol{r};E) \quad , \tag{2.77}$$

with the Green function being defined as the resolvent of the single-particle Kohn-Sham hamiltonian, eq. (2.3), $G(E) = (E - \mathcal{H})^{-1}$. The derivative of an inverse matrix can be calculated using the identity,

$$\mathbf{1} = AA^{-1} \Rightarrow 0 = A'A^{-1} + A(A^{-1})' \Rightarrow (A^{-1})' = -A^{-1}A'A^{-1} \quad , \tag{2.78}$$

which applied to the derivative of the Green function with respect to the direction of the magnetic moment yields,

$$\begin{aligned}\frac{\delta G_{ii}(\boldsymbol{r},\boldsymbol{r};E)}{\delta \hat{e}_j} &= \sum_k \int_{\mathcal{V}_k} \mathrm{d}\boldsymbol{r}'\, G_{ik}(\boldsymbol{r},\boldsymbol{r}';E)\, \frac{\delta \mathcal{H}_k}{\delta \hat{e}_j}\, G_{ki}(\boldsymbol{r}',\boldsymbol{r};E) \\ &= -\sum_k \int_{\mathcal{V}_k} \mathrm{d}\boldsymbol{r}'\, G_{ik}(\boldsymbol{r},\boldsymbol{r}';E)\, \boldsymbol{\sigma} \cdot \frac{\delta \boldsymbol{B}_k}{\delta \hat{e}_j}\, G_{ki}(\boldsymbol{r}',\boldsymbol{r};E) \\ &= -\int_{\mathcal{V}_j} \mathrm{d}\boldsymbol{r}'\, G_{ij}(\boldsymbol{r},\boldsymbol{r}';E)\, \boldsymbol{\sigma}\, G_{ji}(\boldsymbol{r}',\boldsymbol{r};E)\, B_j^{\text{xc}}(\boldsymbol{r}') \quad .\end{aligned} \tag{2.79}$$

Using the energy derivative of the Green function,

$$\frac{\mathrm{d}G_{ii}(\boldsymbol{r},\boldsymbol{r};E)}{\mathrm{d}E} = -\sum_k \int_{\mathcal{V}_k} \mathrm{d}\boldsymbol{r}'\, G_{ik}(\boldsymbol{r},\boldsymbol{r}';E)\, G_{ki}(\boldsymbol{r}',\boldsymbol{r};E) \quad , \tag{2.80}$$

a simple form for the magnetic torque can be obtained,

$$\begin{aligned}\boldsymbol{\tau}_j = -\frac{\delta \epsilon_{\text{band}}}{\delta \hat{e}_j} &= -\frac{1}{\pi} \text{Im Tr} \int^{E_{\text{F}}} \mathrm{d}E \int_{\mathcal{V}_j} \mathrm{d}\boldsymbol{r}\; G_{jj}(\boldsymbol{r},\boldsymbol{r};E)\, \boldsymbol{\sigma}\, B_j^{\text{xc}}(\boldsymbol{r}) \\ &= \int_{\mathcal{V}_j} \mathrm{d}\boldsymbol{r}\; \boldsymbol{m}_j(\boldsymbol{r})\, B_j^{\text{xc}}(\boldsymbol{r}) \quad ,\end{aligned} \tag{2.81}$$

where $\boldsymbol{m}_j(\boldsymbol{r})$ has to be understood as the output magnetization obtained by starting from an initial magnetization $\boldsymbol{m}_j^{\text{in}}(\boldsymbol{r})$ and $B_j^{\text{xc}}(\boldsymbol{r})$ is the exchange correlation magnetic field in the direction of the input magnetic moment. In our case the rigid spin approximation, $\boldsymbol{m}_j^{\text{in}}(\boldsymbol{r}) = \boldsymbol{e}_j^{\text{in}} m_j^{\text{in}}(\boldsymbol{r})$, is used to set up the exchange-correlation magnetic field and the output magnetization $\boldsymbol{m}_j(\boldsymbol{r})$ has full spherical complexity meaning that the rigid spin approximation is not used to obtain the magnetic torques.

In the KKRimp code the magnetization of cell j is obtained via the $\boldsymbol{r} = \boldsymbol{r}'$ part of the density matrix, eq. (2.54), yielding,

$$\boldsymbol{m}_j(\boldsymbol{r}) = \sum_L \boldsymbol{m}_{j,L}(r) Y_L(\hat{r}) \quad . \tag{2.82}$$

The exchange-correlation magnetic field in the LSDA combined with the rigid spin approximation is parallel to the direction of the input magnetic moment, $\hat{e}_j$,

$$\boldsymbol{B}_j^{\text{xc}}(\boldsymbol{r}) = \hat{e}_j B_j^{\text{xc}}(\boldsymbol{r}) = \hat{e}_j \sum_L B_{j,L}^{\text{xc}}(r) Y_L(\hat{r}) \quad , \tag{2.83}$$

where $B_L^{\text{xc}}(r)$ is already convoluted with the shape function including the geometrical information of the cell. The magnetic torque can be calculated via,

$$\boldsymbol{\tau}_j = \sum_L \int_{\mathcal{V}_j} \mathrm{d}r\; r^2\, \boldsymbol{m}_{j,L}(r)\, B_{j,L}^{\text{xc}}(r) \quad . \tag{2.84}$$

Since in the ASA the potential, and therefore also the exchange-correlation magnetic field, is spherical the calculation of the torque simplifies to,

$$\boldsymbol{\tau}_j = \int_{\mathcal{V}_j} \mathrm{d}r\, r^2\, \boldsymbol{m}_{j,(0,0)}(r)\, B^{\text{xc}}_{j,(0,0)}(r) \quad . \tag{2.85}$$

The magnetic torques allow for a straight-forward comparison of DFT and an atomistic spin model, like e.g. the Heisenberg model which will be discussed in Chapter 4, by comparing to the corresponding torque in the particular model, $\boldsymbol{\tau}_j = \delta\mathcal{H}_{\text{Heisenberg}}/\delta\hat{e}_j$. Furthermore, magnetic torques can be used to set up a magnetic constraining field as will be discussed in the next section.

Magnetic constraining fields

For many magnetic systems internal magnetic interactions can yield complicated magnetic ground states. Different examples will be discussed throughout this thesis. Finding those ground states from first-principles can be cumbersome. However, the fundamental theorems of DFT being a ground state theory are only valid in the ground state. This drawback is often neglected since it turned out that many quantities obtained from DFT are not sensitive to the underlying magnetic structure. However, to ensure that a particular magnetic structure is the ground-state configuration magnetic constraining fields can be used in order to stabilize arbitrary (non-collinear) magnetic structures. Different approaches to magnetic constraints have been developed and applied in literature, e.g. in Refs. [113, 115].

Here, we define three different types of constraining fields. Having the previous section in mind, a constraining field can be constructed using the magnetic torques exerted to a magnetic structure [113],

$$\boldsymbol{B}^{\text{c,torque}}_i = -\boldsymbol{\tau}_i / m_i \quad . \tag{2.86}$$

Another type of constraint can be defined using the exchange-correlation field [115], exploiting the rigid spin approximation,

$$B^{\text{c,xc}}_i(\boldsymbol{r}) = \boldsymbol{c}_i B^{\text{xc}}_i(\boldsymbol{r}) \quad , \tag{2.87}$$

where $\boldsymbol{c}_i$ is a vector which is perpendicular to the constraining direction $\hat{e}^{\text{constr}}$. Constraining based on the exchange-correlation field has theoretically the advantage of accounting for the different strengths of the magnetic moment, which are encoded in the exchange-correlation magnetic field, on the radial mesh.

The last type of constraining uses a homogeneous magnetic field, $\boldsymbol{c}_i$, which has no radial dependence and is perpendicular to the constraining direction.

What all three methods have in common is the need for self-consistency. For the torque method after every iteration the obtained torque has to be added to the constraining field until the torque vanishes. Note that this method strictly speaking does not constrain the direction of the magnetic moment, but allows a self-consistent determination of the magnetic torques exerted on a magnetic configuration. The reason for this is that the magnetic torque is defined by the product of the magnetization density with the exchange-correlation magnetic field. The exchange-correlation magnetic field therefore weights the magnetization density differently for different radial regions resulting in a small discrepancy between the output magnetic moment and the output magnetic torque.

Therefore, the second and third method are better suited to constrain a ground-state configuration. The direction of the vector $\boldsymbol{c}_i$, either scaled by the exchange-correlation magnetic field or being constant, is obtained from a projection of the output direction on to the perpendicular plane of the constraining direction using the projection

$$\mathcal{P}_i^{\perp} = \mathbf{1} - \hat{e}_i^{\text{constr}} \otimes \hat{e}_i^{\text{constr}} \quad , \tag{2.88}$$

and updating the scaling factors after each iteration via,

$$\boldsymbol{c}_i^{\text{new}} = \mathcal{P}_i^{\perp} \boldsymbol{c}_i^{\text{old}} - \mathcal{P}_i^{\perp} \hat{e}_i^{\text{out,scf}} \quad , \tag{2.89}$$

where $\hat{e}_i^{\text{out,scf}}$ is the averaged output direction of the (non-collinear) magnetization in cell i. To speed up the convergence a linear mixing scheme between $\boldsymbol{c}_i^{\text{new}}$ and $\boldsymbol{c}_i^{\text{old}}$ can be used. The self-consistent procedure ensures that the output direction is the same as the input direction of the magnetic moment and therefore the system is in its magnetic ground state, for the applied constraining magnetic field.

Magnetic constraining fields will be used in Chapters 4 and 5 of this thesis to obtain self-consistently the magnetic torque and map from first-principles to an atomistic spin model, and to stabilize arbitrary non-collinear structures, respectively.

2.3. Time-dependent density functional theory

Density functional theory being originally formulated as a ground state theory is not capable of treating time-dependent phenomena. An extension to the latter category was achieved by Runge and Gross in 1984 [117] by introducing the time-dependent equivalent to the Hohenberg-Kohn theorem. The Runge-Gross theorem basically states that two densities $n(\boldsymbol{r}, t)$ and $n'(\boldsymbol{r}, t)$, which evolve from a common initial state $\Psi(\boldsymbol{r}, t_0)$ under the influence of two different potentials $V(\boldsymbol{r}, t)$ and $V'(\boldsymbol{r}, t)$, differ if the potentials differ by more than a purely time-dependent constant. The time-dependent extension of the stationary Kohn-Sham equation is straight-forward by using the time-dependent Schrödinger equation,

$$\mathrm{i}\, \frac{\partial \phi_i(\boldsymbol{r}, t)}{\partial t} = \mathcal{H}_{\text{KS}}\, \phi_i(\boldsymbol{r}, t) \quad , \tag{2.90}$$

and the time-dependent generalization of the Kohn-Sham hamiltonian, $\mathcal{H}_{\text{KS}}$, from eq. (2.3). Contrary to stationary DFT the exchange-correlation potential is not defined via a functional derivative of another quantity. Furthermore, the exchange-correlation potential in general depends on the entire history of $n(\boldsymbol{r}, t)$.

The most used simplification to those problems is the so-called adiabatic approximation for the exchange-correlation potential. Within the adiabatic approximation the potential is approximated by a functional derivative of a static exchange-correlation energy,

$$V_{\text{xc}}(\boldsymbol{r}, t) = \left.\frac{\delta E_{\text{xc}}[n, \boldsymbol{m}]}{\delta n(\boldsymbol{r})}\right|_{n(\boldsymbol{r},t), \boldsymbol{m}(\boldsymbol{r},t)} \quad \text{and} \quad \boldsymbol{B}_{\text{xc}}(\boldsymbol{r}, t) = -\left.\frac{\delta E_{\text{xc}}[n, \boldsymbol{m}]}{\delta \boldsymbol{m}(\boldsymbol{r})}\right|_{n(\boldsymbol{r},t), \boldsymbol{m}(\boldsymbol{r},t)} \quad , \tag{2.91}$$

neglecting all the history dependence of the exchange-correlation potentials. The adiabatic approximation is expected to work well for system close to equilibrium, e.g. in the linear response regime.

Time-dependent density functional theory (TD-DFT) is widely used in different fields of physics. It can be used to treat time-dependent phenomena in real time [89], which is needed for example for strong laser fields. One of its main strength, however, lies in the use of linear response theory, which allows for an efficient treatment of diverse time-dependent effects [89]. In this thesis, we focus on the latter case and apply TD-DFT to the magnetic susceptibility, which is discussed in the next section.

2.3.1. The magnetic susceptibility

The magnetic susceptibility, χ, describes the response of the magnetization density to an external time-dependent magnetic field,

$$\boldsymbol{m}(\boldsymbol{r},t) = \int \mathrm{d}\boldsymbol{r}' \int \mathrm{d}t' \,\underline{\underline{\chi}}(\boldsymbol{r},\boldsymbol{r}';t-t')\,\boldsymbol{B}(\boldsymbol{r}',t') \quad . \tag{2.92}$$

It is based on linear response theory, which will be briefly recapped in the following. A more comprehensive description can be found in any standard textbook on many body physics, e.g. [118, 119] or in my Master thesis [77].

Linear response theory

The linear response formalism is used to describe the response of any observable A to an external weak perturbation in linear order. Assume a time-dependent perturbation $\mathcal{H}'(t)$, which is turned on at a time t_0,

$$\mathcal{H}(t) = \mathcal{H}_0 + \Theta(t-t_0)\,\mathcal{H}'(t) \quad , \tag{2.93}$$

where $\Theta(t)$ is the Heaviside step function and $\mathcal{H}_0$ is the unperturbed hamiltonian. The knowledge of the full eigensystem of the time-dependent hamiltonian allows for the calculation of the time-dependent expectation value of any observable,

$$\langle A\rangle(t) = \sum_n f_n(t)\,\langle n(t)|A|n(t)\rangle \quad , \tag{2.94}$$

where $f_n(t)$ is the time-dependent occupation factor of the eigenstate $|n(t)\rangle$ obtained from the time-dependent Schrödinger equation. Solving the time-dependent Schrödinger equation, however, is a complex task, which might be feasible but not needed for many problems. A drastic simplification can be achieved by treating $\mathcal{H}'(t)$ as a perturbation, which yields the so-called Kubo formula,

$$\delta\langle A\rangle(t) = \langle A\rangle(t) - \langle A\rangle_0 = -\mathrm{i}\int_{t_0}^{t} \mathrm{d}t'\,\langle[A(t),\mathcal{H}'(t')]\rangle_0 \quad , \tag{2.95}$$

where $\langle\rangle_0$ indicates that the expectation value is evaluated with respect to the unperturbed hamiltonian $\mathcal{H}_0$ using its time-independent eigenstates, and the commutator

$[A, B] = AB - BA$ is used. Thus, for a weak perturbation the knowledge of the eigensystem of the unperturbed system is sufficient to calculate the time-dependent expectation value of any observable, which is a remarkable result on its own. The main quantity of interest is the so-called retarded correlation function,

$$\mathcal{C}_{A,\mathcal{H}'}(t - t') = -\mathrm{i}\,\Theta(t - t')\,\langle[A(t), \mathcal{H}'(t')]\rangle_0 \quad . \tag{2.96}$$

It is often convenient to work in the frequency space, e.g. for time-periodic perturbations, $\mathcal{H}'(t) = B(t)\delta f(t)$, where $f(t)$ is a simple function and $B(t)$ is the operator. Using a Fourier transformation eq. (2.95) yields,

$$\delta\langle A\rangle(\omega) = \mathcal{C}_{A,B}(\omega)\,\delta f(\omega) \quad , \tag{2.97}$$

with the Fourier transformed correlation function,

$$\mathcal{C}_{A,B}(\omega + \mathrm{i}\eta) = \int \mathrm{d}t\, e^{\mathrm{i}(\omega+\mathrm{i}\eta)t}\, \mathcal{C}_{A,B}(t) \quad , \tag{2.98}$$

where $\eta \to 0^+$ is added to prevent from divergences. The correlation function can be calculated using different approaches. Since in this thesis the KKR Green function method is used the obvious approach is to calculate the correlation function using Green functions. In Appendix B a detailed derivation of the correlation function using the so-called Matsubara formalism and complex analysis is shown for the specific case of the spin-spin correlation function. The final result relates the correlation function to the single-particle Green function discussed in section 2.2.1,

$$\begin{aligned} \mathcal{C}_{AB}(\omega + \mathrm{i}0^+) = \int \frac{\mathrm{d}E}{2\pi\mathrm{i}} f(E) \Big\{ & - \mathrm{Tr}\left[A\,G(\omega + E + \mathrm{i}0^+)\,B\,G(E + \mathrm{i}0^+)\right] \\ & + \mathrm{Tr}\left[A\,G(\omega + E + \mathrm{i}0^+)\,B\,G(E - \mathrm{i}0^+)\right] \\ & - \mathrm{Tr}\left[A\,G(E + \mathrm{i}0^+)\,B\,G(E - \omega - \mathrm{i}0^+)\right] \\ & + \mathrm{Tr}\left[A\,G(E - \mathrm{i}0^+)\,B\,G(E - \omega - \mathrm{i}0^+)\right] \Big\} \quad , \end{aligned} \tag{2.99}$$

where $G(E \pm \mathrm{i}0^+)$ is the retarded or advanced Green function, respectively. The correlation function fulfills some basic symmetry relations [120],

$$\mathcal{C}_{A,B}(0) = \mathcal{C}_{B,A}(0) \tag{2.100}$$

$$\mathrm{Re}\,\mathcal{C}_{A,B}(\omega) = \mathrm{Re}\,\mathcal{C}_{A,B}(-\omega) \tag{2.101}$$

$$\mathrm{Im}\,\mathcal{C}_{A,B}(\omega) = -\mathrm{Im}\,\mathcal{C}_{A,B}(-\omega) \quad . \tag{2.102}$$

Having recapped the most important points of linear response theory, we can continue with the general description of a magnetic susceptibility in frequency space,

$$\underline{n}(\boldsymbol{r},\omega) = \int \mathrm{d}\boldsymbol{r}' \, \underline{\underline{\chi}}(\boldsymbol{r},\boldsymbol{r}',\omega)\underline{V}(\boldsymbol{r}',\omega) \quad , \tag{2.103}$$

where we combined the charge and spin degrees of freedom by using the notation

$$\underline{n} = \begin{pmatrix} m_x \\ m_y \\ m_z \\ n \end{pmatrix} \qquad \text{and} \qquad \underline{V} = \begin{pmatrix} B_x \\ B_y \\ B_z \\ V \end{pmatrix} \quad , \tag{2.104}$$

and $\underline{\underline{\chi}}$ being a 4×4 matrix describes the combined response of charge and magnetization density under the influence of a perturbation represented by an external magnetic field or an external potential. The susceptibility can be decomposed into a transversal part, $\chi_\perp$, and a longitudinal part, $\chi_\parallel$,

$$\underline{\underline{\chi}} = \begin{pmatrix} \chi_{xx} & \chi_{xy} & \chi_{xz} & \chi_{x0} \\ \chi_{yx} & \chi_{yy} & \chi_{yz} & \chi_{y0} \\ \chi_{zx} & \chi_{zy} & \chi_{zz} & \chi_{z0} \\ \chi_{0x} & \chi_{0y} & \chi_{0z} & \chi_{00} \end{pmatrix} = \begin{pmatrix} \chi_\perp & \chi_{\perp,\parallel} \\ \chi_{\parallel,\perp} & \chi_\parallel \end{pmatrix} \quad . \tag{2.105}$$

For collinear systems without spin-orbit coupling the two parts completely decouple resulting in a block diagonal structure of $\underline{\underline{\chi}}$.

Using the Kubo formula, eq. (2.95), the magnetic susceptibility is given by the so-called spin-spin correlation function,

$$\chi^{\alpha\beta}(\boldsymbol{r},\boldsymbol{r}',\omega) = \mathcal{C}_{\sigma_\alpha,\sigma_\beta}(\boldsymbol{r},\boldsymbol{r}',\omega + \mathrm{i}0^+) \quad , \tag{2.106}$$

where σ_α are the Pauli matrix including the identity matrix with $\alpha = \{x, y, z, 0\}$. Using the general definition of the correlation function in terms of a single-particle Green function, eq. (2.99), the spin-spin correlation function can be calculated via,

$$\begin{aligned} \chi^{\alpha\beta}(\boldsymbol{r},\boldsymbol{r}',\omega) = \int & \frac{\mathrm{d}E}{2\pi\mathrm{i}} f(E) \\ \times\Big\{ & - \mathrm{Tr}\left[\boldsymbol{\sigma}^\alpha \, G(\boldsymbol{r},\boldsymbol{r}';\omega + E + \mathrm{i}0^+) \, \boldsymbol{\sigma}^\beta \, G(\boldsymbol{r}',\boldsymbol{r};E + \mathrm{i}0^+)\right] \\ & + \mathrm{Tr}\left[\boldsymbol{\sigma}^\alpha \, G(\boldsymbol{r},\boldsymbol{r}';\omega + E + \mathrm{i}0^+) \, \boldsymbol{\sigma}^\beta \, G(\boldsymbol{r}',\boldsymbol{r};E - \mathrm{i}0^+)\right] \\ & - \mathrm{Tr}\left[\boldsymbol{\sigma}^\alpha \, G(\boldsymbol{r},\boldsymbol{r}';E + \mathrm{i}0^+) \, \boldsymbol{\sigma}^\beta \, G(\boldsymbol{r}',\boldsymbol{r};E - \omega - \mathrm{i}0^+)\right] \\ & + \mathrm{Tr}\left[\boldsymbol{\sigma}^\alpha \, G(\boldsymbol{r},\boldsymbol{r}';E - \mathrm{i}0^+) \, \boldsymbol{\sigma}^\beta \, G(\boldsymbol{r}',\boldsymbol{r};E - \omega - \mathrm{i}0^+)\right] \Big\} \quad . \end{aligned} \tag{2.107}$$

Evaluated using the single-particle Green function of the Kohn-Sham system, this equation yields the response of the non-interacting particles to an external field. This susceptibility is therefore called the Kohn-Sham susceptibility, χ_{KS}. In order to obtain the full susceptibility of the system of interacting particles, the principles of TD-DFT are used, which is explained in the next section.

Linear response within TD-DFT

The response of the Kohn-Sham system to an external field yields a variation of the charge and magnetization densities, which in turn affects the exchange-correlation potentials. The effective change of the Kohn-Sham hamiltonian due to external fields can be obtained using the functional derivatives with respect to the charge and magnetization densities,

$$\delta\mathcal{H}^{\mathsf{KS}}(\boldsymbol{r},t) = \mu_{\mathsf{B}}\,\boldsymbol{\sigma}\cdot\delta\boldsymbol{B}(\boldsymbol{r},t) + \delta V(\boldsymbol{r},t) + \int \mathrm{d}\boldsymbol{r}' \int \mathrm{d}t'\, \underline{\mathcal{K}}(\boldsymbol{r},\boldsymbol{r}',t-t')\cdot\delta\underline{n}(\boldsymbol{r}',t') \quad , \tag{2.108}$$

where the so-called kernel, $\mathcal{K}$, was defined as the functional derivative of the Kohn-Sham hamiltonian with respect to the densities,

$$\underline{\mathcal{K}}(\boldsymbol{r},\boldsymbol{r}',t-t') = \left.\frac{\delta\mathcal{H}^{\mathsf{KS}}(\boldsymbol{r},t)}{\delta\underline{n}(\boldsymbol{r}',t')}\right|_{\underline{n}(\boldsymbol{r},t)} \quad , \tag{2.109}$$

which contains all the information on how the Kohn-Sham system reacts to an external perturbation of the densities. In the adiabatic local density approximation approximation, which is used throughout this thesis, the kernel is evaluated for the ground state densities and is therefore time-independent. The magnetic kernel contains the response of the exchange-correlation potentials on perturbation of the magnetic density,

$$\mathcal{K}^{m}(\boldsymbol{r},\boldsymbol{r}') = \delta(\boldsymbol{r}-\boldsymbol{r}')\left[\left.\frac{\delta V^{\mathsf{xc}}[n,\boldsymbol{m}]}{\delta\boldsymbol{m}(\boldsymbol{r})}\right|_{\mathsf{GS}} + \boldsymbol{\sigma}\cdot\left.\frac{\delta\boldsymbol{B}^{\mathsf{xc}}[n,\boldsymbol{m}]}{\delta\boldsymbol{m}(\boldsymbol{r})}\right|_{\mathsf{GS}}\right] \quad , \tag{2.110}$$

while the charge kernel picks up an additional contribution from the Hartree potential,

$$\mathcal{K}^{n}(\boldsymbol{r},\boldsymbol{r}') = \frac{2}{|\boldsymbol{r}-\boldsymbol{r}'|} + \delta(\boldsymbol{r}-\boldsymbol{r}')\left[\left.\frac{\delta V^{\mathsf{xc}}[n,\boldsymbol{m}]}{\delta n(\boldsymbol{r})}\right|_{\mathsf{GS}} + \boldsymbol{\sigma}\cdot\left.\frac{\delta\boldsymbol{B}^{\mathsf{xc}}[n,\boldsymbol{m}]}{\delta n(\boldsymbol{r})}\right|_{\mathsf{GS}}\right] \quad , \tag{2.111}$$

resulting in a numerically cumbersome non-local kernel.

Since the aim is to obtain the response of the densities to an external perturbation, the actual change of the Kohn-Sham hamiltonian has to be connected to the change in the densities. Using the time-ordered Green function (see e.g. [118]) the densities can be obtained from,

$$n_{\alpha}(\boldsymbol{r},t) = -\mathrm{i}\,\mathrm{Tr}\,\sigma_{\alpha}\,G(\boldsymbol{r},\boldsymbol{r},t,t^{+}) \quad . \tag{2.112}$$

Using the Dyson equation the change in the Green function can be obtained by,

$$G(\boldsymbol{r},\boldsymbol{r}',t-t') = G_0(\boldsymbol{r},\boldsymbol{r}',t-t') + \int \mathrm{d}\boldsymbol{r}'' \int \mathrm{d}t''\, G_0(\boldsymbol{r},\boldsymbol{r}'',t-t'')\,\delta\mathcal{H}^{\mathsf{KS}}(\boldsymbol{r}'',t'')\,G(\boldsymbol{r}'',\boldsymbol{r}',t''-t') \quad , \tag{2.113}$$

with the time-ordered Green function of the unperturbed system, $G_0(\boldsymbol{r},\boldsymbol{r}',t-t')$. Using the definition of the change in the Kohn-Sham hamiltonian, eq. (2.108), and identifying the magnetic susceptibility of the Kohn-Sham system as,

$$\chi^{\alpha\beta}_{\mathsf{KS}}(\boldsymbol{r},\boldsymbol{r}',t-t') = -\mathrm{i}\mathrm{Tr}\,\sigma_{\alpha}\,G_0(\boldsymbol{r},\boldsymbol{r}',t-t')\,\sigma_{\beta}\,G_0(\boldsymbol{r}',\boldsymbol{r},t'-t) \quad , \tag{2.114}$$

a Dyson-like equation for the susceptibility of the full system can be found,

$$\chi = \chi_{\mathrm{KS}} + \chi_{\mathrm{KS}}\,\mathcal{K}\,\chi \quad , \tag{2.115}$$

where spatial dependencies and integrals were suppressed for the sake of simplicity. Similarly to the Dyson equation this equation can be solved via inversion of by iterating giving access to the so-called renormalized susceptibility of the system of interacting particles.

3

Induced magnetism and the inter-atomic orbital moment

In this chapter, the magnetism induced in non-magnetic surfaces by magnetic nanostructures is discussed. Special focus is given to the orbital component of the magnetism in this class of systems. After a brief discussion of the two available theories, namely the classical and the modern theory of orbital magnetism, we verify that the classical theory applies to the discussed class of systems. Based on a novel formalism, a new component to the orbital magnetic moment, the so-called inter-atomic orbital moment, which can be related to the net currents flowing through the atoms and can be as large or even large than the common atomic orbital moment, is found. The physical origin of the different components of the induced magnetism is identified and a potential experimental observation based on magnetic stray fields is discussed. Different systems are investigated ranging from single adatoms to nanoclusters composed out of three atoms deposited on surfaces. The impact of the chemical nature of the nanostructure is analyzed using mono-atomic structures composed out of Cr, Mn, Fe, and Co, while the effect of the spin-orbit coupling strength and the spin polarizability is analyzed by *using different heavy metal substrates, namely the (111) facets of Rh, Pd, Ag, Ir, Pt and Au.*

Parts of the presented work have been published in

*S. Brinker et al. Physical Review B **98**, 094428 (2018)*
I have contributed to this publication in the following way: I set up the general framework for the calculation of the charge currents and the inter-atomic orbital magnetic moment, which I implemented in our local KKR code. I performed the density functional theory calculations. I analyzed the results and wrote most of the manuscript.

*S. Brinker et al. Physical Review Materials **4**, 024404 (2020)*
I have contributed to this publication in the following way: The calculation framework is based on my previous publication [121]. I performed the DFT calculations based on our local KKR codes developed in Jülich and on the plane wave code Quantum Espresso. I implemented and calculated magnetic stray fields in our local KKR codes. I analyzed the results and wrote most of the manuscript.

3.1. Introduction

Nanostructures and especially adatoms deposited on surfaces are important in the field of spintronics, e.g. as building blocks of future data storage devices. Apart from the nanostructure itself, the surface supporting the nanostructure is crucial. The same nanostructure can behave completely differently if placed on a different surface, highlighting the importance of the surface electrons and their scattering at the nanostructure. A well-studied effect are the Friedel oscillations [64] present in the charge and spin densities of the surface electrons [65]. Friedel oscillations also mediate interactions between two different magnetic nanostructures deposited on surfaces giving rise to the so-called Ruderman-Kittel-Kasuya-Yosida interactions [38, 122, 123], which will be discussed in detail in Chapter 6. The importance of the induced magnetism was revealed by experimental studies of a system hosting giant induced moments – magnetic atoms dissolved in Pd [69, 70]. Theoretical studies of the Pd system involved up to thousand atoms [124, 125], showing the long range of this effect. Pd is known to be highly susceptible to a magnetic perturbation resulting in a high spin polarizability. Surfaces hosting large spin-orbit coupling in addition give rise to chiral interactions like the Dzyaloshinskii-Moriya interaction or the chiral biquadratic interaction discussed in Chapter 4, and to the magnetic anisotropy energy (MAE) being crucial for the magnetic stability of nanostructures discussed in Chapter 6. The spin-orbit coupling itself couples the orbital degree of freedom to the spin degree of freedom resulting in a lifting of the orbital degeneracy, which is the main source of finite ground-state currents and in turn orbital magnetism. The orbital magnetism classically emerges from a ground-state charge current distribution, $\boldsymbol{j}(\boldsymbol{r})$, using classical electrodynamics [75],

$$\boldsymbol{m}_\text{o} = \frac{1}{2}\int \mathrm{d}\boldsymbol{r}\, \boldsymbol{r} \times \boldsymbol{j}(\boldsymbol{r}) \quad , \tag{3.1}$$

or equivalently using the expectation value of the angular momentum operator, $\boldsymbol{m}_\text{o} = \langle \boldsymbol{L} \rangle$. The classical definition is well-defined for localized current distributions, like e.g. present in finite nanostructure or molecules. For extended system, however, the position operator is ill-defined breaking the classical theory. This problem was circumvented in the so-called modern theory of orbital magnetism, which was originally formulated using different approaches in reciprocal space [126–128], and which was more recently also extended to a real-space formulation [129–131]. One approach is that instead of extended Bloch states localized Wannier functions are used, for which the position operator is well-defined. Starting from a finite sample it can be shown that the orbital magnetism is decomposed into an atomic-like local component and an itinerant surface contribution, which is also relevant for the bulk. In this thesis, however, we focus on a so far not studied class of systems, finite magnetic nanostructure deposited on extended surfaces not hosting magnetism on their own, for which it is a priori unclear if the classical theory applies or if the modern theory has to be used. Note that in the classical limit the modern theory and the classical theory yield the same results. Using giant clusters including up to 3000 atoms, we will show that the classical theory is still applicable, meaning that ground-state currents can be used to calculate the orbital magnetic moment. In the next section, the calculation scheme is illustrated.

3.1.1. The inter-atomic orbital moment

In most first-principles simulations using the classical theory the orbital moment is calculated by evaluating the angular moment operator in an atomic basis set giving rise to the atomic orbital moment. Here, we will take the computationally more demanding path and compute the orbital moment via the ground-state current and eq. (3.1). Using the KKR formalism the integration has to be split into the various cells corresponding to the different atoms,

$$\boldsymbol{m}_{\mathrm{o}} = \frac{1}{2}\sum_i \left[\boldsymbol{R}_i \times \boldsymbol{j}_i^{\mathrm{net}} + \int_{\mathcal{V}_i} \mathrm{d}\boldsymbol{r}\,(\boldsymbol{r}-\boldsymbol{R}_i)\times \boldsymbol{j}_i(\boldsymbol{r})\right] \tag{3.2}$$

$$= \sum_i \left[\boldsymbol{m}_{\mathrm{o},i}^{\mathrm{ia}} + \boldsymbol{m}_{\mathrm{o},i}^{\mathrm{a}}\right] = \boldsymbol{m}_{\mathrm{o}}^{\mathrm{ia}} + \boldsymbol{m}_{\mathrm{o}}^{\mathrm{a}} \quad , \tag{3.3}$$

where the net current $\boldsymbol{j}_i^{\mathrm{net}} = \int_{\mathcal{V}_i} \mathrm{d}\boldsymbol{r}\,\boldsymbol{j}(\boldsymbol{r})$ was defined. The first term defines the so-called inter-atomic orbital moment, $\boldsymbol{m}_{\mathrm{o}}^{\mathrm{ia}}$, which originates from the net currents flowing through the atoms. The second term is the more familiar atomic orbital moment, $\boldsymbol{m}_{\mathrm{o}}^{\mathrm{a}}$, resulting from locally circulating currents within each cell. Note that for a bound current distribution, $\int \mathrm{d}\boldsymbol{r}\,\boldsymbol{j}(\boldsymbol{r}) = 0$, this separation is invariant under a gauge transformation of the global origin, which can be seen by applying a global shift, $\boldsymbol{R}_i \to \boldsymbol{R}_i + \boldsymbol{R}$,

$$\boldsymbol{m}_{\mathrm{o}} \to \boldsymbol{m}_{\mathrm{o}} + \frac{1}{2}\boldsymbol{R}\times\sum_i \boldsymbol{j}_i^{\mathrm{net}} = \boldsymbol{m}_{\mathrm{o}} \quad . \tag{3.4}$$

Contrary to the atomic orbital moment, which can also be obtained from the usual evaluation of the angular momentum operator in an atomic basis, the knowledge of the ground-state net currents is crucial for the inter-atomic orbital moment. The inter-atomic orbital moment itself was first discussed in my Master thesis [77], but a calculation scheme involving large enough real space clusters and therefore also a systematic study of the effect was missing.

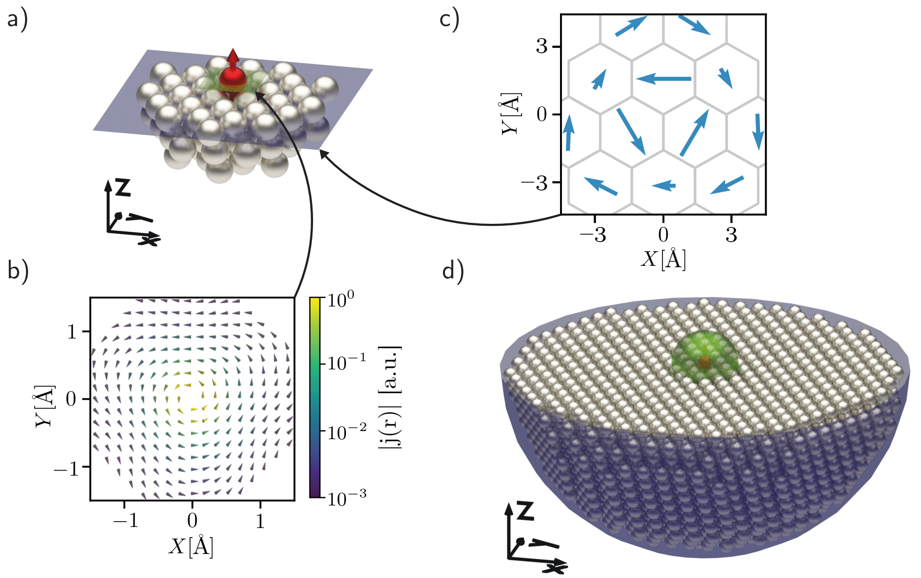

Figure 3.1.: Ground-state charge current generated by an Fe adatom deposited on the Pt(111) surface. (a) Atomic structure. The adatom with its magnetic moment is represented by the red sphere and the arrow, respectively, and deposited in the fcc-stacking position on the grey spheres indicating the Pt surface atoms. The vertical distance between the adatom and the surface is reduced to 75% of the bulk interlayer distance. The blue and green planes indicate the cuts used for panels (b) and (c), respectively. (b) Ground-state current within the Fe adatom. The color scale is logarithmic in atomic units. (c) Net currents $\boldsymbol{j}_i^{\text{net}}$ in the first layer of Pt(111). (d) Geometry of the giant cluster, which consists of a small central cluster of radius 2.8 Å indicated by the green sphere, and a large outer cluster with a maximal radius of $R_{\text{h}} = 27.2$ Å comprising 2685 Pt atoms indicated by the blue sphere.

3.2. Proof of the concept – adatoms on the Pt(111) surface

In this section, the example of 3d adatoms deposited on the Pt(111) surface will be used to illustrate the calculation scheme used for the inter-atomic orbital moments. A comprehensive analysis of the induced magnetism of 3d adatoms deposited on several surfaces including Pt(111) and including geometrical and general computational details, will be discussed in Section 3.3. The prototypical test system is an Fe adatom on the Pt(111) surface illustrated in Fig. 3.1a. In this section, we assume that the vertical distance between the Fe adatom and the surface is 75 $\%$ of the Pt interlayer distance resulting in an effective relaxation of 25 $\%$ towards the surface. The precise relaxations for all adatoms are discussed later in Section 3.3.1. The magnetic moments of all atoms composing the cluster are assumed to be collinear, with the freedom of a ferro- and antiferromagnetic alignment. The ground-state currents in a constant z cut plane through the Fe adatom is shown in Fig. 3.1b. Within the Fe cell the current dis-

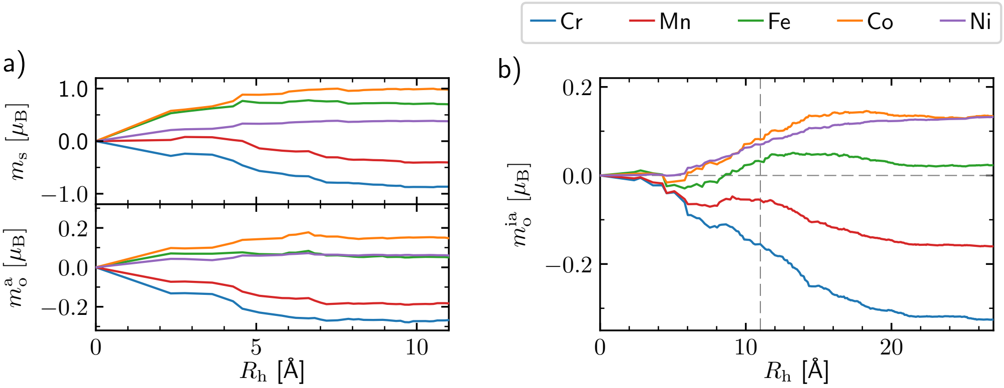

Figure 3.2.: Convergence of the different induced magnetic moments. Shown are the net magnetic moments induced to the Pt(111) surface in the presence of several adatoms, as function of the hemispherical cluster radius, R_h. (a) Local net spin moments and local atomic orbital moments, m_s and m_o^a. (b) Net inter-atomic orbital moments m_o^ia. The vertical dashed line at 11 Å indicates the largest computationally feasible cluster (169 Pt atoms). The convergence requires the usage of an effective hemispherical cluster with $R_\mathrm{h} = 27.2$ Å (2685 Pt atoms).

tribution complies with the C_{3v} symmetry of the system resulting in a purely localized current swirling around the Fe adatom. Evaluating the cross product of the position with the current in the local frame of the cell, eq. (3.3), gives rise to the atomic contribution of the orbital moment. For the shown Fe adatom the local atomic contribution in the Fe adatom is $0.13\,\mu_\mathrm{B}$, which is in perfect agreement with the direct evaluation of the angular momentum operator $\boldsymbol{L}$ in the atomic basis of the Fe adatom according to eq. (2.10).

In addition to the locally swirling current, a finite net current can emerge if the local symmetry of the atom allows it. The net currents computed according to eq. (2.53) flowing through the atoms comprising the first Pt layer are shown in Fig. 3.1c. These net currents give rise to the inter-atomic orbital moment. Due to the definition of the inter-atomic orbital moment the net currents need to decay with the distance r to the adatoms faster than $1/r^3$ for the spatial summation to converge, which is a priori unclear. To investigate the convergence of the different contributions to the induced magnetism a hemispherical cluster, like the one shown in Fig. 3.1d, is constructed and all the magnetic contributions inside the hemisphere are summed up as function of the hemispherical radius, R_h. Note that we take advantage of the embedding boundary conditions afforded by the KKR method to circumvent spurious periodic effects that would arise in a supercell calculation, and thus gain access to ever-increasing hemispherical cluster sizes. The resulting local magnetic moments, namely the spin moment m_s and the atomic orbital moment m_o^a, are shown in Fig. 3.2a for the Cr, Mn, Fe, Co and Ni adatom deposited on the Pt(111) surface. Both contributions are well converged for a cluster radius of approximately 7.5 Å corresponding to 55 Pt atoms. In contrast, the inter-atomic orbital moment shown in Fig. 3.2b is not converged even for a cluster radius of 11 Å (169 Pt atoms), which corresponds to the largest computationally feasible cluster using a connected cluster in our local KKR codes. As the plot indicates hemispherical clusters with approximately $R_\mathrm{h} = 22$ Å

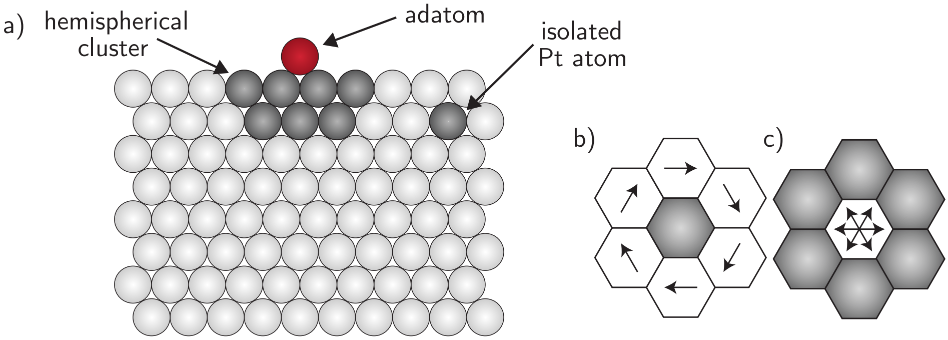

Figure 3.3.: Illustration of the construction used to obtain effective giant hemispherical clusters and to efficiently evaluate the inter-atomic orbital moment. (a) Geometric construction. The adatom is surround by a small central cluster ensuring a stable local environment and for each position in the giant hemisphere an isolated Pt atom is added. (b) Illustration of the net currents induced by a central atom to its surrounding. (c) Illustration of the net current induced to a central atom by its surrounding. For a symmetric surrounding the induced net current vanishes.

have to be used in order to converge the inter-atomic orbital moment, which can be achieved by a special construction explained in the next paragraph. This shows that the inter-atomic orbital moment is much more long-ranged than its local counterparts, and therefore has the potential for a new mechanism to mediate long-ranged interactions. Note that the range of the induced moments is related to the properties of the substrate, mainly the spin polarizability and the spin-orbit coupling strength, and does not depend on the chemical nature of the adatom. Its magnitude, however, is related to both the surface and the adatom. A detailed study will be given in later sections of this chapter.

In order to extract the inter-atomic orbital moment in such large hemispherical clusters, we used several calculations each consisting of a small central cluster with an additional single Pt atom for which the net current is evaluated. Due to the KKR embedding scheme this procedure allows to treat the variation in the electronic structure of the additional Pt atom in the presence of the magnetic adatom. The setup is illustrated in Fig. 3.3a. Using the C_{3v} symmetry of the system, namely the threefold rotational symmetry and the three mirror planes of the (111) surface, which is retained in the presence of the magnetic adatom, the number of necessary calculations can be reduced by approximately a factor of 6. For each atom in the irreducible part of the hemispherical cluster a single non-self-consistent calculation was performed from which the inter-atomic orbital moment of this atom and its symmetry-related atoms was extracted. This procedure does not work for the local contributions to the magnetic moment, for which a large connected cluster would have to be constructed. The reason is that the local quantities heavily depend on their immediate environment. The induced spin moment for example is induced by the presence of the adatom, but it is enhanced due to the spin polarization of the local environment of each Pt atom. Similarly, the atomic orbital moment is immediately related to the spin moment due to the presence of spin-orbit coupling. Contrary to the local quantities it turns out that the inter-atomic orbital moment does not depend crucially on the local environment of the Pt atom. A central atom in a symmetric environment will induce

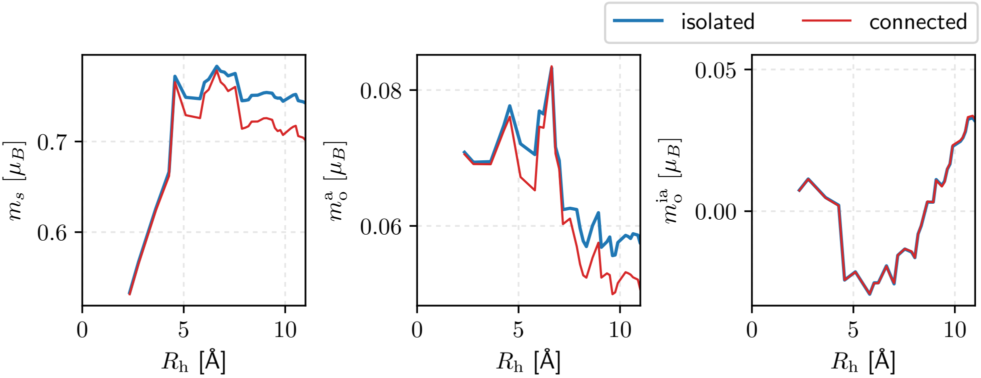

Figure 3.4.: Different net induced magnetic moments for an Fe adatom on Pt(111) as function of the hemispherical cluster size. Shown are the induced spin moment m_s, the induced atomic orbital moment m_o^a, and the inter-atomic orbital moment m_o^ia. Compared are two different methods: The first method uses a connected cluster of up to 169 Pt atoms and is determined self-consistently (red curve). The second method sums up several non-self-consistent calculations of a small cluster containing only the Fe adatom and its nearest neighbors plus one additional isolated Pt atom (blue curve).

swirling net currents to its neighbors as illustrated in Fig. 3.3b. Conversely, in this perfectly symmetric environment each neighboring atom will generate contributions to the net current of the central atom that will tend to cancel each other out, which means that the environment of an atom does not induce any effective net current as illustrated in Fig. 3.3c. Thus, in contrast to the local magnetic moments the environment of a substrate atom cannot easily enhance the net current, which is therefore mostly induced by the central adatom.

To further strengthen the aspect of the environmental dependence, Fig. 3.4 shows the net induced moment for two different sets of calculations as function of the hemispherical cluster size. The reference calculation is a connected cluster containing 169 Pt atoms, which was calculated self-consistently. For the second calculation the procedure described before is used: We added a single Pt atom to a (self-consistent) small cluster containing the adatom with its nearest neighbors (3 Pt atoms) and scanned the full hemisphere using multiple one-shot calculations. For close distances this procedure yields reasonable results for all the different contributions, since the central cluster is also self-consistent. However, for larger cluster sizes the spin as well as the atomic orbital moment deviate drastically from the reference calculation. We would like to highlight that even though the magnitude differs the relative alignment (ferromagnetic or antiferromagnetic with respect to the adatom's spin moment) is obtained correctly resulting in a similar shape of both calculations. In conclusion, the local environment yields an enhancement of the spin as well as the atomic orbital moment, but the structure itself (ferro or antiferro) is purely determined by the perturbation of the adatom, which might be due to the well-known strong Stoner enhancement of the Pt spin susceptibility. In contrast, the inter-atomic orbital moment shows no deviation between the two different calculations highlighting that this contribution does not depend significantly on the environment, but is mostly induced by the perturbation due to the presence of the magnetic adatom.

In this section, we showed how the inter-atomic orbital moment can be calculated from a giant hemispherical cluster calculation and highlighted the first important conclusions: It is the most long-ranged magnetic contribution and it should have a distinct physical origin due to its independence of the local environment.

3.3. Induced magnetism in single adatoms deposited on various transition metal surfaces

In this section, a comprehensive study of the induced surface magnetism, placing the inter-atomic orbital moment into context, will be presented. We will analyze the importance of all the different contributions to the induced magnetism and highlight the physical origin of the different contributions by attributing them to an effective magnetic susceptibility. The impact of the chemical nature of the nanostructure is investigated by analysing Cr, Mn, Fe, and Co adatoms. The impact of the substrate is analyzed using the (111) facets of Rh, Pd, Ag, Ir, Pt, and Au, which allows to distinguish the effects of the spin-orbit coupling strength and the effects of the spin polarizability. Rh, Pd, Ir, and Pt have d valence states, while Ag and Au have s valence states with a Rashba-like spin splitting [132]. The spin polarizability is largest for Pd and Pt and the spin-orbit coupling of Ir, Pt, and Au dominates the one of Rh, Pd, and Ag. Since the adatom is the source of all the induced magnetism, we start with geometrical and magnetic details of 3*d* adatoms deposited on the different transition metal surfaces.

3.3.1. Geometrical and computational details

Adatoms deposited on surfaces are known to relax towards the surface [134], which in turn enhances the hybridization with the surface and therefore impacts all the electronic properties including the magnetic properties. In the used KKR codes the calculation of total energies and the related forces is cumbersome due to numerical imprecisions in the energies. To circumvent these technical difficulties, we use the DFT code Quantum Espresso [135], which is based on a plane wave basis, to calculate the geometrical details of each system. The drawback compared to the KKR codes is the lack of an embedding technique resulting in the need for large supercells to avoid interactions between periodic replica. To obtain the vertical relaxation of an arbitrary adatom deposited on a surface, we construct a 4×4 supercell with five substrate layers and a vacuum corresponding to five interlayer distances on which a single adatom is placed. The generalized gradient approximation is used to treat the exchange correlation effects using the PBEsol [101] functional with ultrasoft pseudopotentials from the pslibrary.1.0.0 [136]. The kinetic energy cutoff needed to define the plane wave basis is set to $100\,\mathrm{Ry}$. In a first step, the theoretical bulk lattice constant, a_0, for each substrate is obtained using a Monkhorst-Pack grid containing 8×8×8 k-points. The theoretical bulk lattice constants for all considered substrates are in very good agreement with the experimental reference values from Ref. [133], which is shown in Table 3.1. In a second step, the slabs containing five substrate layers and a vacuum region equivalent to five interlayer distances is constructed. Due to the open boundary, the first surface layer shows a weak relaxation of less than $2\,\%$

	Rh	Pd	Ag	Ir	Pt	Au
a_0^{exp} [Å]	3.793	3.876	4.063	3.832	3.913	4.061
a_0 [Å]	3.785	3.881	4.064	3.839	3.914	4.084
Δ_{surface}	$-1.9\,\%$	$0.1\,\%$	$-1.2\,\%$	$-1.8\,\%$	$0.3\,\%$	$-0.1\,\%$
Δ_{Cr}	$13.2\,\%$	$19.1\,\%$	$12.1\,\%$	$11.4\,\%$	$19.4\,\%$	$17.3\,\%$
Δ_{Mn}	$14.6\,\%$	$17.9\,\%$	$15.8\,\%$	$11.7\,\%$	$17.9\,\%$	$21.1\,\%$
Δ_{Fe}	$18.7\,\%$	$26.2\,\%$	$19.8\,\%$	$17.9\,\%$	$25.9\,\%$	$27.7\,\%$
Δ_{Co}	$20.8\,\%$	$26.1\,\%$	$21.4\,\%$	$20.6\,\%$	$27.5\,\%$	$27.0\,\%$
$m_{\text{Cr}}[\mu_{\text{B}}]$	3.15	3.32	3.86	3.07	3.11	3.77
$m_{\text{Mn}}[\mu_{\text{B}}]$	3.65	3.99	4.17	3.70	3.88	4.14
$m_{\text{Fe}}[\mu_{\text{B}}]$	3.20	3.34	3.16	3.08	3.28	3.22
$m_{\text{Co}}[\mu_{\text{B}}]$	2.09	2.27	2.02	1.93	2.17	2.00

Table 3.1.: Ground state properties of the considered adatoms deposited on the (111) facets of several surfaces obtained from Quantum Espresso calculations. First, the theoretical bulk lattice constants in comparison to the experimental ones including zero-points correction, taken from Ref. [133], are shown. Next, the vertical relaxation of the first surface layer without the adatoms Δ_{surface}, the vertical relaxations of the different adatoms $\Delta_{\text{Cr/Mn/Fe/Co}}$, and the obtained spin magnetic moments $m_{\text{Cr/Mn/Fe/Co}}$ are shown. Positive values for the relaxations indicate a relaxation towards the surface and $0\,\%$ corresponds to the bulk interlayer distance.

for all substrates shown in Table 3.1. In a last step, the supercell calculation containing the adatoms using the self-consistent bulk lattice constant is performed using a Monkhorst-Pack grid containing 2×2×1 k-points. The adatom as well as the substrate atoms are allowed to spin polarize collinearly.

Fig. 3.5 shows the relaxations of the adatoms towards the surfaces of the different substrates in terms of the bulk inter-layer distance, $d = (1 - \Delta)\, a_0/\sqrt{3}$. In the calculation the adatom as well as the first substrate layer are allowed to relax vertically. The relaxation is obtained

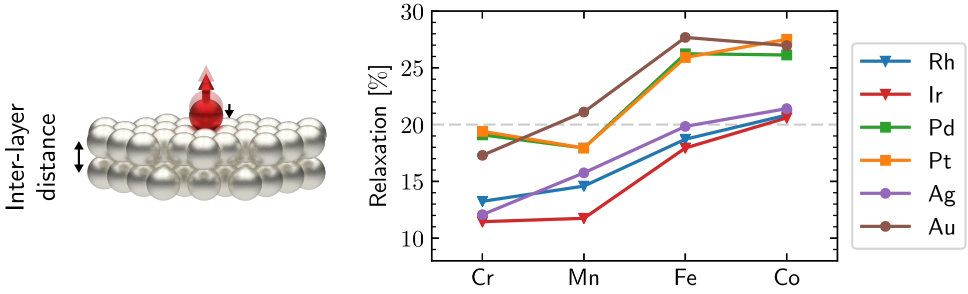

Figure 3.5.: Vertical relaxations towards the surface in terms of the bulk inter-layer distances for Cr, Mn, Fe, and Co deposited on the (111) facet of Rh, Pd, Ag, Ir, Pt, and Au.

from averaging the vertical distance between the adatom and all atoms in the first surface layer, which are slightly inequivalent due to the presence of the adatom. For all substrates the relaxation shows a linear trend as function of the element. Going from Cr to Co increases the number of *d* electrons, which in turn localizes spatially the *d* states of the adatom and therefore increases the relaxation towards the surface. Overall, the adatoms deposited on the Au surface exhibits the strongest relaxation towards the surface. Au has *s* valence states with a fully occupied *d* shell making it fairly localized compared to the other substrate elements and therefore increases the relaxation.

For the sake of computational complexity and comparability, we restrict ourselves in the upcoming discussions to a relaxation of $20\,\%$ for all adatoms on all substrates. However, the effect of the relaxations on the different magnetic contributions will be discussed in detail in Section 3.3.5.

In the following sections, we present various results obtained using the KKR codes. The host systems are set up by considering slabs of 22 layers for each substrate except Pt, for which 40 layers are used, enclosed by two vacuum regions equivalent to four interlayer distances each. The experimental lattice constants are used (see Table 3.1) and the potential is treated in the atomic sphere approximation, but making use of the full charge density. The k-mesh contains 150×150×1 points. The exchange correlation effects are treated in the local spin density approximation as parametrized by Vosko, Wilk and Nusair [97]. Spin-orbit coupling is added to the scalar relativistic approximation already in the periodic calculations of the pristine slabs. Using the embedding technique, hemispherical real space clusters containing approximately 170 host atoms are constructed from which the magnetic anisotropy energy and the magnetic moments are extracted, with the only exception being the inter-atomic orbital moment, whose computational construction was already discussed in the Section 3.2.

3.3.2. Magnetic anisotropy energies

The magnetic anisotropy describes the preference of a magnetic moment to point in a particular direction. Since this is the first time it is mentioned in this thesis, we will briefly discuss it in the following.

Magnetic anisotropy

The magnetic anisotropy of a material can have different origins. Here, we will only focus on the magnetocrystalline anisotropy and neglect e.g. the so-called shape anisotropy, which is a macroscopic effect originating from dipole-dipole interactions. The magnetocrystalline anisotropy originates from the spin-orbit coupling and immediately reflects the symmetries of the crystal lattice in the energy profile as function of the orientation of the magnetic moment. For the sake of simplicity, we focus on a single magnetic moment in the following. The energy as function of the spherical angles ϑ and φ specifiying the orientation of the magnetic moment can be expressed in a basis of spherical harmonics,

$$E^{\mathrm{MAE}}(\vartheta,\varphi) = \sum_L E_L Y_L(\vartheta,\varphi) \quad , \tag{3.5}$$

which has to fulfill the symmetries of the underlying crystal lattice and the general time-reversal symmetry, which implies that only $L = (\ell, m)$ with even ℓ are allowed. For example for the case of the C_{3v} symmetry discussed in this section only the spherical harmonics with $L = \{(2,0),(4,0),(4,-3)\}$ are allowed up to $\ell = 4$. The ℓ index immediately reflects the order in the magnetic moment. Thus, the MAE in second order for the C_{3v} symmetry has the form,

$$E^{\mathsf{MAE}}_{C_{3v}}(\vartheta,\varphi) = E_{(2,0)} Y_{(2,0)}(\vartheta,\varphi) = K_{zz}\cos^2(\vartheta) \quad , \tag{3.6}$$

where the magnetic anisotropy constant K_{zz} was defined. The m index indicates the φ dependence. As shown above the C_{3v} symmetry does not allow any in-plane anisotropy in second order, meaning that all directions within the x-y–plane are equivalent.

Another general formulation of the magnetic anisotropy in second order is given by,

$$E^{\mathsf{MAE}} = \boldsymbol{e}^{\mathsf{T}} K\, \boldsymbol{e} \qquad \text{with} \qquad K = \begin{pmatrix} K_{xx} & K_{xy} & K_{xz} \\ K_{xy} & K_{yy} & K_{yz} \\ K_{xz} & K_{yz} & K_{zz} \end{pmatrix} \quad , \tag{3.7}$$

where K is a symmetric traceless matrix and $\boldsymbol{e} = \big(\cos(\varphi)\sin(\vartheta), \sin(\varphi)\sin(\vartheta), \cos(\vartheta)\big)$ is the unit direction of the magnetic moment. The matrix K has five independent parameters (due to the traceless property of the matrix), which is equivalent to the previous formulation based on spherical harmonics of $\ell = 2$. Since real symmetric matrices have an orthogonal eigenbasis, three orthogonal directions can be attributed to the magnetic anisotropy matrix K. The eigenvector with the smallest eigenvalue is attributed to the so-called easy-axis, which is the energetically favoured axis. The so-called hard-axis is the one with the highest eigenvalue. In the C_{3v} symmetry with the rotational axis along the z direction, the x and y direction are equivalent, and the magnetic anisotropy matrix takes a simple diagonal form with only one free parameter, e.g. K_{zz}. Depending on the sign of K_{zz} the anisotropy is called easy-axis ($K_{zz} < 0$) or easy-plane ($K_{zz} > 0$) anisotropy.

The magnetic anisotropy within KKR can be obtained from band energy differences using the magnetic force theorem [137]. Another more sophisticated method will be presented in Chapter 4. In practice, we start from a self-consistent calculation with the magnetic moment oriented in a certain direction for instance the z-direction, and the energy profile according to eq. (3.5) is evaluated by additional one-shot calculations with a new orientation from which the band energy is extracted. Due to the simple angular dependence, only one additional orientation, either in the x or y direction, is needed in case of the C_{3v} symmetry,

$$K_{zz} = E^{\mathsf{band}}(0,0) - E^{\mathsf{band}}(\pi/2,0) \quad . \tag{3.8}$$

The magnetic anisotropy energy for the considered adatoms deposited on all the surfaces is shown in Fig. 3.6a. Negative values indicate that an out-of-plane configuration is preferred by the magnetic anisotropy. Depending on the substrate the magnetic anisotropy can favor out-of-plane or in-plane configurations, even for the same adatom deposited on the geometrically identical (111) facet of an fcc surface. This once again highlights the importance of the sub-

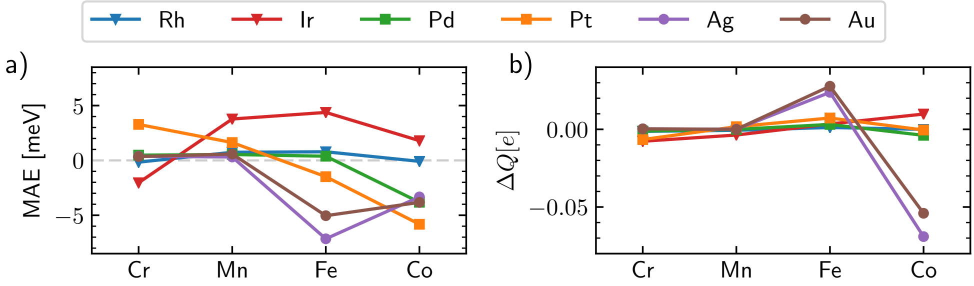

Figure 3.6.: Magnetocrystalline anisotropy of Cr, Mn, Fe, and Co deposited on the (111) facet of Rh, Pd, Ag, Ir, Pt and Au. The magnetic anisotropy energy obtained from band energy differences is shown in panel (a). Negative values indicate an out-of-plane anisotropy. The change of the charge upon rotating the magnetic moment from the z direction towards the x direction in a non-self-consistent way, i.e. based on the magnetic force theorem [137], is shown in panel (b).

strate electrons and the related induced magnetism. Since the magnetic anisotropy originates from spin-orbit coupling it is not surprising that the strength of the magnetic anisotropy is correlated to the strength of spin-orbit coupling in the substrate. For Ir, Pt and Au a significantly larger magnetic anisotropy is found than for Rh, Pd and Ag with the exception of Fe and Co on Ag. Fig. 3.6b shows the change of the charge in the cluster upon rotating the magnetic moment from the z to the x direction. A large change of this charge indicates that the necessary assumptions of the magnetic force theorem are broken, which might be the case for Fe and Co on Ag and Au [138].

Even though the orientation of the magnetic moment plays a key role for the induced magnetism, we focus on the out-of-plane configuration in the following for two reasons: First, more elements show an out-of-plane configuration as can be seen in Fig. 3.6a, and second, the computational cost associated to the construction of the giant cluster described in Section 3.2 is three times higher for an in-plane configuration than for an out-of-plane configuration due to the lower magnetic symmetry of an in-plane configuration.

3.3.3. Importance of the different magnetic contributions

The various magnetic moments for all the adatoms deposited on all the surfaces are shown in Table 3.2 and illustrated in Fig. 3.7. The spin moment of the adatoms reflect Hund's rule with the same trend on all the surfaces. Mn has the largest spin moment on all surfaces, which is related to Hund's rule, since Mn as an isolated atom is half-filled resulting in an magnetic moment of 5 μ_B. For the other atoms a parabolic behaviour is present. The substrates influence the spin moment of the adatom via its hybrization with the surface. Within the 4d and the 5d substrates the hybridization increases when decreasing its filling, i.a. going from Ag → Pd → Rh and Au → Pt → Ir, which in turn reduces the spin moment of the adatom. The hybridization affects the width of the d-peaks in the local density of states of the different adatoms on the

Surface	Atom	$m_{\rm s}^{\rm ad}[\mu_{\rm B}]$	$m_{\rm o}^{\rm ad}[\mu_{\rm B}]$	$M_{\rm s}[\mu_{\rm B}]$	$M_{\rm o}^{\rm a}[\mu_{\rm B}]$	$M_{\rm o}^{\rm ia}[\mu_{\rm B}]$	$P_{\rm s}^{\rm ad}$
Rh(111)	Cr	2.87	0.014	-1.07	-0.093	0.03	0.66
	Mn	3.81	0.023	-0.64	-0.049	0.02	0.18
	Fe	3.24	0.111	0.17	0.010	0.02	-0.51
	Co	2.03	0.190	0.58	0.016	-0.01	-0.71
Pd(111)	Cr	3.46	0.009	-1.48	-0.231	-0.01	0.83
	Mn	4.28	0.021	-0.13	-0.078	-0.01	0.43
	Fe	3.55	0.131	1.60	0.142	0.00	-0.73
	Co	2.32	0.357	1.85	0.196	-0.01	-0.90
Ag(111)	Cr	4.26	0.018	0.43	-0.032	0.01	0.76
	Mn	4.60	0.009	0.20	0.009	0.01	-0.66
	Fe	3.47	0.550	0.04	-0.007	0.04	-0.97
	Co	2.19	0.668	-0.02	-0.011	0.02	-0.97
Ir(111)	Cr	2.71	0.010	-0.66	-0.094	0.00	0.63
	Mn	3.68	0.050	-0.41	-0.083	-0.03	0.09
	Fe	3.11	0.136	0.06	-0.037	-0.03	-0.56
	Co	1.87	0.173	0.30	0.000	-0.04	-0.73
Pt(111)	Cr	3.32	0.057	-0.70	-0.232	-0.25	0.79
	Mn	4.16	0.047	-0.05	-0.110	-0.07	0.34
	Fe	3.48	0.152	0.88	0.083	0.03	-0.69
	Co	2.22	0.301	0.86	0.138	0.12	-0.87
Au(111)	Cr	4.05	0.004	0.37	0.000	0.05	0.86
	Mn	4.54	0.013	0.29	0.039	0.01	-0.41
	Fe	3.50	0.408	0.15	0.037	-0.01	-0.95
	Co	2.22	0.434	0.06	0.027	-0.04	-0.96

Table 3.2.: Magnetic properties of 3d magnetic adatoms on several (111) surfaces. Shown are the spin moment $m_{\rm s}^{\rm ad}$ and orbital moment $m_{\rm o}^{\rm ad}$ of the adatom and total induced spin moment $M_{\rm s}$, total induced atomic orbital moment $M_{\rm o}^{\rm a}$, total inter-atomic orbital moment $M_{\rm o}^{\rm ia}$, and relative spin polarization at the Fermi energy $P_{\rm s}^{\rm ad} = \frac{\rho_\downarrow(E_{\rm F})-\rho_\uparrow(E_{\rm F})}{\rho_\downarrow(E_{\rm F})+\rho_\uparrow(E_{\rm F})}$ for Cr, Mn, Fe and Co adatoms deposited on the (111) surface of Rh, Pd, Ag, Ir, Pt and Au.

surfaces shown in Fig. 3.8. Adatoms on Ag and Au show narrow peaks, which have a nearly Lorentzian-like form, indicating a weak hybridization, which is related to the s valence states of those substrates. In contrast, the other surfaces have d valence states with decreasing filling and localization going from Pd and Pt to Rh and Ir, and therefore increasing hybridization. The orbital moments of the adatoms are originating from the spin-orbit interaction and can in first order perturbation theory be related to the spin polarization of the adatoms at the Fermi level. Cr and Mn have a small orbital moment due to their small local density of states at the Fermi energy for most surfaces. Fe and Co have d peaks at or close to the Fermi energy for most elements resulting in large orbital moments of the adatoms. Increasing the hybridization lowers the density of states for those two elements resulting in weaker orbital moments. The induced moments shown in Fig. 3.7c-d, show more complicated trends and physical ori-

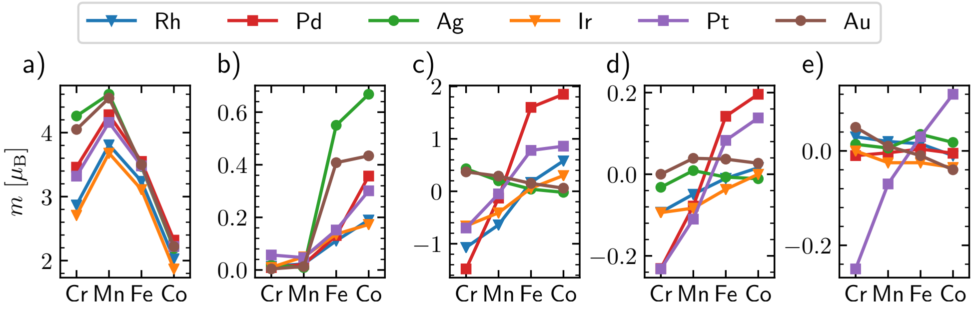

Figure 3.7.: Different magnetic contributions for Cr, Mn, Fe, and Co deposited on the (111) facet of Rh, Pd, Ag, Ir, Pt, and Au. Shown are a) the spin moment of the adatom, b) the orbital moment of the adatom, c) the induced spin moments to the substrate, d) the induced atomic orbital moments to the substrate, and e) the inter-atomic orbital moments in the substrate. All magnetic moments are in units of μ_B, as indicated on the left.

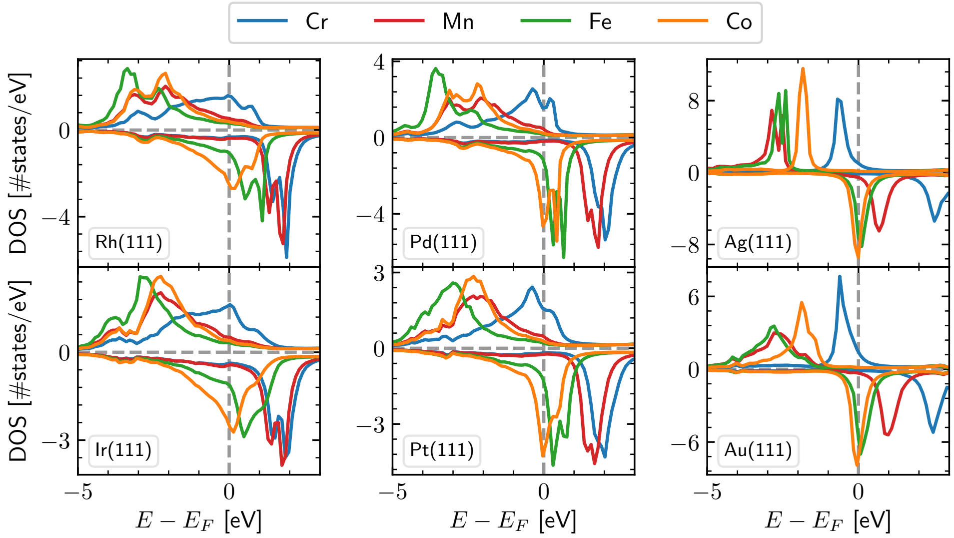

Figure 3.8.: Local density of states of the adatom for Cr, Mn, Fe, and Co deposited on the (111) facets of Rh, Pd, Ag, Ir, Pt, and Au.

gins. The induced spin moment is related to the spin polarizability of a surface. Pd is known to be highly susceptible to magnetism explaining its large induced moment for all elements except Mn. Mn shows a weak induced moments for most of the surfaces, which is in fact surprising since Mn comprises the largest atomic spin moment among the discussed adatoms. The induced atomic orbital moment is nearly proportional to the induced spin moment since it directly originates from the local spin-orbit coupling and the induced spin moment in each substrate site. This is why the substrates with larger spin-orbit coupling (Ir, Pt and Au) show

surface	M_{s}		M_{o}^{a}		M_{o}^{ia}	
	$\chi_P[\mu_{\text{B}}]$	χ_m	$\chi_P[\mu_{\text{B}}]$	χ_m	$\chi_P[\mu_{\text{B}}]$	χ_m
Rh(111)	1.13	-0.12	0.067	-0.014	-0.024	0.005
Pd(111)	1.87	0.08	0.230	-0.005	0.002	-0.001
Ag(111)	-0.18	0.07	0.005	-0.004	0.010	0.004
Ir(111)	0.65	-0.10	0.055	-0.022	-0.028	-0.006
Pt(111)	0.93	0.03	0.204	-0.016	0.186	-0.020
Au(111)	-0.10	0.07	0.019	0.005	-0.044	0.005

Table 3.3.: Susceptibilities obtained from fitting the data of Table 3.2 to eq. (3.9) for each contribution to the induced moment on the different surfaces.

a significantly enhanced orbital moment. Contrary the inter-atomic orbital moment shows distinct trends being not directly related to any of the previously discussed trends for the other magnetic contributions. The combination of large spin-orbit coupling with large spin polarizability seems to significantly favour the Pt surface over all other surfaces with respect to the inter-atomic orbital moment.

To investigate the origin of the induced moments in more detail, we identified two crucial quantities determining the strength of the induced moments as function of the chemical nature of the adatom and the surface, which are first the spin moment of the adatom m_{s}^{ad} and second the relative spin polarization of the adatoms at the Fermi energy $P_{\text{s}}^{\text{ad}} = \frac{\rho_\downarrow(E_{\text{F}})-\rho_\uparrow(E_{\text{F}})}{\rho_\downarrow(E_{\text{F}})+\rho_\uparrow(E_{\text{F}})}$. Formulating linear dependencies, which define effective susceptibilities, yields,

$$\begin{aligned} & m^{\text{ind}} = \chi_m m_{\text{s}}^{\text{ad}} + \chi_P P_{\text{s}}^{\text{ad}} \\ \text{or} \qquad & \frac{m^{\text{ind}}}{m_{\text{s}}^{\text{ad}}} = \chi_m + \chi_P \frac{P_{\text{s}}^{\text{ad}}}{m_{\text{s}}^{\text{ad}}} \quad . \end{aligned} \tag{3.9}$$

The relative spin polarization for all systems is shown in Table 3.2. The susceptibilities χ_P and χ_m can be obtained for each surface by fitting the linear dependence shown in eq. (3.9) for each surface. The resulting coefficients are shown in Table 3.3 and the quality of the fit is shown in Fig. 3.9. The fits show only small deviations from the fitted data points indicating that our assumption, eq. (3.9), holds for most surfaces. Only for the Ag surface the data points deviate noticeably from the linear behaviour. The fitted susceptibilities are in particular useful to categorize the physical origin of the different induced magnetic quantities. In fact, for the induced spin moments the Pd surface, which is known for its high spin polarizability, shows the largest χ_P. In general the $4d$ elements show a larger χ_P than their $5d$ counterparts, due to the larger spin polarizability. The dependencies on the magnetic moment of the adatom are of the same order for all surfaces, with the only exception being the Pt surface. The sign of χ_m immediately reflects the nature of the coupling of the total induced spin moment to the spin moment of the atom, with a positive sign meaning an overall ferromagnetic coupling, and a negative sign indicating an overall antiferromagnetic coupling. The induced atomic orbital moment follows similar trends than the induced spin moment with a generally more balanced distribution between the $4d$ and the $5d$ elements due to the larger spin-orbit coupling for the $5d$ substrates compensating for the reduction of the Stoner enhancement when going from the $4d$

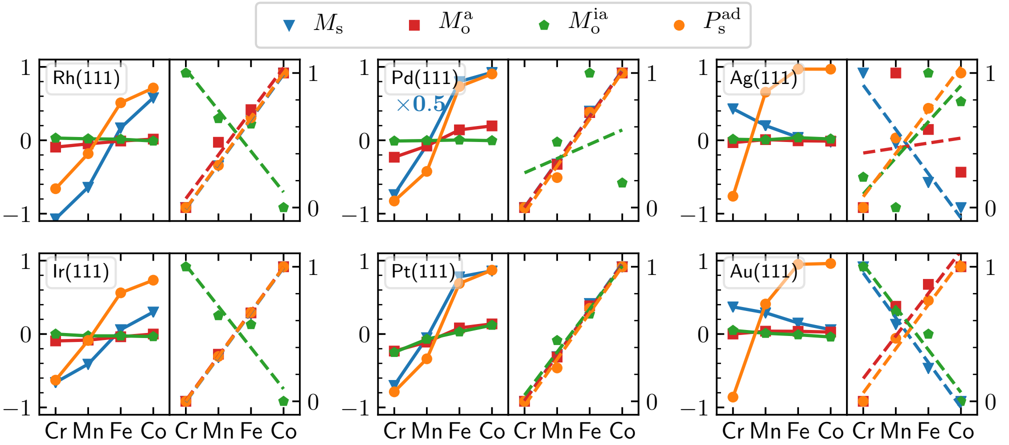

Figure 3.9.: Linear relations between the induced magnetic moments and the local magnetism of the adatoms deposited on different surfaces. Left panels: Spin moment m_{s}, atomic orbital moment $m_{\mathrm{o}}^{\mathrm{a}}$ and inter-atomic orbital moment $m_{\mathrm{o}}^{\mathrm{ia}}$ (in units of μ_{B}), and relative spin polarization at the Fermi energy $P_{\mathrm{s}}^{\mathrm{ad}}$ of each adatom on each surface. Right panels: Quantities of the left panels divided by the corresponding spin moment of each adatom, $m_{\mathrm{s}}^{\mathrm{ad}}$ (see eq. (3.9)). The dashed lines are linear fits to the data from which the susceptibilities are extracted. The data is normalized (0 to 1) to show the linear behaviours in the same plot.

to the $5d$ elements. The trends for the inter-atomic orbital moment are less clear and can not be easily explained by the previous two mechanisms. Since these trends are different and we already saw in Section 3.2 that the inter-atomic orbital moment differs from the other induced magnetic moments when it comes to its environmental dependence, the inter-atomic orbital moment must have a distinct physical origin.

Apart from the interesting trends and the distinct physical origin, the inter-atomic orbital moment shows its relevance in the absolute magnitude. For many systems it has a noticeable contribution to the total induced orbital magnetism and also to the induced magnetism in general. For Rh and Ir it is of the same order of magnitude as the induced atomic orbital moments. For Ag and Au it sometimes even dominates its atomic counterpart. However, those four systems show only small induced orbital moments and therefore the absolute relevance of the inter-atomic contribution is reduced. For Pd and Pt, which are the surfaces hosting the largest induced spin and atomic orbital moments, it shows very different behaviours. In Pd, which has large induced atomic orbital moments of up to $0.23\,\mu_{\mathrm{B}}$ in the case of Cr, the inter-atomic orbital moment is irrelevant with a maximal magnitude of $0.01\,\mu_{\mathrm{B}}$. For Pt the inter-atomic orbital moment shows its full importance being a relevant correction not only for the induced atomic orbital moments, but also for the orbital magnetism in general. For all elements on that surface it shows a significant magnitude. In the case of Cr it even dominates its atomic counterpart being a correction of more than $140\,\%$ to the total atomic orbital moment.

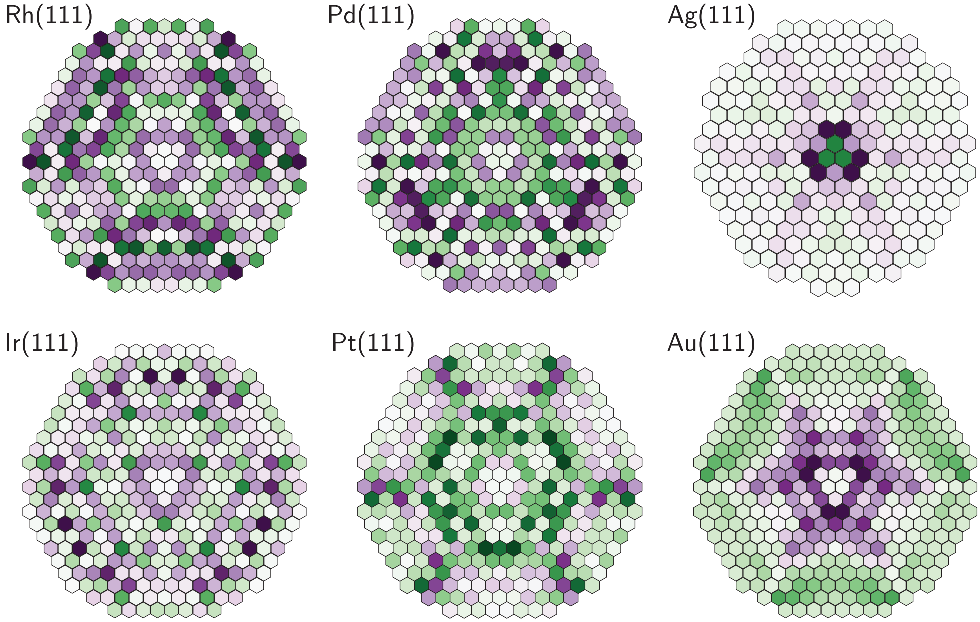

Figure 3.10.: Inter-atomic orbital moment of the substrate atoms comprising the first surface layer for a Co adatom deposited on the (111) facet of Rh, Pd, Ag, Ir, Pt, and Au. The moments are scaled by the square of the distance to the adatom. and the different surfaces do not have a common color scale for the purpose of visualization. Green indicates an alignment with respect to the moment of the adatom, while purple indicates an anti-alignment.

3.3.4. Spatial anisotropy of the inter-atomic orbital moment

In the previous sections we analyzed the inter-atomic orbital moment with respect to its physical origin and its relevance. For the case of Pt the extraordinary long range of the inter-atomic orbital moment was discussed in Section 3.2. In this section, the spatial anisotropy of the inter-atomic orbital moment is analyzed. Fig. 3.10 shows the inter-atomic orbital moment in the first surface layer of all considered substrates scaled by the square of the distance to the adatom. The Co adatom is chosen as example. All surfaces show oscillations as function of the distance, which are similar to the well-known Friedel oscillation of the charge and spin densities [64]. The wavelength of the oscillations is increasing within the 4d and 5d elements (Rh → Pd → Ag and Ir → Pt → Au). For an impurity embedded in a Rashba electron gas [139] it is known that the wavelength of oscillations of the orbital density is related to the Fermi wavelength, $\lambda_{\mathrm{F}} = \frac{2\pi}{k_{\mathrm{F}}}$. The system, which is closest to a Rashba system, is the Au(111) surface. Experimental measurements of the Fermi wavelength in Au(111) yield $\lambda_{\mathrm{F}} = 32.7\,\text{Å} - 37.6\,\text{Å}$ [140]. The Au surface shows the first change of sign at six nearest neighbor distances, a, resulting in a distance of $d \approx 6a = 6a_0/\sqrt{2} = 17.2\,\text{Å}$ corresponding to a wavelength of 34.4 Å, which is in perfect agreement with the Fermi wavelength. The Rashba model is isotropic in k-space and therefore the oscillations should not show any anisotropies. Real materials, however,

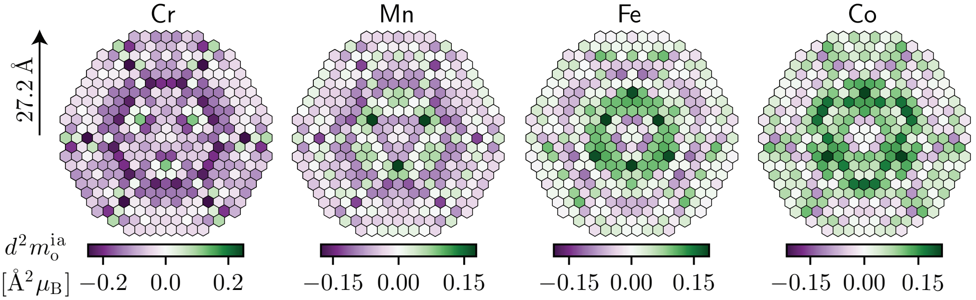

Figure 3.11.: Inter-atomic orbital moment of the substrate atoms comprising the first surface layer for all considered elements deposited on Pt(111). The values are scaled by the square of the distance to the adatom.

have more complex Fermi surfaces, which are known to be the source of anisotropic Friedel oscillations and can give rise to focusing effects [141].

This can be also seen in the inter-atomic orbital moment. The Ag and Au surfaces show a fairly isotropic behaviour with their nearly isotropic Fermi surfaces. The other surfaces have much more complicated Fermi surfaces, which might give rise to the seen anisotropies. The Pt surface even shows some kind of focusing effect in between the high symmetry lines of the C_{3v} surface.

Apart from the anisotropies, the spatial plots indicate the range of the inter-atomic orbital moment. On Ag the effective range is the shortest including only a couple of shells. On Pt and Au the range goes up to approximately 7-8 nearest neighbor distances, which is equal to approximately $20\,\text{Å}$. Rh, Pd and Ir show the longest ranges. It is not even clear if the used giant hemispherical clusters containing nearly 3000 atoms are large enough for those systems to converge the inter-atomic orbital moment. However, due to the small absolute moments, we did not investigate this further. Note again that the shown plots in Fig. 3.10 are scaled by the square of the distance to the adatom.

To investigate the dependence on the chemical nature of the adatoms, Fig. 3.11 shows the inter-atomic orbital moment in the first surface layer for the considered adatoms deposited on the Pt(111) surface, which was found to host the largest inter-atomic orbital moments. The range of the inter-atomic orbital moment is approximately the same, which agrees with the previous assumption that the range is an property of the substrate and does not depend on the specific adatom. A crucial difference between the adatoms is the direction of the induced currents, anti-clockwise or clockwise, resulting in a ferromagnetic or antiferromagnetic alignment of the inter-atomic orbital moment with respect to the spin moment of the adatom. Cr shows a purely anti-ferromagnetic alignment with the exception of only a few single atoms, which results in the large magnitude of the inter-atomic orbital moment. Increasing the filling by going to Mn and Fe results in more oscillations between ferro- and anti-ferromagnetic alignments. In particular, Fe shows approximately as many atoms in the anti-ferromagnetic state as in the ferromagnetic state resulting in a nearly vanishing inter-atomic orbital moment. For Co nearly all antiferromagnetic regions vanished and the ferromagnetic alignment dominates resulting again in a large inter-atomic orbital moment.

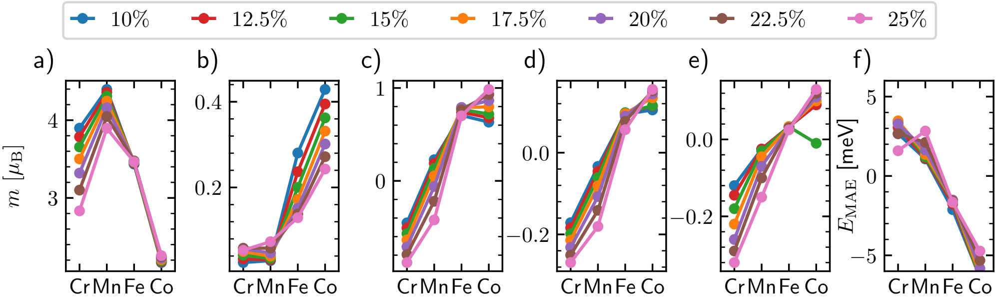

Figure 3.12.: Dependence of the magnetic quantities on the vertical relaxation of the adatom towards the Pt(111) surface. a) Spin moment of the adatom. b) Orbital moment of the adatom. c) Induced spin moments. d) Induced atomic orbital moments. e) Induced inter-atomic orbtial moments. f) Magnetic anisotropy energy. The magnetic moments are in units of μ_B as indicated on the left.

3.3.5. Impact of the relaxation and confinement effects

To investigate the impact of the geometry on the different magnetic quantities, we varied the vertical relaxation of the adatoms deposited on the Pt(111) surface starting from $10\,\%$ up to $25\,\%$. The resulting magnetic moments are shown in Fig. 3.12a-e. The spin moment of the adatoms shows a strong dependence on the relaxation for Cr and Mn, while Fe and Co are not noticeably affected. The relaxation directly affects the strength of the hybridization of the adatom with the surface. As can be seen in the local density of states in Fig. 3.8, Cr and Mn have a majority peak at the Fermi level and close to the Fermi level, respectively, and unfilled minority peaks. A stronger hybridization leads to a broadening of those peaks, which in turn lowers the spin moment. Contrary, Fe and Co have nearly filled and stronger bounded majority states resulting in a stable spin moment as function of the relaxation. The orbital moment of the adatom is most affected for Fe and Co, which have the highest spin polarization at the Fermi level. Due to the hybridization and the associated broadening of the peaks, the spin polarization lowers and therefore the orbital moment decreases. The induced magnetic moments depend on the relaxation directly via the effect on the hybridization and indirectly via the effect of the relaxation on the local spin moment, which is the source of the induced moments. In general, all the induced moment are enhanced for stronger relaxations. The relaxation affects most Cr and Mn, which is most probably related to the strong dependence of the local spin moment for those two elements. In addition to dependence of the magnetic moments, Fig. 3.12f shows the dependence of the magnetic anisotropy energy on the relaxation, which shows a similar trend as the spin moment of the adatoms. The MAE of Fe and Co is not strongly affected by the increasing relaxation, while Cr and Mn show a stronger dependence on the relaxation. However, a simple trend cannot be discerned in the magnetic anisotropy energy. While Mn seems to increase its magnetic anisotropy energy with increasing relaxation, Cr show the largest magnetic anisotropy energy for $17.5\,\%$ and the lowest for $25\,\%$ and $10\,\%$ of relaxation.

Possible confinement effects are investigated by analyzing the dependence of the different magnetic quantities on the number of layers in the slab, which is shown in Fig. 3.13. An exper-

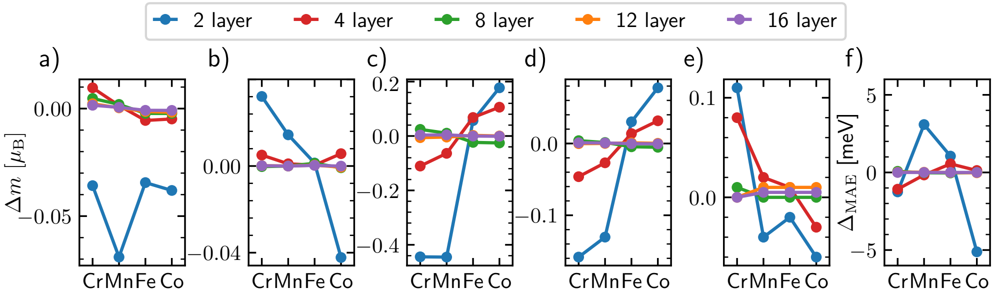

Figure 3.13.: Dependence of the magnetic quantities on the thickness of the Pt slab for different numbers of layers (2, 4, 8, 12, and 16 layer). Shown are the deviations from the reference calculations using 40 layers of Pt. a) Spin moment of the adatom. b) Orbital moment of the adatom. c) Induced spin moments. d) Induced atomic orbital moments. e) Induced inter-atomic orbtial moments. f) Magnetic anisotropy energy. The magnetic moments are in units of μ_B as indicated on the left.

imental realisation of this would be the deposition of Pt thin films of different thicknesses on top of another substrate with a lower spin polarizability and a weaker spin-orbit coupling resulting in negligible induced moments arising from the second substrate. The values are compared to our reference slab containing 40 layers. The spin moment and the orbital moment of the adatom is not affected much by the thickness of the slab. Only for a two layer slab significant deviations are found. The induced moments show strong deviations from the reference

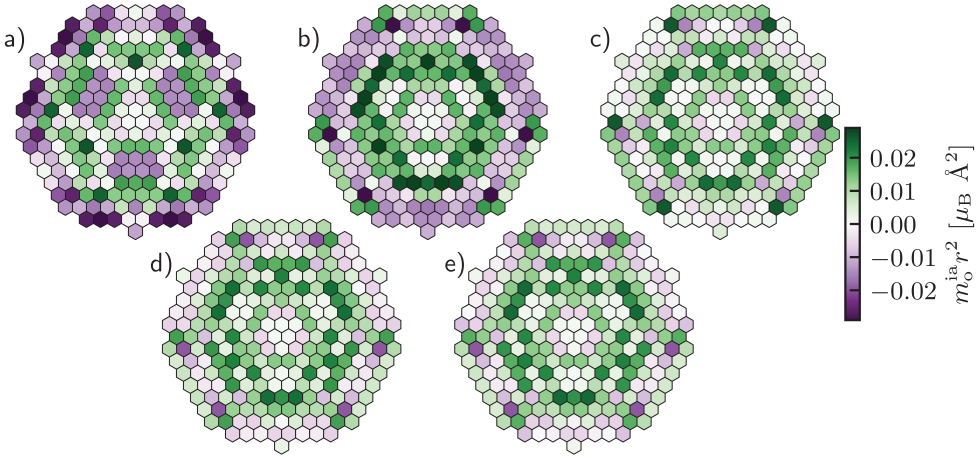

Figure 3.14.: Inter-atomic orbital moment in the first surface layer for an Co adatom deposited on Pt(111) as function of the thickness of the slab. The inter-atomic orbital moments are scaled by the square of the distance to the adatom. a) 2 layers. b) 4 layers. c) 8 layers. d) 12 layers. e) 16 layers.

calculation indicating that the total magnetic moments can be tuned and engineered via confinement effects. In general, a slab containing more than 8 layers yields magnetic moments sufficiently close to the reference calculation.

Fig. 3.14 shows the spatial distribution of the inter-atomic orbital moment in the first Pt surface layer for a Co adatom as function of the thickness of the Pt slab. While the results for 8, 12 and 16 layers are almost the same as the reference calculation shown in Fig. 3.10, strong confinement effects are found for 2 and 4 layers. The additional reflections of the Friedel oscillations at the other surface leads to interference effects, which change the oscillatory behaviour of the inter-atomic orbital moment and influence its range. It is clearly visible that the range of the inter-atomic orbital moment is increased for the two layer system compared to the other cases. Therefore, the confinement effects allow to engineer not only the magnitude of the induced moments, but also their the range, which might open a new avenue of manipulating long-ranged interactions.

3.3.6. Impact of the orientation of the magnetic moment of the adatom

As discussed in Section 3.3.2, the magnetic anisotropy energy favours not always the out-of-plane spin configuration, which was the assumed configuration in the previous sections. Table 3.4 shows the dependence of all magnetic moments on the orientation of the magnetic moment for the different considered adatom deposited on the Pt(111) surface. As an example for an in-plane configuration the x direction was chosen. The spin moment of all the adatoms does not depend on the particular orientation, which also holds for the induced spin moments. Contrary, the orbital moment of the adatom crucially depends on the orientation of the magnetic moment, since it originates from the spin-orbit interaction, which is affected by the relative orientation between the magnetic moment and the underlying lattice. As a general trend, the

Adatom		$m_\mathrm{s}^\mathrm{ad}[\mu_\mathrm{B}]$	$m_\mathrm{o}^\mathrm{ad}[\mu_\mathrm{B}]$	$M_\mathrm{s}[\mu_\mathrm{B}]$	$M_\mathrm{o}^\mathrm{a}[\mu_\mathrm{B}]$	$M_\mathrm{o}^\mathrm{ia}[\mu_\mathrm{B}]$
Cr	z	3.32	0.06	-0.70	-0.23	-0.25
	x	3.32	0.17	-0.62	-0.27	0.03
Mn	z	4.16	0.05	-0.05	-0.11	-0.07
	x	4.16	0.09	-0.03	-0.11	0.06
Fe	z	3.48	0.15	0.88	0.08	0.03
	x	3.48	0.17	0.81	0.13	0.05
Co	z	2.22	0.30	0.86	0.14	0.12
	x	2.22	0.18	0.84	0.17	0.04

Table 3.4.: Different magnetic contributions for the considered magnetic adatoms on the Pt(111) surface. Compared are a self-consistent out-of-plane configuration, where the magnetic moment points in the z direction, and a self-consistent in-plane configuration, where the magnetic moment points in the x direction. Shown are the spin moment of the adatom m_s^ad, the orbital moment of the adatom m_o^ad, the total induced spin moment M_s, the total induced atomic orbital moment M_o^a, and the total induced inter-atomic orbital moment M_o^ia.

orbital moments of the adatoms are larger in the ground state of the particular atom, which is the in-plane state for Cr and Mn and the out-of-plane state for Fe and Co [68]. Only for Fe the orbital moment is not influenced by the orientation. The induced atomic orbital moment being a direct consequence of the induced spin moments and the spin-orbit coupling are not noticeably changed by the orientation of the magnetic moment. However, the inter-atomic orbital moments have the strongest dependence on the orientation of the magnetic moment. For Cr and Co, their magnitude drastically decreases upon rotating the moment from the z to the x direction. The reason for this is the physical origin of the inter-atomic orbital moment, which are the net currents. Most relevant are the currents in the plane, which is perpendicular to the magnetic moment. This plane, however, contains only half the atoms when rotating from the z to the x direction. Furthermore, due to the continuity equation the currents have to swirl in closed loops, which is much more difficult since half of the perpendicular plane contains vacuum. As a consequence, the inter-atomic orbital moment is less relevant for in-plane configurations.

3.3.7. Magnetic stray fields

The question we want to ask in this section is if and how the induced magnetism can be probed in an experiment. A potential probing mechanism could be based on the magnetic stray fields. The magnetic stray fields of a finite current distribution were introduced as part of Section 2.2.4. The stray field induced by all the different contributions of the orbital moments can be calculated via eq. (2.66) using the full ground-state current distribution including the net currents. The stray field can be separated into contributions from the monopole term, the dipole term and the quadrupole term. Since the quadrupole term turns out to be irrelevant it will be neglected in the following. For the spin moment, the classical dipole approximation given in eq. (2.70) is used. All the approximations are valid as long as $\boldsymbol{r}$ is outside of the atomic cells in which the current is defined, which is fulfilled for any realistic observation point. Fig. 3.15 shows the stray fields generated by a Co adatom deposited on the Pt(111) surface in a plane parallel to the surface and $1\,\mathrm{nm}$ away from it. The contribution from the spin and orbital moment of the adatom is shown in Fig. 3.15a. It is strongly localized and has a maximal magnitude of $\sim 3\,\mathrm{mT}$. The induced spin moment and the induced atomic orbital moment are shown in Fig. 3.15b and c, respectively. Both have a broader shape than the field induced by the moments of the adatom. The broadest shape can be seen for the stray field generated by the inter-atomic orbital moment in Fig. 3.15d. The shape differs significantly from the other contributions, but also the maximal magnitude is disproportionately less important. Fig. 3.16a shows a line cut of all the contributions in the far distance regime at a vertical distance of $10\,\mathrm{nm}$. In this case all the shapes are identical, and therefore equivalent to the dipole approximation, and the amplitude of each contribution scales according to the corresponding total magnetic moment.

In conclusion, the importance of the induced magnetism is reflected in the deviations of the shape and the related maximal magnitude from the single dipole approximation. Fig. 3.16 shows this effect by comparing the fields generated by the full distribution of the different magnetic moments to the case of a single dipole at the origin with the moment of the full cluster and a single dipole representing the contribution coming purely from the adatom. Any deviation from the dipolar approximation can be immediately identified, since the dipolar field

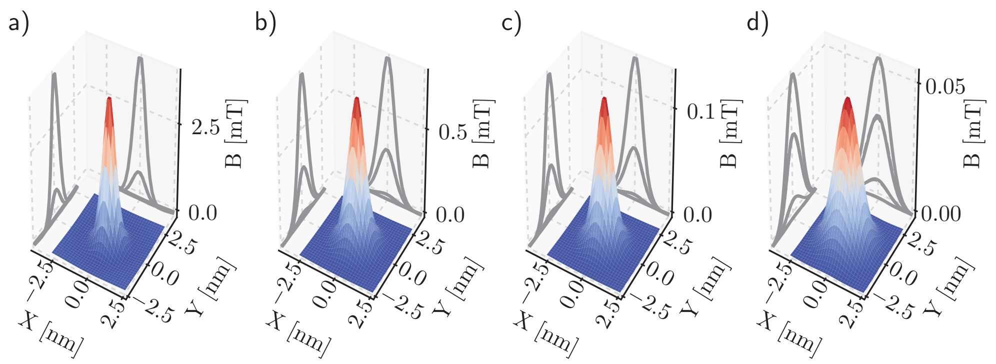

Figure 3.15.: Magnetic stray field at a vertical distance of 1 nm to the surface originating from different magnetic contributions for a Co adatom deposited on Pt(111). a) Stray field from the spin and orbital moment of the adatom. b) Stray field from the induced spin moments. c) Stray field from the induced atomic orbital moments. d) Stray field from the induced inter-atomic orbital moments. Shown is the z component of the field.

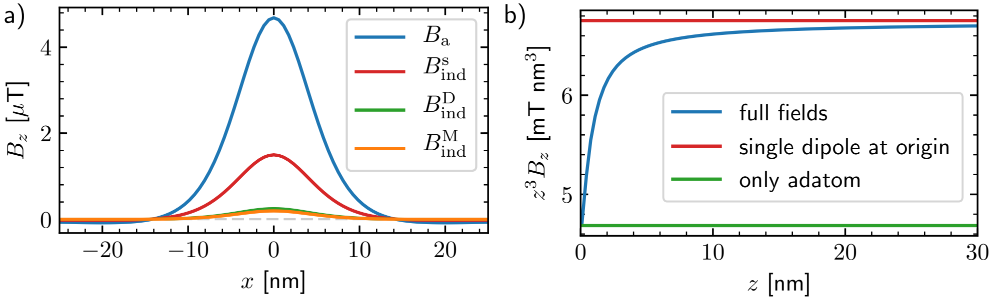

Figure 3.16.: Stray fields generated by a Co adatom on Pt(111). a) Magnetic stray field in the far field at a vertical distance of 10 nm to the surface. Shown are the stray field generated by the total magnetic moment of the adatom B_{a}, the field generated by the induced spin moment $B^{\text{s}}_{\text{ind}}$, and the field from the atomic orbital moment $B^{\text{D}}_{\text{ind}}$, as well as the inter-atomic orbital moment $B^{\text{M}}_{\text{ind}}$. b) Magnetic stray field on top of the Co adatom as function of the vertical distance z. Shown is the field obtained from the full current distribution and taking all positions of the spin moments into account (blue curve), the field generated by a single dipole having the same total magnetic moment as the full cluster, and the field generated by only the magnetic moments of the adatom. The field is scaled by z^3 to show the deviation from the dipole approximation.

scales with $1/z^3$. In the far field, the single dipole at the origin represents well the full field. In the limit of approaching the atom, the full field is approaching the field generated by the single adatom. The spatial extend of the deviation from those two limits is a good indicator for the range of the induced magnetism and the importance of the induced magnetism.

A feasible experimental observation could be based on nitrogen vacancy centers in nanodiamonds [142], which are very sensitive to magnetic field being able to resolve magnetic fields of the order of $1\,\mathrm{nT}$. Sensing the magnetic field vertically above the adatom as function of the distance would allow for an identification of the importance of the induced magnetism as discussed in relation to Fig. 3.16b. Both, the spatial resolution as well as the resolution with respect to the magnetic field, would allow for such an classification. However, in the first experiments which probed a single magnetic atom [142] a vertical distance of the nitrogen vacancy to the surface of approximately $50\,\mathrm{nm}$ was reported. It remains unclear if experimentally the vertical distance can be reduced enough to obtain a noticeable deviation from the dipolar approximation.

3.3.8. Finite nanostructures: The case of compact trimers

In the previous sections, we discussed the various effects related to induced magnetism in systems based on single adatoms deposited on surfaces. In this section, the effect the size of the magnetic nanostructure is briefly considered. As prototypical test system $3d$ transition metal compact trimers deposited on the Pt(111) surface are chosen. For compact trimers there are four different possible stacking positions – the fcc and hcp stacking sites, as well as the top and hollow stackings, where top means that a Pt atom is below the center of the trimer, while hollow has no Pt atom below the trimer. Here we focus on the fcc-top stacked trimers.The vertical relaxation is assumed to be close to the relaxation of single adatoms and set to $20\,\%$. The resulting magnetic contributions are shown in Table 3.5 for Cr, Mn, Fe, and Co trimers. Note that we assume collinear out-of-plane ferromagnetic magnetic structures for all the trimers, which is a good assumption for Fe and Co, which exhibit a strong ferromagnetic coupling, but bad for Cr and Mn, which are frustrated due to their anti-ferromagnetic interaction. The nature of the coupling will be discussed in detail in Chapter 4. Comparing the different magnetic contributions to the ones of the adatoms, the spin moment of each trimer atom is nearly unaffected. The orbital moment is reduced by up to $30\,\%$ for the case of the Co trimer. The additional hybridization to the neighboring trimer atoms results in the reduction of the orbital moment. In general, the induced moments are enhanced by the presence of the additional trimer atoms, but it is not directly proportional to the number of atoms. For

Trimer	$m_{\mathrm{s}}^{\mathrm{tri}}[\mu_{\mathrm{B}}]$	$m_{\mathrm{o}}^{\mathrm{tri}}[\mu_{\mathrm{B}}]$	$M_{\mathrm{s}}[\mu_{\mathrm{B}}]$	$M_{\mathrm{o}}^{\mathrm{a}}[\mu_{\mathrm{B}}]$	$M_{\mathrm{o}}^{\mathrm{ia}}[\mu_{\mathrm{B}}]$
Cr	3.20	0.04	-1.03	-0.53	0.05
Mn	4.07	0.05	0.40	-0.24	0.12
Fe	3.32	0.12	1.63	0.14	0.06
Co	2.19	0.20	2.12	0.32	0.21

Table 3.5.: Magnetic contributions for fcc-top stacked compact trimers composed out of Cr, Mn, Fe and Co deposited on the Pt(111) surface. Shown are the spin moments $m_{\mathrm{s}}^{\mathrm{tri}}$ and the orbital moment $m_{\mathrm{o}}^{\mathrm{tri}}$ of each trimer atom, the total induced spin moment M_{s}, the total induced atomic orbital moment $M_{\mathrm{o}}^{\mathrm{a}}$ and the total inter-atomic orbital moment $M_{\mathrm{o}}^{\mathrm{ia}}$

example for the Co trimer, the induced spin moment is enhanced by a factor of 2.5, the induced atomic orbital moment is 2.3 times larger, and the inter-atomic orbital moment is 1.8 times larger. While the small deviation from 3 for the induced spin and atomic orbital moment can be explained by the change of the electronic structure due to the formation of the hybridized trimer d-orbitals, the inter-atomic orbital moment deviates more drastically, which can be related to the complex Friedel-like oscillations discussed in relation to Fig. 3.11. Adding up multiple atoms, the complex interplay of the oscillations leads to destructive interference-like effects. Note that the Pt surface can also change its response to the nanostructure upon adding atoms, e.g. the Mn adatom lead to an anti-ferromagnetically coupled induced spin moment, while the overall response of the Pt surface to the Mn trimer is ferromagnetic.

3.4. Conclusions and outlook

In this chapter, the magnetism induced to a non-magnetic surface in the presence of a magnetic nanostructure was investigated. A new contribution to the orbital component of the induced magnetism was identified – the inter-atomic orbital moment. A special construction of giant hemispherical clusters allowed for an efficient calculation of the inter-atomic orbital moment including up to 3000 atoms, which is needed in order to account for the exceptional long range of the inter-atomic orbital moment of e.g. $\sim 22\,\text{Å}$ in the Pt(111) surface. A comprehensive analysis of induced magnetism in general was presented for Cr, Mn, Fe and Co adatoms deposited on the (111) facets of Rh, Pd, Ag, Ir, Pt and Au. The effects of the hybridization of the adatoms with the surface, which can be tuned by either decreasing the vertical distance between the adatoms to the surface or by decreasing the filling of the substrate within the $4d$ and $5d$ elements, was investigated and found to crucially affect the spin and orbital moments of the adatoms, as well as the induced spin moment and the induced atomic orbital moment. The induced atomic orbital moment originating from the spin-orbit interaction was shown to be closely correlated to the induced spin moment, while the inter-atomic orbital moment has a distinct origin. First, contrary to the other magnetic contributions it does not depend on the local environment, and second, it shows distinct susceptibilities attributed to the spin moment of the adatoms and the spin polarizability at the Fermi energy. The inter-atomic orbital moment was found to show complex Friedel-like oscillations, which for the case of the Au(111) surface could be related to the oscillation found for an impurity embedded in the two-dimensional Rashba electron gas. The importance of geometrical details was carefully analysed and we investigated how confinement effects can be used to manipulate the induced magnetism. The magnetic stray field originating from the magnetic contributions was analyzed, and we proposed how to experimentally disentangle the long-ranged induced magnetism from the local magnetism using experimental techniques being sensitive to magnetic field, like e.g. scanning nitrogen vacancy center microscopy.

The inter-atomic orbital moment has the potential to help understanding the puzzle of orbital magnetism. For many systems there has been and still is a disagreement between the orbital moments observed in experiment and the orbital moments predicted by first-principles method [42]. Furthermore, the orbital component of the induced magnetism may provide, due to its particularly long range, a new avenue of long-ranged interactions with a potential benefit for future information technology.

Even though, a comprehensive analysis including several aspects was presented in this chapter, we were still lacking a precise description for multi-atomic nanostructures, e.g. including non-collinearities or in complex magnetic textures, such as isolated magnetic skyrmions in a ferromagnetic layer [143].

4

Higher-order magnetic exchange interactions

The formation of skyrmions and other complex magnetic textures, which are promising building blocks for future data storage and processing devices, is based on chiral interactions with the well-known Dzyaloshinskii-Moriya interaction being the main driving mechanism. Higher-order interactions are also known to have a significant impact on several non-collinear structures, stabilizing for example a nanoskyrmion lattice. In this chapter, we present a comprehensive and systematic analysis of higher-order magnetic interactions with a special focus on chiral interactions. The emergence of higher-order interactions from a microscopic model based on the ideas of Levy and Fert is shown. Using an intuitive diagrammatic technique, we present a microscopic theory of magnetic interactions up to arbitrary order going beyond the usual bilinear interactions. The microscopic theory allows us to systematically catalogue all possible *higher-order interactions from which especially those of chiral nature are of interest. Using the prototypical test systems of magnetic dimers and trimers deposited on the Pt(111) surface, we identify the most relevant higher-order pair interactions and the most important 3-site interactions. We find the chiral biquadratic pair interaction as a new chiral interaction being the biquadratic equivalent of the DMI and discuss its implications not only to magnetic dimers but also to extended systems like a nanoskyrmion lattice.*

Parts of the presented work have been published in

S. Brinker et al. New Journal of Physics ***21****, 083015 (2019)*
I have contributed to this publication in the following way: I developed the analytical model for the description of higher-order exchange interactions. I performed the DFT calculations and developed the mapping procedure from DFT to the spin cluster expansion based on magnetic torques and constraining fields, which I implemented in our local KKR codes developed in Jülich. I analyzed the results and wrote most of the manuscript.

S. Brinker et al. Physical Review Research ***2****, 033240 (2020)*
I have contributed to this publication in the following way: I analyzed the multi-site interactions based on the microscopic model and a heuristic symmetry analysis together with Dr. Manuel dos Santos Dias. I performed the DFT calculations. I also contributed to the manuscript by analyzing and discussing the results and their theoretical context, and offering corrections.

4.1. Introduction

The field of spintronics relies on the fundamental understanding of magnetism and the possible manipulation of magnetic systems. Nowadays the enormous and ever-increasing amount of data is mainly stored using magnetic devices, which can be manipulated based on the seminal works of Peter Grünberg [4] and Albert Fert [5] and the discovery of the giant magnetoresistance. In a magnetic device bits are stored in domains of strongly coupled magnetic atoms containing thousands of atoms, which are stabilized by the magneto crystalline anisotropy favouring a specific magnetic easy-axis. The atoms of each bit can be collectively manipulated acting like a single magnetic moment. However, the data storage density in conventional hard disks is approaching its limits, which is mainly based on the interactions between the ever-shrinking domains. New concepts of magnetic data storage are evolving, e.g. based on non-collinear structures like domain walls [15], magnetic skyrmions [10], or other more recently discovered magnetic structures like magnetic bobbers [11]. Skyrmions and bobbers are promising building blocks of future spintronics devices due to the non-trivial topology of their magnetic structure resulting in an increased stability. The ultimate goal in terms of storage density is the usage of a single atom as a data bit. However, single adatoms face the problems of magnetic stability and of possible interactions with its surrounding preventing them from being used as single magnetic bits. We will discuss this approach in more detail in Chapter 6.

In this chapter, we focus on the fundamental interactions between magnetic atoms needed for the understanding of the previously mentioned technologies. The interactions enable the formation of strongly coupled magnetic domains in conventional hard disks, but also give rise to highly non-collinear structures like the magnetic skyrmion. Since the seminal work of Heisenberg [49] magnetic materials are often modeled by isotropically interacting spin moments,

$$\mathcal{H}_{\text{iso}} = \frac{1}{2}\sum_{ij} J_{ij}\, \boldsymbol{e}_i \cdot \boldsymbol{e}_j \quad , \tag{4.1}$$

with the isotropic exchange interaction J_{ij} coupling the spin moments of site i and j, and $\boldsymbol{e}_i$ being the unit direction of the magnetic moment. The isotropic exchange favours a ferromagnetic ($J < 0$) or anti-ferromagnetic ($J > 0$) alignment between the moments. In a magnetic dimer this immediately results in a collinear configuration, but for a system with more than two atoms the anti-ferromagnetic exchange can give rise to competing interactions resulting in non-collinear states. A well-known example is the Néel state in an anti-ferromagnetically coupled triangular lattice [52] or the complex magnetic structure of α-Mn [53]. Different physical mechanisms are generating an effective exchange between two atoms. The most prominent mechanisms are the so-called direct exchange, the double exchange, the superexchange [144], and the Ruderman–Kittel–Kasuya–Yosida (RKKY) interaction [145–147]. The direct exchange originates from the direct hopping of an electron between two magnetic atoms based on the Coulomb repulsion. The superexchange is mediated by a hopping to an orbital of a nearest neighbor atom and typically results in an anti-ferromagnetic interaction. In contrast to the other mechanisms, the RKKY interaction is an effective interaction mediated by the electrons at the Fermi surface, having in general a longer range than the other mechanisms as discussed in Chapter 6.

An important extension to the isotropic atomistic spin model of Heisenberg is related to the discovery of a chiral interaction by Dzyaloshinskii [54] and Moriya [55]. The so-called Dzyaloshinkii-Moriya interaction (DMI) is present in systems with large spin-orbit coupling and broken inversion symmetry. In the atomistic form it can be described by the Dzyaloshinkii-Moriya vector $\boldsymbol{D}_{ij}$,

$$\mathcal{H}_{\text{DMI}} = \frac{1}{2}\sum_{ij} \boldsymbol{D}_{ij} \cdot (\boldsymbol{e}_i \times \boldsymbol{e}_j) \quad , \tag{4.2}$$

with $\boldsymbol{D}_{ji} = -\boldsymbol{D}_{ij}$. The DMI favours an effective angle of 90° between two magnetic moments of a distinct chirality defined by the vector $\boldsymbol{D}_{ij}$. It supports the formation of spin spiral [56], attributes a certain rotational sense to a domain wall [148, 149], and opened a new avenue of chiral nanostructures, like magnetic skyrmions and magnetic bobbers. It also impacts the magnetic stability of nanostructures [38], which is discussed in more detail in Chapter 6. The Dzyaloshinkii-Moriya vector underlies certain symmetry rules, which are known as the Moriya rules and were originally derived in terms of a phenomenological theory [55]. Levy and Fert derived the symmetry rules based on a microscopic theory [87, 88], which also lead to a widely used intuitive picture for interfacial DMI. The key essence of the Levy-Fert model is the microscopic separation of atoms hosting magnetism and atoms hosting a strong spin-orbit coupling. The interaction between the magnetic atoms is mediated by the heavy atom with large spin-orbit coupling, which gives rise to the DMI, which is first order in the spin-orbit coupling.

The last member in the class of bilinear magnetic exchange interactions is the anisotropic exchange interaction, which is sometimes also called symmetric exchange or compass term [150], and has the form,

$$\mathcal{H}_{\text{aniso}} = \frac{1}{2}\sum_{ij} \boldsymbol{e}_i^{\mathsf{T}}\, J_{ij}^{\text{aniso}} \boldsymbol{e}_j \quad , \tag{4.3}$$

where J_{ij}^{aniso} is a symmetric traceless matrix, with $J_{ij}^{\text{aniso}} = J_{ji}^{\text{aniso}}$. Being a real symmetric matrix similarly to the magnetic anisotropy discussed in Section 3.3.2, it defines an easy-axis and a hard-axis resulting in a collinear ground state with both magnetic moments aligning with the easy-axis. For inequivalent magnetic moments and in combination with the magnetic anisotropy, it can also be the source of non-collinearities as shown in Chapter 6. However, in contrast to the DMI, it is not chiral and does not lead to the formation of magnetic skyrmions in extended systems. Since it is second order in the spin-orbit interaction, it is also often smaller than the other bilinear interactions. As a consequence, the anisotropic exchange is neglected in most studies and not well-studied. One of the few prominent examples for which it shows its relevance is the Kitaev interaction in a honeycomb lattice [151–153].

For most systems, the bilinear magnetic exchange interactions are capturing most of the physics. However, some systems show effects which can not be explained by the bilinear interactions alone. A prominent example is ^{3}He [154] showing strong indications of the importance of isotropic higher-order interactions. In higher order, apart from the usual pair interactions, e.g. the isotropic biquadratic interaction, $B_{ij}\left(\boldsymbol{e}_i \cdot \boldsymbol{e}_j\right)^2$, multi-site interactions can emerge. Theoretically these isotropic higher-order interactions were derived from a Hubbard model at half filling [155–158], from a Kondo-lattice model [159–161]. Theoretically their main impact originates from the non-linearities added to the Heisenberg hamiltonian. Similarly to a Fourier series, an arbitrary magnetic state can be expressed by a super position of spin spirals, or so-called single-$\boldsymbol{Q}$-states,

$$\boldsymbol{m}_i = \sum_n \boldsymbol{A}_n e^{\mathrm{i}\,\boldsymbol{R}_i \cdot \boldsymbol{Q}_n} \quad , \tag{4.4}$$

where $\boldsymbol{A}_n$ is an expansion coefficient of the $\boldsymbol{Q}_n$-state and $\boldsymbol{R}_n$ is the position of the moment $\boldsymbol{m}_i$. Note that the series is not necessarily finite, and that not every superposition yields a realistic magnetic state, since for periodic systems, where all atoms are equivalent, $|\boldsymbol{m}_i| = m$ has to hold. However, certain structures can be described by a superposition of a couple of single-$\boldsymbol{Q}$-states, e.g. the antiferromagnetic *uudd* state [57, 58], which is a $2\boldsymbol{Q}$-state, and the $3\boldsymbol{Q}$-state [52]. The bilinear Heisenberg hamiltonian is linear and so does not energetically distinguish multi-$\boldsymbol{Q}$ states from single-$\boldsymbol{Q}$ states, while the higher-order interactions add non-linearities to the hamiltonian, which can result in the stabilization of these phases, even though the underlying single-$\boldsymbol{Q}$ are not energetically favoured.

More recently higher-order interactions, which are of chiral nature, have attracted a high attention. The puzzling magnetic ground state of Fe chains on the Re(0001) surface was tried to be explained by Lászlóffy et al. [60] using a chiral three-site interaction. Note that in Chapter 7, we will analyze this particular system with results contradicting Ref. [60]. Furthermore, Grytsiuk et al. [61] found significant chiral multi-site interactions in MnGe, which they related to the topological orbital moment and the scalar spin chirality, $\boldsymbol{e}_i \cdot (\boldsymbol{e}_j \times \boldsymbol{e}_k)$. Both of these works were produced parallel to the work presented in this Chapter and they have the same physical origin as discussed in Section 4.2.

Magnetic exchange interactions can be extracted from DFT using different schemes. Plane wave codes often rely on the calculation of the total energy of different magnetic states, which can be fitted to a magnetic hamiltonian. The assumed spin model is fitted to these input data. Therefore in contrast to the KKR method, the direct evaluation of the exchange interaction between two atoms is not possible. The used procedure in KKR is based on the magnetic force theorem [137] and the infinitesimal rotation method [137, 162]. In the following a short description of this method is given.

Magnetic exchange interactions within KKR (infinitesimal rotation method)

Magnetic exchange interactions can be obtained based on infinitesimal rotations of the magnetic structure invoking the magnetic force theorem [137]. The impact of an infinitesimal rotation of the moments i and j can be related to the derivative of the band energy with respect to the directions of the magnetic moments. Assuming that the DFT results map to an effective atomistic spin model, the change in the energy can be related to the associated change in the spin model,

$$\frac{\delta}{\delta e_i^\alpha}\frac{\delta}{\delta e_j^\beta}\epsilon_{\text{band}} = \frac{\delta}{\delta e_i^\alpha}\frac{\delta}{\delta e_j^\beta}E_{\text{spin-model}} \quad . \tag{4.5}$$

For the Heisenberg model the different components of the bilinear exchange tensor, $J_{ij}^{\alpha\beta}$, containing the isotropic exchange interaction, the DMI, and the anisotropic exchange interaction are obtained via,

$$\frac{\delta}{\delta e_i^\alpha}\frac{\delta}{\delta e_j^\beta}E_{\text{Heisenberg}} = \frac{1}{2}J_{ij}^{\alpha\beta} \quad . \tag{4.6}$$

The equivalent change in the band energy can be calculated using the Green function formalism, which similar to the derivation of the magnetic torques in Section 2.2.4 yields,

$$\begin{aligned}\frac{\delta}{\delta e_i^\alpha}\frac{\delta}{\delta e_j^\beta}\epsilon_{\text{band}} =& \frac{1}{\pi}\text{Im Tr}\int^{E_F}\mathrm{d}E\int\mathrm{d}\boldsymbol{r}\int\mathrm{d}\boldsymbol{r}' \\ &\times G_{ij}(\boldsymbol{r},\boldsymbol{r}';E)\left(B_j^{\text{xc}}(\boldsymbol{r}')\,\sigma^\beta\right)G_{ji}(\boldsymbol{r}',\boldsymbol{r};E)\left(B_i^{\text{xc}}(\boldsymbol{r})\,\sigma^\alpha\right)\end{aligned} \quad , \tag{4.7}$$

which provides a very efficient way of calculating the exchange interactions. In practice, three different collinear orientations along x, y and z are used, and from each the transversal part of the exchange tensor is extracted. One shortcoming of this method is related to the impact of induced moments. The Heisenberg model implicitly considers the interacting magnetic moments as magnetic moments of fixed length being independent of the orientation of the magnetic moment. For weak magnetic moments, like e.g. induced magnetic moments in a surface, this assumption is violated resulting in a loss of the applicability of the Heisenberg model. Those moments are often excluded and an effective Heisenberg model containing only the strong magnetic moments is set up. The infinitesimal rotation method being a non-self-consistent approach is not capable of directly including the impact of the weak moments on the exchange interaction between the large moments. To account for this, throughout this thesis we make use of a renormalization scheme first proposed by Polesya et al. [163]. The Heisenberg hamiltonian is split into two groups containing the large moments labeled i and j and the weak induced moments labeled α and β,

$$\mathcal{H} = \frac{1}{2}\sum_{ij}\boldsymbol{m}_i\tilde{J}_{ij}\boldsymbol{m}_j + \frac{1}{2}\sum_{\alpha j}\boldsymbol{m}_\alpha\tilde{J}_{\alpha j}\boldsymbol{m}_j + \frac{1}{2}\sum_{i\beta}\boldsymbol{m}_i\tilde{J}_{i\beta}\boldsymbol{m}_\beta + \frac{1}{2}\sum_{\alpha\beta}\boldsymbol{m}_\alpha\tilde{J}_{ij}\boldsymbol{m}_\beta \quad , \tag{4.8}$$

where the magnetic moments $\boldsymbol{m}$ were used instead of their unit directions and $\tilde{J}_{ij} = J_{ij}/|\boldsymbol{m}_i||\boldsymbol{m}_j|$. Since the proximity-induced magnetic moments arise purely from the presence of the strong magnetic atoms, a susceptibility $\chi_{\alpha,j}$ can be assigned, which in linear order leads to

$$\boldsymbol{m}_\alpha = \sum_j \chi_{\alpha,j} \boldsymbol{m}_j \quad . \tag{4.9}$$

For strongly ferromagnetic systems, the susceptibility being in general a 3×3-matrix can be approximated by a scalar. Furthermore, the induced moments originate mainly from its nearest-neighbors yielding,

$$\boldsymbol{m}_\alpha = \chi_\alpha \sum_{\langle \alpha,j \rangle} \boldsymbol{m}_j \quad \text{with} \quad \chi_\alpha = \text{sgn}\left(\boldsymbol{m}_\alpha \cdot \sum_{\langle \alpha,j \rangle} \boldsymbol{m}_j \right) \|\boldsymbol{m}_\alpha\| / \sum_{\langle \alpha,j \rangle} \|\boldsymbol{m}_j\| \quad , \tag{4.10}$$

where $\langle \alpha, j \rangle$ denotes a summation over nearest-neighbors. Combining eqs. (4.8) and (4.10) yields renormalized exchange tensor, which takes indirectly the impact of the induced moments in to account,

$$\tilde{J}_{ij}^{\text{renorm}} = \tilde{J}_{ij} + \sum_{\langle \alpha,i \rangle} \chi_\alpha \tilde{J}_{\alpha j} + \sum_{\langle \beta,j \rangle} \chi_\beta \tilde{J}_{i\beta} + \sum_{\langle \alpha,i \rangle} \sum_{\langle \beta,j \rangle} \chi_\alpha \chi_\beta \tilde{J}_{\alpha\beta} \quad . \tag{4.11}$$

Another shortcoming of the infinitesimal rotations method is that in its original formulation it is not capable of extracting higher-order interactions. However, note that the method can be generalized to include higher-order terms [164], which will not be discussed in this thesis.

In this chapter, we follow a different approach utilizing the magnetic torques, which will be explained in the next section.

4.1.1. Mapping DFT to a spin model: The torque method

In order to map a first-principles calculation to a atomistic spin model, the complicated energy landscapes as function of the direction of the magnetic moments can be compared. The most general formulation of an atomistic spin model is given by the spin cluster expansion [165, 166],

$$\begin{aligned} E_{\text{SCE}}[\{\boldsymbol{e}\}] = & \sum_i \sum_{L_i \neq 0} K_i^{L_i} Y_{L_i}(\boldsymbol{e}_i) + \sum_{\substack{i,j \\ i \neq j}} \sum_{\substack{L_i \neq 0 \\ L_j \neq 0}} J_{ij}^{L_i L_j} Y_{L_i}(\boldsymbol{e}_i) Y_{L_j}(\boldsymbol{e}_j) \\ & + \sum_{\substack{i,j,k \\ i \neq j \neq k}} \sum_{\substack{L_i \neq 0 \\ L_j \neq 0 \\ L_k \neq 0}} J_{ijk}^{L_i L_j L_k} Y_{L_i}(\boldsymbol{e}_i) Y_{L_j}(\boldsymbol{e}_j) Y_{L_k}(\boldsymbol{e}_k) + \ldots \quad , \end{aligned} \tag{4.12}$$

which accounts for the on-site magnetic anisotropy K (see Section 3.3.2), as well as pair interaction J_{ij} and multi-site interaction like e.g. the three-site interaction J_{ijk}. We consider real spherical harmonics, Y_L, as tabulated in Appendix C. Time-reversal symmetry,

$$E_{\mathrm{SCE}}[\{\boldsymbol{e}\}] = E_{\mathrm{SCE}}[\{-\boldsymbol{e}\}] \tag{4.13}$$

restricts the different terms in the spin cluster expansion to an even parity, which in turn requires an even combine ℓ, since $Y_L(-\boldsymbol{e}) = (-1)^{\ell} Y_L(\boldsymbol{e})$. The magnetic anisotropy therefore contains only the $\ell = \{2, 4, 6, \ldots\}$ components, while for the pair interactions the combinations $(\ell_i, \ell_j) = \{(1,1), (2,2), (1,3), \ldots\}$ are allowed. The ℓ index indicates the order of the different terms. For the magnetic anisotropy the $\ell = 2$ component is quadratic in the magnetic moment, while the $\ell = 4$ component is proportional to the magnetic moment to the fourth power. Similarly the $(\ell_i, \ell_j) = (1,1)$ components of the pair interactions yield the bilinear interactions, while the $(\ell_i, \ell_j) = (2,2)$ components describe the biquadratic interactions. It is easy to see that there is a one-to-one correspondence between the bilinear pair interactions and the $(1,1)$ components of the spin cluster expansion. Each $\ell = 1$ spherical harmonic yields three independent components, resulting in a total of nine independent components. Similarly the bilinear Heisenberg model can be described by a 3×3 matrix with nine independent elements. The mapping is given by

$$\begin{pmatrix} J^{xx} & J^{xy} & J^{xz} \\ J^{yx} & J^{yy} & J^{yz} \\ J^{zx} & J^{zy} & J^{zz} \end{pmatrix} = \frac{3}{4\pi} \begin{pmatrix} J^{(1,1),(1,1)} & J^{(1,1),(1,-1)} & J^{(1,1),(1,0)} \\ J^{(1,-1),(1,1)} & J^{(1,-1),(1,-1)} & J^{(1,-1),(1,0)} \\ J^{(1,0),(1,1)} & J^{(1,0),(1,-1)} & J^{(1,0),(1,0)} \end{pmatrix} \quad . \tag{4.14}$$

The four-spin generalization of the Heisenberg hamiltonian including all possible interactions in cartesian components is given by,

$$\mathcal{H}_{\text{biquad}} = \sum_{ijkl} \sum_{\alpha\beta\gamma\delta} B^{\alpha\beta\gamma\delta}_{ijkl} e^{\alpha}_i e^{\beta}_j e^{\gamma}_k e^{\delta}_l \quad , \tag{4.15}$$

or restricting ourselves to the biquadratic pair interaction, but still including all possible forms,

$$\mathcal{H}^{\text{pair}}_{\text{biquad}} = \sum_{ij} \sum_{\alpha\beta\gamma\delta} B^{\alpha\beta\gamma\delta}_{ij} e^{\alpha}_i e^{\beta}_j e^{\gamma}_i e^{\delta}_j \quad , \tag{4.16}$$

which has in principle 81 elements indicating the complexity of the general biquadratic interaction. However, it is possible to show that due to the symmetry relations, $B^{\alpha\beta\gamma\delta}_{ij} = B^{\gamma\beta\alpha\delta}_{ij} = B^{\alpha\delta\gamma\beta}_{ij} = B^{\gamma\delta\alpha\beta}_{ij} = B^{\beta\alpha\delta\gamma}_{ji}$, not all of those elements are independent. In total, it turns out that 25 elements of the biquadratic tensor $B^{\alpha\beta\gamma\delta}_{ij}$ are independent. Using the spin cluster expansion, the biquadratic pair interaction is described by the $(\ell_i, \ell_j) = (2,2)$ components. Each channel contains five elements, which are by construction orthogonal and independent, resulting in a total of 25 elements for the biquadratic pair interaction. Thus, there is also a one-to-one correspondence between the spin cluster expansion and the Heisenberg model on the biquadratic level. The relation between the different terms is more complicated than the one for the bilinear pair interactions, eq. (4.14), and is not shown here.

In order to map a first-principles calculation to the spin cluster expansion, the energy can be fitted for several different magnetic configurations. To construct the magnetic configuration different approaches can be used, e.g. using random numbers, which is not efficient but easy to set up. Here, we use a systematic approach making use of the so-called Lebedev angular mesh [167]. The Lebedev mesh was designed to integrate efficiently spherical functions. It contains different orientation depending on the maximal considered angular momentum index ℓ. For example, in the $\ell = 1$ channel it contains the six cartesian directions, $\{\pm\hat{x}, \pm\hat{y}, \pm\hat{z}\}$, describing perfectly the p-orbitals associated to this channel. For the biquadratic pair interactions, the Lebedev mesh up to $\ell = 2$ has to be used, which contains 14 different directions (the 6 directions for the cartesian axes as in the $\ell = 1$ case plus the 8 directions corresponding to the body diagonals of a cube), for each magnetic moment. For a magnetic dimer it results in a total of $14 \times 14 = 196$ directions, which immediately shows the drawback of this systematic study: For systems containing multiple atoms, the total number of configurations scales exponentially to 14^n, where n is the number of atoms.

The calculation of total energies suffers from some numerical imprecisions making its usage unreliable. To overcome this issue, instead of the total energy, the magnetic torques can be used to map KKR to a spin model [116]. The derivative with respect to the azimuthal angle ϑ and the polar angle φ of atom i yield,

$$\frac{\partial E(\{\vartheta,\varphi\})}{\partial\vartheta_i} = \frac{\partial E}{\partial \boldsymbol{e}_i}\cdot\frac{\partial \boldsymbol{e}_i}{\partial\vartheta_i} = \boldsymbol{\tau}_i\cdot\frac{\partial \boldsymbol{e}_i}{\partial\vartheta_i} \quad \text{and} \quad \frac{\partial E(\{\vartheta,\varphi\})}{\partial\varphi_i} = \frac{\partial E}{\partial \boldsymbol{e}_i}\cdot\frac{\partial \boldsymbol{e}_i}{\partial\varphi_i} = \boldsymbol{\tau}_i\cdot\frac{\partial \boldsymbol{e}_i}{\partial\varphi_i} \quad , \tag{4.17}$$

where $\boldsymbol{\tau}_i$ is the torque acting on atom i defined in Section 2.2.4. On the other hand, the corresponding derivatives in the spin cluster expansions are known allowing for a multi-dimensional linear fit to obtain the full parametrization in the spin cluster expansion from the first-principles input.

The torque method is a very precise method, which is only limited by the number of inequivalent non-collinear configurations used in the first-principles calculation in order to map to the spin model. It allows for a parametrization up to arbitrary order, and arbitrary number of sites. Furthermore, using the constraining field discussed in Section 2.2.4 it can be used to obtain the exchange interactions self-consistently including potential effects of induced moments, which do not participate in the Heisenberg model, yielding a fully renormalized effective model for the considered constrained atoms. However, this comes also with some downsides: It is computationally very demanding. The exponentially scaling number of non-collinear configurations and the self-consistency make this approach for a magnetic dimer approximately 1000 times more time consuming than employing the infinitesimal rotation method. A speed up can be achieved for systems exhibiting symmetries, resulting in a reduction of the needed non-collinear configurations, which for the dimer sum up to 196 different directions needed to account for all biquadratic interactions. The most basic symmetry present in any magnetic system not exposed to an external magnetic field is the time-reversal symmetry, which reduces the number of configurations by a factor of 2. Further spatial symmetries can be used to reduce the number of irreducible configurations. For a magnetic dimer in the C_s symmetry having a single mirror plane the total number of irreducible non-collinear configuration is 56, while for a dimer in the C_{2v} symmetry only 36 configurations are needed to describe pair interactions up to the biquadratic level. A magnetic trimer in the C_{3v} symmetry has 252 irreducible magnetic configurations, which is a substantial reduction considering the anticipated $14^3 = 2744$ initial configurations.

In this chapter, a comprehensive discussion of higher-order interaction with the focus on pair interactions is given. Using a systematic perturbative expansion of the total energy in a microscopic model, we explain a framework to classify and catalogue all possible magnetic interactions using an intuitive diagrammatic approach. Symmetry properties of the upcoming interactions are discussed, and the most important chiral correction to the typical bilinear Heisenberg model is discovered – the so-called chiral biquadratic interaction (CBI). Using the torque method, we investigate all possible biquadratic pair interactions in realistic systems. The considered prototypical test systems are magnetic dimers consisting of $3d$ transition metals deposited on the Pt(111), Pt(001), Ir(111), and Re(0001) surface. All the surfaces with their large spin-orbit coupling are ideal hosts for significant chiral interactions to emerge. We find the CBI to be the most relevant new interaction and discuss its importance and implications not only for dimers but also for extended systems. The last part of this chapter is dedicated to the multi-site interactions. Using as prototypical test system magnetic trimers deposited on the Pt(111) surface we investigate three-site interactions, being of isotropic and chiral nature.

4.2. Microscopic derivation of magnetic interactions

In this section, a microscopic theory for the identification and classification of magnetic interactions based on an underlying non-interacting electronic model is presented. It is based on the ideas of the Levy-Fert model [87, 88]. The starting point is a general spin-independent hamiltonian, $\mathcal{H}_0$, which contains e.g. the kinetic energy and an external potential, but which does not need to be classified further. Every additional correction to the hamiltonian that involves spin-dependent terms, $\Delta\mathcal{H}$, can be treated using the Dyson equation,

$$\mathcal{H} = \mathcal{H}^0 + \Delta\mathcal{H} \quad \Rightarrow \quad G(E) = G^0(E) + G^0(E)\,\Delta\mathcal{H}\,G(E) \quad . \tag{4.18}$$

The electronic grand potential $\Omega = U - TS - \mu N$, where U is the internal energy, T is the temperature, S is the entropy, μ is the chemical potential and N is the number of particles, defines the total energy, which can be calculated from the Green function via the density matrix, eq. (2.54),

$$\Omega = -\frac{1}{\beta}\int_{-\infty}^{\infty}\mathrm{d}E\,\ln\left(1+e^{\beta(\mu-E)}\right)\int \mathrm{d}\boldsymbol{r}\,\mathrm{Tr}\,\rho(\boldsymbol{r},\boldsymbol{r};E) \quad , \tag{4.19}$$

where $\beta = 1/k_\mathrm{B}T$ with the Boltzmann constant k_B and the temperature T, and μ is the chemical potential. Using recursively the Dyson equation and omitting the spatial dependencies for the sake of simplicity, the electronic grand potential can be written as,

$$\begin{aligned}\Omega &= -\frac{1}{\beta}\,\mathrm{Im}\int_{-\infty}^{\infty}\mathrm{d}E\,\ln\left(1+e^{\beta(\mu-E)}\right)\mathrm{Tr}\left(G^0(E) + G^0(E)\sum_{p=1}^{\infty}\left[\Delta\mathcal{H}\,G^0(E)\right]^p\right)\\ &= \Omega^0 + \sum_{p=1}^{\infty}\Omega^p \quad ,\end{aligned} \tag{4.20}$$

where Ω^0 is the unperturbed (non-magnetic) contribution to the electronic grand potential, and Ω^p is the perturbation of order p. Using the relation

$$\mathrm{Tr}\,G^0(E)\big[\Delta\mathcal{H}\,G^0(E)\big]^p = -\frac{1}{p}\frac{\partial}{\partial E}\,\mathrm{Tr}\left[\Delta\mathcal{H}\,G^0(E)\right]^p \tag{4.21}$$

and integrating by parts with respect to the energy, the correction to the electronic grand potential in order p can be expressed by

$$\Omega^{p} = -\frac{1}{\pi}\,\mathrm{Im}\int_{-\infty}^{\infty}\mathrm{d}E\, f(E;\mu)\,\frac{1}{p}\,\mathrm{Tr}\left[\Delta\mathcal{H}\, G^{0}(E)\right]^{p} \quad , \tag{4.22}$$

where $f(E;\mu)$ is the Fermi distribution function. Eq. (4.22) can be used to set up a diagrammatic perturbation theory.

As perturbations we consider first the magnetic part of the hamiltonian, $\mathcal{H}^{\mathsf{mag}}$, and second the spin-orbit coupling, $\mathcal{H}^{\mathsf{soc}}$. The magnetic part can be modelled by a local spin splitting U splitting the spin components in the spatial direction of the magnetic moment $\boldsymbol{e}$,

$$\mathcal{H}^{\mathsf{mag}} = \sum_{i}\mathcal{H}_{i}^{\mathsf{mag}} = \sum_{i} U_{i}\,\boldsymbol{e}_{i}\cdot\boldsymbol{\sigma} \quad , \tag{4.23}$$

while the spin-orbit coupling is considered in its local form coupling the angular momentum to the spin of the electrons,

$$\mathcal{H}^{\mathsf{soc}} = \sum_{a}\mathcal{H}_{a}^{\mathsf{soc}} = \sum_{a}\lambda_{a}\,\boldsymbol{L}\cdot\boldsymbol{\sigma} \quad . \tag{4.24}$$

We intentionally used the indices i and a to distinguish magnetic sites from spin-orbit coupling sites, which will also be used when setting up the diagrammatic approach. The perturbation $\Delta\mathcal{H} = \mathcal{H}^{\mathsf{mag}} + \mathcal{H}^{\mathsf{soc}}$ can be used in eq. (4.22), resulting in a double expansion, $\Omega^{p,k}$, where p is the total order of the perturbation and the magnetic perturbation is contained k-times, while the spin-orbit coupling is contained $(p-k)$-times. From the basic requirement of Ω not breaking the time-reversal symmetry, we can conclude that an even power of k has to be contained in the perturbation resulting in,

$$\Omega = \Omega^{0} + \Omega^{\mathsf{soc}} + \sum_{p}\sum_{k}^{p/2}\Omega^{p,2k}[\{\boldsymbol{e}\}] \quad . \tag{4.25}$$

The isotropic interactions are generated by the $2k = p$ terms, which have no scattering at a spin-orbit coupling site. To illustrate this, the $\Omega^{2,2}$ is composed out of all possible pair interactions,

$$\Omega^{2,2} = \frac{1}{2}\sum_{ij}\Omega_{ij}^{2,2} \quad , \tag{4.26}$$

with,

$$\begin{aligned}
\Omega_{ij}^{2,2} &= -\frac{1}{\pi}\,\mathrm{Im}\int_{-\infty}^{\infty}\mathrm{d}E\, f(E;\mu)\,\mathrm{Tr}\,\mathcal{H}_{i}^{\mathrm{mag}}G_{ij}^{0}(E)\mathcal{H}_{j}^{\mathrm{mag}}G_{ji}^{0}(E)\\
&= -\frac{1}{\pi}\,\mathrm{Im}\int_{-\infty}^{\infty}\mathrm{d}E\, f(E;\mu)\,\mathrm{Tr}\, U_{i}G_{ij}^{0}(E)U_{j}G_{ji}^{0}(E)\big(\boldsymbol{e}_{i}\cdot\boldsymbol{e}_{j}\,\sigma_{0} + \mathrm{i}\,(\boldsymbol{e}_{i}\times\boldsymbol{e}_{j})\cdot\boldsymbol{\sigma}\big)\\
&= J_{ij}^{2,2}\,\boldsymbol{e}_{i}\cdot\boldsymbol{e}_{j} \quad ,
\end{aligned} \tag{4.27}$$

where we used the trace of the product of Pauli matrices listed in Appendix D. Note that the trace of a single Pauli matrix vanishes except for the unit matrix. In the next order, up to four different magnetic sites can be involved, ,

$$\Omega^{4,4} = \frac{1}{2}\sum_{ijkl} \Omega^{4,4}_{ijkl} \quad , \tag{4.28}$$

where

$$\begin{aligned}\Omega^{4,4}_{ijkl} &= -\frac{1}{\pi}\,\mathrm{Im}\int_{-\infty}^{\infty}\mathrm{d}E\, f(E;\mu)\,\mathrm{Tr}\,\mathcal{H}^{\mathrm{mag}}_i G^0_{ij}(E)\mathcal{H}^{\mathrm{mag}}_j G^0_{jk}(E)\mathcal{H}^{\mathrm{mag}}_k G^0_{kl}(E)\mathcal{H}^{\mathrm{mag}}_l G^0_{li}(E)\\ &= J^{4,4}_{ijkl}\left((\boldsymbol{e}_i\cdot\boldsymbol{e}_j)(\boldsymbol{e}_k\cdot\boldsymbol{e}_l) - (\boldsymbol{e}_i\cdot\boldsymbol{e}_k)(\boldsymbol{e}_j\cdot\boldsymbol{e}_l) + (\boldsymbol{e}_i\cdot\boldsymbol{e}_l)(\boldsymbol{e}_j\cdot\boldsymbol{e}_k)\right) \quad .\end{aligned} \tag{4.29}$$

This general four-site interaction contains several familiar terms, which are discussed in the following starting from the pair interactions with in total two sites i and j. For three scatterings at the same site, it corrects the bilinear interaction, e.g. with the term $\Omega^{4,4}_{iiij} \propto \boldsymbol{e}_i \cdot \boldsymbol{e}_j$. For two consecutive scatterings at the same site, it yields a constant term, e.g. $\Omega^{4,4}_{iijj} = \text{const.}$. If consecutive scatterings occur at different sites the well-known isotropic biquadratic pair interaction, $\Omega^{4,4}_{ijij} = \Omega^{4,4}_{ij} = J^{4,4}_{ij}(2\,(\boldsymbol{e}_i\cdot\boldsymbol{e}_j)^2 + 1)$, shows up. Considering scatterings at three distinct sites gives rise to the 4-spin 3-site interaction plus another correction to the bilinear two-site interaction, $\Omega^{4,4}_{ijil} \propto 2\,(\boldsymbol{e}_i\cdot\boldsymbol{e}_j)(\boldsymbol{e}_i\cdot\boldsymbol{e}_l) - \boldsymbol{e}_j\cdot\boldsymbol{e}_l$.

As a next step, the scattering at spin-orbit coupling sites can be included to the perturbation. The lowest order is $p = 3$ containing two scattering at magnetic sites and one scattering at a spin-orbit coupling site yielding,

$$\Omega^{3,2} = \frac{1}{3}\sum_{i,j} \Omega^{3,2}_{ij} \quad , \tag{4.30}$$

with

$$\begin{aligned}\Omega^{3,2}_{ij} &= -\frac{1}{\pi}\,\mathrm{Im}\int_{-\infty}^{\infty}\mathrm{d}E\, f(E;\mu)\,3\sum_a \mathrm{Tr}\,\mathcal{H}^{\mathrm{mag}}_i G^0_{ij}(E)\mathcal{H}^{\mathrm{mag}}_j G^0_{ja}(E)\mathcal{H}^{\mathrm{soc}}_a G^0_{ai}(E)\\ &= -\frac{1}{\pi}\,\mathrm{Im}\int_{-\infty}^{\infty}\mathrm{d}E\, f(E;\mu)\,6\sum_a \mathrm{i}\,\mathrm{Tr}\,G^0_{ai}(E)U_i G^0_{ij}(E)U_j G^0_{ja}(E)\lambda_a\,\boldsymbol{L}\cdot(\boldsymbol{e}_i\times\boldsymbol{e}_j)\\ &= \frac{3}{2}\sum_a \boldsymbol{D}^{3,2}_{ij,a}\cdot(\boldsymbol{e}_i\times\boldsymbol{e}_j) = \frac{3}{2}\boldsymbol{D}^{3,2}_{ij}\cdot(\boldsymbol{e}_i\times\boldsymbol{e}_j) \quad ,\end{aligned} \tag{4.31}$$

which is the well-known Dzyaloshinskii-Moriya interaction, which is first order in spin-orbit coupling. The prefactors account for the multiple equivalent possibilities of inserting the scattering at the spin-orbit coupling site. Since our interest in the microscopic model is based on the form of the possible interactions and not their magnitude, we will not discuss those prefactors in detail. In second order in spin-orbit orbit coupling one finds the following correction to the bilinear interactions,

$$\Omega^{4,2} = \frac{1}{4}\sum_{i,j} \Omega^{4,2}_{ij} \quad . \tag{4.32}$$

The exact place of the scattering at the spin-orbit coupling sites is now relevant. There can be either a consecutive scattering at two spin-orbit coupling sites or the scattering at the spin-orbit coupling site occurs in between two scatterings at magnetic sites, resulting in,

$$\begin{aligned}
\Omega^{4,2}_{ij} &= -\frac{1}{\pi}\,\mathrm{Im}\int_{-\infty}^{\infty}\!\mathrm{d}E\,f(E;\mu)\,4\sum_{a,b}\mathrm{Tr}\,\mathcal{H}^{\mathrm{mag}}_i G^0_{ij}(E)\mathcal{H}^{\mathrm{mag}}_j G^0_{ja}(E)\mathcal{H}^{\mathrm{soc}}_a G^0_{ab}(E)\mathcal{H}^{\mathrm{soc}}_b G^0_{bi}(E)\\
&\quad -\frac{1}{\pi}\,\mathrm{Im}\int_{-\infty}^{\infty}\!\mathrm{d}E\,f(E;\mu)\,2\sum_{a,b}\mathrm{Tr}\,\mathcal{H}^{\mathrm{mag}}_i G^0_{ia}(E)\mathcal{H}^{\mathrm{soc}}_a G^0_{ja}(E)\mathcal{H}^{\mathrm{mag}}_j G^0_{jb}(E)\mathcal{H}^{\mathrm{soc}}_b G^0_{bi}(E)\\
&= 2\left(J^{4,2}_{ij}\,\boldsymbol{e}_i\cdot\boldsymbol{e}_j + \boldsymbol{e}_i\cdot D^{4,2}_{ij}\cdot\boldsymbol{e}_j + \boldsymbol{e}_i\cdot A^{4,2}_{ij}\cdot\boldsymbol{e}_j\right) \quad . \qquad (4.33)
\end{aligned}$$

The consecutive scattering at two spin-orbit coupling sites gives rise to $D^{4,2}_{ij}$, which is defined by,

$$\begin{aligned}
D^{4,2,\alpha\beta}_{ij} &= \frac{1}{\pi}\,\mathrm{Im}\int_{-\infty}^{\infty}\!\mathrm{d}E\,f(E;\mu)\,4\sum_{a,b}\mathrm{Tr}\,U_i G^0_{ij}(E)U_j G^0_{ja}(E)\lambda_a L^\alpha c\lambda_b L^\beta G^0_{bi}(E)\\
&\quad -\frac{1}{\pi}\,\mathrm{Im}\int_{-\infty}^{\infty}\!\mathrm{d}E\,f(E;\mu)\,4\sum_{a,b}\mathrm{Tr}\,U_i G^0_{ij}(E)U_j G^0_{ja}(E)\lambda_a L^\beta G^0_{ab}(E)\lambda_b L^\alpha G^0_{bi}(E) \quad , \qquad (4.34)
\end{aligned}$$

where $\alpha,\beta = \{x,y,z\}$, which is an anti-symmetric matrix, $D^{4,2,\alpha\beta}_{ij} = -D^{4,2,\beta\alpha}_{ij}$ and therefore is a higher-order correction to the bilinear Dzyaloshinskii-Moriya interaction. The component $J^{4,2}_{ij}$ gives a higher-order correction to the bilinear isotropic interaction, while the only new contribution is generated by $A^{4,2}_{ij}$, which is defined by,

$$\begin{aligned}
A^{4,2,\alpha\beta}_{ij} &= -\frac{1}{\pi}\,\mathrm{Im}\int_{-\infty}^{\infty}\!\mathrm{d}E\,f(E;\mu)\,2\sum_{a,b}\mathrm{Tr}\,U_i G^0_{ia}(E)\lambda_a L^\alpha G^0_{aj}(E)U_j G^0_{jb}(E)\lambda_b L^\beta G^0_{bi}(E)\\
&\quad -\frac{1}{\pi}\,\mathrm{Im}\int_{-\infty}^{\infty}\!\mathrm{d}E\,f(E;\mu)\,2\sum_{a,b}\mathrm{Tr}\,U_i G^0_{ia}(E)\lambda_a L^\beta G^0_{aj}(E)U_j G^0_{jb}(E)\lambda_b L^\alpha G^0_{bi}(E) \quad . \qquad (4.35)
\end{aligned}$$

This is a symmetric matrix and contributes to the anisotropic part of the bilinear exchange, eq. (4.3), being second order in spin-orbit coupling.

Having the previous perturbative expansions and results in mind, we can set up a diagrammatic approach to simplify the identification of new kinds of magnetic interactions. The aim is to identify not the precise strength of each interaction, but only to find its functional form, and its physical origin based on scatterings at magnetic sites and spin-orbit coupling sites. The building blocks of the Feynman-like diagrams are the magnetic and spin-orbit coupling sites, and the connecting Green functions.

We identified the following diagrammatic rules for the setup of diagrams yielding unique interactions:

1. Each diagram contains p vertices, from which $2k$ represent magnetic sites ($\mathcal{H}^{\mathrm{mag}}$) and $p-2k$ represent spin-orbit coupling sites ($\mathcal{H}^{\mathrm{soc}}$), which are connected by p oriented lines representing the Green functions (G^0). Magnetic sites are represented by a circle without filling, while the spin-orbit coupling sites are represented by a circle with a grey filling.
2. The same magnetic side cannot appear consecutively, like e.g. $\Omega^{4,4}_{iijj}$, but it can appear multiple times, like e.g. $\Omega^{4,4}_{ijij}$.

3. Spin-orbit coupling sites cannot be connected to each other, like in $\Omega^{4,4}_{ijab}$, but they can appear repeatedly.
4. The form of the magnetic interaction can be obtained from the trace of the ordered product of the constituents of each diagram.

Note that a similar diagrammatic approach can be used for a perturbative expansion of the magnetic anisotropy, with the main difference being the second rule.

To illustrate the diagrammatic approach, the diagrams for the previously discussed interactions are shown in the following. The isotropic bilinear interaction can be represented by a bubble diagram connecting two magnetic sites,

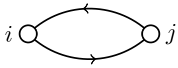

$$\rightarrow \mathrm{Tr}\, U_i G^0_{ij} U_j G^0_{ji}\, \sigma^\alpha \sigma^\beta\, e^\alpha_i e^\beta_j \propto \boldsymbol{e}_i \cdot \boldsymbol{e}_j \quad . \tag{4.36}$$

The Dzyaloshinskii-Moriya interaction adds an additional spin-orbit coupling site in between the two magnetic sites,

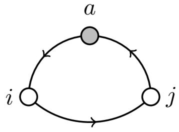

$$\rightarrow \mathrm{Tr}\, U_i G^0_{ij} U_j G^0_{ja} \lambda_a L^\gamma_a G^0_{ai}\, \sigma^\alpha \sigma^\beta \sigma^\gamma\, e^\alpha_i e^\beta_j$$

$$\propto \mathrm{Tr}\, G^0_{ai} U_i G^0_{ij} U_j G^0_{ja} \lambda_a \boldsymbol{L}_a \cdot (\boldsymbol{e}_i \times \boldsymbol{e}_j) \quad . \tag{4.37}$$

Note that the orbital part of the trace in this example is relevant for the evaluation of the angular momentum operator, and the angular momentum operator can only be moved complying with the cyclic properties of the trace, while the directions of the magnetic moments can be freely moved within the trace. The next example is the anisotropic bilinear exchange, which is represented by two scatterings at spin-orbit coupling sites,

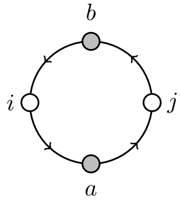

$$\rightarrow \mathrm{Tr}\, U_i G^0_{ia} \lambda_a L^\beta_a G^0_{aj} U_j G^0_{jb} \lambda_b L^\delta_b G^0_{bi}\, \sigma^\alpha \sigma^\beta \sigma^\gamma \sigma^\delta\, e^\alpha_i e^\gamma_j$$

$$\propto \mathrm{Tr}\, U_i G^0_{ia} \lambda_a L^\beta_a G^0_{aj} U_j G^0_{jb} \lambda_b L^\delta_b G^0_{bi}\, e^\alpha_i e^\gamma_j\, \left(\delta_{\alpha\beta}\delta_{\gamma\delta} - \delta_{\alpha\gamma}\delta_{\beta\delta} + \delta_{\beta\gamma}\delta_{\alpha\delta}\right) \quad . \tag{4.38}$$

This diagram yields a correction to the bilinear isotropic exchange ($\delta_{\alpha\gamma}\delta_{\beta\delta}$) and the symmetric part of the bilinear exchange tensor ($\delta_{\alpha\beta}\delta_{\gamma\delta} + \delta_{\beta\gamma}\delta_{\alpha\delta}$). According to the diagrammatic rules, there are no other diagrams including only two scattering at magnetic sites, and in fact we recovered all the known terms up to the bilinear level. Turning our attention now to the biquadratic interactions with four scatterings at magnetic sites, we find for the isotropic biquadratic pair interaction,

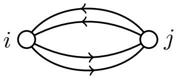

$$\to \mathrm{Tr}\, U_i G^0_{ij} U_j G^0_{ji} U_i G^0_{ij} U_j G^0_{ji}\, \sigma^\alpha\sigma^\beta\sigma^\gamma\sigma^\delta\, e_i^\alpha e_j^\beta e_i^\gamma e_j^\delta \propto 2(\boldsymbol{e}_i\cdot\boldsymbol{e}_j)^2 \quad . \tag{4.39}$$

On the biquadratic level there is a new kind of diagrams allowed involving more than two magnetic sites. For example, a three site interaction can be represented by,

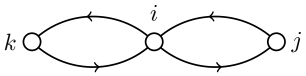

$$\begin{aligned}&\to \mathrm{Tr}\, U_i G^0_{ij} U_j G^0_{ji} U_i G^0_{ik} U_k G^0_{ki}\, \sigma^\alpha\sigma^\beta\sigma^\gamma\sigma^\delta\, e_i^\alpha e_j^\beta e_i^\gamma e_k^\delta \\ &\propto 2(\boldsymbol{e}_i\cdot\boldsymbol{e}_j)(\boldsymbol{e}_i\cdot\boldsymbol{e}_k) - (\boldsymbol{e}_j\cdot\boldsymbol{e}_k) \quad ,\end{aligned} \tag{4.40}$$

and a four site interaction by,

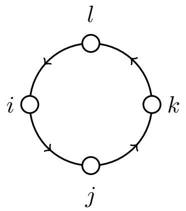

$$\begin{aligned}&\to \mathrm{Tr}\, U_i G^0_{ij} U_j G^0_{jk} U_k G^0_{kl} U_l G^0_{li}\, \sigma^\alpha\sigma^\beta\sigma^\gamma\sigma^\delta\, e_i^\alpha e_j^\beta e_k^\gamma e_l^\delta \\ &\propto (\boldsymbol{e}_i\cdot\boldsymbol{e}_j)(\boldsymbol{e}_k\cdot\boldsymbol{e}_l) - (\boldsymbol{e}_i\cdot\boldsymbol{e}_k)(\boldsymbol{e}_j\cdot\boldsymbol{e}_l) + (\boldsymbol{e}_i\cdot\boldsymbol{e}_l)(\boldsymbol{e}_j\cdot\boldsymbol{e}_k) \quad ,\end{aligned} \tag{4.41}$$

which agrees with the derivation of $\Omega^{4,4}_{ijkl}$ in eq. (4.29).

One strength of the diagrammatic approach is the intuitive construction of new interactions, which are expected from perturbation theory. The first new pair interaction appears on the biquadratic level, once spin-orbit coupling sites are included. Allowing for one scattering at a spin-orbit coupling site in between the magnetic sites yields,

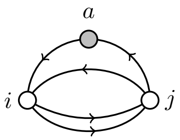

$$\begin{aligned}&\to \mathrm{Tr}\, G^0_{ai} U_i G^0_{ij} U_j G^0_{ji} U_i G^0_{ij} U_j G^0_{ja} \lambda_a L^\eta_a\, \sigma^\alpha\sigma^\beta\sigma^\gamma\sigma^\delta\sigma^\eta\, e_i^\alpha e_j^\beta e_i^\gamma e_j^\delta \\ &\propto \mathrm{Tr}\, G^0_{ai} U_i G^0_{ij} U_j G^0_{ji} U_i G^0_{ij} U_j G^0_{ja} \lambda_a\, \boldsymbol{L}_a\cdot(\boldsymbol{e}_i\times\boldsymbol{e}_j)(\boldsymbol{e}_i\cdot\boldsymbol{e}_j) \quad ,\end{aligned} \tag{4.42}$$

which is the biquadratic equivalent to the Dzyaloshinskii-Moriya interaction. Due to its chiral nature, we call this interaction the chiral biquadratic interaction (CBI), which analogously to the DMI is defined by the chiral biquadratic vector $\boldsymbol{C}_{ij}$,

$$\mathcal{H}_{\mathsf{CBI}} = \frac{1}{2}\sum_{ij} \boldsymbol{C}_{ij}\cdot(\boldsymbol{e}_i\times\boldsymbol{e}_j)(\boldsymbol{e}_i\cdot\boldsymbol{e}_j) \quad . \tag{4.43}$$

The CBI is the main interest of this chapter, and will be analysed in detail in the following sections.

Before that, we want to mention a few other interactions, which can be easily derived from the diagrammatic approach and which were recently discussed in literature. The three-site version of the CBI can be derived starting from eq. (4.40),

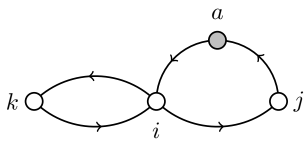

$$\rightarrow \mathrm{Tr}\, G^0_{ai}U_iG^0_{ik}U_kG^0_{ki}U_iG^0_{ij}U_jG^0_{ja}\lambda_a L^\eta_a\, \sigma^\alpha\sigma^\beta\sigma^\gamma\sigma^\delta\sigma^\eta\, e^\alpha_i e^\beta_k e^\gamma_i e^\delta_j$$

$$\propto \mathrm{Tr}\, G^0_{ai}U_iG^0_{ij}U_jG^0_{ji}U_iG^0_{ij}U_jG^0_{ja}\lambda_a\, \boldsymbol{L}_a\cdot(\boldsymbol{e}_i\times\boldsymbol{e}_j)(\boldsymbol{e}_i\cdot\boldsymbol{e}_k) \quad . \tag{4.44}$$

This three-site equivalent of the CBI attracted recently interest in two different publications. It was first used to explain the chirality of Fe chains deposited on the Re(0001) surface [60]. First-principles calculations of the magnetic structure showed a disagreement with respect to the chirality when the found spin structure was compared to the one emerging from a bilinear Heisenberg model. Including the three-site CBI Laszloffy *et al.* were able to explain the different chiralities. The three-site CBI also helped to explain the puzzle of the spin structure of MnGe [61]. Grytsiuk *et al.* rewrote the three-site CBI and connected it to the topological orbital moment and the scalar spin chirality, $\boldsymbol{e}_i\cdot(\boldsymbol{e}_j\times\boldsymbol{e}_k)$, yielding, $(\tau_{ijk}\cdot\boldsymbol{e}_i)(\boldsymbol{e}_i\cdot(\boldsymbol{e}_j\times\boldsymbol{e}_k))$. Note that up to a lower-order correction factor, $\propto \tau_{ijk}\cdot(\boldsymbol{e}_j\times\boldsymbol{e}_k)$, which is a DMI contribution between atoms j and k mediated by atom i, the latter form is equivalent to eq. (4.44).

Grytsiuk *et al.* also introduced a sixth order interaction, the bicubic isotropic interaction, being represented by,

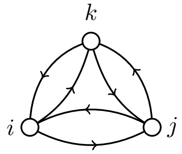

$$\rightarrow \mathrm{Tr}\, U_iG^0_{ij}U_jG^0_{jk}U_kG^0_{ki}U_iG^0_{ik}U_kG^0_{kj}U_jG^0_{ji}\, \sigma^\alpha\sigma^\beta\sigma^\gamma\sigma^\delta\sigma^\eta\sigma^\zeta\, e^\alpha_i e^\beta_j e^\gamma_k e^\delta_i e^\eta_k e^\zeta_j$$

$$\propto (\boldsymbol{e}_i\cdot\boldsymbol{e}_j)(\boldsymbol{e}_j\cdot\boldsymbol{e}_k)(\boldsymbol{e}_k\cdot\boldsymbol{e}_i) \quad , \tag{4.45}$$

where corrections to lower-order terms were neglected. They expressed the latter one as the square of the scalar spin chirality, $(\boldsymbol{e}_i\cdot(\boldsymbol{e}_j\times\boldsymbol{e}_k))^2$. However, the physical origin of this interactions is not necessarily the topological orbital moment as claimed by Grytsiuk *et al.* As can be seen from the diagrammatic expansion, the interaction rises from consecutive scattering at the sites i, j and k and vice versa.

4.2.1. Symmetries in the microscopic model

The strength of the microscopic model is not only the systematic derivation of possible interactions, but also the microscopic derivation of spatial symmetry rules for a particular interaction. In this section, first the well-known Moriya rules for the DMI are derived from the microscopic model, and second, an equivalent derivation sheds light on the symmetry rules of the CBI. The relevant spatial symmetries considered by Moriya [55] for a pair of of magnetic moments at sites i and j connected by the vector $\boldsymbol{R}_{ij}$ are,

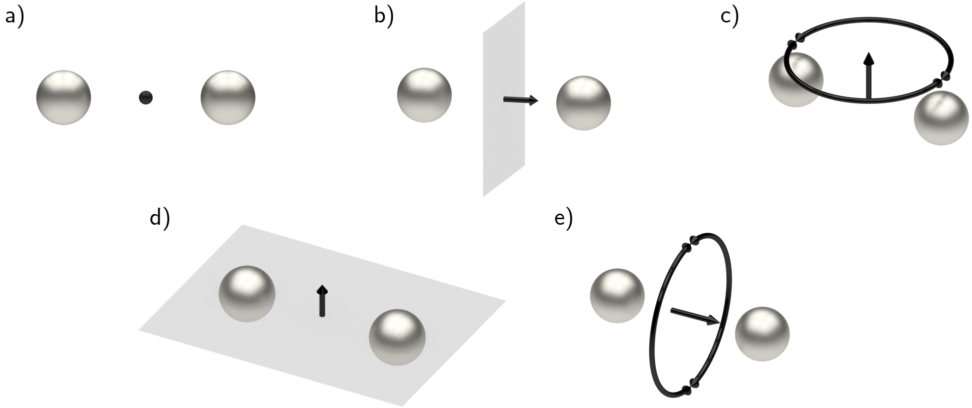

Figure 4.1.: Illustration of the different considered spatial symmetries. The straight black arrows indicate the normal vectors of mirror operations and rotations, which the circular arrows indicate rotations. a) Inversion center in between i and j. b) Mirror plane with the normal vector $\boldsymbol{n} \perp \boldsymbol{R}_{ij}$, c) Two-fold rotation by an axis defined by $\boldsymbol{n} \perp \boldsymbol{R}_{ij}$, d) Mirror plane with $\boldsymbol{n} \parallel \boldsymbol{R}_{ij}$, and e) Two-fold rotation along an axis $\boldsymbol{n} \parallel \boldsymbol{R}_{ij}$ (in general an n-fold rotation with $n \geq 2$ is considered).

a) inversion center in between i and j,
b) mirror plane with the normal vector $\boldsymbol{n} \perp \boldsymbol{R}_{ij}$,
c) two-fold rotation by an axis defined by $\boldsymbol{n} \perp \boldsymbol{R}_{ij}$,
d) mirror plane with $\boldsymbol{n} \parallel \boldsymbol{R}_{ij}$, and
e) n-fold rotation along an axis $\boldsymbol{n} \parallel \boldsymbol{R}_{ij}$ with $n \geq 2$.

The symmetries are depicted in Fig. 4.1. Each global symmetry can be described by a combination of local transformations consisting of mirror operations along the plane perpendicular to $\boldsymbol{n}$, $\mathcal{M}_{\boldsymbol{n}}$, or rotations by an axis $\boldsymbol{n}$ by an angle of α, $\mathcal{R}_{\boldsymbol{n}}(\alpha)$, and permutations of the sites. For the pair interaction two classes of symmetries can be defined depending on whether the sites i and j are permuted or not. The symmetries a, b, and c belong to the the former category, while d and e belong to the latter one. In terms of the diagrams a permutation corresponds to the same diagram with the Green function inverted, $G^0_{ij} \to G^0_{ji}$. The local transformations affect the spatial variables of the Green functions in the same way and do not need to be considered in more detail. The magnetic hamiltonian is also not affected, but the transformation of the spin-orbit coupling hamiltonian needs to be considered. The angular momentum transforms like a pseudo vector under inversion ($\mathcal{I}$), mirroring by the plane normal to $\boldsymbol{n}$ ($\mathcal{M}_{\boldsymbol{n}}$), and rotation by α along the axis $\boldsymbol{n}$ ($\mathcal{R}_{\boldsymbol{n}}(\alpha)$),

$$\mathcal{I}\,\boldsymbol{L} = \boldsymbol{L} \quad , \tag{4.46}$$

$$\mathcal{M}_{\boldsymbol{n}}\,\boldsymbol{L} = \mathcal{P}^{\parallel}_{\boldsymbol{n}}\,\boldsymbol{L} - \mathcal{P}^{\perp}_{\boldsymbol{n}}\boldsymbol{L} \quad , \tag{4.47}$$

$$\mathcal{R}_{\boldsymbol{n}}(\alpha)\,\boldsymbol{L} = \mathcal{P}^{\parallel}_{\boldsymbol{n}}\,\boldsymbol{L} + \cos\alpha\,\mathcal{P}^{\perp}_{\boldsymbol{n}}\boldsymbol{L} + \sin\alpha\,(\boldsymbol{n} \times \boldsymbol{L}) \quad , \tag{4.48}$$

where the projection on the parallel and perpendicular direction to $\boldsymbol{n}$ was used, $\mathcal{P}^{\parallel}_{\hat{\boldsymbol{n}}}\boldsymbol{L} = (\hat{\boldsymbol{n}}\cdot\boldsymbol{L})\,\hat{\boldsymbol{n}}$ and $\mathcal{P}^{\perp}_{\hat{\boldsymbol{n}}}\boldsymbol{L} = \boldsymbol{L} - (\hat{\boldsymbol{n}}\cdot\boldsymbol{L})\,\hat{\boldsymbol{n}}$, respectively. The transformations can be used, to relate certain diagrams to each other. We illustrate this using the example of the Dzyaloshinskii-Moriya interaction and the symmetry operation of type (b). Via the mirror symmetry the following two sets of diagrams are related,

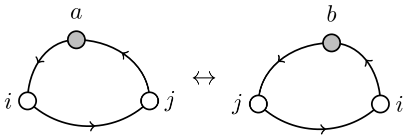

, (4.49)

and

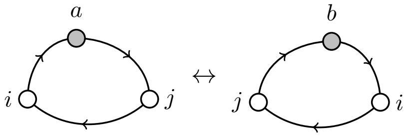

, (4.50)

where b is the spin-orbit coupling site, which is related to a via the mirror symmetry. Note that the propagation direction of the connecting Green functions has not changed. The relation can be seen, when explicitly writing the forms of the diagrams,

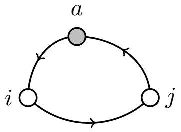

$$\rightarrow\ \mathrm{Tr}\, G^0_{ai}\, U_i\, G^0_{ij}\, U_j\, G^0_{ja}\, \lambda_a\, \boldsymbol{L}\cdot(\boldsymbol{e}_i\times\boldsymbol{e}_j) \quad , \tag{4.51}$$

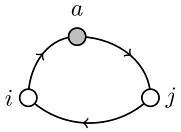

$$\rightarrow\ \mathrm{Tr}\, G^0_{aj}\, U_j\, G^0_{ji}\, U_i\, G^0_{ia}\, \lambda_a\, \boldsymbol{L}\cdot(\boldsymbol{e}_j\times\boldsymbol{e}_i) \quad , \tag{4.52}$$

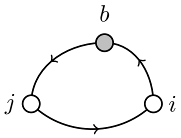

$$\rightarrow\ \mathrm{Tr}\, G^0_{bj}\, U_j\, G^0_{ji}\, U_i\, G^0_{ib}\, \lambda_b\, \boldsymbol{L}\cdot(\boldsymbol{e}_j\times\boldsymbol{e}_i) \quad , \tag{4.53}$$

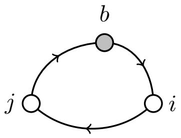

$$\rightarrow\ \mathrm{Tr}\, G^0_{bi}\, U_i\, G^0_{ij}\, U_j\, G^0_{jb}\, \lambda_b\, \boldsymbol{L}\cdot(\boldsymbol{e}_i\times\boldsymbol{e}_j) \quad . \tag{4.54}$$

Using the diagram, eq. (4.53), we can illustrate the action of the mirror symmetry. The Green functions transform like $M_{\hat{\boldsymbol{n}}}\, G^0_{ij} M^{-1}_{\hat{\boldsymbol{n}}} = G^0_{ji}$, $M_{\hat{\boldsymbol{n}}}\, G^0_{ja} M^{-1}_{\hat{\boldsymbol{n}}} = G^0_{ib}$, and $M_{\hat{\boldsymbol{n}}}\, G^0_{ai} M^{-1}_{\hat{\boldsymbol{n}}} = G^0_{bj}$, yielding,

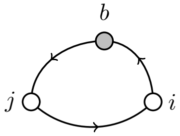

$$\rightarrow \mathrm{Tr}\, M_{\hat{\boldsymbol{n}}}\, G^0_{ai} M^{-1}_{\hat{\boldsymbol{n}}} U_j\, M_{\hat{\boldsymbol{n}}}\, G^0_{ij} M^{-1}_{\hat{\boldsymbol{n}}} U_i\, M_{\hat{\boldsymbol{n}}}\, G^0_{ja} M^{-1}_{\hat{\boldsymbol{n}}} \lambda_b\, \boldsymbol{L} \cdot (\boldsymbol{e}_j \times \boldsymbol{e}_i)$$

$$\begin{aligned} &= \mathrm{Tr}\, G^0_{ai}\, U_i\, G^0_{ij}\, U_j\, G^0_{ja}\, \lambda_a\, (M^{-1}_{\hat{\boldsymbol{n}}} \boldsymbol{L}\, M_{\hat{\boldsymbol{n}}}) \cdot (\boldsymbol{e}_j \times \boldsymbol{e}_i) \\ &= \mathrm{Tr}\, G^0_{ai}\, U_i\, G^0_{ij}\, U_j\, G^0_{ja}\, \lambda_a\, (\mathcal{P}^{\perp}_{\hat{\boldsymbol{n}}} \boldsymbol{L} - \mathcal{P}^{\parallel}_{\hat{\boldsymbol{n}}} \boldsymbol{L}) \cdot (\boldsymbol{e}_i \times \boldsymbol{e}_j) \quad , \end{aligned} \tag{4.55}$$

where $M^{-1}_{\hat{\boldsymbol{n}}} U_j\, M_{\hat{\boldsymbol{n}}} = U_i$ was used. Adding eqs. (4.51) and (4.55) shows that only the perpendicular component of $\boldsymbol{L}$ is finite and the parallel component vanishes,

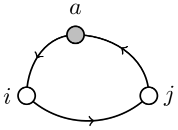

$+$

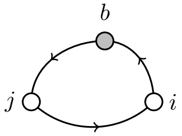

$$\begin{aligned} &\rightarrow 2\mathrm{Tr}\, G^0_{ai}\, U_i\, G^0_{ij}\, U_j\, G^0_{ja}\, \lambda_a\, \mathcal{P}^{\perp}_{\hat{\boldsymbol{n}}} \boldsymbol{L} \cdot (\boldsymbol{e}_i \times \boldsymbol{e}_j) \\ &\sim \mathcal{P}^{\perp}_{\hat{\boldsymbol{n}}} \boldsymbol{D}_{ij} \cdot (\boldsymbol{e}_i \times \boldsymbol{e}_j) \quad . \end{aligned} \tag{4.56}$$

The Dzyaloshinskii-Moriya vector $\boldsymbol{D}_{ij}$ is obtained, when summing over all spin-orbit coupling sites and evaluating the spatial integrals, which leads to the Moriya rule for the symmetry of type b, $\mathcal{P}^{\parallel}_{\boldsymbol{n}} \boldsymbol{D}_{ij} = 0$. Thus, the DMI vector lies in the mirror plane. The same procedure can be applied to the other symmetry operations yielding for (a) $\boldsymbol{D}_{ij} = \boldsymbol{0}$, (b) $\mathcal{P}^{\parallel}_{\boldsymbol{n}} \boldsymbol{D}_{ij} = \boldsymbol{0}$, (c) $\mathcal{P}^{\parallel}_{\boldsymbol{n}} \boldsymbol{D}_{ij} = \boldsymbol{0}$, (d) $\mathcal{P}^{\perp}_{\boldsymbol{n}} \boldsymbol{D}_{ij} = \boldsymbol{0}$, and (e) $\mathcal{P}^{\perp}_{\boldsymbol{n}} \boldsymbol{D}_{ij} = \boldsymbol{0}$, which are the well-known Moriya rules [55, 88, 168].

In terms of the diagrammatics, the CBI is very similar to the DMI. The only difference is the additional loop connecting directly the sites i and j,

DMI

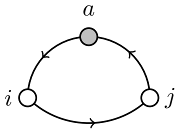

$\Rightarrow$

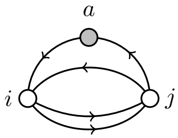

CBI . (4.57)

This loop is invariant under all the symmetry transformations, which implies that exactly the same derivation for the symmetry rules applies to the CBI. Thus the Moriya rules are also valid for the CBI yielding the conditions (a) $\boldsymbol{C}_{ij} = \boldsymbol{0}$, (b) $\mathcal{P}^{\parallel}_{\hat{\boldsymbol{n}}} \boldsymbol{C}_{ij} = \boldsymbol{0}$, (c) $\mathcal{P}^{\parallel}_{\hat{\boldsymbol{n}}} \boldsymbol{C}_{ij} = \boldsymbol{0}$, (d) $\mathcal{P}^{\perp}_{\hat{\boldsymbol{n}}} \boldsymbol{C}_{ij} = \boldsymbol{0}$, and (e) $\mathcal{P}^{\perp}_{\hat{\boldsymbol{n}}} \boldsymbol{C}_{ij} = \boldsymbol{0}$. Note that these symmetry relations apply to the chiral biquadratic pair interaction and not to the multi-site chiral biquadratic interaction. However, using the presented formalism it is also possible to derive symmetry rules for multi-site interactions from a microscopic model, but the identification of the symmetry related diagrams is more cumbersome.

Using the microscopic model, we were able to identify new interesting interactions, especially the chiral biquadratic pair interaction, and we could get some first insights in the properties of this interaction by identifying the symmetry rules. However, the model does not give any insights in how relevant this new interaction in terms of its magnitude and what are its implications in realistic systems. Also, the symmetry often just constrains the direction of the chiral biquadratic vector to a plane (symmetries b and c) and not in an precise direction (only for symmetries d and e). Even though the CBI and the DMI follow the same symmetry rules, this implies that they do not necessarily point in the same direction. In the next section, we address those points by investigating higher-order pair interactions in realistic systems.

4.3. Higher-order pair interactions in realistic systems: The chiral biquadratic interaction

In this section, a systematic and comprehensive first-principles study of higher-order pair interactions is presented. Using magnetic constraining fields and the torque method described in Section 4.1.1, we identify all magnetic pair interactions up to the biquadratic level, including not only the isotropic biquadratic and the CBI (4 parameters), but all possible interactions (25 parameters). As a prototypical test system we use magnetic dimers deposited on different surfaces, which all host a large spin-orbit interactions being relevant for the emergence of chiral interactions. We use two different facets of the Pt surface, the (111) and the (100), which results in a C_s and a C_{2v} symmetry for the dimer, respectively. The impact of the substrate is analysed using the Ir(111) surface and the Re(0001) surface. Especially the Re substrate is interesting, since a strong multi-site interaction was reported for Fe chains on Re [60].

4.3.1. Dimers deposited on surfaces

Computational details

The computational set up is identical to the set up used for the adatoms described in Section 3.3.1 with only a few differences. The main difference is that the full potential instead of the atomic sphere approximation is used. It turned out that using full potential is necessary since the magnetic exchange interactions are very sensitive especially to the electronic structure close to the Fermi level. The dimers were placed in the fcc-stacking position for the Pt(111) and Ir(111) surface, the fourfold hollow position for the Pt(100) surface, and the hcp-stacking position for the Re(0001) surface. For the geometric relaxation, test calculations showed that there is not much difference between single adatoms and magnetic dimers and therefore, we used the same relaxation for the dimers as for the adatoms. The relaxations for all the adatoms on the considered surfaces are listed in Table 4.1. The geometric set up for the (111) surfaces is illustrated in Fig. 4.2a. The embedding regions contain the dimers and their nearest-neighbor substrate atoms. The torque method as explained in Section 4.1.1 is applied, to obtain all magnetic pair interactions up to the biquadratic level.

	Cr	Mn	Fe	Co	Ni	KKR geometry
Pt(111)	19.4 %	17.9 %	25.9 %	27.5 %	25.2 %	20 %
Pt(001)	34.4 %	33.3 %	32.2 %	30.4 %	—	30 %
Ir(111)	11.4 %	11.7 %	17.9 %	20.6 %	—	15 %
Re(0001)	16.1 %	12.7 %	18.6 %	21.8 %	—	15/20 %

Table 4.1.: Geometrical relaxations towards the surface in terms of the interlayer distance for magnetic adatoms deposited on the Pt(111), the Pt(001), the Ir(111) and the Re(0001) surface. The relaxations are obtained from Quantum Espresso using the procedure described in Section 3.3.1. For the setup of the geometry in KKR a common relaxation indicated in the last column is used.

Results

The dimers on the (111) surface obeys the C_s symmetry, which results in a substantial simplification of the magnetic parameters. The on-site anisotropy of each individual dimer atom does not obey any local symmetry being completely unrestricted. However, the dimer atoms are related to each other by the mirror plane implying the following connection between the two on-site anisotropy matrices,

$$K_2 = \mathcal{M}_x K_1 \mathcal{M}_x^{-1} \quad , \tag{4.58}$$

with

$$\mathcal{M}_x = \begin{pmatrix} -1 & 0 & 0 \\ 0 & 1 & 0 \\ 0 & 0 & 1 \end{pmatrix} \quad . \tag{4.59}$$

The general bilinear exchange interaction has to obey the symmetry of the mirror plane,

$$J_{21} = J_{12}^{\mathsf{T}} = \mathcal{M}_x J_{12} \mathcal{M}_x^{-1} \quad , \tag{4.60}$$

resulting in

$$J_{12} = \begin{pmatrix} J_{xx} & D_z & -D_y \\ -D_z & J_{yy} & J_{yz} \\ D_y & J_{yz} & J_{zz} \end{pmatrix} \quad . \tag{4.61}$$

For the biquadratic exchange tensor, see eq. (4.16), one finds the relation $B_{12}^{\alpha\beta\gamma\delta} = (-1)^{N_x} B_{12}^{\beta\alpha\delta\gamma}$, where N_x is the number of times x appears in $\alpha\beta\gamma\delta$. The resulting irreducible full parametrization of the Heisenberg model containing the magnetic anisotropy ($K_{zz} = -K_{xx} - K_{yy}$ by convention), the bilinear magnetic exchange, and the biquadratic magnetic exchange are shown in Table 4.2 for Cr, Mn, Fe, Co, and Ni dimers deposited on the Pt(111) surface. Combining the knowledge of the microscopic model and the full parametrization, the most import contributions were identified – the isotropic bilinear and biquadratic exchange and the chiral DMI

Pt(111)	Cr	Mn	Fe	Co	Ni
K_1^{xx}	−1.23	−0.49	0.14	3.14	0.60
K_1^{xy}	−0.24	0.13	0.23	0.34	0.02
K_1^{xz}	−0.18	0.15	0.42	0.17	−0.01
K_1^{yy}	−2.24	0.02	1.27	3.66	0.64
K_1^{yz}	0.08	−0.23	−0.06	0.01	−0.04
J_{12}^{xx}	36.30	59.02	−43.65	−76.89	−5.36
J_{12}^{yy}	34.94	58.63	−41.80	−76.96	−5.28
J_{12}^{zz}	36.23	57.94	−43.45	−76.52	−5.59
J_{12}^{yz}	0.26	0.42	−0.33	−1.11	−0.11
D_{12}^{y}	8.54	−3.30	−7.27	7.06	0.75
D_{12}^{z}	1.85	−0.13	0.30	−3.57	−0.37
B_{12}^{xxxx}	−8.99	0.56	−1.57	0.61	−0.87
B_{12}^{xxxy}	−0.08	−0.02	−0.05	−0.09	−0.08
B_{12}^{xxxz}	−1.28	0.31	−1.28	0.82	−0.22
B_{12}^{xxyy}	−6.83	0.43	−1.40	0.67	−0.67
B_{12}^{xxyz}	0.00	0.00	−0.01	0.08	−0.01
B_{12}^{xxzz}	−6.72	0.42	−1.06	0.26	−0.65
B_{12}^{xyxy}	4.47	−0.31	1.01	−0.53	0.44
B_{12}^{xyxz}	0.03	−0.01	−0.03	−0.06	0.01
B_{12}^{xyyy}	−0.04	−0.03	−0.02	−0.14	−0.08
B_{12}^{xyyz}	−0.59	0.15	−0.67	0.39	−0.11
B_{12}^{xyzy}	−0.01	0.00	0.00	−0.01	0.00
B_{12}^{xyzz}	0.00	−0.02	−0.02	−0.02	−0.04
B_{12}^{yyyy}	−8.90	0.66	−1.95	0.74	−0.90
B_{12}^{yyyz}	−0.02	0.00	0.04	0.03	−0.01
B_{12}^{yyzz}	−6.66	0.56	−1.24	0.35	−0.64
$\Delta\alpha^{\text{full}}$	−3°	3°	7°	−4°	−8°
$\Delta\alpha^{\text{J+D}}$	−13°	3°	10°	−5°	−8°
$\Delta\alpha^{\text{J+D+C}}$	−10°	3°	6°	−4°	−13°
$\Delta\alpha^{\text{J+D+C+B}}$	−6°	3°	6°	−4°	−10°

Table 4.2.: Independent magnetic exchange parameters of the Cr, Mn, Fe, Co and Ni dimers deposited on the Pt(111) surface in [meV] and the canting angles of the magnetic moments of the dimers $\Delta\alpha$. These are computed following two approaches: the numerical minimization of the spin model containing all the extracted magnetic interactions (full), or the analytic solution of the simplified model, eg. (4.63), containing only different combinations of the isotropic bilinear interaction J, the isotropic biquadratic interaction B and the y-components of chiral interactions, the DMI D and CBI C.

an the CBI. On the biquadratic level there is no other significant contribution for all considered dimers (also on the other considered surfaces).

Table 4.3 collects the most important interactions and magnetic properties of the considered

Dimer		M (μ_B)	C_y	D_y	B	J	$\Delta\alpha^{2\mathrm{s}}$	$\Delta\alpha^{4\mathrm{s}}$
Pt(111)	Cr	3.26	2.5	8.5	−11.7	35.8	−13°	−6°
	Mn	4.05	−0.6	−3.3	0.8	58.5	3°	3°
	Fe	3.32	2.6	−7.3	−2.2	−43.0	10°	6°
	Co	2.12	−1.6	7.1	0.8	−76.8	−5°	−4°
	Ni	0.62	0.5	0.8	−1.1	−5.4	−8°	−10°
Pt(001)	Cr	2.53	2.5	11.2	−9.7	−35.3	−18°	−14°
	Fe	3.24	−0.2	−9.5	−1.5	15.0	32°	28°
Ir(111)	Cr	3.02	3.2	10.7	−12.1	29.5	−20°	−8°
	Fe	3.06	1.3	−14.6	−3.6	−16.3	42°	32°
Re(0001)	Cr	2.18	0.4	−18.1	−3.4	−16.4	48°	40°
	Fe	2.29	0.3	0.5	0.1	−2.3	−12°	−19°

Table 4.3.: Magnetic properties of several dimers on different surfaces. Shown is the spin moment per dimer atom M, the y-component of the CBI C_y and of the DMI D_y, the isotropic biquadratic interaction B, the isotropic bilinear interaction J, and the canting angle obtained from all interactions ($\Delta\alpha^{4\mathrm{s}}$) or keeping only J and D_y ($\Delta\alpha^{2\mathrm{s}}$), see eq. (4.63).

dimers on all surfaces. Starting with the Pt(111) surface, the isotropic exchange is dominating for all dimers. Cr and Mn show a strong antiferromagnetic coupling, while Fe, Co and Ni couple ferromagnetically. Cr has a significant isotropic biquadratic interaction reaching $\sim 30\,\%$ of the isotopic bilinear interaction, while for the other dimers on Pt(111) is mostly negligible. Cr, Fe and Co show large chiral interactions, with the chiral vectors pointing mainly in the y-direction. For all three dimers the CBI is with approximately $30\,\%$ of the DMI a significant higher-order correction. Interestingly, the canting planes illustrated in Fig. 4.2b defined by the two chiral vectors differ significantly for most dimers. The angle β with respect to the x-y plane is shown in Fig. 4.2c. Most angles are close to 90° indicating a large y component of the chiral vectors. For the Co dimer the directions of the chiral vectors differs by more than 20°.

To illustrate the impact of the chiral interactions on the magnetic ground state of the dimers, the effective opening angle between the two magnetic moments of the dimer (canting angle) can be considered. Keeping only the mentioned interactions, the energy as function of the canting angle α is given by

$$E(\alpha) = J\cos\alpha + D_y \sin\alpha + B\cos^2\alpha + C_y \sin\alpha\cos\alpha \quad , \tag{4.62}$$

where $\boldsymbol{e}_1 \cdot \boldsymbol{e}_2 = \cos(\alpha)$ and $(\boldsymbol{e}_1 \times \boldsymbol{e}_2)_y = \sin(\alpha)$ was used. Writing the canting angle as $\alpha = \alpha_J + \Delta\alpha$, where $\alpha_J = \{0°, 180°\}$ indicates a ferromagnetic ($J < 0$) or antiferromagnetic ($J > 0$) coupling, respectively, the minimal canting angle is given by,

$$\begin{aligned} E(\alpha_\mathrm{min}) &\approx E(\alpha_J) - \big(\mathrm{sgn}(J)D_y - C_y\big)\,\Delta\alpha + \big(|J| - 2B\big)\,\frac{(\Delta\alpha)^2}{2} \\ \Rightarrow \Delta\alpha &= \frac{180°}{\pi}\,\frac{\mathrm{sgn}(J)D_y - C_y}{|J| - 2B} \quad . \end{aligned} \tag{4.63}$$

The canting angles obtained from the full parametrization by minimizing the full Heisenberg model and from subsets of the considered interactions are shown in Table 4.2 for the case of

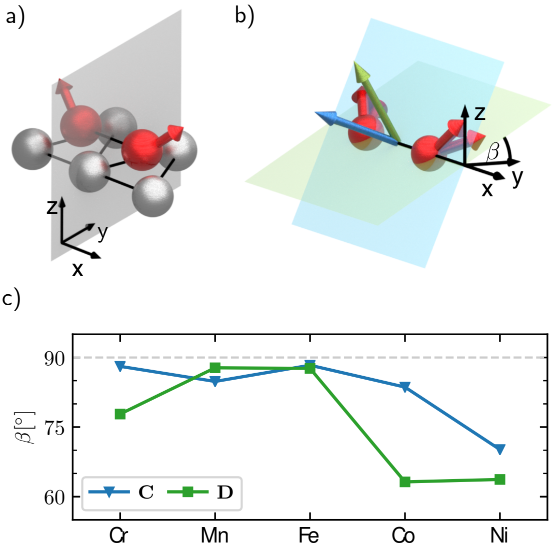

Figure 4.2.: Geometry of the magnetic dimers and canting planes related to the DMI and the CBI. a) Geometry of the magnetic dimer (red spheres) on a (111) substarte (grey spheres). The mirror plane is indicated in grey. b) Canting planes generated by the DMI (green arrow with green plane) and the CBI (blue arrow with blue plane). In the C_S symmetry both vectors are constrained to lie in the mirror plane, but the particular direction can differ. c) Angle β of the canting planes with respect to the x-y plane for Cr, Mn, Fe, Co and Ni dimers deposited on Pt(111).

the Pt(111) surface. Here, we focus on the two different canting angles shown in Table 4.3 – the one obtained from all the considered interactions and the one obtained from only the bilinear interactions using eq. (4.63). For Mn and Co on Pt(111) the bilinear interactions, and especially the isotropic bilinear interaction, dominate resulting in only small differences between the two canting angles. However, for Cr and Fe the two canting angles differ by up to $50\,\%$ showing the importance of the CBI and the isotropic biquadratic interaction.

The CBI was found to be most relevant in the Cr and Fe dimer. Therefore, the study of those two dimers on Pt(001), the Ir(111) and the Re(0001) surfaces is shown in Table 4.3. Interestingly, the local symmetry felt by the dimer can have a significant impact. The magnetic interactions in Cr and Fe dimers on the (001) facet of Pt indicate the huge impact the symmetry of the surface can have. Both dimers change the sign of their bilinear interaction compared to the case of the (111) facet, resulting in an ferromagnetically coupled Cr dimer and an antiferromagnetically coupled Fe dimer. The DMI of the two dimers is enhanced on the Pt(001) surface. The CBI of the Fe dimer is noticeably less relevant on the (001) surface, while the CBI of the Cr dimer is as important as on the (111) facet. On the Ir(111) surface the dimers show a very strong DMI, even compared to the isotropic bilinear interaction, resulting in large canting angles. Accounting for the biquadratic interactions, the canting angles are substantially influenced. The Re surface shows interesting magnetic interactions, since the isotropic bilinear

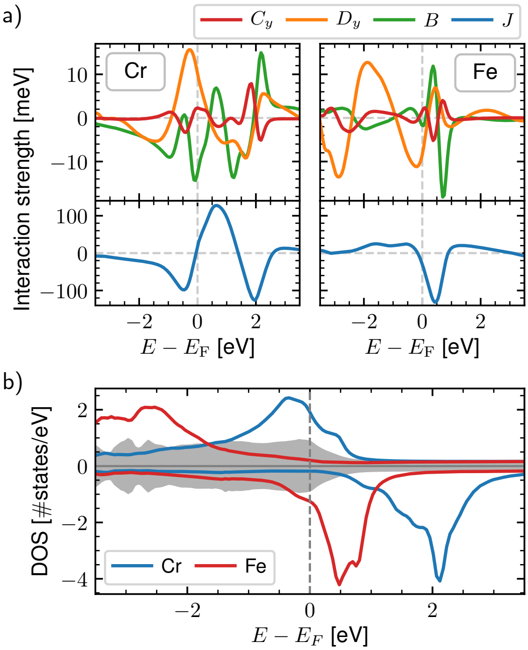

Figure 4.3.: Dependence of the magnetic interaction on the electronic structure for the Cr and Fe dimer deposited on the Pt(111) surface. a) Dependence of the magnetic interactions on the artificially shifted position of the Fermi level. Shown are the y components of the CBI C_y and of the DMI D_y, the isotropic biquadratic interaction B_y, and the isotropic bilinear interaction J as function of the energy. b) Local density of states of the Cr (blue curve) and Fe (red curve) dimers. The grey background indicates the density of states of the Pt surface.

interactions are very weak compared to the other surfaces. For the Cr dimer the DMI dominates the isotropic interactions being the most relevant interaction in terms of its magnitude. This is also indicated in the large canting angle of 48°, which is only weakly affected when the biquadratic interactions are included. Interestingly, the CBI is tiny and irrelevant in the case of the Cr dimer. The Fe dimer on Re(0001) shows the weakest interactions of all considered systems.

To investigate the electronic origin of the different interactions, Fig. 4.3 shows the dependence of the magnetic interactions on the artificially shifted position of the Fermi level and the density of states of the Cr and Fe dimer deposited on the Pt(111) surface. The energy dependence is equivalent to a dependence on the electronic filling. Both isotropic interactions show large peaks around the Fermi level for both dimers. The chiral interactions show a more extended energy dependence, especially for the Fe dimer, where the DMI shows strong oscillations below the Fermi level. The density of states indicates that the Fe minority states are right above the Fermi level at $\sim 0.5\,\mathrm{eV}$, and the majority states are strongly bound. The Cr majority states are at the Fermi level, while the minority states are at $\sim 2\,\mathrm{eV}$. The peaks of the isotropic interactions coincide with the electronic states of the dimer atoms. The isotropic interactions originate from scatterings between the magnetic dimer atoms, as can be seen from eqs. (4.36) and (4.39), resulting in a strong dependence on the filling of the electronic states of the dimer atoms. In contrast, the chiral interactions involve also the Pt substrate, and especially the Pt d-states, via the scattering at the spin-orbit coupling sites, see eqs. (4.37) and (4.42), resulting in an additional dependence on the electronic states of the substrate. Using the diagrams, the CBI is expected to show in relative terms less dependence on the substrate than the DMI. In fact, for the Cr dimer the CBI is irrelevant below $\sim -1\,\mathrm{meV}$, while the DMI extends up to $\sim -2.5\,\mathrm{meV}$.

4.3.2. Implications of the chiral biquadratic interaction

From dimers to spin spirals

The chiral biquadratic interaction has multiple implications for the magnetic ground state of a system. For the previously considered case of a magnetic dimer, it was shown already that the CBI influences the canting angles and the canting planes, and therefore directly influences the vector spin chirality, $\boldsymbol{e}_1 \times \boldsymbol{e}_2$. In order to get more insights, we focus on a simplified model including only the bilinear isotropic interaction J and the y-component of the chiral interactions D_y and C_y resulting in a ground state spin structure in the x-z-plane. The energy as function of the opening angle α is given by,

$$E(\alpha) = J\cos(\alpha) + D_y \sin(\alpha) + C_y \sin(\alpha)\cos(\alpha) \quad , \tag{4.64}$$

where $\boldsymbol{e}_1 \cdot \boldsymbol{e}_2 = \cos(\alpha)$ and $(\boldsymbol{e}_1 \times \boldsymbol{e}_2)_y = \sin(\alpha)$ was used. Fixing $C_y > 0$, the pure CBI supports two groundstates with $\alpha_{\text{min}} = \{-45°, 135°\}$. Noteworthy, the two ground states have different signs meaning that the CBI supports both vector chiralities, and only in the presence of other interaction a specific chirality is chosen. Adding for example the isotropic bilinear interaction, the CBI supports the $-45°$ opening angle for a ferromagnetic coupling and the $135°$ opening angle for an antiferromagnetic coupling.

Going from a dimer to a spin spiral, a similar energy landscape as shown in eq. (4.64) can be found. Assuming a spin spiral propagating along the chain in the x direction with the magnetic moments rotating in the x-z plane the unit directions of each spin i can be described by,

$$\boldsymbol{e}_i = \sin(Qx_i)\boldsymbol{e}_x + \cos(Qx_i)\boldsymbol{e}_z \quad , \tag{4.65}$$

where x_i is the position of spin i and Q is the spin spiral wave vector. Taking into account the nearest neighbor interactions and using basic trigonometric identities a one-to-one correspondence between the energy of the dimer and the energy of the spin spiral can be found. The opening angle α in eq. (4.64) is related to the spin spiral wave vector by $Q \to \alpha/a$.

The magnetic ground state as function of the three considered interaction is shown in Fig. 4.4. For large isotropic exchange, $|J| \gg |D_y|, |C_y|$, the classical limits of ferromagnetic coupling, $\alpha = 0°$, and antiferromagnetic coupling, $\alpha = \pm 180°$ are recovered. Interestingly, depending on the ratio between the chiral interactions D_y/C_y the antiferromagnetic state is approached from different chiralities. Since $C_y > 0$ the CBI supports the $\alpha = 135°$ state for an antiferromagnetic isotropic coupling. In contrast, a positive DMI supports the $\alpha = -90°$ state. Thus, for $D_y > C_y$

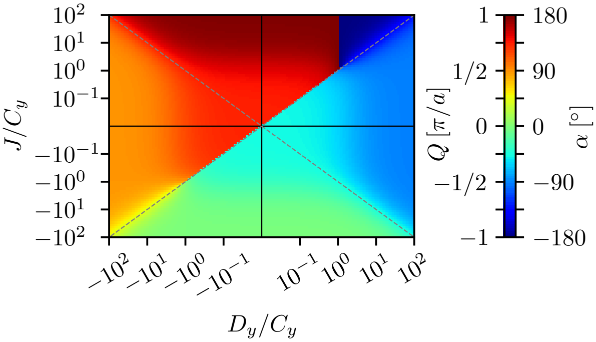

Figure 4.4.: Ground state spin structure as function of the magnetic interactions. Shown are the canting angle α of a magnetic dimer and the equivalent spin spiral vector Q as function of the DMI D_y, the bilinear exchange J, and the CBI C_y. C_y is assumed to be positive.

the antiferromagentic state is approached from a negative chirality ($\alpha < 0$), while for $D_y < C_y$ it is approached from a positive chirality ($\alpha > 0$). In the limit of large DMI, $|D_y| \gg |J|, |C_y|$, the $\alpha = \pm 90°$ states are obtained. For large CBI and $J > D_y$ the ground state $\alpha = 135°$ is obtained, while for $J < D_y$ the $\alpha = -45°$ is found. Noteworthy, the transition between those states is sharp indicating a change of the chirality induced by the CBI.

Two-dimensional extended structures

Higher-order interactions are known to stabilize several multi-$\boldsymbol{Q}$-states in two-dimensional structures [23, 52, 57, 58]. In particular, the seminal work of Heinze *et al.* [23] showed the stabilization mechanisms of a nanoskyrmion lattice. Experimentally a nanoskyrmion lattice was found in an Fe monolayer on Ir(111), but the usual bilinear interactions were not capable of justifying its energetically preference over other multi-$\boldsymbol{Q}$ states. Taking into account an isotropic four-site interaction, see eq. (4.41), lead to the an energetically favoured nanoskyrmion lattice. Here, we want to investigate how the CBI affects some of the two-dimensional structures considered in the work of Heinze. Note that the aim is not to calculate the strength of the CBI in the particular system, but to analyse which magnetic structure is favoured by the CBI. We start from a hexagonal lattice of spins, which form a particular magnetic structure. The hexagonal lattice has three high-symmetry points in the Brillouin zone, the Γ, K and M points. Heinze defines two $\boldsymbol{Q}$-vectors in the Brillouin zone, called $\boldsymbol{Q}_1$ and $\boldsymbol{Q}_2$, and two associated $\boldsymbol{Q}$-vectors pointing in the high-symmetry directions $\Gamma - M$ and $\Gamma - K$, called $\boldsymbol{Q}_K$ and $\boldsymbol{Q}_M$. Fig. 4.5a-f shows all the considered magnetic structures, which are the single-$\boldsymbol{Q}$ spin spirals with $\boldsymbol{Q} = \boldsymbol{Q}_1$ (a) and $\boldsymbol{Q} = \boldsymbol{K}$ (d, Neel state, not considered by Heinze), the multi-$\boldsymbol{Q}$ states $\boldsymbol{Q}_M$-star (b) and $\boldsymbol{Q}_M$-vortex (c), the nanoskyrmion lattice (e) and the nanovortex lattice (f). Linear combinations of the single-$\boldsymbol{Q}$-states, $\boldsymbol{Q}_1$ and $\boldsymbol{Q}_2$, give rise to multi-$\boldsymbol{Q}$ states, the so-called $\boldsymbol{Q}_M$-star and $\boldsymbol{Q}_M$-vortex. By flipping the x-direction of the spins in a particular region, the $\boldsymbol{Q}_M$-star transforms into the nanoskyrmion lattice and the $\boldsymbol{Q}_M$-vortex transforms into the nanovortex lattice.

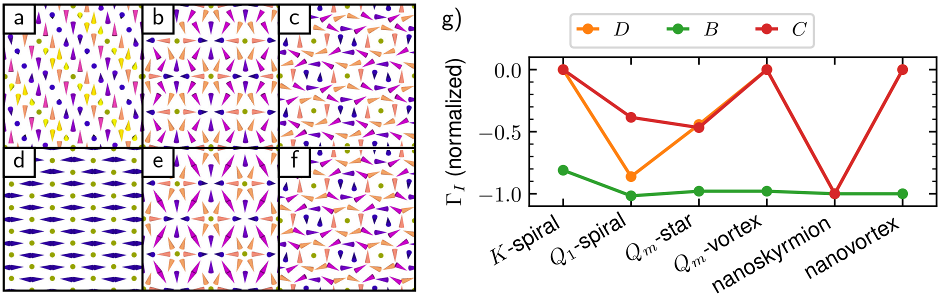

Figure 4.5.: Impact of higher-order interactions on two-dimensional magnetic structures on an hexagonal lattice. The considered magnetic structures are the single-$\boldsymbol{Q}$-states formed by the $\boldsymbol{Q}_1$-vector (a) and the $\boldsymbol{K}$-vector (d, Néel state), the $\boldsymbol{Q}_M$-star (b) and $\boldsymbol{Q}_M$-vortex (c), and the related nanoskyrmion lattice (e) and nanovortex lattice (f). The impact of the DMI D, the CBI C, and the isotropic biquadratic interaction B on the energy prefactor (see main text) for each magnetic structure is shown in (g). The structures were taken from the Heinze *et al.* [23].

To describe the impact of all the interactions on the energetics of each magnetic structure, we describe the energy by $E = N\Gamma_I I$, where N is the number of spins, $I = \{B, C, D\}$ is the magnitude of each magnetic interaction, and Γ_I is a prefactor depending on the interaction and the particular magnetic structure. Thus, we encode not only the magnetic structure in the prefactor, but also how each magnetic structure affects the particular magnetic structure. We exclude the isotropic bilinear interaction from this consideration, since it was shown to be complex and long-ranged [23], and we want to restrict ourselves to nearest neighbor interactions for the sake of simplicity. The DMI and CBI vectors are assumed to lie in the plane and are chosen according to the C_{3v} symmetry of the (111) surface. Fig. 4.5g shows the prefactor Γ_I for each interaction and for all magnetic structures. The isotropic biquadratic interaction has only a weak dependence on the magnetic structure. Apart from the Neel state, all the states are energetically nearly degenerated. The DMI clearly favours two structures, the $\boldsymbol{Q}_1$-spiral and the nanoskyrmion lattice. The CBI is very similar to the DMI, but clearly disfavours the $\boldsymbol{Q}_1$-spiral resulting in an overall favouring of the nanoskyrmion lattice. This shows that the CBI play a decisive role in the complex magnetism of two-dimensional structures.

4.4. Higher-order multi-site interactions

The previously discussed CBI was shown to be relevant in terms of its magnitude and its possibly deciding role in the magnetism of two-dimensional structures. The derivation in the microscopic model showed that the CBI, as well as the biquadratic isotropic interaction, are subsets of higher-order multi-site interactions including up to four sites. From the microscopic model, there is no reason why the higher order pair interactions (e.g. the isotropic biquadratic or the CBI) would be more relevant in terms of their magnitudes than their multi-site equivalents. For example the isotropic four-spin three-site interaction, eq. (4.40), or the isotropic four-spin four-site interaction, eq. (4.41), have the same physical origin as the biquadratic isotropic pair interaction, eq. (4.39). All originate from four scattering events at magnetic sites. In this section, we want to shed light on the importance of multi-site interactions by investigating three-site interactions in realistic systems.

4.4.1. Compact trimers on the Pt(111) surface

As a prototypical test system we chose compact magnetic trimers composed out of Cr and Fe deposited on the Pt(111) surface, since we found those compounds to show the most dominant higher-order interactions in the case of a magnetic dimer. As discussed in relation to the orbital magnetism of compact trimers in Section 3.3.8, compact trimers preserve the C_{3v} of the substrate. Furthermore, they are intensively studied with respect to their magnetic stability, which will be discussed in Chapter 6, highlighting the importance of a detailed understanding of the internal interactions.

Computational details

The computational setup is similar to the one used for the magnetic dimers discussed in Section 4.3.1. Similar to the higher order pair interactions, we use the torque method to map first-principles calculations to a spin model including multi-site interactions. In order to extract the interactions up to the biquadratic level, 252 different irreducible magnetic configuration are considered.

Results

Since the complexity of the general spin cluster expansion, eq. (4.12), rises drastically for multi-site interactions, we restrict ourselves to the interactions, which are at most linear in spin-orbit coupling. In addition to the previously discussed pair interactions, including the isotropic pair interactions and the chiral pair interactions, two new interactions are possible – namely the isotropic four-spin three-site interaction and the 3-site chiral interaction. The isotropic four-spin three-site interaction, which was derived in eq. (4.40), has the form,

$$\mathcal{H}_{\text{4-spin 3-site}} = \sum_{i\neq j\neq k} M_{ijk}(\boldsymbol{e}_i \cdot \boldsymbol{e}_j)(\boldsymbol{e}_i \cdot \boldsymbol{e}_k) = M \sum_{i\neq j\neq k}^{3} (\boldsymbol{e}_i \cdot \boldsymbol{e}_j)(\boldsymbol{e}_i \cdot \boldsymbol{e}_k) \quad , \tag{4.66}$$

where the C_{3v} symmetry of the trimer was used, while the 3-site chiral interaction, eq. (4.44), has the form,

$$\mathcal{H}_{\text{3-site chiral}} = \sum_{i\neq j\neq k} \boldsymbol{C}_{ijk} \cdot (\boldsymbol{e}_i \times \boldsymbol{e}_j)(\boldsymbol{e}_i \cdot \boldsymbol{e}_k) \quad . \tag{4.67}$$

The chiral 3-site vector $\boldsymbol{C}_{ijk}$ can be constructed from the symmetry of the lattice. The compact trimer with all its symmetries is depicted in Fig. 4.6. Starting from the element $\boldsymbol{C}_{123}$ the

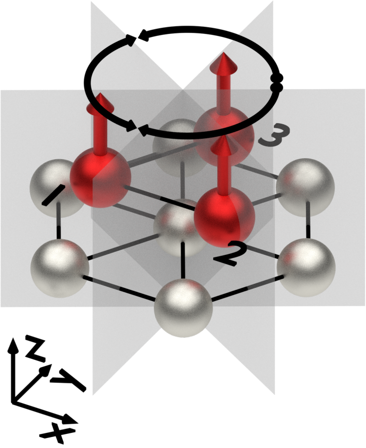

Figure 4.6.: Compact fcc-top stacked trimer deposited on the (111) facet of Pt. The symmetries related to the C_{3v} symmetry of the trimer are indicated by grey planes (mirror symmetries) and the arrows (rotational symmetries). The trimer atoms are numerated.

mirror plane relates the vector to $\boldsymbol{C}_{213} = (C^x_{123}, -C^y_{123}, -C^z_{123})$. The 3-fold rotational symmetry relates all the other possible permutations to the previously mentioned ones, e.g. $\boldsymbol{C}_{231} = \mathcal{R}_z(120\,°)\boldsymbol{C}_{123}$. The full spin hamiltonian of the trimer is defined by,

$$\mathcal{H}_{\text{trimer}} = \sum_i^3 \boldsymbol{e}_i^{\mathsf{T}} K_i \boldsymbol{e}_i + \frac{1}{2} J \sum_{i \neq j}^3 \boldsymbol{e}_i \cdot \boldsymbol{e}_j + \frac{1}{2} \sum_{i \neq j} \boldsymbol{D}_{ij} \cdot (\boldsymbol{e}_i \times \boldsymbol{e}_j) + \mathcal{H}_{\text{4-spin 3-site}} + \mathcal{H}_{\text{3-site chiral}} \quad , \tag{4.68}$$

where the anisotropy matrices and the DMI vectors are related by the rotational symmetry of the lattice, $K_{i+1} = \mathcal{R}_z(120\,°) K_i \mathcal{R}_z^{\mathsf{T}}(120\,°)$ and $\boldsymbol{D}_{i+1,j+1} = \mathcal{R}_z(120\,°)\boldsymbol{D}_{ij}$ (where the indices i and j have to be understood as a subset of $\{1,2,3\}$). The on-site anisotropy and the DM vector have additional local symmetry constraints due to the local mirror planes resulting in further simplification, which are easiest to show for the x-mirror plane,

$$K_3 = \begin{pmatrix} K_{xx} & 0 & 0 \\ 0 & K_{yy} & K_{yz} \\ 0 & K_{yz} & -K_{xx} - K_{yy} \end{pmatrix} \quad \text{and} \quad \boldsymbol{D}_{12} = \begin{pmatrix} 0 \\ D_y \\ D_z \end{pmatrix} \quad . \tag{4.69}$$

Table 4.4 shows all the magnetic interactions for the Cr and Fe trimers deposited on the Pt(111) surface. Comparing the pair interactions to the ones found for magnetic dimers on the same substrate, it can be seen that the additional scattering site renormalizes the pair interactions. Focusing on the Fe-based systems the bilinear isotropic interaction is $-43\,\mathrm{meV}$ in the case of the dimer, but $-50\,\mathrm{meV}$ in the case of the trimer. In the trimer the chiral biquadratic pair interaction is also relevant with approximately $25\,\%$ of the DMI for both systems. Similarly to

	Cr/Pt(111)	Fe/Pt(111)
K_3^{xx}	-1.4	0.2
K_3^{yy}	-0.8	-0.1
K_3^{yz}	-1.0	1.6
J_{xx}	68.8	-50.8
J_{yy}	68.1	-49.3
J_{zz}	68.2	-49.9
D_{12}^y	-5.9	4.9
D_{12}^z	-3.8	0.9
J_{yz}	0.4	-0.6
B	-6.1	-1.2
C_{12}^y	-2.0	-1.2
C_{12}^z	-0.1	0.0
M	3.8	2.2
C_{123}^x	0.0	0.1
C_{123}^y	-0.1	-0.0
C_{123}^z	-1.3	-0.7

Table 4.4.: Magnetic interactions in different compact fcc-top-stacked trimers deposited on the Pt(111) surface in units of [meV]. Considered are all interactions up to the biquadratic level and up to first-order in spin-orbit coupling. The full set of interactions can be obtained from the shown interaction by applying the symmetry rules of the trimer.

the case of the dimers, the direction of the CBI vector differs from the one of the DMI vector. Noteworthy, the newly emerging three-site interactions show an overall large magnitude. The isotropic 4-spin 3-site interaction reaches a magnitude of $2.2\,\mathrm{meV}$ for the Fe-based trimer surpassing its 2-site equivalent. Also the chiral 3-site interaction shows a significant magnitude and is comparable to the chiral biquadratic pair interaction for both trimers.

4.5. Conclusions and outlook

In this chapter, the interesting physics of higher-order magnetic exchange interactions are discussed. A generic diagrammatic theory allowed us to systematically identify and classify all magnetic interactions by the means of a Levy-Fert model. The two physical mechanisms, namely scattering at magnetic sites and scattering at spin-orbit coupling sites, were identified as the origin of magnetic exchange interactions. Apart from the well-known bilinear interactions, our theory shed light on higher-order interactions with a special focus on chiral interactions, which were so far only discussed in case-by-case studies [60, 61]. On the level of pair interactions, we identified the chiral biquadratic interaction as the biquadratic equivalent to the DMI eventually allowing for the stabilization of new magnetic phases. Using the prototypical test system of magnetic dimers deposited on heavy metal substrates hosting large spin-orbit coupling, we found a new term that we called CBI, which is the most relevant chiral correction on the biquadratic level. With up to $35\,\%$ of the DMI it was shown to be a significant contribution for most considered dimers. Using the electronic structure of the magnetic dimers, we identified the physical origins of the different magnetic interactions being a complex interaction between the substrate d-states and the dimer d-states. We discussed the implications of the CBI on magnetic dimers and spin spirals. Remarkably, the CBI on its own supports both chiralities with an opening angle of $\alpha = \{135\,°, -45\,°\}$. Only in the presence of the other interactions, the CBI favours a certain chirality. Depending on the ratio between the other interactions, the CBI can give rise to sharp transitions between the two different chiralities. Using several two-dimensional magnetic structures based on the work of Heinze et al. [23], we found that the CBI could favour the nanoskyrmion lattice over all other considered magnetic structures. Especially in systems with complex competing magnetic interactions, the CBI could play a deciding role.

We also investigated multi-site higher order interactions and found that they can exceed their 2-site equivalents. Using the example of magnetic trimers on the Pt(111) surface, we found for example an isotropic 4-spin 3-site interaction, which is more important than the isotropic biquadratic pair interaction. Also the 3-site chiral interaction was found to be as important as the chiral biquadratic pair interaction. The 3-site chiral interaction is of particular interest, since it was found to have an impact on the chirality of an Fe chain deposited on Re(0001) [60] and it helped understanding the complex magnetic interactions in MnGe [61].

In general, the higher-order magnetic interactions can potentially help understanding the complex magnetism of different non-collinear systems. They might help understanding and making material-specific predictions for the formation and stabilization of complex magnetic structures like magnetic bobbers. Even though, we showed its existence and its relevance for prototypical test systems composed out of up to three atoms a detailed exploration of higher-order interactions in extended systems is missing. In extended systems, only specific subsets of higher-order interactions were investigated so far, which is also due to the combinatorial nature in extended systems. Their spatial range is unkown, so they should be computed in real space going beyond nearest-neighbors. The identification of pair interactions in a three dimensional system is straight-forward, but the identification of triangles and quadrilaterals involved in 3-site and 4-site interactions, respectively, is a cumbersome task with an exponential scaling. Also a general fitting based on the spin cluster expansion, as done for pair interactions in Section 4.3.1, is not only computationally demanding, but also its interpretation is highly complicated. Therefore, the work discussed in this Chapter can set the ground for the identification of the most relevant higher-order interactions, which in turn can be applied to extended systems. To complete this study, a systematic analysis based on a tetramer could give additional insights in the 4-site interactions.

We also expect higher-order interactions to not only influence the magnetic ground state, but also have a non-trivial impact on the transport and topological properties, the spin dynamics and the related lifetimes of magnetic structures. The latter two quantities will be discussed in Chapters 5 and 6, respectively.

5

Magnetization dynamics in non-collinear nanostructures

The field of spintronics is based on the ability to manipulate the spin degrees of freedom and therefore the magnetic state. In this chapter, we focus on the description of magnetization dynamics in non-collinear systems by the means of the Landau-Lifshitz-Gilbert (LLG) model, which has two important ingredients – the internal magnetic interactions and the so-called Gilbert damping describing the dissipation of angular momentum. Special attention is given to the Gilbert damping, which for non-collinear systems is not well-understood. Using a perturbative expansion of an Anderson model, we identify the possible atomistic dependencies of the Gilbert damping on the underlying magnetic texture. We show the importance of these dependencies based on the model and based on first-principles calculations using time-dependent DFT. Our findings can be used to extend the usual LLG model to account for non-collinear

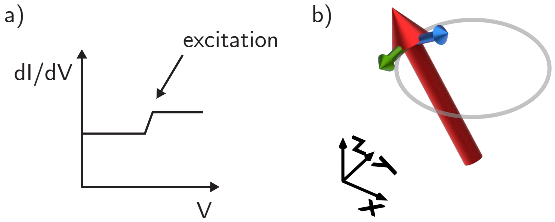

Figure 5.1.: Magnetic exciations in magnetic nanostructures. a) Schematic differential conductivity, $\mathrm{d}I/\mathrm{d}V$, seen in inelastic scanning tunneling microscopy experiments. The step in the $\mathrm{d}I/\mathrm{d}V$ curve indicates an excitation. b) Illustration of the Landau-Lifshitz-Gilbert model. A classical spin (red arrow) precesses in the the presence of an external field. The blue arrow indicates the direction of a damping term, while the green arrow indicates the direction of the precession term.

magnetism, which can potentially advance the field of atomistic spin dynamics by providing a more realistic description of the Gilbert damping tensor.

5.1. Introduction

The manipulation and processing of magnetic data bits in data storage devices are highly dynamical processes. On the way towards the miniaturization of such devices, it is a necessity to not only gain an atom-by-atom understanding of the static properties of magnetic nanostructures, which were discussed in the previous chapters, but also understand the dynamical properties of magnetic nanostructures. In particular, the interaction of magnetic structures with external magnetic fields is of great interest from both, the theoretical and the experimental point of view. The magnetic excitations of nanostructures comprising just a few atoms can be experimentally probed using for example inelastic scanning tunneling spectroscopy (ISTS). The measured differential conductivity, $\mathrm{d}I/\mathrm{d}V$, can show a sudden increase at a specific energy indicating the opening of a new tunneling channel, which corresponds to an excitation as illustrated in Fig. 5.1a. Several systems were addressed experimentally using the ISTS technique – ranging from single adatoms [27, 31–34], to larger nanostructures [29, 30] on metals, but also structures deposited on insulators [44, 169]. Theoretically the ISTS spectra can be addressed from two different approaches – model-based using a quantum spin hamiltonian or from first-principles using time-dependent DFT. In Chapter 6, a detailed explanation of the magnetic excitations in terms of a quantum spin model will be given. In this chapter, we focus on the time-dependent DFT and the semi-classical description using the so-called Landau-Lifshitz-Gilbert (LLG) equation. Since the LLG equation is one of the most relevant ingredients in the rest of this chapter it will be briefly introduced in the following.

Landau-Lifshitz-Gilbert model

A theory for the time-dependent motion of a macroscopic magnetic moment in the presence of an external magnetic field was first discussed by Landau and Lifshitz [50] and later refined by Gilbert [51] resulting in the well-known Landau-Lifshitz-Gilbert model. The LLG model is intensely applied in the whole field of spintronics. Originally being a phenomenological theory with applications to macroscopic systems, its range of applications successively increased. It is used to describe spin dynamics of systems in all dimensions – ranging from three-dimensional bulk magnets [170] down to the 0-dimensional case of single atoms [107]. For the atomistic description the LLG model has two important ingredients: the effective magnetic field, $\boldsymbol{B}^{\text{eff}}$, felt by the considered atom i rising from internal interactions and the so-called Gilbert damping being in general a tensorial and non-local quantity [171], $\mathcal{G}_{ij}$. In a general form it is given by,

$$\frac{\mathrm{d}\boldsymbol{m}_i}{\mathrm{d}t} = -\gamma \boldsymbol{m}_i \times \left(\boldsymbol{B}_i^{\text{eff}} + \sum_j \mathcal{G}_{ij} \cdot \frac{\mathrm{d}\boldsymbol{m}_j}{\mathrm{d}t} \right) \quad , \tag{5.1}$$

where $\gamma = 2$ is the gyromagnetic ratio. In a simplified form the LLG can also be written as,

$$\frac{\mathrm{d}\boldsymbol{m}_i}{\mathrm{d}t} = -\tilde{\gamma} \boldsymbol{m}_i \times \left(\boldsymbol{B}_i^{\text{eff}} + \alpha_i \frac{\mathrm{d}\boldsymbol{m}_i}{\mathrm{d}t} \right) \quad , \tag{5.2}$$

where the damping tensor was assumed to be local and isotropic. In this form the gyromagnetic ratio, $\tilde{\gamma}$, potentially differs from 2 due to an effective renormalization from the substrate, which in the general form, eq. (5.1), is reflected in the tensorial damping. The simplified form has two terms, a precession-like term $\boldsymbol{m}_i \times \boldsymbol{B}_i^{\text{eff}}$ and a damping-like term $\boldsymbol{m}_i \times \frac{\mathrm{d}\boldsymbol{m}_i}{\mathrm{d}t}$, which are illustrated in Fig. 5.1b as green and blue arrows, respectively. The precession term drives the precession of the magnetic moment around the effective magnetic field, while the damping term tries to bring the magnetic moment into alignment with the effective magnetic field, leading to a characteristic lifetime of the precessional dynamics.

Internal magnetic interactions are well-described by a generalized Heisenberg model including magnetic anisotropies and magnetic exchange interactions, which are eventually of higher-order as discussed in Chapter 4. The atomistic spin models give access to the effective magnetic field used in the LLG model,

$$\boldsymbol{B}_i^{\text{eff}} = -\frac{\mathrm{d}\mathcal{H}_{\text{spin}}}{\mathrm{d}\boldsymbol{m}_i} \quad . \tag{5.3}$$

However, less is known about the Gilbert damping tensor especially in non-collinear magnets. The usual assumption of local and isotropic Gilbert damping was contradicted, since even experimentally signatures of giant anisotropic Gilbert damping were found [172, 173]. An experimental breakthrough was the measurement of the domain wall creep motion, which depends on the chirality of the domain wall [174]. The domain wall creep motion was attributed to a chiral damping and a chiral renormalization of the gyromagnetic ratio [174–178], where chiral in most of the theories means that the damping in a spin spiral with vector $\boldsymbol{Q}$ differs from the one in a spin spiral with $-\boldsymbol{Q}$, i.e., it depends on the rotational sense of the magnetic moments constituting the spiral.

Most first-principles studies of the Gilbert damping were either focusing on collinear systems or were case-by-case studies of specific non-collinear structures lacking a general understanding of the fundamental behaviour of the Gilbert damping in dependence on the non-collinear state of the system. Some dependencies of the Gilbert damping tensor on the spin spiral vector and especially on the chirality of a system were proposed in previous studies [175, 177–179]. However, a detailed microscopic picture based on a atomistic formulation even without spin-orbit coupling is missing, which is the main motivation of this Chapter.

In this Chapter, we want to gain a deep understanding of the spin dynamics in non-collinear systems. Our main interest is the connection between the LLG model and the magnetic susceptibility as obtained from TD-DFT. However, since spin dynamics in non-collinear systems require a whole new level of complexity compared to the dynamics of ferromagnetic system, we approach this from two perspectives: First, we analyse the spin dynamics in a single orbital Anderson model involving multiple sites. The model allows us to not only gain insights in the dependencies of the Gilbert damping on the minimal ingredients, but also enables a systematic analysis in non-collinear systems. Similarly to the procedure applied to higher-order interactions in Chapter 4, a systematic study of all possible microscopic dependencies of the Gilbert damping tensor on the non-collinear orientation of the magnetic moments is presented. Using a perturbative expansion and diagrammatic techniques, we shed some light on the origin and the functional dependencies of the Gilbert damping tensor on the orientations of the magnetic moments in an atomistic form, which will be analyzed numerically in a two- and three-site Anderson model. As a second step, we perform first-principles TD-DFT calculations using the prototypical test systems of magnetic dimers deposited on the Au(111) surface and apply the gained knowledge from the Anderson model to map the transverse magnetic susceptibility obtained from the TD-DFT calculation to the LLG model.

5.2. Magnetization dynamics in non-collinear structures

The response of a magnetic moment $\boldsymbol{m}_i$ at site i to an external magnetic field $\boldsymbol{B}_j$ at site j can be described using the magnetic susceptibility χ_{ij},

$$\boldsymbol{m}_i = \chi_{ij}\boldsymbol{B}_j \quad . \tag{5.4}$$

For a system of interacting electrons this magnetic susceptibility can be obtained from TD-DFT as described in Section 2.3.1. Note that χ_{ij} is the renormalized susceptibility as described in Section 2.3.1, which encodes all collective excitations of the interacting electron system in addition to the single-particle excitations already contained in the Kohn-Sham susceptiblity. Since the magnetic susceptibility is a very complicated quantity being a frequency-dependent 4×4 matrix with a real and imaginary part, its interpretation can be cumbersome, which is why more intuitive models like the above mentioned LLG model are used to interpret the spin dynamics. The transversal part of the magnetic susceptibility offers an ideal starting point for a comparison to the LLG, since it does not influence the magnitude of the magnetic moments (which is one of the main conditions of the LLG model). The first question we have to address is: How to define the transversal part of the susceptibility in a non-collinear system?

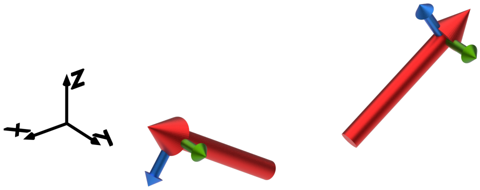

Figure 5.2.: Local frames of two non-collinear magnetic moments. The global frame is indicated in black. The local frames as described by the Rodrigues rotation formula, eq. (5.5), are indicated by the red arrow (local z-axis), the green arrow (local y-axis) and the blue arrow (local x-axis).

The local frame

A vector, which is transverse to a magnetic moment, can be easily defined in a local frame, which is built out of three orthogonal direction with one direction pointing along the magnetic moment as illustrated in Fig. 5.2. To define the site-dependent local frame of a specific magnetic configuration defined by the polar angle ϑ_i and the azimuthal angle φ_i of site i, the Rodrigues rotation formula can be used yielding the rotation matrix in real space,

$$\mathcal{R}(\vartheta_i,\varphi_i) = \begin{pmatrix} \cos^2\varphi_i\cos\vartheta_i + \sin^2\varphi_i & \cos\varphi_i\sin\varphi_i\cos\vartheta_i - \cos\varphi_i\sin\varphi_i & -\cos\varphi_i\sin\vartheta_i \\ -2\cos\varphi_i\sin\varphi_i\sin^2\frac{\vartheta_i}{2} & \cos^2\varphi_i + \sin^2\varphi_i\cos\vartheta_i & -\sin\varphi_i\sin\vartheta_i \\ \cos\varphi_i\sin\vartheta_i & \sin\varphi_i\sin\vartheta_i & \cos\vartheta_i \end{pmatrix} \quad . \tag{5.5}$$

The corresponding rotation in spin space can be defined using Pauli matrices by,

$$\mathcal{R}^{\mathsf{s}}(\vartheta_i,\varphi_i) = \cos(\vartheta_i/2)\sigma_0 + \mathrm{i}\,\sin(\vartheta_i/2)\big(\sin(\varphi_i)\,\sigma_x - \cos(\varphi_i)\,\sigma_y\big) \quad , \tag{5.6}$$

which defines the susceptibility in the local frame of i and j by rotating the vector of Pauli matrices $\boldsymbol{\sigma}$ via,

$$\boldsymbol{\sigma}_i^{\mathsf{loc}} = \mathcal{R}_i^{\mathsf{s}}\boldsymbol{\sigma}\,(\mathcal{R}_i^{\mathsf{s}})^{\dagger} \quad . \tag{5.7}$$

The local frame formulation allows to easily define transversal excitations for each individual atom, which correspond to the $\{x, y\}$ block of the on-site susceptibility. However, in the inter-site case it is not obvious to define transversal excitations. The $\{x, y\}$ block of the inter-site susceptibility defines the transversal response of a magnetic moment at site i (transverse to its local frame) to the action of a magnetic field transverse to the magnetic moment of site j. Note that in the non-collinear case without spin-orbit coupling even for the on-site susceptibility the transversal and the longitudinal part are not decoupled.

The connection between the magnetic susceptibility and the LLG model

The magnetic susceptibility contains a lot of information making it difficult to interpret. Apart from the energies of the excitations the susceptibility contains information about the energy broadening of the excitations and also directional information encoded in the transversal and longitudinal parts of the susceptibility. To simplify the interpretation, the magnetic susceptibility can be mapped to an effective LLG model [107, 180]. The generalized LLG equation, eq. (5.1), in its frequency form ($\frac{\mathrm{d}}{\mathrm{d}t} \rightarrow -\mathrm{i}\,\omega$),

$$-\mathrm{i}\,\omega \boldsymbol{m}_i = -\gamma \boldsymbol{m}_i \times \left(\boldsymbol{B}_i^{\mathsf{eff}} - \mathrm{i}\,\omega \sum_j \mathcal{G}_{ij} \cdot \boldsymbol{m}_j \right) \quad , \tag{5.8}$$

becomes in the local frames of i and j,

$$-\mathrm{i}\,\omega \boldsymbol{m}_i^{\mathsf{loc}} = -\gamma \boldsymbol{m}_i^{\mathsf{loc}} \times \left(\mathcal{R}_i \boldsymbol{B}_i^{\mathsf{eff}} - \mathrm{i}\,\omega \sum_j \mathcal{R}_i \mathcal{G}_{ij} \mathcal{R}_j^{\mathsf{T}} \boldsymbol{m}_j^{\mathsf{loc}} \right) \quad . \tag{5.9}$$

For a comparison of the LLG with the magnetic susceptibility of the spin model, the LLG equation has to be treated in linear response. The magnetic moments are assumed to be perturbed around its equilibrium value M_i,

$$\boldsymbol{m}_i^{\mathsf{loc}} = M_i \boldsymbol{e}_i^z + m_i^x \boldsymbol{e}_i^x + m_i^y \boldsymbol{e}_i^y \quad , \tag{5.10}$$

where $\boldsymbol{e}_i^{\alpha}$ is the unit vector in direction α in the local frame of site i as illustrated in Fig. 5.2. Similarly the perturbing magnetic field can be defined as,

$$\boldsymbol{B}_i = \boldsymbol{B}_i^{\mathsf{ext}} + b_i^x \boldsymbol{e}_i^x + b_i^y \boldsymbol{e}_i^y \quad , \tag{5.11}$$

where $\boldsymbol{B}_i^{\mathsf{ext}}$ is the external field, which is not necessarily aligned with the local moment, and $b_i^{x/y}$ is the transversal dynamic part of the magnetic field. Using the ground-state condition of vanishing magnetic torques, $M_i \boldsymbol{e}_i^z \times \left(\boldsymbol{B}_i^{\mathsf{ext}} + \boldsymbol{B}_i^{\mathsf{int}} \right) = 0$, and restricting to bilinear interactions, which result in an internal field of,

$$\boldsymbol{B}_i^{\mathsf{int}} = -\frac{\mathrm{d}\mathcal{H}}{\mathrm{d}\boldsymbol{m}_i} = -\frac{1}{M_i M_j} \sum_j J_{ij} \boldsymbol{m}_j \quad , \tag{5.12}$$

the inverse susceptibility, $\chi^{-1} \boldsymbol{m} = \boldsymbol{b}$, can be identified as,

$$\chi_{i\alpha j\beta}^{-1}(\omega) = \delta_{ij} \left(\delta_{\alpha\beta} \frac{B_{iz}^{\mathsf{eff}}}{M_i} + \frac{\mathrm{i}\,\omega}{\gamma M_i} \epsilon_{\alpha\beta\mu} \right) + \frac{1}{M_i M_j} (\mathcal{R}_i J_{ij} \mathcal{R}_j^{\mathsf{T}})_{\alpha\beta} + \mathrm{i}\,\omega (\mathcal{R}_i \mathcal{G}_{ij} \mathcal{R}_j^{\mathsf{T}})_{\alpha\beta} \quad , \tag{5.13}$$

with $\alpha, \beta = \{x, y\}$ corresponding to the local frames of sites i and j, respectively. The effective field $B_{iz}^{\mathsf{eff}} = B_{iz}^{\mathsf{ext}} + B_{iz}^{\mathsf{int}}$ is responsible for the stabilization of the magnetic structure and therefore points in the direction of the local magnetic moment of site i. It is possible to use a more generalized spin model including higher order interactions, as discussed in Chapter 4, yielding additional terms in eq. (5.13). However, since the interest of this Chapter is not in the interaction, but in the general form of the Gilbert damping tensor, $\mathcal{G}_{ij}$, we will not discuss this in more detail.

Thus, from eq. (5.13) follows that the Gilbert damping is related to the linear in frequency imaginary part of the inverse susceptibility,

$$\frac{\mathrm{d}}{\mathrm{d}\omega} \mathrm{Im}\, \chi_{i\alpha j\beta}^{-1}(\omega = 0) = \delta_{ij} \left(\frac{1}{\gamma M_i} \epsilon_{\alpha\beta\mu} \right) + (\mathcal{R}_i \mathcal{G}_{ij} \mathcal{R}_j^{\mathsf{T}})_{\alpha\beta} \quad . \tag{5.14}$$

The renormalized susceptibility χ_{ij} of the interacting electron system can be mapped to the form given by the susceptiblity of the spin model. The former one is related to the Kohn-Sham susceptibility, i.e. the susceptibility of the non-interacting electrons, via a Dyson equation, eq. (2.115). Depending on the structure of the kernel $\mathcal{K}$ the imaginary part of the renormalized susceptibility is equivalent to the same quantity of the Kohn-Sham susceptibility simplifying the computational costs [181].

Properties of the Gilbert damping tensor

The Gilbert damping tensor in general depends on the magnetic moments of the full system, $\mathcal{G}_{ij} = \mathcal{G}_{ij}(\{\boldsymbol{m}\})$, as explained for example in Ref. [176]. It is convenient to split the tensor into a part, which is even under magnetization reversal, $\mathcal{S}_{ij}(\{\boldsymbol{m}\}) = \mathcal{S}_{ij}(-\{\boldsymbol{m}\})$, and a part which is odd under magnetization reversal, $\mathcal{A}_{ij}(\{\boldsymbol{m}\}) = -\mathcal{A}_{ij}(-\{\boldsymbol{m}\})$, with

$$\mathcal{G}_{ij}(\{\boldsymbol{m}\}) = \mathcal{S}_{ij}(\{\boldsymbol{m}\}) + \mathcal{A}_{ij}(\{\boldsymbol{m}\}) \quad . \tag{5.15}$$

Using the Onsager reciprocity relations,

$$\chi_{AB}(\omega, \boldsymbol{B}, \{\boldsymbol{m}\}) = \chi_{BA}(\omega, -\boldsymbol{B}, -\{\boldsymbol{m}\}) \quad , \tag{5.16}$$

and the relation between the susceptibility and the Gilbert damping tensor, eq. (5.14), it follows,

$$\begin{aligned} & \mathcal{G}_{ij}(\{\boldsymbol{m}\}) = \mathcal{G}^{\mathsf{T}}_{ji}(-\{\boldsymbol{m}\}) \\ \Rightarrow \quad & \mathcal{G}_{ij}(-\{\boldsymbol{m}\}) = \mathcal{S}_{ij}(\{\boldsymbol{m}\}) - \mathcal{A}_{ij}(\{\boldsymbol{m}\}) = \mathcal{G}^{\mathsf{T}}_{ji}(\{\boldsymbol{m}\}) = \mathcal{S}^{\mathsf{T}}_{ji}(\{\boldsymbol{m}\}) + \mathcal{A}^{\mathsf{T}}_{ji}(\{\boldsymbol{m}\}) \quad . \end{aligned} \tag{5.17}$$

Thus, $\mathcal{S}_{ij} = \mathcal{S}^{\mathsf{T}}_{ji}$ is symmetric and $\mathcal{A}_{ij} = -\mathcal{A}^{\mathsf{T}}_{ji}$ is anti-symmetric upon changin the site indices i and j, from which follows that the on-site Gilbert damping tensor ($i = j$) can be split into a symmetric matrix being even in the magnetic moments and an anti-symmetric matrix being odd in the magnetic moments. The isotropic on-site part of the symmetric matrix, $\mathcal{S}_{ii}$, is equivalent to the Gilbert damping parameter introduced in Section 5.1. The on-site anti-symmetric contribution can be interpreted by using the LLG equation in first order,

$$\frac{\mathrm{d}\boldsymbol{m}_i}{\mathrm{d}t} \approx -\gamma \boldsymbol{m}_i \times \left(\boldsymbol{B}^{\mathsf{eff}}_i - \gamma \mathcal{A}_{ii}\left(\boldsymbol{m}_i \times \boldsymbol{B}^{\mathsf{eff}}_i\right)\right) \quad . \tag{5.18}$$

Writing the anti-symmetric on-site part as $\mathcal{A}^{\alpha\beta}_{ii} = \epsilon^{\alpha\beta\gamma} A^{\gamma}_i$ the second term of the LLG simplifies to,

$$\begin{aligned} \left[\mathcal{A}_{ii}\left(\boldsymbol{m}_i \times \boldsymbol{B}^{\mathsf{eff}}_i\right)\right]^{\alpha} = & \epsilon^{\alpha\beta\gamma} A^{\gamma}_i \left(\boldsymbol{m}_i \times \boldsymbol{B}^{\mathsf{eff}}_i\right)^{\beta} \\ = & (\boldsymbol{A}_i \cdot \boldsymbol{m}_i) B^{\alpha,\mathsf{eff}}_i - (\boldsymbol{A}_{\mathsf{i}} \cdot \boldsymbol{B}^{\mathsf{eff}}_i) m^{\alpha}_i \quad , \end{aligned} \tag{5.19}$$

which is either parallel to $\boldsymbol{B}^{\mathsf{eff}}_i$ or parallel to $\boldsymbol{m}_i$ resulting in a renormalization of γ or in no effect, respectively. Thus, we attributed the anti-symmetric on-site part of the Gilbert damping tensor to the renormalization of the gyromagnetic ratio, and therefore a renormalization of the precession rate.

The general form of the symmetric and anti-symmetric tensors is given by,

$$\mathcal{S}^{\alpha\beta}_{ij}(\{\boldsymbol{m}\}) = \mathcal{S}^{(0),\alpha\beta}_{ij} + \mathcal{S}^{(2),\alpha\beta\gamma\delta}_{ijkl} m^{\gamma}_k m^{\delta}_l + \dots \tag{5.20}$$

$$\mathcal{A}_{ij}^{\alpha\beta}(\{\boldsymbol{m}\}) = \mathcal{A}_{ijk}^{(1),\alpha\beta\gamma} m_k^\gamma + \mathcal{A}_{ijklm}^{(3),\alpha\beta\gamma\delta\eta} m_k^\gamma m_l^\delta m_m^\eta + \dots \quad , \tag{5.21}$$

which shows the possible complex dependencies of the Gilbert damping tensor on the magnetic texture. To further investigate the physically allowed dependencies, we use a perturbative expansion of an Anderson model inspired by the derivation of higher-order exchange interactions in Chapter 4, which is done in the next Section.

5.3. Anderson model

Our starting point is a single orbital Anderson model [182],

$$\mathcal{H} = \sum_{ij} \left[\delta_{ij}\left(E_d - \mathrm{i}\Gamma - U_i \boldsymbol{m}_i \cdot \boldsymbol{\sigma} - \boldsymbol{B}_i \cdot \boldsymbol{\sigma}\right) - \left(1 - \delta_{ij}\right) t_{ij}\right] \quad , \tag{5.22}$$

where i and j sum over all n sites, E_d is the energy of the localized orbitals, Γ is the hybridization with the electron bath in the wide band limit, U_i is the local exchange interaction responsible for the formation of a magnetic moment, $\boldsymbol{m}_i$ is the magnetic moment of site i, $\boldsymbol{B}_i$ is an constraining or external magnetic field, σ are the Pauli matrices, and t_{ij} is the hopping parameter between site i and j, which can be in general spin-dependent. Spin-orbit coupling mediated by the electron bath can be added as spin-dependent hopping using a Rashba-like spin-momentum locking $t_{ij} = t\cos\varphi_\mathrm{R}\,\sigma_0 - \mathrm{i}t\sin\varphi_\mathrm{R}\,\boldsymbol{n}_{ij}\cdot\boldsymbol{\sigma}$, where the spin-dependent hopping is characterized by its strength defined by φ_R and its direction $\boldsymbol{n}_{ij} = -\boldsymbol{n}_{ji}$, similar to the Ref. [183]. The eigenenergies and eigenstates of this non-hermitian hamiltonian are given by,

$$\mathcal{H}|n\rangle = (E_n - \mathrm{i}\Gamma)|n\rangle \quad , \tag{5.23}$$

from which the single particle Green function can be constructed according to eq. (2.8). The magnitude of the magnetic moment is determined self-consistently using

$$\boldsymbol{m}_i = -\frac{1}{\pi}\,\mathrm{Im}\,\mathrm{Tr}\int^{E_\mathrm{F}} \mathrm{d}E\,\boldsymbol{\sigma}\,G_{ii}(E) \quad , \tag{5.24}$$

where $G_{ii}(E)$ is the local Green function of site i depending on the magnetic moment. Using the magnetic torque exerted on the moment of site i (see Section 2.2.4),

$$\frac{\mathrm{d}\mathcal{H}}{\mathrm{d}\hat{e}_i} = -\boldsymbol{m}_i B_i^\mathrm{eff} \quad , \tag{5.25}$$

magnetic constraining fields can be defined ensuring the stability of an arbitrary non-collinear configuration,

$$\boldsymbol{B}_i^{\mathrm{constr},\perp} = -\mathcal{P}_\perp^{\boldsymbol{m}_i}\frac{\boldsymbol{m}_i}{|\boldsymbol{m}_i|}B_i^\mathrm{eff} \quad , \tag{5.26}$$

where $\mathcal{P}_\perp^{\boldsymbol{m}_i}$ is the projection on the plane perpendicular to the moment $\boldsymbol{m}$. In the same way a longitudinal constraining field, $\boldsymbol{B}_i^{\mathrm{constr},\|}$, can be used to stabilize an arbitrary magnetic moment $0 < |m_i| < 1$. The constraining fields are added to the hamiltonian, eq. (5.22), and determined self-consistently.

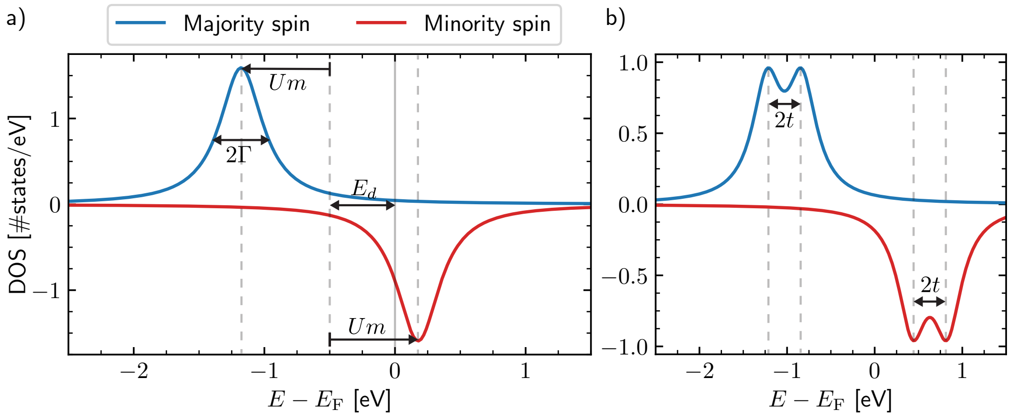

Figure 5.3.: Spin-resolved density of states of the Anderson model. The minority spin is negative for the sake of illustration. a) Single-site Anderson model with $U = 1.0\,\mathrm{eV}$, $E_d = -0.5\,\mathrm{eV}$, $\Gamma = 0.2\,\mathrm{eV}$, and a self-consistent magnetic moment of $m = 0.68$. b) Two-site Anderson model with $U = 1.0\,\mathrm{eV}$, $E_d = -0.2\,\mathrm{eV}$, $\Gamma = 0.2\,\mathrm{eV}$, $t = 0.2\,\mathrm{eV}$, and a self-consistent magnetic moment of $m = 0.83$. The two sites are assumed to be ferromagnetically aligned.

The main ingredients of the Anderson model affect the electronic structure in different ways, which can be best seen in the local density of states. Since an understanding of the different ingredients is crucial for the remaining chapter, we start by explaining the different quantities. The spin-resolved density of states of a single-site Anderson model is shown in Fig. 5.3a. The energy of the localized states, E_d, yields a shift of both spin channels with respect to the Fermi energy. The spins are split by $\pm Um$ from this reference energy, resulting in a total spin splitting of $2Um$. Each localized state is broadened by Γ. The broadening takes effectively the hybridization with an electron bath into account, which is similar to the hybridization of a real nanostructure with its supporting surface in an effective model.

Fig. 5.3b shows the density of states for a two-site Anderson model including a hopping t between the sites. The hopping leads to the formation of molecular-like bonding and antibonding states (two per spin channel) with an additional splitting of $2t$ within the minority and the majority state, respectively. Adding multiple sites to the Anderson model affects the formation of the molecular states and a more complex splitting can emerge. For example in a three-site Anderson model with all the sites interacting with each other, similar to a compact trimer, the three molecular states are split into two energies, one being two-fold degenerate and one being non-degenerate.

5.3.1. The magnetic susceptibility

The magnetic susceptibility can be defined starting from the Kubo formula and the general description of a correlation function, eq. (2.99), which gives rise to the single particle excitations.

Writing the Green functions explicitly in terms of the eigenbasis of the Hamiltonian, eq. (2.8), which for this model is non-hermitian, eq. (5.23), the following form of a correlation function can be obtained,

$$\begin{aligned}\chi_{AB}(\omega+\mathrm{i}0^+) = &\sum_{n,m} A_{mn}B_{nm}\,\frac{f_m(0,\Gamma)-f_n(0,\Gamma)}{E_{mn}+\omega+\mathrm{i}0^+}\\ &-\sum_{n,m}\frac{\Gamma\,A_{mn}B_{nm}}{2\Gamma-\mathrm{i}\,(E_{mn}+\omega)}\,\frac{f_n(\omega,\Gamma)+f_m(0,\Gamma)-f_m(-\omega,\Gamma)-f_n(0,\Gamma)}{E_{mn}+\omega+\mathrm{i}0^+}\\ &-\mathrm{i}\sum_{n,m}\frac{\Gamma\,A_{mn}B_{nm}}{2\Gamma-\mathrm{i}\,(E_{mn}+\omega)}\,\frac{g_n(\omega,\Gamma)-g_m(0,\Gamma)+g_m(-\omega,\Gamma)-g_n(0,\Gamma)}{E_{mn}+\omega+\mathrm{i}0^+} \quad .\end{aligned} \tag{5.27}$$

where we used partial fraction decomposition, the abbreviations $A_{nm} = \langle n|A|m\rangle$ and $E_{mn} = E_m - E_n$, and

$$f_n(x,y) = \mathrm{sgn}(y)\frac{1}{2} + \frac{1}{\pi}\arctan\left(\frac{x-E_n}{y}\right) \tag{5.28}$$

$$g_n(x,y) = \frac{1}{2\pi}\log\left(y^2+(x-E_n)^2\right) \quad . \tag{5.29}$$

In case of the magnetic susceptibility the matrices A and B are Pauli matrices with additional site projections. The important ingredients of the susceptibility are the matrix elements $A_{mn}B_{nm}$, which determine the strength of the susceptibility, but also if a certain element is finite or not, and the energy differences E_{mn}, which determine the poles of the susceptibility. To gain insights in the spectrum of the magnetic susceptibility of the Anderson model, we discuss in the following different test cases ranging from a single atom to a non-collinear dimer.

Single atom

With the magnetic moment along the z-direction, the single-site Anderson model has the simple hamiltonian,

$$\mathcal{H}_0 = \begin{pmatrix} E_d - Um - B & 0 \\ 0 & E_d + Um + B \end{pmatrix} \quad , \tag{5.30}$$

where the columns are $\{|\uparrow\rangle, |\downarrow\rangle\}$ indicating the spin channel.

Since the hamiltonian is diagonal the eigenenbasis is fully defined. The energy differences are given by

$$\begin{array}{cc|cc} & & \multicolumn{2}{c}{|n\rangle} \\ & E_{mn} & |\uparrow\rangle & |\downarrow\rangle \\ \hline |m\rangle & |\uparrow\rangle & 0 & -2Um-2B \\ & |\downarrow\rangle & 2Um+2B & 0 \end{array} \quad , \tag{5.31}$$

while the matrix elements are defined as,

$$\langle m|\sigma_\alpha|n\rangle\langle n|\sigma_\beta|m\rangle = \begin{cases} \langle m|\sigma_\alpha|n\rangle\langle n|\sigma_\beta|m\rangle & , \text{ if } \; m \neq n \; \text{ and } \; \alpha,\beta \in \{x,y\} \\ \langle m|\sigma_\alpha|n\rangle\langle n|\sigma_\beta|m\rangle & , \text{ if } \; m = n \; \text{ and } \; \alpha,\beta \in \{z,0\} \\ 0 & , \text{ else} \end{cases} \quad . \tag{5.32}$$

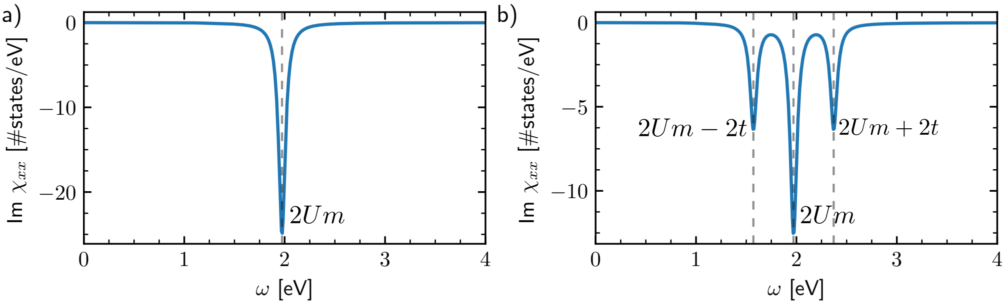

Figure 5.4.: Magnetic susceptibility in the Anderson model. Shown is the on-site xx-component. a) Single-site Anderson model with $U = 1.0$ eV, $E_d = -0.2$ eV, $\Gamma = 0.02$ eV, and a self-consistent magnetic moment of $m = 0.99$. b) Two-site Anderson model with $U = 1.0$ eV, $E_d = -0.2$ eV, $\Gamma = 0.02$ eV, $t = 0.2$ eV and a self-consistent magnetic moment of $m = 0.99$.

It immediately follows that longitudinal excitations have a zero energy peak meaning that even static perturbations can influence the filling and the magnetic moment of the system. Transversal perturbations, however, have a high excitation energy of $\pm(2Um + 2B)$ corresponding to a spin flip.

Fig. 5.4a shows a numerical result for the xx-component of the magnetic susceptibility with a clear peak at $2Um$ in the imaginary part.

Ferromagnetic dimer

For a ferromagnetic configuration the hamiltonian of the Anderson model is block-diagonal in spin space ($\mathbf{m}_1 = \mathbf{m}_2 = m\,\boldsymbol{e}_z$):

$$\mathcal{H}_0 = \begin{pmatrix} E_d - Um - B & -t & 0 & 0 \\ -t & E_d - Um - B & 0 & 0 \\ 0 & 0 & E_d + Um + B & -t \\ 0 & 0 & -t & E_d + Um + B \end{pmatrix} \quad , \tag{5.33}$$

where columns are $|1{\uparrow}\rangle$, $|2{\uparrow}\rangle$, $|1{\downarrow}\rangle$, $|2{\downarrow}\rangle$ with the first index being the site index and the second index indicating the direction of the spin. The two blocks can be diagonalized using Pauli matrices for site space,

$$\mathcal{H}_0^{\uparrow} = E_d - Um - B - t\,\tau_x \quad \Longrightarrow \quad E_s^{\uparrow} = E_d - Um - B - s\,t \quad , \qquad |s{\uparrow}\rangle\langle s{\uparrow}| = \frac{1 + s\,\tau_x}{2} \quad , \tag{5.34}$$

$$\mathcal{H}_0^{\downarrow} = E_d + Um + B - t\,\tau_x \quad \Longrightarrow \quad E_s^{\downarrow} = E_d + Um + B - s\,t \quad , \qquad |s{\downarrow}\rangle\langle s{\downarrow}| = \frac{1 + s\,\tau_x}{2} \quad . \tag{5.35}$$

with $s = \pm 1$, which are the eigenvalues of the Pauli matrices. The site projectors are

$$\tau_i = \frac{1 + u_i\,\tau_z}{2} \quad , \tag{5.36}$$

with $u_i = +$ for $i = 1$ and $u_i = -$ for $i = 2$.
Consider for definiteness $\chi_{i\alpha,j\alpha}(\omega + \mathrm{i}\eta)$. Then $A = \tau_i\sigma_\alpha$ and $B = \tau_j\sigma_\alpha$ and the matrix elements are

$$\begin{aligned} \langle m|\tau_i\sigma_\alpha|n\rangle\langle n|\tau_j\sigma_\alpha|m\rangle &= \left\{ \begin{array}{ll} \left.\begin{array}{l} \mathrm{Tr}\,|s_m\!\uparrow\rangle\langle s_m\!\uparrow|\tau_i|s_n\!\downarrow\rangle\langle s_n\!\downarrow|\tau_j \\ \mathrm{Tr}\,|s_m\!\downarrow\rangle\langle s_m\!\downarrow|\tau_i|s_n\!\uparrow\rangle\langle s_n\!\uparrow|\tau_j \end{array}\right\} , & \text{for } \alpha \in \{x, y\} \\ \left.\begin{array}{l} \mathrm{Tr}\,|s_m\!\uparrow\rangle\langle s_m\!\uparrow|\tau_i|s_n\!\uparrow\rangle\langle s_n\!\uparrow|\tau_j \\ \mathrm{Tr}\,|s_m\!\downarrow\rangle\langle s_m\!\downarrow|\tau_i|s_n\!\downarrow\rangle\langle s_n\!\downarrow|\tau_j \end{array}\right\} , & \text{for } \alpha \in \{z, 0\} \end{array} \right. \\ &= \frac{1 + u_i u_j + s_m s_n - u_i u_j s_m s_n}{8} \quad . \end{aligned} \tag{5.37}$$

Similarly, the general form with $A = \tau_i\sigma_\alpha$ and $B = \tau_j\sigma_\beta$ can be derived.
The spin character of one of the eigenstates fixes the spin character of the other one. There are only two possibilities,

$$s_m s_n = +1 : \quad \frac{1 + u_i u_j + s_m s_n - u_i u_j s_m s_n}{8} = \frac{1}{4} \quad , \tag{5.38}$$

$$s_m s_n = -1 : \quad \frac{1 + u_i u_j + s_m s_n - u_i u_j s_m s_n}{8} = \frac{u_i u_j}{4} \quad . \tag{5.39}$$

The eigenvalue differences are

$$\begin{array}{cc|cccc} & & & |n\rangle & & \\ & E_{mn} & |+\uparrow\rangle & |-\uparrow\rangle & |+\downarrow\rangle & |-\downarrow\rangle \\ \hline & |+\uparrow\rangle & 0 & -2t & -2Um - 2B & -2Um - 2B - 2t \\ |m\rangle & |-\uparrow\rangle & 2t & 0 & -2Um - 2B + 2t & -2Um - 2B \\ & |+\downarrow\rangle & 2Um + 2B & 2Um + 2B - 2t & 0 & -2t \\ & |-\downarrow\rangle & 2Um + 2B + 2t & 2Um + 2B & 2t & 0 \end{array} \quad . \tag{5.40}$$

For $\omega > 0$, the excitation energies are given by the upper triangle of the table ($\omega = -E_{mn}$).

Using eq. (5.27) and the matrix elements given in eq. (5.37), one finds for $\alpha \in \{x, y\}$ the following matrix elements,

$$\begin{array}{cc|cccc} & & & |n\rangle & & \\ & A_{mn}B_{nm} & |+\uparrow\rangle & |-\uparrow\rangle & |+\downarrow\rangle & |-\downarrow\rangle \\ \hline & |+\uparrow\rangle & 0 & 0 & \frac{1}{4} & \frac{u_i u_j}{4} \\ |m\rangle & |-\uparrow\rangle & 0 & 0 & \frac{u_i u_j}{4} & \frac{1}{4} \\ & |+\downarrow\rangle & \frac{1}{4} & \frac{u_i u_j}{4} & 0 & 0 \\ & |-\downarrow\rangle & \frac{u_i u_j}{4} & \frac{1}{4} & 0 & 0 \end{array} \quad . \tag{5.41}$$

For $\alpha \in \{z, 0\}$ one finds the following matrix elements,

$$\begin{array}{cc|cccc} & & & |n\rangle & & \\ & A_{mn}B_{nm} & |{+}\!\uparrow\rangle & |{-}\!\uparrow\rangle & |{+}\!\downarrow\rangle & |{-}\!\downarrow\rangle \\ \hline & |{+}\!\uparrow\rangle & \frac{1}{4} & \frac{u_iu_j}{4} & 0 & 0 \\ & |{-}\!\uparrow\rangle & \frac{u_iu_j}{4} & \frac{1}{4} & 0 & 0 \\ |m\rangle & |{+}\!\downarrow\rangle & 0 & 0 & \frac{1}{4} & \frac{u_iu_j}{4} \\ & |{-}\!\downarrow\rangle & 0 & 0 & \frac{u_iu_j}{4} & \frac{1}{4} \end{array} \quad . \tag{5.42}$$

Combining the energy differences, eq. (5.40), and the previous matrix elements, it can be seen that the transversal susceptibility should show three different peaks, while the longitudinal susceptibility should show only one peak for $\omega > 0$. The different excitations can be easily explained using the density of states of the ferromagnetic dimer shown in Fig. 5.3b. Since we do not include spin-orbit coupling in this simple example, a longitudinal perturbation does not couple the two different spin channels. Therefore, the longitudinal perturbation can only excite the spectrum within each spin channel resulting in the excitation energy $2t$. The transversal perturbation, however, can induce a spin flip, which results in the three different excitation energies, which mainly depend on the local spin splitting Um.

To illustrate the discussed behaviour, Fig. 5.4b shows a numerical result for the xx-component of the imaginary part of the on-site magnetic susceptibility with three peaks at $2Um$ and $2Um \pm 2t$.

Renormalized magnetic susceptibility

Similarly to the renormalization scheme in TD-DFT discussed in Section 2.3, the susceptibility in the Anderson model is renormalized due to the indirect impact of a magnetic perturbation on the Anderson hamiltonian. The magnetic kernel, which takes care of the renormalization in a Dyson-like equation, see eq. (2.110), is given in the Anderson model by,

$$\mathcal{K}^m = \frac{\delta \mathcal{H}}{\delta \boldsymbol{m}} = -U \quad , \tag{5.43}$$

giving rise to the renormalized susceptibility,

$$\chi = (1 - \mathcal{K}\chi^0)^{-1}\chi^0 \quad . \tag{5.44}$$

The renormalized susceptibility shows excitations at lower energies, corresponding to realistic excitations of the system of interacting particles in addition to the previously discussed single-particle excitations. Neglecting spin-orbit coupling, the transverse susceptibility of a single atom shows a zero frequency divergence, indicating a Goldstone mode. All directions are equivalent and the magnetic moment of the atom can be rotated (which can be seen as an excitation from its original orientation) without energetic efforts [184]. For a coupled dimer in total two modes emerge, the zero frequency acoustical mode corresponding to an in-phase precessional motion of both local magnetic moments, and an optical mode at $\omega \approx 2\,\frac{t^2}{U}$ corresponding to an anti-phase motion of the local magnetic moments with a phase difference of $180\,°$. Note that t^2/U is the well-known result for the magnetic exchange interaction in this kind of models.

5.3.2. Perturbative expansion of the Anderson model

Starting from the Anderson model hamiltonian, eq. (5.22), we can split the hamiltonian into an on-site part, $\mathcal{H}_0$, and an inter-site part, $\mathcal{H}_t$, corresponding to the hopping,

$$\mathcal{H} = \mathcal{H}^0 + \mathcal{H}^t \quad . \tag{5.45}$$

In the following, we treat the inter-site hamiltonian as a perturbation meaning that the on-site part, which is mainly driven by the spin splitting Um, is larger than the hopping resulting in $Um/t \gg 1$. Using the Dyson equation, eq. (2.12), the Green function can be systematically expanded in the hopping,

$$G_{ij} = G_i^0 \delta_{ij} + G_i^0 \, \mathcal{H}_{ij}^t \, G_j^0 + G_i^0 \, \mathcal{H}_{ik}^t \, G_k^0 \, \mathcal{H}_{kj}^t \, G_j^0 + \mathcal{O}(t^3) \quad , \tag{5.46}$$

where G_i^0 is the local on-site Green function of site i. Since we do not add spin-orbit coupling to the on-site hamiltonian, the on-site Green function takes the form,

$$G_i^0 = A_i \sigma_0 + B_i \, \boldsymbol{m}_i \cdot \boldsymbol{\sigma} \quad , \tag{5.47}$$

where A_i corresponds to the spin-independent part and B_i is a spin dependent part in the direction of the magnetic moment of site i. Spin-orbit coupling can be added to the hopping using the Rashba-like spin-momentum locking as described in the beginning of Section 5.3. We treat spin-orbit coupling as an additional perturbation of the form $\mathcal{H}_{ij}^{\text{soc}} = i\lambda_{ij} \boldsymbol{n}_{ij} \cdot \boldsymbol{\sigma}$, where λ_{ij} is the spin-orbit coupling strength and $\boldsymbol{n}_{ij}$ is the direction attributed to the spin-orbit coupling.

Since our interest is in the form of the Gilbert damping, and therefore also in the form of the magnetic susceptibility, the perturbative expansion can be applied to the magnetic susceptibility. The general form of the magnetic susceptibility in terms of the Green function, eq. (2.107), depends on a combination of two Green functions with different energy arguments, which are labeled as ω and 0 in the following. The relevant structure is then identified as,

$$\chi_{i\alpha j\beta}(\omega) \sim \mathrm{Tr}\, \sigma_i^\alpha G_{ij}(\omega) \sigma_j^\beta G_{ji}(0) \quad . \tag{5.48}$$

Note that even though the latter equation relates to the susceptibility of non-interacting particles, the dependencies on the magnetic moment should not be affected by the renormalization procedure since the kernel does not depend on the non-collinearity. Similarly to the derivation of higher-order interactions in Chapter 4, the sake of the perturbative expansion is to gather insights in the possible forms and dependencies on the magnetic moments of the Gilbert damping, and not to calculate explicitly the strength of the Gilbert damping from this expansion. Therefore, we focus on the structure of eq. (5.48), even though the susceptibility has more ingredients, which are of a similar form.

Instead of writing all the perturbations explicitly, we set up a diagrammatic approach, which has the following ingredients and rules:

1. Each diagram contains the operators A and B, which are σ^α and σ^β for the magnetic susceptibility. The operators are represented by a white circle with the site and spin index: ○ $i\alpha$
2. Hoppings are represented by grey circles indicating the hopping from site i to j: ● ij . The vertex corresponds to $\mathcal{H}_{ij}^t = t_{ij}$

3. Spin-orbit coupling is described as a spin-dependent hopping from site i to j and represented by: ● ij,α . The vertex corresponds to $\mathcal{H}^{\text{soc}}_{ij} = i\lambda_{ij}\hat{n}^{\alpha}_{ij}\sigma^{\alpha}$
4. The bare spin-independent (on-site) Green functions are represented by directional lines with an energy attributed to it: $\xrightarrow{\omega}$. The Green function connects operators and hoppings. The line corresponds to $A_i(\omega)$.
5. The spin-dependent part of the bare Green function is represented by: $\overset{\omega,\alpha}{\dashrightarrow}$. α indicates the spin direction. The direction ensures the right order within the trace (due to the Pauli matrices, the different objects in the diagram do not commute). The line corresponds to $B_i(\omega)m_i^{\alpha}\sigma^{\alpha}$.

Note that the diagrammatic rules might be counter-intiutive, since local quantities (the Green function) are represented by lines, while non-local quantities (the hopping from i to j) are represented by vertices. However, these diagrammatic rules allow a much simplified description and identification of all the possible forms of the Gilbert damping, without having to write lengthy perturbative expansions.

To get a feeling for the diagrammatic approach, we start with the simplest example: the on-site susceptibility without any hoppings to a different site, which describes both the single atom and the lowest order term for interacting atoms. The possible forms are,

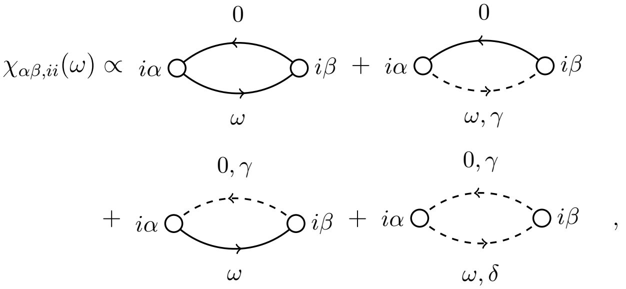

(5.49)

which evaluate to,

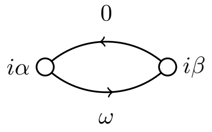

$$= \mathrm{Tr}\,\sigma^{\alpha}\sigma^{\beta}A_i(\omega)A_i(0) = \delta_{\alpha\beta}A_i(\omega)A_i(0) \tag{5.50}$$

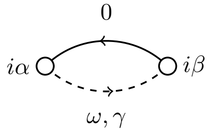

$$= \mathrm{Tr}\,\sigma^{\alpha}\sigma^{\gamma}\sigma^{\beta}B_i(\omega)A_i(0)m_i^{\gamma} = \mathrm{i}\epsilon_{\alpha\gamma\beta}B_i(\omega)A_i(0)m_i^{\gamma} \tag{5.51}$$

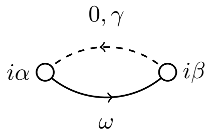

$$= \mathrm{Tr}\,\sigma^{\alpha}\sigma^{\beta}\sigma^{\gamma}A_i(\omega)B_i(0)m_i^{\gamma} = \mathrm{i}\epsilon_{\alpha\beta\gamma}A_i(\omega)B_i(0)m_i^{\gamma} \tag{5.52}$$

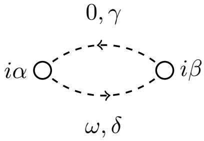

$$= \mathrm{Tr}\,\sigma^{\alpha}\sigma^{\delta}\sigma^{\beta}\sigma^{\gamma}B_i(\omega)B_i(0)m_i^{\delta}m_i^{\gamma}$$

$$= \left(\delta_{\alpha\delta}\delta_{\beta\gamma}+\delta_{\alpha\gamma}\delta_{\beta\delta}-\delta_{\alpha\beta}\delta_{\gamma\delta}\right)B_i(\omega)B_i(0)m_i^{\delta}m_i^{\gamma} \quad . \tag{5.53}$$

The first diagram yields an isotropic contributions, the second and third diagrams yield an antisymmetric contribution, which is linear in the magnetic moment, and the last diagram yields a symmetric contribution being quadratic in the magnetic moment. Note that the energy dependence of the Green functions is crucial, since otherwise the sum of eqs. (5.51) and (5.52) vanishes. In particular this means that the static susceptibility has no dependence linear in the magnetic moment, while the the slope of the susceptibility can have a dependence linear in the magnetic moment. The static part of the susceptibility maps to the magnetic exchange interactions, which are known to be even in the magnetic moment due to time reversal symmetry (see Chapter 4).

Combining all the functional forms of the diagrams, we find the following possible dependencies of the on-site Gilbert damping on the magnetic moments,

$$\mathcal{G}_{ii}^{\alpha\beta}(\{\boldsymbol{m}\}) \propto \{\delta_{\alpha\beta}, \epsilon_{\alpha\beta\gamma}m_i^{\gamma}, m_i^{\alpha}m_i^{\beta}\} \quad . \tag{5.54}$$

Since we work in the local frames, $\boldsymbol{m}_i = (0,0,m_i^z)$, the last dependence is a purely longitudinal term, which is not relevant for the transversal dynamics discussed in this work.

If we still focus on the on-site term, but allow for two hoppings to another atom and back, we find the following new diagrams,

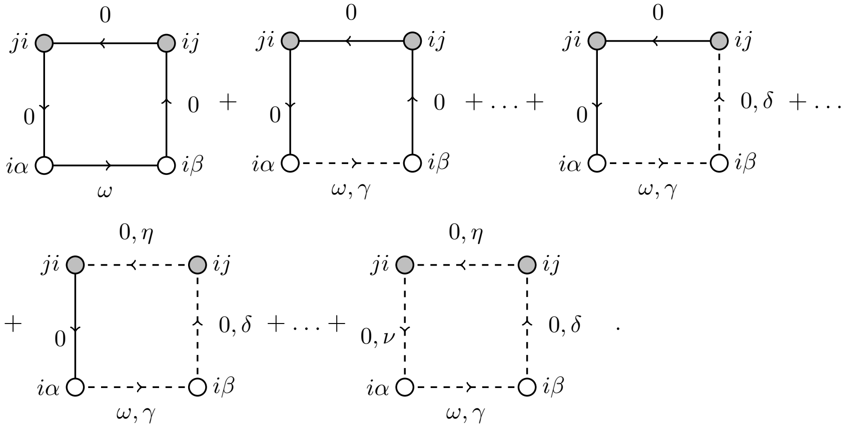

(5.55)

The dashed line in the second diagram can be inserted in any of the four sides of the square, with the other possibilities omitted. Likewise for the diagrams with two or three dashed lines, the different possible assignments have to be considered. The additional hopping to the site j yields a dependence of the on-site magnetic susceptibility and therefore also the on-site Gilbert damping tensor on the magnetic moment of site j. In total, the following new dependencies are found,

$$\mathcal{G}_{ii}^{\alpha\beta}(\{\boldsymbol{m}\}) \propto \{\epsilon_{\alpha\beta\gamma}m_j^{\gamma}, \delta_{\alpha\beta}\left(\boldsymbol{m}_i\cdot\boldsymbol{m}_j\right), \epsilon_{\alpha\beta\gamma}m_i^{\gamma}\left(\boldsymbol{m}_i\cdot\boldsymbol{m}_j\right), m_i^{\alpha}m_j^{\beta}+m_i^{\beta}m_j^{\alpha}\} \quad . \tag{5.56}$$

The first term describes the dependence of the anti-symmetric Gilbert damping on the moment of site j. Using eq. (5.19) it can be thought of as an correction to the gyromagnetic ratio depending on the angle between $\boldsymbol{m}_i$ and $\boldsymbol{m}_j$. Similarly, the second term describes an effective damping, which is isotropic and depends on the angle between $\boldsymbol{m}_i$ and $\boldsymbol{m}_j$. The third term is in terms of its interpretation using eq. (5.19) equivalent to the first one. The last term contributes to the longitudinal part of the Gilbert damping, which is negleted. In total, we can identify the following structure of the on-site Gilbert damping,

$$\begin{aligned}\mathcal{G}_{ii} = \sum_j \Big[& \Big(\mathcal{S}_i\delta_{ij} + \mathcal{S}_i^{ij,(1)}\,(\boldsymbol{e}_i\cdot\boldsymbol{e}_j) + \mathcal{S}_i^{ij,(2)}\,(\boldsymbol{e}_i\cdot\boldsymbol{e}_j)^2\Big)\begin{pmatrix}1 & 0 & 0\\ 0 & 1 & 0\\ 0 & 0 & 1\end{pmatrix} \\ & + \left(\mathcal{A}_i\delta_{ij} + \mathcal{A}_i^{ij}\,(\boldsymbol{e}_i\cdot\boldsymbol{e}_j)\right)\begin{pmatrix}0 & e_i^z & -e_i^y\\ -e_i^z & 0 & e_i^x\\ e_i^y & -e_i^x & 0\end{pmatrix}\Big] \quad ,\end{aligned} \tag{5.57}$$

where we used the unit directions of the magnetic moments to allow for a better comparability between the different quantities.

Adding spin-orbit coupling to the picture drastically complicates the possible dependencies. In the diagramms spin-orbit coupling is added by replacing one spin-independent hopping vertex by a spin-dependent one,

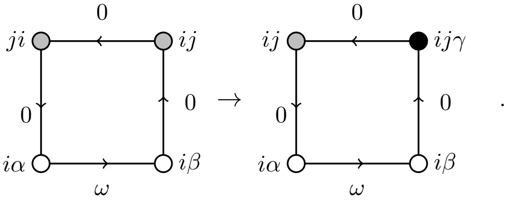

(5.58)

For the on-site Gilbert damping one finds in first-order spin-orbit coupling the following new dependencies,

$$\begin{aligned}\mathcal{G}_{ii}(\{\boldsymbol{m}\}) \propto \{&\epsilon_{\alpha\beta\gamma}\hat{n}_{ij}^{\gamma}, \hat{n}_{ij}^{\alpha}\hat{n}_{ji}^{\beta}, \hat{n}_{ij}^{\beta}m_i^{\alpha}, \hat{n}_{ij}^{\alpha}m_i^{\beta}, \delta_{\alpha\beta}(\hat{\boldsymbol{n}}_{ij}\cdot\boldsymbol{m}_i), \delta_{\alpha\beta}(\hat{\boldsymbol{n}}_{ij}\cdot\boldsymbol{m}_j),\\ &\hat{n}_{ij}^{\beta}m_j^{\alpha}, \hat{n}_{ij}^{\alpha}m_j^{\beta}, m_i^{\alpha}(\hat{\boldsymbol{n}}_{ij}\times\boldsymbol{m}_i)^{\beta}, m_i^{\beta}(\hat{\boldsymbol{n}}_{ij}\times\boldsymbol{m}_i)^{\alpha},\\ &\delta_{\alpha\beta}\hat{\boldsymbol{n}}_{ij}\cdot(\boldsymbol{m}_i\times\boldsymbol{m}_j), m_i^{\alpha}(\hat{\boldsymbol{n}}_{ij}\times\boldsymbol{m}_j)^{\beta}, m_i^{\beta}(\hat{\boldsymbol{n}}_{ij}\times\boldsymbol{m}_j)^{\alpha}, (\hat{\boldsymbol{n}}_{ij}\cdot\boldsymbol{m}_j)\epsilon_{\alpha\beta\gamma}m_i^{\gamma},\\ &m_i^{\alpha}m_i^{\beta}(\hat{\boldsymbol{n}}_{ij}\cdot\boldsymbol{m}_j), (m_i^{\alpha}m_j^{\beta} - m_i^{\beta}m_j^{\alpha})(\hat{\boldsymbol{n}}_{ij}\cdot\boldsymbol{m}_j), \hat{n}_{ij}^{\beta}m_i^{\alpha}(\boldsymbol{m}_i\cdot\boldsymbol{m}_j), \hat{n}_{ij}^{\alpha}m_i^{\beta}(\boldsymbol{m}_i\cdot\boldsymbol{m}_j)\} \quad .\end{aligned} \tag{5.59}$$

We identified using the Anderson model as test system (see next section) the following terms as the most relevant ones originating from spin-orbit coupling,

$$\begin{aligned}\mathcal{G}_{ii}^{\mathsf{soc}} = \sum_j \Big[& \mathcal{S}_i^{\mathsf{soc},ij}\;\boldsymbol{n}_{ij}\cdot(\boldsymbol{e}_i\times\boldsymbol{e}_j)\begin{pmatrix}1 & 0 & 0\\ 0 & 1 & 0\\ 0 & 0 & 1\end{pmatrix} + \mathcal{S}_i^{\mathsf{soc},ij,(2)}\;(\boldsymbol{n}_{ij}\cdot\boldsymbol{e}_i)(\boldsymbol{n}_{ij}\cdot\boldsymbol{e}_j)\begin{pmatrix}1 & 0 & 0\\ 0 & 1 & 0\\ 0 & 0 & 1\end{pmatrix} \\ & + \mathcal{A}_i^{\mathsf{soc},ij}\;\boldsymbol{n}_{ij}\cdot(\boldsymbol{e}_i\times\boldsymbol{e}_j)\begin{pmatrix}0 & e_i^z & -e_i^y\\ -e_i^z & 0 & e_i^x\\ e_i^y & -e_i^x & 0\end{pmatrix}\end{aligned}$$

$$+\,\mathcal{A}_i^{\mathsf{soc},ij,(2)}\,(\boldsymbol{n}_{ij}\cdot\boldsymbol{e}_j)\begin{pmatrix}0 & n_{ij}^z & -n_{ij}^y\\ -n_{ij}^z & 0 & n_{ij}^x\\ n_{ij}^y & -n_{ij}^x & 0\end{pmatrix}\Bigg]\quad . \tag{5.60}$$

Thus, similar to the magnetic Dzyaloshinskii-Moriya interaction, spin-orbit coupling gives rise to a dependence of the Gilbert damping on the vector chirality, $\boldsymbol{e}_i\times\boldsymbol{e}_j$. The term chiral damping used in literature refers to the dependence of the Gilbert damping on the chirality, but it was not shown so far how this dependence evolves from a microscopic model, and how it looks like in an atomistic model.

Another contribution to the Gilbert damping originates from the inter-site part, thus encoding the dependence of the moment site i on the dynamics of the moment of site j via $\mathcal{G}_{ij}$. This contribution is often neglected in literature, since for many systems it is believed to have no significant impact. Using the microscopic model, a different class of diagrams is responsible for the inter-site damping. In the lowest order in t/Um the diagrams contain already two hopping events,

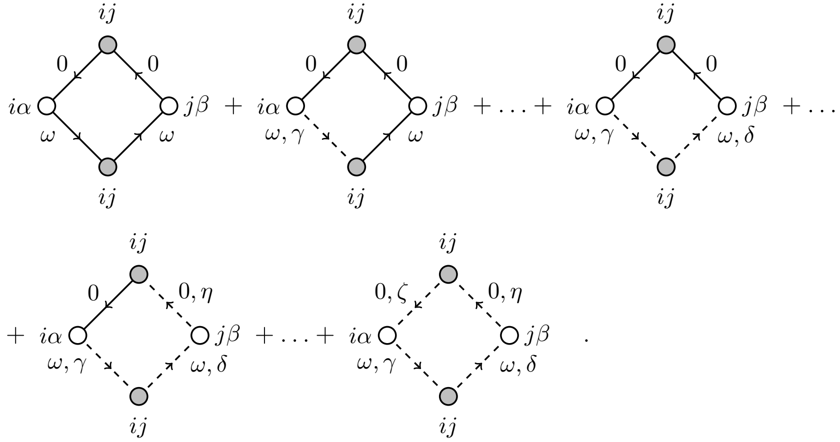

(5.61)

The evaluation of these diagrams yields similar dependencies as the second order diagrams shown in eqs. (5.56) and (5.59), but being symmetric in i and j. We use for the inter-site term without spin-orbit coupling the following form,

$$\begin{aligned}\mathcal{G}_{ij}^{\alpha\beta} &= \left(\mathcal{S}_{ij}+\mathcal{S}_{ij}^{\mathrm{dot}}\,(\boldsymbol{e}_i\cdot\boldsymbol{e}_j)\right)\begin{pmatrix}1&0&0\\0&1&0\\0&0&1\end{pmatrix}_{\alpha\beta}\\ &\quad+\left(\mathcal{A}_{ij}+\mathcal{A}_{ij}^{\mathrm{dot}}\,(\boldsymbol{e}_i\cdot\boldsymbol{e}_j)\right)\left[\begin{pmatrix}0&e_i^z&-e_i^y\\-e_i^z&0&e_i^x\\e_i^y&-e_i^x&0\end{pmatrix}_{\alpha\beta}+\begin{pmatrix}0&e_j^z&-e_j^y\\-e_j^z&0&e_j^x\\e_j^y&-e_j^x&0\end{pmatrix}_{\alpha\beta}\right]\\ &\quad+\mathcal{S}_{ij}^{\mathrm{cross}}\,(\boldsymbol{e}_i\times\boldsymbol{e}_j)^{\alpha}\,(\boldsymbol{e}_i\times\boldsymbol{e}_j)^{\beta}+\mathcal{S}_{ij}^{\mathrm{ba}}e_i^{\beta}e_j^{\alpha}\quad .\end{aligned} \tag{5.62}$$

There are two new terms, which were not considered for the on-site Gilbert damping. The first one, $\mathcal{S}_{ij}^{\mathrm{cross}}$, depends on the product of the α- and the β-component of the vector chirality, $(\boldsymbol{e}_i\times\boldsymbol{e}_j)$, which originates from the last diagram in eq. (5.61). Note that this diagram can not be cancelled by any other diagram using permutations or other symmetry operations, since it is unique. The second additional contribution is the last term in eq. (5.62), $\mathcal{S}_{ij}^{\mathrm{ba}}$, which depends on moment j in the local frame of atom i and moment i in the local frame of atom j. This contribution is a purely non-collinear contribution, since for collinear alignments it corresponds to the longitudinal part, which is not considered in this work.

Spin-orbit coupling can be added similar to eq. (5.58) by replacing one hopping by a spin-dependent hopping. From test calculations using the Anderson model, we identified the following terms as the most important ingredients to the inter-site damping originating from spin-orbit coupling,

$$\begin{aligned}\mathcal{G}_{ij}^{\mathsf{soc},\alpha\beta} =& \mathcal{S}_{ij}^{\mathsf{soc}}\, \boldsymbol{n}_{ij}\cdot(\boldsymbol{e}_i\times\boldsymbol{e}_j)\begin{pmatrix}1&0&0\\0&1&0\\0&0&1\end{pmatrix}_{\alpha\beta} + \mathcal{S}_{ij}^{\mathsf{soc},ba} n_{ij}^{\beta}(\boldsymbol{e}_i\times\boldsymbol{e}_j)^{\alpha}\\ &+\mathcal{A}_{ij}^{\mathsf{soc}}\begin{pmatrix}0&n_{ij}^z&-n_{ij}^y\\-n_{ij}^z&0&n_{ij}^x\\n_{ij}^y&-n_{ij}^x&0\end{pmatrix}_{\alpha\beta}\quad .\end{aligned} \tag{5.63}$$

In general, many more terms are allowed and might be important depending on the system of interest. However, due to the complexity of the inter-site damping, we restricted ourselves to the above mentioned.

As a last remark of this section, we want to briefly mention the possibility of multi-site dependencies of the Gilbert damping. Similarly to the magnetic exchange interactions, the Gilbert damping tensor can depend on the magnetic moment of multiple sites. For the on-site Gilbert damping the diagram,

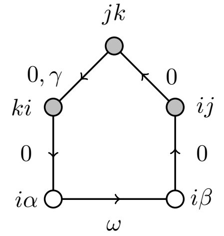

(5.64)

with additional spin-dependent Green functions can yield a dependence on three sites. In this way a dependence on the scalar spin-chirality, $\boldsymbol{e}_i\cdot(\boldsymbol{e}_j\times\boldsymbol{e}_k)$, can emerge, which might have some non-trivial impact on complex magnetic textures. However, in this chapter we will focus on the two-site dependencies.

In conclusion, the microscopic model shed some light on the, in general very complex, dependencies of the Gilbert damping on the magnetic texture. However, from the perturbative expansions themselves it is a priori unclear how important the different contributions are. We will address this point in the remainder of this chapter, starting with the Anderson model.

5.3.3. The Gilbert damping tensor from a two-site Anderson model

In this section, we apply the gained knowledge of the perturbative expansion of the Gilbert damping tensor of the previous section, to a two-site Anderson model. In order to account

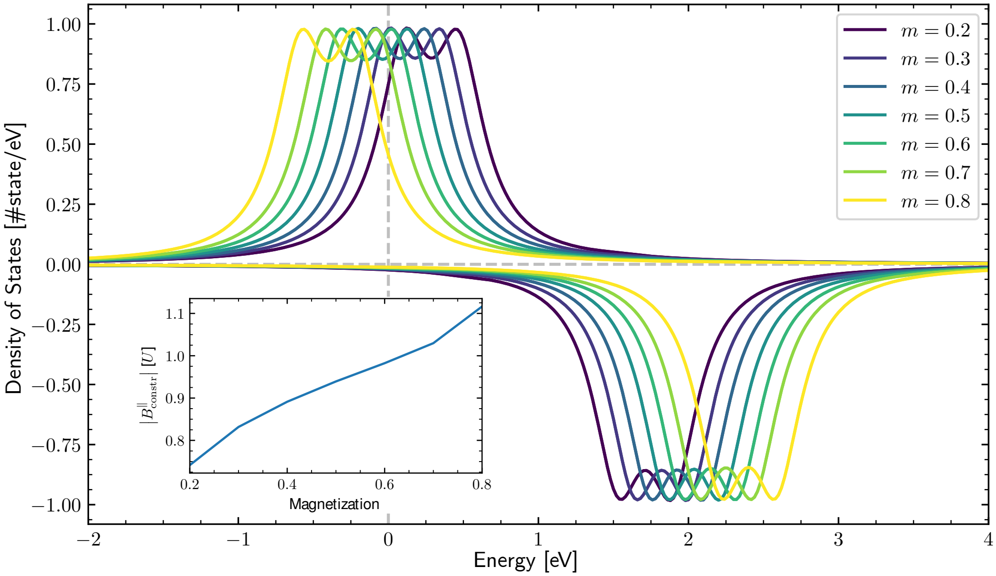

Figure 5.5.: Density of states for different magnetizations in the range from 0.2 to 0.8. Shown is the ferromagnetic reference state. The magnetizations are self-consistently constrained using a longitudinal magnetic field, which is shown in the inset. Model parameters: $U = 1.0\,\mathrm{eV}$, $E_d = 1.0\,\mathrm{eV}$, $t = 0.2\,\mathrm{eV}$, $\Gamma = 0.2\,\mathrm{eV}$, $\varphi_{\mathrm{R}} = 0°$.

for the dependencies of non-collinearities and systematically investigate their impact on the Gilbert damping, we use an approach similar to the one discussed in Chapter 4, but instead of fitting torques to an effective model, we utilize the relation between the slope of the imaginary part of the magnetic susceptibility and the Gilbert damping tensor given in eq. (5.14). The magnetic susceptibility is calculated for 14^2 independent non-collinear states, which were generated by using the Lebedev mesh [167]. For each magnetic state the Gilbert damping of the form discussed in eqs. (5.57), (5.60), (5.62), and (5.63) is fitted using a least-squares fit to the slope of the magnetic susceptibility.

The two-site Anderson model is set up using an energy shift of $E_d = 1.0\,\mathrm{eV}$ and a spin splitting of $U = 1.0\,\mathrm{eV}$. The magnetic moment for each configuration is stabilized self-consistently using magnetic constraining fields in a range of $m = 0.2$ to $m = 0.8$. The inter-site hopping is set to $t = 0.2\,\mathrm{eV}$ and the hybridization to $\Gamma = 0.2\,\mathrm{eV}$. We performed two sets of calculations: one without spin-dependent hopping, $\varphi_{\mathrm{R}} = 0°$, and one with a spin-dependent hopping, $\varphi_{\mathrm{R}} = 20°$, which mimics the effect of spin-orbit coupling. The density of states for the different magnetizations is shown in Fig. 5.5. Starting from the nearly half-filled case at $m = 0.8$, the Fermi level scans the full peak up to the tail of the majority spin channel for $m = 0.2$. The minority spin channel is basically unfilled for all values of the magnetization. The longitudinal magnetic constraining fields are shown in the inset of Fig. 5.5. The constraining field yields an additional spin splitting and is therefore linearly increasing as function of the magnetization. The different damping parameters are shown in Fig. 5.6. The damping, which is independent of the rela-

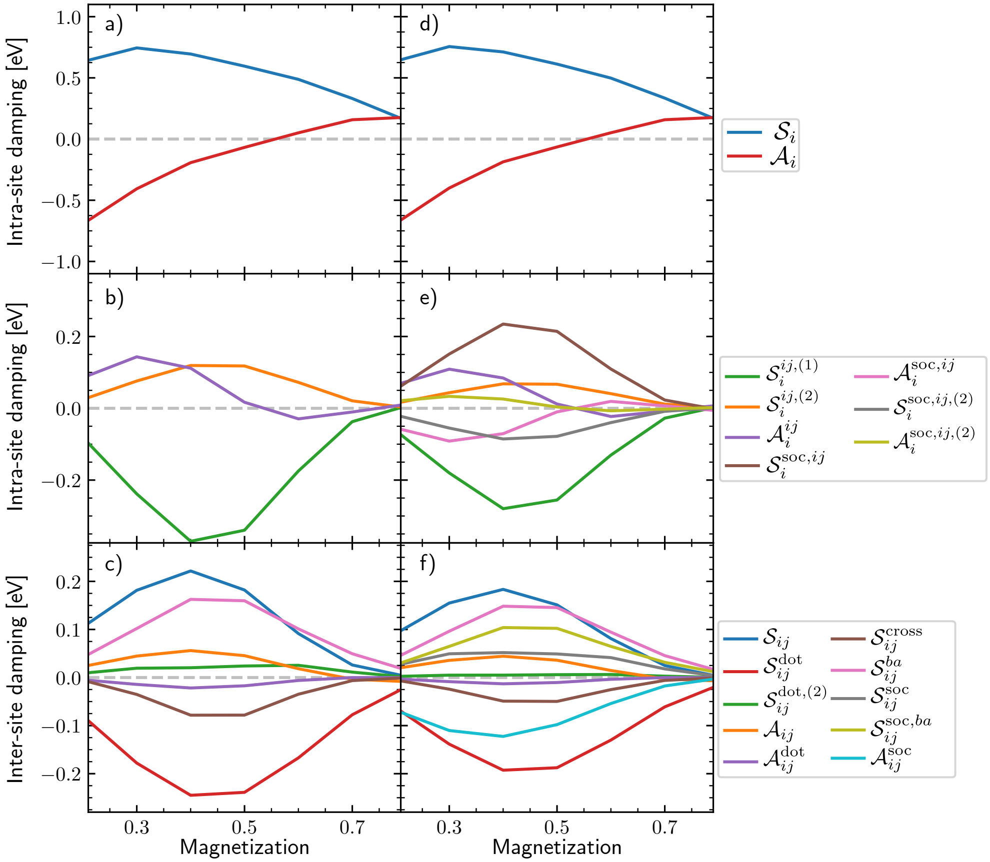

Figure 5.6.: Gilbert damping as function of the magnetic moment for a two-site Anderson model without (a-c) and with (d-f) spin-orbit coupling as parametrized in eqs. (5.57), (5.60), (5.62), and (5.63). A longitudinal magnetic field is used to self-consistently constrain the magnetic moment. The parameters are extracted from fitting to the inverse of the transversal susceptibility for several non-collinear configurations based on a Lebedev mesh. Model parameters: $U = 1.0\,\mathrm{eV}$, $E_d = 1.0\,\mathrm{eV}$, $t = 0.2\,\mathrm{eV}$, $\Gamma = 0.2\,\mathrm{eV}$, $\varphi_{\mathrm{R}} = 0°$ (a-c) and $\varphi_{\mathrm{R}} = 20°$ (d-f).

tive orientation of the two sites, is shown in Fig. 5.6a for the case without spin-orbit coupling. The symmetric damping-like intra-site contribution $\mathcal{S}_i$ dominates the damping tensor for most magnetizations and has a maximum at $m = 0.3$. The anti-symmetric intra-site contribution $\mathcal{A}_i$, which renormalizes the gyromagnetic ratio, approximately changes sign when the Fermi level passes the peak of the minority spin channel at $m \approx 0.5$ and has a significantly larger amplitude for small magnetizations. Both contributions depend mainly on the broadening Γ, which mimics the coupling to an electron bath and is responsible for the absorption of spin currents, which in turn are responsible for the damping of the magnetization dynamics. Therefore, it is not surprising that spin-orbit coupling does not affect those contributions, see Fig. 5.6d.

The directional dependencies of the intra-site damping are shown in Fig. 5.6b. With our choice of parameters, the correction to the damping-like symmetric Gilbert damping can reach half of the direction-independent term. This means that the damping can vary between $\approx 0.4-1.0$ for a ferromagnetic and an antiferromagnetic state at $m = 0.4$. Also for the renormalization of the gyromagnetic ratio a significant correction, which in the ferromagnetic case always lowers and in the antiferromagnetic case enhances the amplitude, is found. Adding spin-orbit coupling renormalizes the previously discussed contributions and gives rise to new terms, which is shown in Fig. 5.6e. The most dominant new contribution is the chiral contribution depending on the cross product of the moments i and j, which in terms of amplitude is comparable to the isotropic dot product terms. Interestingly, while the inter-site damping terms in general is known to be less relevant than the intra-site damping, we find that this does not hold for the directional dependence of the damping. The inter-site damping is shown in Fig. 5.6c. Even though the directional-independent term, $\mathcal{S}_{ij}$, is nearly one order of magnitude smaller than the equivalent intra-site contribution, this does not hold for the directional-dependent terms, which are comparable to the intra-site equivalents.

5.4. First-principles investigation of the Gilbert damping in non-collinear structures

In this section, the non-collinear effects to the Gilbert damping will be investigated in realistic systems using first-principles. As prototypical test systems adatoms and dimers deposited on the Au(111) surface are used. The Au(111) surface is an ideal playground for the investigation of this novel effects, since it hosts a large spin-orbit coupling, which are expected to yield strong chiral effects, and due to its Rashba-like electronic structure it is not as complex as for example the Pt or Ir surface, which were discussed in previous sections. Furthermore, in Section 3 it was shown that the Au surface has significant less spin polarizability than the other mentioned surfaces, which lowers the impact of the spin-polarized substrate atoms on the spin dynamics. To illustrate the different effects on the Gilbert damping, we start with the prototypical test system of magnetic adatoms in the uniaxial symmetry of the Au(111) surface. For the adatoms no non-local effects can contribute to the Gilbert damping. To account for those effects from first-principles, we investigate in the second part of this section magnetic dimers deposited on the Au(111) surface.

5.4.1. Adatoms deposited on the Au(111) surface

The Gilbert damping tensor of a single adatom without spin-orbit coupling has the form shown in relation to eq. (5.54),

$$\mathcal{G}_i^0 = \mathcal{S}_i \begin{pmatrix} 1 & 0 & 0 \\ 0 & 1 & 0 \\ 0 & 0 & 1 \end{pmatrix} + \mathcal{A}_i \begin{pmatrix} 0 & e_i^z & -e_i^y \\ -e_i^z & 0 & e_i^x \\ e_i^y & -e_i^x & 0 \end{pmatrix} \quad . \tag{5.65}$$

Note that spin-orbit coupling can induce additional anisotropies, as shown in eq. (5.59). The most important ones for the case of a single adatom are $\{\epsilon_{\alpha\beta\gamma}\hat{n}_{ij}^{\gamma}, \hat{n}_{ij}^{\alpha}\hat{n}_{ji}^{\beta}\}$, which in the C_{3v}

Damping parameters	Cr / Au(111)	Mn / Au(111)	Fe / Au(111)	Co / Au(111)
$\mathcal{S}_i$	0.083	0.014	0.242	0.472
$\mathcal{A}_i$	0.204	0.100	0.200	0.024
$\mathcal{S}_i^{\text{soc}}$	0.000	0.000	0.116	0.010
$\mathcal{A}_i^{\text{soc}}$	0.000	0.000	−0.022	0.012
$\gamma_{x/y}^{\text{renorm}}$	1.42	1.67	1.43	1.91
γ_z^{renorm}	1.42	1.67	1.48	1.87

Table 5.1.: Gilbert damping parameters of Cr, Mn, Fe and Co adatoms deposited on the Au(111) surface as parametrized in eqs. (5.65) and (5.60). The spin-orbit orbit coupling vector (see Section 5.3) is pointing in the z-direction due to the C_{3v} symmetry. The renormalized gyromagnetic ratio γ^{renorm} is calculated according to eqs. (5.67) for an in-plane magnetic moment and an out-of-plane magnetic moment.

symmetry result in

$$\mathcal{G}_i = \mathcal{G}_i^0 + \mathcal{S}_i^{\text{soc}} \begin{pmatrix} 0 & 0 & 0 \\ 0 & 0 & 0 \\ 0 & 0 & 1 \end{pmatrix} + \mathcal{A}_i^{\text{soc}} \begin{pmatrix} 0 & 1 & 0 \\ -1 & 0 & 0 \\ 0 & 0 & 0 \end{pmatrix} \quad , \tag{5.66}$$

since the sum of all spin-orbit coupling vectors points in the out-of-plane direction with $\hat{\boldsymbol{n}}_{ij} \to \boldsymbol{e}_z$. Thus, the Gilbert damping tensor of adatoms deposited on the Au(111) surface can be described by the four parameters shown in eqs. (5.65) and (5.60), which are shown in Table 5.1 for Cr, Mn, Fe and Co adatoms. Cr and Mn, which are nearly half-filled, show only a small damping-like contribution $\mathcal{S}_i$, while Fe and Co having states at the Fermi level show a significant damping of up to 0.47 in the case of Co. The antisymmetric part $\mathcal{A}_i$ of the Gilbert damping tensor results in an effective renormalization of the gyromagnetic ratio γ, as shown in relation to eq. (5.19), which using the full LLG equation, eq. (5.1), and approximating $\boldsymbol{m}_i \cdot \frac{\mathrm{d}\boldsymbol{m}_i}{\mathrm{d}t} = 0$ is given by,

$$\gamma^{\text{renorm}} = \gamma \frac{1}{1 + \gamma(\boldsymbol{e}_i \cdot \boldsymbol{A}_i)} \quad , \tag{5.67}$$

where $\boldsymbol{A}_i$ describes the vector $\boldsymbol{A}_i = \left(\mathcal{A}_i\,,\, \mathcal{A}_i\,,\, \mathcal{A}_i + \mathcal{A}_i^{\text{soc}}\right)$. For Cr and Fe there is a significant renormalization of the gyromagnetic ratio resulting in approximately 1.4. In contrast, Co shows only a weak renormalization with 1.9 being close to the gyromagnetic ratio of 2. The spin-orbit coupling effects are negigible for most adatoms except for Fe, which shows a small anisotropy in the renormalized gyromagentic ratio ($\approx 10\,\%$) and a large anisotropy in the damping-like term of nearly $50\,\%$.

5.4.2. Dimers deposited on the Au(111) surface

In this section, we focus on magnetic dimers, which in contrast to single adatoms can show non-local contributions and dependencies on the relative orientation of the magnetic moments

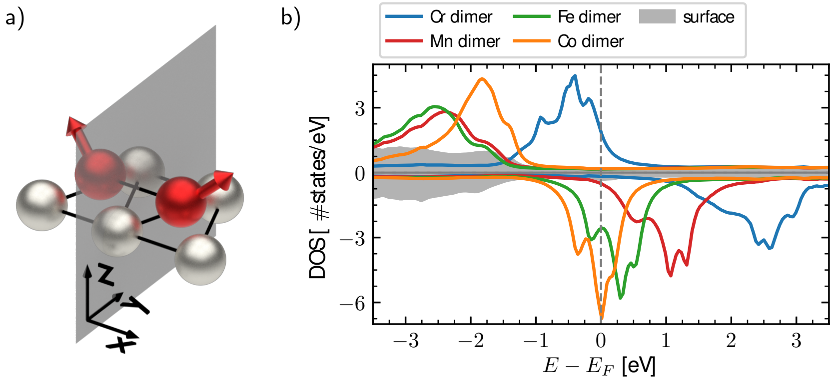

c)

	m_{spin}
Cr	4.04
Mn	4.48
Fe	3.42
Co	2.20

Figure 5.7.: Magnetic dimers deposited on the Au(111) surface. a) Illustration of a non-collinear magnetic dimer (red spheres) deposited on the (111) facets of Au (grey spheres). From the initial C_{3v} spatial symmetry of the surface the dimers preserve the mirror plane (indicated grey) in the y-z plane. b) Local density of states of the Cr, Mn, Fe and Co dimers deposited on the Au(111) surface. The grey background indicates the surface density of states. The dimers are collinear in the z-direction. c) Spin moment of each dimer atom in units of $[\mu_{\mathrm{B}}]$.

of the dimer atoms. Fig. 5.7 shows an illustration of the dimer on the Au(111) surface and the corresponding local density of states for the Cr, Mn, Fe and Co dimer deposited on the Au(111) surface. The density of states originates mainly from the d-states of the dimer atoms. It can be seen that the dimers exhibit a much more complicated hybridization than the Anderson model. In addition the crystal field splits the different d-states resulting in a higher complexity than the model. However, the main features are comparable: For all dimers there is either a fully occupied majority channel (Mn, Fe, and Co) or a fully unoccupied minority channel (Cr). The other spin channel determines the magnetic moment of the dimer atoms, which is shown in Fig. 5.7c. Using the maximal spin moment, which is according to Hund's rule 5 μ_{B}, the first-principles results can be converted to the single-orbital Anderson model corresponding to approximately $m = \{0.81, 0.90, 0.68, 0.44\}$ for Cr, Mn, Fe, and Co, respectively. Thus by this comparison, we expect large non-collinear contributions for Fe and Co, while Cr and Mn should show only weak non-local dependencies.

The obtained parametrization is shown in Table 5.2. The Cr dimer shows a weak directional dependence, while the Mn dimer shows nearly no directional dependence. For both the overall damping is weak, but there is a significant correction to the gyromagnetic ratio. In contrast, the Fe and Co dimers show a very strong directional dependence. Originating from the isotropic dependencies of the damping-like contributions, the damping of the Fe dimer can vary between 0.21 in the ferromagnetic state and 0.99 in the antiferromagnetic state. For the Co dimer the inter-site damping is even dominated by the bilinear and biquadratic term, while the constant damping is negligible. In total, there is a very good qualitative agreement between the expectations derived from studying the Anderson model and the first-principles results.

Damping parameters	Cr / Au(111)	Mn / Au(111)	Fe / Au(111)	Co / Au(111)
$\mathcal{S}_i$	0.0911	0.0210	0.2307	0.5235
$\mathcal{S}_i^{ij,(1)}$	0.0376	0.0006	-0.3924	-0.2662
$\mathcal{S}_i^{ij,(2)}$	0.0133	-0.0006	0.3707	0.3119
$\mathcal{A}_i$	0.2135	0.1158	0.1472	0.0915
$\mathcal{A}_i^{ij}$	0.0521	0.0028	-0.0710	-0.0305
$\mathcal{S}_{ij}$	-0.0356	0.0028	0.2932	0.0929
$\mathcal{S}_{ij}^{\text{dot}}$	-0.0344	-0.0018	-0.3396	-0.4056
$\mathcal{S}_{ij}^{\text{dot},(2)}$	0.0100	0.0001	0.1579	0.2468
$\mathcal{A}_{ij}$	-0.0281	-0.0044	0.0103	0.0011
$\mathcal{A}_{ij}^{\text{dot}}$	-0.0175	0.0000	-0.0234	-0.0402
$\mathcal{S}_{ij}^{\text{cross}}$	0.0288	0.0002	-0.2857	-0.0895
$\mathcal{S}_{ij}^{\text{ba}}$	0.0331	0.0036	0.2181	0.2651
$\mathcal{S}_i^{\text{soc},ij,y}$	0.0034	0.0000	0.0143	-0.0225
$\mathcal{S}_i^{\text{soc},ij,z}$	0.0011	0.0000	-0.0104	0.0156
$\mathcal{A}_i^{\text{soc},ij,y}$	0.0024	-0.0001	-0.0036	0.0022
$\mathcal{A}_i^{\text{soc},ij,z}$	0.0018	-0.0005	0.0039	-0.0144
$\mathcal{S}_{ij}^{\text{soc},y}$	0.0004	0.0001	0.0307	0.0159
$\mathcal{S}_{ij}^{\text{soc},z}$	-0.0011	0.0000	-0.0233	0.0206
$\mathcal{S}_{ij}^{\text{ba,soc},y}$	-0.0027	0.0000	-0.0184	-0.0270
$\mathcal{S}_{ij}^{\text{ba,soc},z}$	0.0005	-0.0001	0.0116	-0.0411

Table 5.2.: Gilbert damping parameters of Cr, Mn, Fe and Co dimers deposited on the Au(111) surface as parametrized in eqs. (5.57), (5.60), (5.62), and (5.63). The spin-orbit orbit coupling vector (see Section 5.3) is assumed to lie in the y-z plane and inverts under permutation of the two dimer atoms.

5.5. Conclusions and outlook

In this Chapter, we presented a comprehensive analysis of magnetization dynamics in non-collinear system with a special focus on the Gilbert damping tensor and its dependencies on the non-collinearity. We showed how the Gilbert damping can be separated into a symmetric and an anti-symmetric part, which are even and odd in the magnetization, respectively. Using a perturbative expansion of the two-site Anderson model, we could identify that both, the intra-site and the inter-site part of the Gilbert damping, depend isotropically on its environment via the effective angle between the two magnetic moments, $\boldsymbol{e}_i \cdot \boldsymbol{e}_j$. Spin-orbit coupling was identified as the source of a chiral contribution to the Gilbert damping, which similarly to the DMI and CBI depends linearly on the vector spin chirality, $\boldsymbol{e}_i \times \boldsymbol{e}_j$. Using the Anderson model, we investigated the importance of the different contributions in terms of their magnitude as function of the magnetization. The non-collinear effects are most dominant for a magnetization of approximately $m = 0.4$, for which the density of states at the Fermi level is maximal. For the limits of half-filling ($m > 0.9$) and no-filling or fully-filled ($m < 0.1$) there are no noticeable non-collinear effects on the Gilbert damping. Using the prototypical test system of Cr, Mn, Fe and

Co dimers deposited on the Au(111) surface, we extracted the effects of the non-collinearity on the Gilbert damping using time-dependent DFT. Overall, the first-principles results agree well with the Anderson model, showing no dependence for the nearly half-filled systems Cr and Mn and a strong dependence on the non-collinearity for Fe and Co having a half-filled minority spin-channel. The realistic systems indicate an even stronger dependence on the magnetic texture than the model with the used parameters. The Fe and the Co dimer show significant isotropic terms up to the biquadratic term, while the chiral contributions originating from spin-orbit coupling have only a weak impact on the total Gilbert damping. However, the chiral contributions can play the deciding role for systems which are degenerate in the isotropic terms, like e.g. spin spirals of opposite chirality.

We expect the found dependencies of the Gilbert damping on the magnetic texture to have a significant and non-trivial impact on the spin dynamics of complex magnetic structures. Our findings can be used to generalize the known LLG model to account for non-collinear systems. The impact of the different contributions to the Gilbert damping, e.g. the chiral and the isotropic contributions, can be analyzed either based on free parameters or based on sophisticated paramtrizations obtained from first principles as discussed in this Chapter. It remains to be explored how the newly found dependencies of the Gilbert damping affect the motion of highly non-collinear magnetic quasi-particles like magnetic skyrmions or magnetic bobbers. Future studies using atomistic spin dynamics simulations could shed some light on this aspect and help for the design of future devices based on spintronics.

6

Stability of magnetic nanostructures on surfaces

This chapter presents a systematic analysis of the magnetic stability of nanostructures on surfaces from first principles. We show how magnetic stability can be predicted using a combination of a master equation model and first-principles input parameters. The master equation *approach based on Fermi's golden rule is used to model the magnetic stability as probed in telegraph noise scanning tunneling microscopy experiments. Using first-principles calculations, we not only determine the parameters of the quantum Heisenberg model, which is used to model the magnetic nanostructure, but also calculate the coupling strength between the magnetic nanostructure and the surface, which is one of the most important ingredients for the prediction of magnetic stability. In addition, we show how the interaction of a nanostructure with another nearby nanostructure can be used to engineer the magnetic stability. We find two distinct destabilization mechanisms, namely the Dzyaloshinskii-Moriya interaction and the anisotropic symmetric exchange interaction, from which the latter one can be tuned by using a symmetric arrangement of nearby nanostructures resulting in a drastic increase of the magnetic stability. The presented results are used to explain experimental measurements, which were performed in the group of Dr. Jens Wiebe at the University of Hamburg.*

Parts of the presented work have been published in

*J. Hermenau†, S. Brinker† et al. Nature Communications **10**, 2565 (2019)*
†J. Hermenau and S. Brinker contributed equally to the work.

I have contributed to this publication in the following way: I performed the DFT calculations and I simulated the telegraph noise experiment based on a master equation model, which I extended together with Dr. Marco Marciani and Dr. Manuel dos Santos Dias. I analyzed the results and found the importance of the various exchange interactions in the different regimes. I contributed to the manuscript via discussions and corrections and I wrote the theoretical parts mainly published in the supplementary information.

6.1. Introduction

In the previous chapters, fundamental theories combined with first-principles calculations were discussed, having in common the ultimate goal of improving the understanding of magnetism on the microscopic level with a potential future application to spintronic devices and especially data storage and processing devices. In order to store a single bit of information in a magnetic nanostructure, the most crucial property is the magnetic stability. Modern hard disks achieve a magnetic stability of more than 10 years [185] meaning that once a bit is encoded in a particular orientation in a magnetic domain, the orientation of this domain is on average stable for more than 10 years. The manipulation of a magnetic bit, namely the read and write process, utilizes the giant magnetoresistance effect [4, 5]. On the path towards the miniaturization of magnetic bits, different experimental techniques have been developed for the manipulation and the probing of magnetic structures down to the level of a single atom. The most prominent ones are X-ray magnetic circular dichroism (XMCD) and spin-polarized scanning tunneling microscopy (SP-STM). XMCD itself cannot probe a single atom, but gives access to a spatial average over a large region. From the difference of the absorption spectrum of left- and right-circular-polarized light the spin and orbital magnetic moment can be obtained using so-called sum rules [186]. One experimental breakthrough was achieved by Donati *et al.* [40] in a recent experiment using the XMCD technique. The first stable single magnetic adatom in the form of Ho deposited on MgO(100) layers on the Ag(100) surface was found. The Ho atom exhibits a magnetic lifetime of $\tau = 1200\,\mathrm{s}$ at a temperature of $10\,\mathrm{K}$, which is partially related

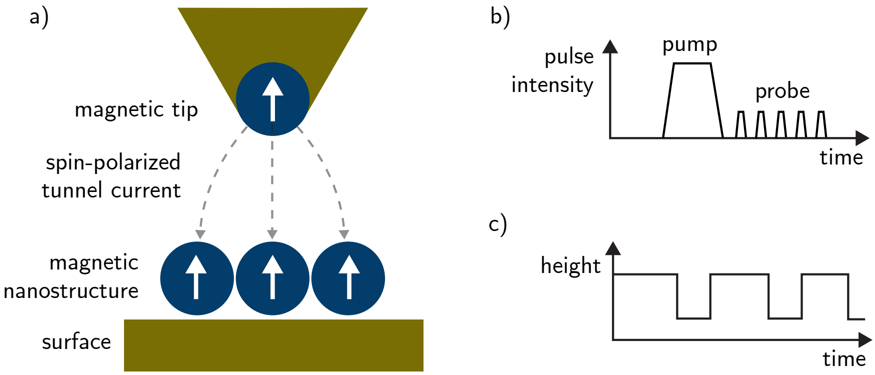

Figure 6.1.: Illustration of the spin-polarized STM and the techniques to probe the magnetic stability. a) A spin-polarized current tunnels between the magnetic tip and the probed nanostructure. b) Illustration of the pump-probe experiment, in which a strong pump pulse is followed by a collection of weak and short probe pulses. c) Illustration of the telegraph noise measurement. The magnetic nanostructure is constantly probed by a spin-polarized tunneling current. Due to the tunnel magnetoresistance, depending on the state of the nanostructure the height of the STM is adjusted if the STM operates in the constant current mode.

to the giant magnetic anisotropy energy found for adatoms on the MgO surface, e.g. $58\,\mathrm{meV}$ for a Co atom [43]. To access directly the magnetic stability of isolated small nanostructures different STM techniques have successfully been used in the last decade. STM allows for a spatial resolution down to the level of a single atom and therefore enables to efficiently manipulate and probe nanostructures (see Figure 6.1a for an illustration). Via lateral atom manipulation [19] single atoms can be moved and combined to build larger nanostructures of nearly arbitrary structure. To probe the magnetic stability two techniques are prevailing – the so-called pump-probe experiments and the telegraph noise experiments. In pump-probe experiments [35] a strong pump pulse is applied to excite the nanostructure, while several probe pulses, which only weakly interact with the nanostructure, are used to probe its current magnetic configuration as indicated in Fig. 6.1b. To identify the magnetic configuration the tunnel magnetoresistance effect is used, which allows for a detection of the magnetic state based on the effective angle, $\boldsymbol{e}_\mathrm{t}\cdot\boldsymbol{e}_\mathrm{s}$, between the magnetic direction of the spin-polarized tip, $\boldsymbol{e}_\mathrm{t}$, and the direction of the magnetic moment of the nanostructure, $\boldsymbol{e}_\mathrm{s}$. It was originally formulated for magnetic layers separated by an insulator [6], and later applied to SP-STM by Wortmann *et al.* [187] in the framework of the ground-breaking theoretical description of non-magnetic STM by Tersoff and Hamann [24, 25]. In contrast to the pump-probe experiment, in telegraph noise experiments a spin-polarized current is constantly interacting with the nanostructure probing the magnetic fluctuations of the nanostructure. If the STM is operating in the so-called constant current mode, in which a constant bias voltage is applied and the height of the STM tip is adjusted in order to stabilize the electric current flowing through the tunnel junction, the different magnetic states can be seen as steps in the height of the STM tip, as illustrated in Fig. 6.1c. The telegraph noise technique has been applied in several different experiments to a variety of systems, e.g. to a five-atom nanostructure composed out of Fe deposited on a Cu(111) surface [34] or to different Fe trimers deposited on a Pt(111) surface [30], which were both the smallest stable magnets on a metallic substrate at the time of their discoveries.

In this Chapter, we focus on the theoretical description of the magnetic lifetimes, i.e. the average time a nanostructure keeps its magnetic orientation, as measured in telegraph noise experiments. The main focus will be the impact of magnetic exchange interactions between two nanostructure on the magnetic stability. Our theoretical findings are used to interpret experimental measurements performed in the group of Dr. Jens Wiebe at the University of Hamburg.

6.1.1. Magnetic stability in telegraph noise experiments

The highly dynamical tunneling process between a magnetic tip and a surface via a magnetic nanostructure is typically modeled in the context of open quantum systems [188]. The magnetic nanostructure is considered as a quantum spin in the quantum Heisenberg model, which is similar to the semi-classical Heisenberg model discussed in Chapter 4, but using the quantum spin operator, $\boldsymbol{S}$, with its associated spin quantum number, S, instead of the classical magnetic moments. The quantum spin operator follows the well-known commutator relations of the angular momentum in quantum mechanics. An eigenbasis containing $2S+1$ eigenstates, which are labeled by the z-projection of the spin, $m = \{-S, -S+1, \dots, S\}$, and the spin quantum number, can be defined using the square of the spin operator and its z-component,

$$\boldsymbol{S}^2|S,m\rangle = S(S+1)|S,m\rangle \quad , \quad S_z|S,m\rangle = m|S,m\rangle \quad . \tag{6.1}$$

The x and y elements of the spin operator are defined in terms of the ladder operators,

$$S_+|S,m\rangle = \sqrt{S(S+1)-m(m+1)}|S,m+1\rangle \tag{6.2}$$

$$S_-|S,m\rangle = \sqrt{S(S+1)-m(m-1)}|S,m-1\rangle \quad , \tag{6.3}$$

with $S_x = (S_+ + S_-)/2$ and $S_x = (S_+ - S_-)/2\mathrm{i}$.

The quantum spin model contains the on-site magnetic anisotropy, as well as the magnetic exchange interactions. Starting with the on-site magnetic anisotropy, we can convert the classical energy expansion of the magnetocrystalline anisotropy in terms of spherical harmonics, as described in Section 3.3.2, to a quantum spin hamiltonian using the Stevens method of operator equivalents [189]. Depending on the symmetry, the set of allowed spherical harmonics can be determined, which is then transformed using the Stevens operators to a quantum spin model. For the C_{3v} symmetry, we already saw that only the following spherical harmonics are allowed,

$$\mathcal{H}^{\mathsf{MAE}}_{C_{3v}}(\vartheta,\varphi) = E_{(2,0)}Y_{(2,0)}(\vartheta,\varphi) + E_{(4,0)}Y_{(4,0)}(\vartheta,\varphi) + E_{(4,3)}Y_{(4,3)}(\vartheta,\varphi) + \mathcal{O}(m^6) \quad , \tag{6.4}$$

which transforms to

$$\mathcal{H}^{\mathsf{MAE}}_{C_{3v}}(\{\boldsymbol{S}\}) = B_{(2,0)}O_2^0 + B_{(4,0)}O_4^0 + B_{(4,3)}O_4^3 + \dots \quad , \tag{6.5}$$

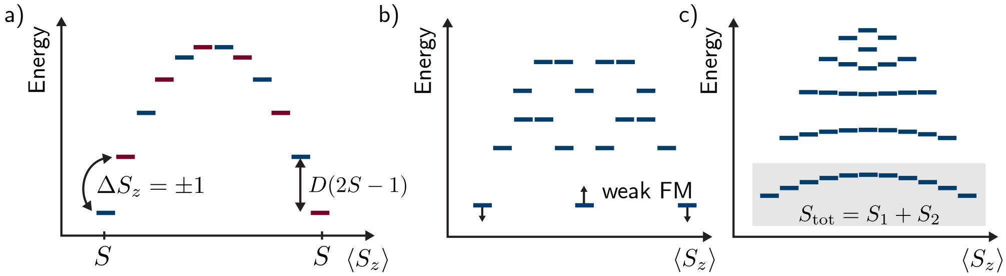

Figure 6.2.: Illustration of the level diagram of a quantum Heisenberg model. a) Single spin with $S = 11/2$ in a uniaxial anisotropy, $\mathcal{H} = DS_z^2$. The two different colors of the energy levels indicate the two groups of states resulting from a small in-plane anisotropy, $E(S_x^2 - S_y^2)$, which mixes all states with $\Delta S_z = \pm 2$. b) Two non-interacting spins with $S_1 = 5/2$ and $S_2 = 5/2$ and uniaxial anisotropy. The level diagram equals two nested parabolas. The arrows indicate the effect of a weak ferromagnetic coupling. c) Two ferromagnetically interacting spins with $S_1 = 5/2$ and $S_2 = 5/2$. The subspace spanning the lowest parabola equals a total spin $S_{\text{tot}} = S_1 + S_2$.

where O_ℓ^m are the Stevens operators [37, 190],

$$\begin{aligned} O_2^0 &= 3S_z^2 - S(S+1) \\ O_4^0 &= 35S_z^4 - 30S(S+1)S_z^2 + 25S_z^2 - 6S(S+1) + 3S^2(S+1)^2 \\ O_4^3 &= \frac{1}{4}\left[S_z(S_+^3 + S_-^3) + (S_+^3 + S_-^3)S_z\right] \quad . \end{aligned} \tag{6.6}$$

The O_2^0 operator describes the well-known uniaxial anisotropy. In a lower symmetry, e.g. the C_S symmetry, additional anisotropies can emerge. The second-order in-plane anisotropy associated to the C_S symmetry is for example given by $O_2^2 = S_x^2 - S_y^2$ describing an anisotropy between the x and the y direction.

To illustrate the quantum spin model including only magnetic anisotropies we assume a large uniaxial anisotropy and in addition a small in-plane anisotropy,

$$\mathcal{H} = DS_z^2 + E(S_x^2 - S_y^2) \quad , \tag{6.7}$$

with $D < 0$ and $|D| \gg |E|$. The energy levels of the eigenstates of this hamiltonian are illustrated in Fig. 6.2a for a spin with $S = 11/2$. Due to the strong uniaxial anisotropy, the $2S+1$ eigenstates have a parabolic energy shape. Both magnetic states $\langle S_z \rangle = \pm S$ are degenerated, corresponding to an alignment and an anti-alignment of the spin with respect to the z axis. The magnetic lifetime is defined as the average time the spin needs to flip between its ground states. In a later part of this section, we will discuss this process in more detail using a master equation model, but here we first want to focus on an intuitive picture. In order to flip from one state to another the spin has to be excited, which in the case of the telegraph noise experiment is done by an electron carrying energy and angular momentum. Due to angular momentum conservation, each electron can excite the local spin according to its energy levels with the restriction of $\Delta S_z = \pm 1$. For a purely uniaxial system, this means that several consecutive electron scatterings have to occur in order to excite the local spin and reach the highest energy of the parabola (Fig. 6.2a). From that point the local spin can exchange angular momentum with an electron bath (e.g. the surface) and relax towards the other site of the parabola resulting in a spin-flip. Therefore, both increasing the uniaxial anisotropy D and the spin S results in a drastic magnetic stabilization of the local spin, since more energy and more scatterings are needed for a spin-flip to occur. A well-known mechanism to destabilize a spin is an in-plane anisotropy, e.g. of the form presented in eq. (6.7). Due to the in-plane anisotropy the eigenstates of the Hamiltonian are linear combinations of the S_z eigenstates with $\Delta S_z = \pm 2$. Thus, the states can be separated into two groups as indicated in Fig. 6.2 by the red and blue levels. For a half-integer spin the two ground states belong to different groups. Due to the mixing of the eigenstates one scattering with an electron and the associate angular momentum transfer of $\Delta S_z = \pm 1$ is enough to excite the spin from one group to the other group and therefore to induce a spin flip, which shows why an in-plane anisotropy can lower the magnetic stability by orders of magnitude due to the opening of new transition channels.

Adding a second spin to the picture, which can interact with the initial spin via an isotropic exchange interaction, J, we obtain the hamiltonian,

$$\mathcal{H} = \sum_i D_i S_{i,z}^2 + J \boldsymbol{S}_1 \cdot \boldsymbol{S}_2 \quad . \tag{6.8}$$

The Hilbert space of this hamiltonian can now be represented in a tensor product basis,

$$|S_1, m_1; S_2, m_2\rangle = |S_1, m_1\rangle \otimes |S_2, m_2\rangle \quad . \tag{6.9}$$

Without exchange coupling the level diagram of the hamiltonian are two nested parabolas corresponding to the two on-site anistropies, as shown in Fig. 6.2b. A weak ferromagnetic coupling would favour energetically the states with maximal S_z projection, $|S_1, S_1; S_2, S_2\rangle$ and $|S_1, -S_1; S_2, -S_2\rangle$, over the antiferromagnetic states $|S_1, S_1; S_2, -S_2\rangle$ and $|S_1, -S_1; S_2, S_2\rangle$. In the other limit of vanishing on-site anisotropy, the exchange hamiltonian can be solved using the well-known addition of angular momentum in quantum mechanics. The total spin operator, $\boldsymbol{S}_\text{tot} = \boldsymbol{S}_1 + \boldsymbol{S}_2$, forms subsets with $S_\text{tot} = \{|S_1 - S_2|, \ldots, S_1 + S_2\}$, and can be used to replace the isotropic term of the exchange, $\boldsymbol{S}_1 \cdot \boldsymbol{S}_2 = \frac{1}{2}\left(\boldsymbol{S}_\text{tot}^2 - \boldsymbol{S}_1^2 - \boldsymbol{S}_2^2\right)$. The case of a strong ferromagnetic coupling with weak magnetic anisotropy is shown in Fig. 6.2c. Energetically the subset with maximal spin projection S_1+S_2 is favoured. Effectively, this subset acts like a single spin with $S = S_1 + S_2$ in an uniaxial anisotropy. Due to its increased spin and the associated increased number of levels the combined spin is much stabler than its two constituents.

The simple picture described in the previous paragraph led to the intuition that combining spins and forming a larger nanostructure in general increases the magnetic stability. To investigate the effect of the coupling between two nanostructures on the magnetic stability, we use a master equation model, which will be discussed in the next section.

6.1.2. Spin stability from a master equation approach

In this section, we present a master equation approach to describe the magnetic stability in telegraph noise experiments. The formalism was presented by Delgado and Fernández-Rossier [191] and is based on the ideas of the field of open quantum systems [192]. First,

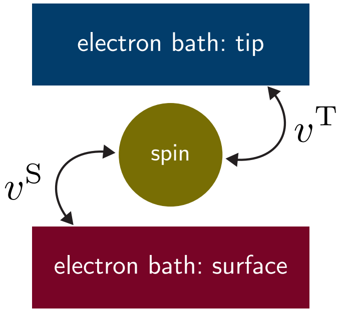

Figure 6.3.: Illustration of the model used by Delgado and Fernández-Rossier [191] to describe a nanostructure on a surface probed by a tip.

we recap the details of the model, and second, we explain how the model can be adapted to investigate the impact of interactions between nanostructures and how to use first-principles methods to predict important ingredients of the model.

The total Hamiltonian can be divided into contributions from the tip, the surface, the magnetic nanostructure and a coupling of the nanostructure to the transport electrons:

$$\mathcal{H} = \mathcal{H}_{\mathsf{T}} + \mathcal{H}_{\mathsf{S}} + \mathcal{H}_{\mathsf{Spin}} + \mathcal{V} \quad . \tag{6.10}$$

The tip and the surface are described as electron baths, which do not need to be specified further, and are denoted by the hamiltonians $\mathcal{H}_{\mathsf{T}}$ and $\mathcal{H}_{\mathsf{S}}$, respectively. The local nanostructure containing N spins is modelled by a quantum spin model as discussed above, which can be described by its eigenstates $|M\rangle$,

$$\mathcal{H}_{\mathsf{spin}}|M\rangle = E_M|M\rangle \quad , \tag{6.11}$$

where the eigenstates are spanned by the generalized N-spin tensor product basis, similar to eq. (6.9). The coupling of the nanostructure to the transport electrons is modeled by a so-called Appelbaum hamiltonian [193],

$$\mathcal{V} = \sum_{\alpha,\eta,\eta',i} T_i^{\eta,\eta',\alpha} S_i^{\alpha} c_{\eta}^{\dagger} \frac{\sigma^{\alpha}}{2} c_{\eta'} \quad , \tag{6.12}$$

where α labels the spin, η labels the single-particle quantum number of the transport electrons, which will simplify to one index for the surface and one for the tip, and i sums over the N spins. $T_i^{\eta,\eta',\alpha}$ is the (spin-dependent) exchange-tunneling interaction between the spin i and the transport electrons. Assuming only kinetic exchange, which is spin-rotational invariant, one can write,

$$T_i^{\eta,\eta',\alpha} = v_i^{\eta} v_i^{\eta'} \mathcal{T}^{\alpha} \quad , \tag{6.13}$$

where $\mathcal{T}^x = \mathcal{T}^y = \mathcal{T}^z = |\mathcal{T}|$ is spin-independent and $v^{\eta} = v^S, v^T$ are dimensionless factors scaling with the hybridization strength between the surface and the spin, as well as the tip and the spin. The key ingredients of the model are illustrated in in Figure 6.3.

Treating the coupling of the spins to the transport electrons via $\mathcal{V}$ as a perturbation the spin dynamics of the nanostructure can be modelled using a master equation, which connects the diagonals of the elements of the density matrix, P_M, and the transition matrix, $W_{MM'}$,

$$\frac{\mathrm{d}P_M}{\mathrm{d}t} = \sum_{M'} P_{M'} W_{M'M} - P_M \sum_{M'} W_{MM'} \quad , \tag{6.14}$$

where the first term described a transition from a state $|M'\rangle$ to the state $|M\rangle$, while the second term described the transition from $|M\rangle$ to a state $|M'\rangle$. The transition rates can be written as

$$W_{MM'} = \sum_{\eta\eta'} W_{MM'}^{\eta\to\eta'} \quad , \tag{6.15}$$

where $W_{MM'}^{\eta\to\eta'}$ is the transition rate of a scattering process from state $|M\rangle$ to $|M'\rangle$ with an electron going from η to η'. This rate is given by

$$W_{MM'}^{\eta\to\eta'} = \sum_{kk',\sigma\sigma'} \Gamma_{k\sigma M,k'\sigma' M'}^{\eta\to\eta'} f_\eta(E_{k\sigma}) \left[1 - f_{\eta'}(E_{k'\sigma'})\right] \quad , \tag{6.16}$$

where $\Gamma_{k\sigma M,k'\sigma' M'}^{\eta\to\eta'}$ is the scattering rate of an electron in lead η with spin σ and wave number k scattering into the lead η' with spin σ' and wave number k' with the spin transition of the nanostructure from $|M\rangle$ to $|M'\rangle$, which can be calculated by using Fermi's golden rule and treating $\mathcal{V}$ as perturbation,

$$\Gamma_{k\sigma M,k'\sigma' M'}^{\eta\to\eta'} = \frac{2\pi}{\hbar} \left| \sum_{\alpha,i} \mathcal{T}^\alpha v_i^\eta v_i^{\eta'} \langle M|S_i^\alpha|M'\rangle \right|^2 \delta(E_{\sigma\eta}(k) + E_M - E_{\sigma'\eta'}(k') - E_{M'}) \quad . \tag{6.17}$$

A detailed derivation of the different scattering rates from tip to tip, tip to surface, surface to tip, and surface to surface are shown in Appendix E. The resulting elastic contributions for site i are,

$$W_{MM'}^{S\to S} = \mathcal{G}_{MM'}^{SS} k_i \left[\left| \sum_j r_{ij}^{\mathsf{S}} S_{j,MM'}^+ \right|^2 + \left| \sum_j r_{ij}^{\mathsf{S}} S_{j,MM'}^- \right|^2 + 2 \left| \sum_j r_{ij}^{\mathsf{S}} S_{j,MM'}^z \right|^2 \right] \quad , \tag{6.18}$$

$$W_{MM'}^{T\to T} = \mathcal{G}_{MM'}^{TT} k_i r_i^2 \left[|S_{i,MM'}^+|^2 \left(1 - \mathcal{P}_{\mathsf{T}}^2\right) + |S_{i,MM'}^-|^2 \left(1 - \mathcal{P}_{\mathsf{T}}^2\right) + 2\left(1 + \mathcal{P}_{\mathsf{T}}\right) |S_{i,MM'}^z|^2 \right] \quad , \tag{6.19}$$

$$W_{MM'}^{T\to S} = \mathcal{G}_{MM'}^{TS} k_i r_i \left[|S_{i,MM'}^+|^2 \left(1 - \mathcal{P}_{\mathsf{T}}\right) + |S_{i,MM'}^-|^2 \left(1 + \mathcal{P}_{\mathsf{T}}\right) + 2|S_{i,MM'}^z|^2 \right] \quad , \tag{6.20}$$

$$W_{MM'}^{S\to T} = \mathcal{G}_{MM'}^{ST} k_i r_i \left[|S_{i,MM'}^+|^2 \left(1 + \mathcal{P}_{\mathsf{T}}\right) + |S_{i,MM'}^-|^2 \left(1 - \mathcal{P}_{\mathsf{T}}\right) + 2|S_{i,MM'}^z|^2 \right] \quad . \tag{6.21}$$

The function $\mathcal{G}_{MM'}^{\eta\eta'}$ is given by

$$\mathcal{G}_{MM'}^{\eta\eta'} = \frac{\Delta_{MM'}^{\eta\eta'}}{1 - \exp\left(-\Delta_{MM'}^{\eta\eta'}/k_{\mathsf{B}}T\right)} \qquad \text{with} \qquad \Delta_{MM'}^{\eta\eta'} = E_M - E_{M'} + \mu_\eta - \mu_{\eta'} \quad , \tag{6.22}$$

where $E_M = \langle M|\mathcal{H}_{\mathsf{spin}}|M\rangle$, k_{B} is the Boltzmann constant, T is the temperature, and μ_η is the chemical potential (containing the external voltage). $S_{i,MM'}^\alpha$ are the matrix elements of the spin of atom i, $S_{i,MM'}^\alpha = \langle M|S_i^\alpha|M'\rangle$. The $\mathcal{G}$ function contains the impact of the temperature on the scattering rates. Note that quantum fluctuations, like e.g. zero-point spin fluctuations [39] are not contained in this model. In total, the scattering rates can be represented by a small set of parameters:

1. The coupling strengths to the surface and the tip, v_{S} and v_{T}, respectively.
2. The density of states at the Fermi level of the surface and the tip, ρ_{S} and ρ_{T}, respectively.
3. An overall prefactor, k, scaling with $k \propto v_{\mathsf{S}}^4 \rho_{\mathsf{S}}^2$.
4. The spin polarization of the tip, $\mathcal{P}_{\mathsf{T}} = \frac{\rho_{\mathsf{T}\uparrow} - \rho_{\mathsf{T}\downarrow}}{\rho_{\mathsf{T}\uparrow} + \rho_{\mathsf{T}\downarrow}}$.
5. The ratio between the spin-dependent and the spin-less coupling, $\zeta = \frac{\mathcal{T}}{\mathcal{T}_0}$.

The Kondo-like couplings are combined in dimensionless factors, $r_i = \frac{\rho_{\mathsf{T}}}{\rho_{\mathsf{S}}} \left(\frac{v_i^{\mathsf{T}}}{v_i^{\mathsf{S}}}\right)^2$ and $r_{ij}^{\mathsf{S}} = \left(\frac{v_i^{\mathsf{S}}}{v_j^{\mathsf{S}}}\right)^2$. The different dependencies on the tip are unknown, both from the experimental point of view, but also from first-principles, since the precise structure of the tip is not known. Therefore, all the parameters are typically fitted to experimental data [30, 34], e.g. temperature dependencies or voltage dependencies of the lifetimes. However, the surface-dependent quantities can be at least estimated from first principles, since the precise structure of the nanostructure is known.

From first-principles via the Anderson model to the Appelbaum hamiltonian

Obviously, the density of states of the surface electrons is known from first principles. The crucial ingredient, which has to be analyzed is the coupling strength of the nanostructure to the surface, v_{S}. This coupling strength is driving the surface-surface scattering processes, which determines the lifetime of an unprobed nanostructure, and also affects the lifetime of a probed nanostructure. This is therefore one of the most important ingredient for technological applications.

To relate first principles to the coupling strength and the Appelbaum hamiltonian, eq. (6.12), we make use of the semi-classical Anderson model, which was discussed in Chapter 5 in its local form. The general Anderson model [182] contains similar to the model used in this section a local spin hamiltonian $\mathcal{H}_{dd}$, an electron bath $\mathcal{H}_{kk}$, and a coupling between those $\mathcal{H}_{kd}$,

$$\mathcal{H} = \mathcal{H}_{dd} + \mathcal{H}_{kk} + \mathcal{H}_{kd} + \mathcal{H}_{dk} \quad . \tag{6.23}$$

The spin hamiltonian is given in a mean-field form by the d-states,

$$\mathcal{H}_{dd} = \sum_i \sum_{mm'} \sum_{\sigma\sigma'} \left[\delta_{\sigma\sigma'} E_{i,mm'}\, c^\dagger_{im\sigma} c_{im'\sigma} + U_{i,m\sigma,m'\sigma'}\, c^\dagger_{im\sigma} c_{im'\sigma'} \right] + \text{h.c.} + \mathcal{H}_{\mathsf{t}} \quad , \tag{6.24}$$

where i sums over the different spins, m labels the considered orbitals, σ is the spin, and $c^\dagger$ and c are creation and annihilation operators, respectively. The energy of the orbitals is given by $E_{i,mm'}$, which is spin independent. The spin splitting can be described by a Coulomb interaction in the mean field approximation described by $U_{i,m\sigma,m'\sigma'}$, where the diagonal part is traceless. The spin hamiltonian contains also the hopping between the sites, which in its most general form is given by

$$\mathcal{H}_{\mathsf{t}} = \sum_{ij} \sum_{mm'} \sum_{\sigma\sigma'} t_{im\sigma,jm'\sigma'}\, c^\dagger_{im\sigma} c_{jm'\sigma'} + \text{h.c.} \quad . \tag{6.25}$$

The hamiltonian of the electron bath is given by,

$$\mathcal{H}_{kk'} = \sum_k \sum_\sigma E_{kk'}\, c^\dagger_{k\sigma} c_{k'\sigma'} + \text{h.c.} \quad . \tag{6.26}$$

The coupling between the local spin hamiltonian and the electron bath, a Kondo-like s-d coupling, is given by,

$$\mathcal{H}_{kd} = \sum_i \sum_{mm'} \sum_\sigma \sum_k \; V_{k,im\sigma}\, a^\dagger_{k\sigma} c_{im\sigma} \quad , \tag{6.27}$$

and $\mathcal{H}_{dk} = \mathcal{H}^\dagger_{kd}$. In Chapter 5 we used an effective hamiltonian of the localized magnetic d-orbitals including the renormalization due to the electron bath, which can be obtained from the Green function of the full system,

$$G(E) = (E - \mathcal{H})^{-1} = \begin{pmatrix} E - \mathcal{H}_{dd} & -\mathcal{H}_{dk} \\ -\mathcal{H}_{kd} & E - \mathcal{H}_{kk} \end{pmatrix}^{-1} \quad , \tag{6.28}$$

by using block matrix inversion

$$G^{-1}_{dd}(E) = \big(E - \mathcal{H}_{dd} - \mathcal{H}_{dk}(E - \mathcal{H}_{kk})^{-1}\mathcal{H}_{kd}\big) \quad , \tag{6.29}$$

where $\mathcal{H}_{dd}$ is the unrenormalized Hamiltonian of the localized sites, $\mathcal{H}_{kd}$ is a part of the hybridization Hamiltonian and $\mathcal{H}_{kk}$ is the hamiltonian of the electron bath. The last part of eq. (6.29) gives rise to

$$\mathcal{H}_{dk}(E - \mathcal{H}_{kk})^{-1}\mathcal{H}_{kd} = \sum_{ij} \sum_{mm'} \sum_{\sigma\sigma'} \sum_{kk'} V^*_{k,im\sigma}(E - E_{kk'})^{-1} V_{k',jm'\sigma'}\, c^\dagger_{im\sigma} c_{jm'\sigma'} \tag{6.30}$$

$$= \sum_{ij} \sum_{mm'} \sum_{\sigma\sigma'} \Delta_{im\sigma,jm'\sigma'}(E)\, c^\dagger_{im\sigma} c_{jm'\sigma'} \quad , \tag{6.31}$$

where $\Delta_{im\sigma,jm'\sigma'}(E)$ is the so-called hybridization function, which in general is a complex quantity with a non-trivial energy dependence. In the wide-band limit it simplifies to the model used in Chapter 5, where a energy-independent hybridization Γ was used.

To relate the Anderson model to the Appelbaum hamiltonian the renormalization of the electron bath electrons has to be considered. Similarly one finds,

$$G^{-1}_{kk}(E) = \big(E - \mathcal{H}_{kk} - \mathcal{H}_{kd}(E - \mathcal{H}_{dd})^{-1}\mathcal{H}_{dk}\big) \quad , \tag{6.32}$$

which gives rise to

$$\mathcal{H}_{kd}(E - \mathcal{H}_{dd})^{-1}\mathcal{H}_{dk} = \sum_{ij} \sum_{mm'} \sum_{\sigma\sigma'} \sum_{kk'} V_{k,im\sigma}(E - E_{im\sigma,jm'\sigma'})^{-1} V^*_{k',jm'\sigma'}\, a^\dagger_{k\sigma} a_{k'\sigma'} \quad . \tag{6.33}$$

Taking only couplings from the electron bath to a state $|im\sigma\rangle$ and vice versa into account, and assuming $V_{k,im\sigma} = V$ the renormalization of the electron bath electrons simplifies to

$$\operatorname{Im} \mathcal{H}_{kd}(E - \mathcal{H}_{dd})^{-1}\mathcal{H}_{dk} = -\pi\rho_d(E)|V|^2 \sum_{kk'} a^\dagger_{k\sigma} a_{k'\sigma'} \quad , \tag{6.34}$$

where $\rho_d(E)$ is the local density of states of the local hamiltonian,

$$\rho_d(E) = -\frac{1}{\pi}\mathrm{Im}\,\mathrm{Tr}\,G_{dd}(E) \quad . \tag{6.35}$$

Under the same assumptions, the renormalized spin hamiltonian simplifies to,

$$\mathrm{Im}\,\mathcal{H}_{dk}(E-\mathcal{H}_{kk})^{-1}\mathcal{H}_{kd} = -\pi\rho_{\mathsf{S}}(E)|V|^2\sum_{ij}\sum_{mm'}\sum_{\sigma\sigma'} c^{\dagger}_{im\sigma}c_{jm'\sigma'} \quad , \tag{6.36}$$

where $\rho_{\mathsf{S}}(E)$ is the density of states of the bath electrons. The effective hybridization Γ of the localized magnetic d-orbitals with the surface electrons can therefore be related to the surface coupling v_{S} in the Appelbaum hamiltonian, which in the wide-band limit (metallic surface) gives,

$$v_{\mathsf{S}}^2 \propto \rho_d(E_{\mathsf{F}})|V|^2 \quad \text{and} \quad \Gamma \propto \rho_{\mathsf{S}}(E_{\mathsf{F}})|V|^2 \quad \Rightarrow \quad v_{\mathsf{S}} \propto \sqrt{\frac{\rho_d(E_{\mathsf{F}})}{\rho_{\mathsf{S}}(E_{\mathsf{F}})}\Gamma} \quad . \tag{6.37}$$

Thus, the Kondo-like coupling can be related to the density of states at the Fermi level of the surface and of the nanostructure and to the effective hybridization between the nanostructure and the surface.

The effective hybridization can be obtained from first principles using for example the Green function, which is available in the KKR formalism. Similar to eq. (6.29) block matrix inversion can be used to define an effective hamiltonian of a nanostructure taking indirectly the effect of the surface into account. To map first principles to an effective hamiltonian we first have to define the effective hamiltonian. Since we are dealing with nanostructures composed out of 3d transition metals, we restrict the effective hamiltonian to their d-orbitals. An extension to the general case is straightforward. We define an Anderson-like hamiltonian, which can be split into on-site contributions and the hoppings between different sites,

$$\mathcal{H}^{\mathsf{eff}} = \sum_i \mathcal{H}_i^{\mathsf{on\text{-}site}} + \sum_{ij}\mathcal{H}_{ij}^{\mathsf{hopping}} \quad , \tag{6.38}$$

with the on-site hamiltonian (omitting the site index),

$$\begin{aligned}\mathcal{H}^{\mathrm{on-site}} = \sum_{mm'}\sum_{ss'}\big(&E_d\,\delta_{mm'}\delta_{ss'} + U\,\boldsymbol{e}\cdot\boldsymbol{\sigma}_{ss'}\delta_{mm'} + \lambda\,\boldsymbol{L}_{mm'}\cdot\boldsymbol{\sigma}_{ss'} + \Delta^{(\mathrm{re})}_{mm'}\delta_{ss'} \\ &+ \mathrm{i}\Gamma\,\delta_{mm'}\delta_{ss'} + \mathrm{i}\Delta^{(\mathrm{im})}_{mm'}\delta_{ss'}\big)c^{\dagger}_{ims}c_{im's'} \quad ,\end{aligned} \tag{6.39}$$

where E_d is the energy of the d-orbitals corresponding to the chemical potential, U is the spin splitting, σ are the Pauli matrices, λ is the strength of the local spin-orbit coupling, $\boldsymbol{L}$ is the angular momentum operator, $\Delta^{(\mathsf{re})}$ is an trace-less orbital-dependent energy shift corresponding to the crystal field splitting, and Γ as well as $\Delta^{(\mathsf{im})}$ (trace-less) are hybridizations with the substrate. Due to the last two contributions coming from the hybridization with the surface the hamiltonian is non-hermitian.

The hopping hamiltonian is given by

$$\mathcal{H}_{ij}^{\mathsf{hopping}} = \sum_{mm'}\sum_{ss'} t_{ims,jm's'}c^{\dagger}_{ims}c_{jm's'} \quad , \tag{6.40}$$

where the hopping matrix $t_{ims,jm's'}$ is in general a complex quantity, which can be spin-dependent and non-hermitian. In Chapter 7, we will make extensive use of this mapping procedure and define effective hamiltonians for large nanostructures. Here, we are only interested in the effective hybridization Γ, which can be used to estimate the coupling of the nanostructure to the surface v_S.

Solution of the master equation

In the previous sections, we discussed how the transition rates can be calculated from a few model parameters and how the surface parameters relate to first principles. Here, we want to focus on how the scattering rates are related to the magnetic stability via the master equation. The master equation can be written in a matrix form as,

$$\frac{\mathrm{d}P_M}{\mathrm{d}t} = \sum_{MM'} A_{MM'} P_{M'} \quad \Rightarrow \quad \frac{\mathrm{d}\boldsymbol{P}}{\mathrm{d}t} = A\boldsymbol{P} \tag{6.41}$$

$$\text{with} \qquad A_{MM'} = W_{M'M} - \delta_{MM'} \sum_{M''} W_{MM''} \quad , \tag{6.42}$$

which can be solved using the matrix exponential,

$$\boldsymbol{P}(t) = \exp(At)\boldsymbol{P}(t=0) \quad . \tag{6.43}$$

Since the scattering rate $|M\rangle \to |M'\rangle$ differs in general from the scattering rate $|M'\rangle \to |M\rangle$, A is a non-hermitian matrix for which left and right eigenvectors have to be used in order to diagonalize it. The diagonal matrix D is given by,

$$D = S^{-1}AS \quad \text{with} \quad S = (\boldsymbol{r}_1, \boldsymbol{r}_2, \ldots) \quad , \quad S^{-1} = \begin{pmatrix} \boldsymbol{l}_1^\mathrm{T} \\ \boldsymbol{l}_2^\mathrm{T} \\ \vdots \end{pmatrix} \quad \text{and} \quad D = \begin{pmatrix} \lambda_1 & 0 & \ldots \\ 0 & \lambda_2 & \ldots \\ \vdots & \vdots & \ddots \end{pmatrix} \quad , \tag{6.44}$$

where λ_n is the eigenvalue corresponding to the right and left eigenvector $\boldsymbol{r}_n$ and $\boldsymbol{l}_n$, respectively, fulfilling,

$$A\boldsymbol{r}_n = \lambda_n \boldsymbol{r}_n \quad \text{and} \quad \boldsymbol{l}_n A = \lambda_n \boldsymbol{l}_n \quad . \tag{6.45}$$

The solution of the ordinary differential equation reduces to an exponential of a diagonal matrix,

$$\boldsymbol{P}(t) = S\exp(Dt)S^{-1}\boldsymbol{P}(t=0) \quad \Rightarrow \quad P_M(t) = \sum_{nM'} r_M^n \exp(\lambda_n t) l_{M'}^n P_{M'}(0) \quad . \tag{6.46}$$

The eigenvalues of A drive different exponential decays. From the physical point of view, A needs an eigenvalue 0 corresponding to the stationary solution. Furthermore, the eigenvalues have to be smaller than 0 to ensure the normalization of $\boldsymbol{P}(t)$ and a convergence to the stationary solution. The different lifetimes can be defined as the inverse of the eigenvalue, $\tau_n = -1/\lambda_n$. The longest lifetime is given by the second largest eigenvalue. If we consider the simple case of a single spin in a uniaxial anisotropy shown in Fig. 6.2a, the longest lifetime should be related to the process of flipping the spin from one ground state to the other. However, the master equation itself cannot describe exactly this process since it always describes processes approaching the stationary solution, which in general is a combination of many states. In the following we approximate the experimentally measured lifetime, which originates from the flipping of a spin from one ground state to the other, by the longest lifetime present in the master equation approach.

Projection scheme

The eigenvalues of A give rise to the different lifetimes present in the system, but they do not give any information about the importance of the associated decay processes. This is of special importance if more than one spin is considered. For example in the case of two uncoupled spins the ground state lifetime of each spin should be recovered. The scheme, which was used so far, gives only rise to the longest lifetime of the system and can not separate the lifetimes associated to each building block of the total system. To overcome this problem, a projection scheme can be used. Assume for the sake of simplicity the state $|M\rangle$ being composed out of a tensor product of two separate spins,

$$|M\rangle = \sum_{m_1 m_2} C^M_{m_1 m_2} |m_1\rangle \otimes |m_2\rangle \quad , \tag{6.47}$$

with the expansion coefficient $C^M_{m_1 m_2}$. Instead of looking at the probability to find the system in the state $|M\rangle$, we can calculate the probability of finding the system in a state $|m_1\rangle$ of the first spin, while the second spin can be in an arbitrary state,

$$\begin{aligned} P_{m_1}(t) =& \sum_{m_2} \langle m_1| \otimes \langle m_2| \left[\sum_M P_M(t) |M\rangle\langle M| \right] |m_1\rangle \otimes |m_2\rangle \\ =& \sum_{m_2}\sum_M P_M(t) |C^M_{m_1 m_2}|^2 = \sum_n \exp(\lambda_n t) \sum_{m_2 M M'} |C^M_{m_1 m_2}|^2\, r^n_M l^n_{M'} P_{M'}(0) \\ =& \sum_n \exp(\lambda_n t) P^n_{m_1} \quad , \end{aligned} \tag{6.48}$$

where eq. (6.46) was used and $P^n_{m_1}$ is a measure for the importance of the process associated to the lifetime τ_n. This expansion coefficient depends on the initial configuration, which in order to describe the flipping process between two ground states should be one of the ground states, e.g. spin up or spin down in the case of the uniaxial anisotropy. For a multi-spin system using this approach the most important process and the related lifetimes can be identified separately for each spin.

6.2. Magnetic stability of a single spin

In this section, the master equation approach will be applied to the case of a single spin. Magnetic nanostructures are often described in the so-called macro spin approximation as a single magnetic unit acting like a single spin, e.g. in the case of a five atomic Fe cluster

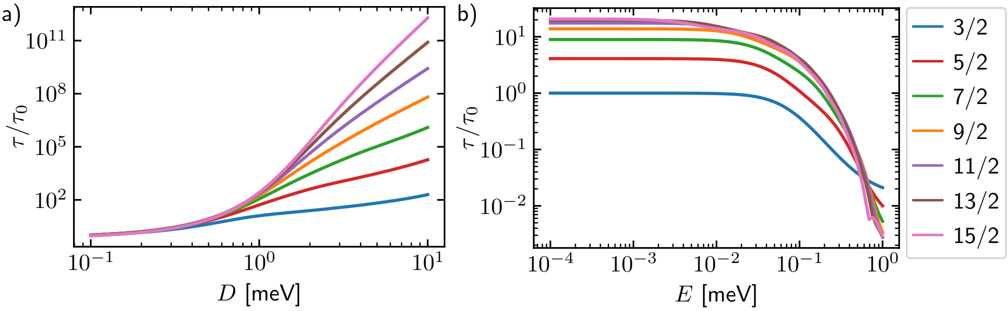

Figure 6.4.: Dependence of the lifetime of a single macro spin on the magnetic anisotropy. Shown are half-integer spins ranging from $S = 3/2$ to $S = 15/2$. a) Out-of-plane anisotropy $D > 0$. b) In-plane anisotropy E with $D = 1\,\text{meV}$. The model parameters are $\mathcal{P}_\mathsf{T} = 0.1$, $v_\mathsf{T}/v_\mathsf{S} = 0.07$, $V = 10\,\text{meV}$, $T = 1\,\text{K}$ and an arbitrary prefactor k, which determines τ_0. The tip parameters were taken from Ref. [38].

deposited on Cu(111) [34] or an Fe trimer deposited on Pt(111) [30]. The quantum spin S can be estimated by the total magnetic moment of the nanostructure including its spin and orbital degrees of freedom. For an Fe adatom on the Pt(111) surface one finds a spin of $S = 5/2$ according to a total magnetic moment of approximately $m = 4.6\,\mu_\mathsf{B}$ (see Table 3.2), while for a fcc-top stacked Fe trimer a magnetic moment of $12\,\mu_\mathsf{B}$ (see Table 3.5) gives rise to a total spin of $S = 12/2$. However, in References [30] and [38] the fcc-top stacked Fe trimer is approximated by $S = 11/2$, which we also assume in the following.

6.2.1. Out-of-plane vs. in-plane magnetic anisotropy

To illustrate the dependence of the magnetic stability on the magnetic anisotropy, we use a half-integer macro spin in an out-of-plane anisotropy D and an in-plane anisotropy E, which result in the spin hamiltonian shown in eq. (6.7) for a $S = 11/2$. We assume the out-of-plane anisotropy to be the dominant anisotropy, $|D| > |E|$. The energy spectrum illustrated in Fig. 6.2a span a parabola of amplitude $\Delta E = |D|(S^2 - 1/4)$ and with a level spacing of $E_n - E_{n+1} = D\,(2S_z - 1)$. The scattering rates, eqs. (6.18) - (6.21), depend via the $\mathcal{G}$ function on the level spacings and the external voltage V, which for experimental temperatures (300 mK ≈ 25 µeV) and realistic anisotropies ($> 0.1\,\text{meV}$) is a linear function for positive energy difference and zero for negative energy differences.

Figure 6.4a shows the dependence of the magnetic lifetimes on a out-of-plane magnetic anisotropy D for several spins. The general trend explained in the introduction is recovered: The magnetic stability increases with the size of the spin S and the out-of-plane anisotropy drastically increases the magnetic stability. The dependence on the magnetic anisotropy also increases with the size of the spin, which is related to the total energy barrier scaling with S^2.

The impact of an in-plane anisotropy is shown in Fig. 6.4b. Even a small in-plane anisotropy of $E/D = 10^{-1}$ can reduce the magnetic stability by an order of magnitude. If the in-plane anisotropy is comparable to the out-of-plane uniaxial anisotropy the lifetimes can drop by up

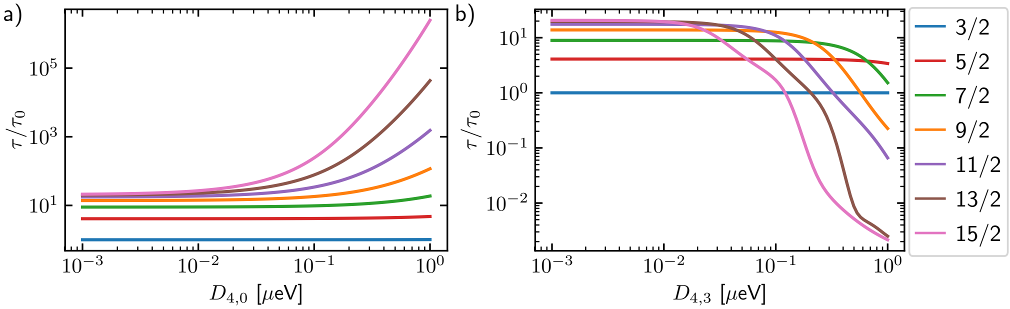

Figure 6.5.: Dependence of the lifetime of a single macro spin on the magnetic anisotropy. Shown are half-integer spins ranging from $S = 3/2$ to $S = 15/2$. a) Out-of-plane fourth-order anisotropy $D_{4,0} > 0$ with $D = 1$ meV. b) In-plane fourth-order anisotropy $D_{4,3}$ with $D = 1$ meV. The model parameters are $\mathcal{P}_\mathsf{T} = 0.1$, $v_\mathsf{T}/v_\mathsf{S} = 0.07$, $V = 10$ meV, $T = 1$ K and an arbitrary prefactor k, which determines τ_0. The tip parameters were taken from Ref. [38].

to three orders of magnitude. Due to the mixing of states with $\Delta S_z = \pm 2$, which is induced by the in-plane anisotropy, the magnetic stability is drastically decreased as argued in Section 6.1.1.

6.2.2. Impact of higher-order magnetic anisotropies

Higher-order magnetic anisotropies are present in any realisitc system, but are often orders of magnitude smaller than the second order anisotropies. Their effect on the magnetic stability is a priori unclear. Here, we focus on the two fourth-order anisotropies, which are allowed in a system with C_{3v} symmetry, discussed in relation to eq. (6.6), resulting in the spin hamiltonian,

$$\mathcal{H} = -D\, S_z^2 - D_{4,0}\, S_z^4 - \frac{1}{2}\, D_{4,3}\, \left(S_z(S_+^3 + S_-^3) + (S_+^3 + S_-^3)S_z\right) \quad . \tag{6.49}$$

Figure 6.5a shows the magnetic stability as function of the fourth-order out-of-plane anisotropy $D_{4,0}$. In total, the dependence is quite similar to the second-order out-of-plane anisotropy, but with an even stronger dependence on the total spin S. The impact of the higher-order in-plane anisotropy is shown in Fig. 6.5b. The in-plane anisotropy mixes states with $\Delta S_z = \pm 3$ resulting in no effect for $S = 3/2$, since no states can be mixed. With increasing spin the fourth-order in-plane anisotropy shows a significant destabilization. Note that the total energy barriers induces by the fourth-order anisotropy scale with S^4.

6.2.3. Effective magnetic anisotropy in the macro spin approximation

In the previous section, we showed how the magnetic stability of a single spin is affected by different anisotropies. The assumption of a single spin is often used even for nanostructures composed out of multiple atoms in the spirit of the so-called macro spin approximation, which is mainly due to the fact that the Hilbert space scales exponentially with the number of considered spins, and therefore, multi-spin quantum models are computationally demanding. Under this assumption, the building blocks of a nanostructure act collectively like a single spin. In Chapter 4 the impacts of internal interactions in a nanostructure using the semi-classical Heisenberg model were discussed. We saw that even with a dominant isotropic ferromagnetic bilinear interaction internal interactions like the DMI or higher-order interactions can yield non-collinearities in the nanostructure. These non-collinearities are neglected within the macro-spin approximation. However, they can affect the magnetic anisotropy of the macro-spin as can be seen as follows. Here, we focus on the case of the fcc-top-stacked Fe trimer deposited on the Pt(111) surface, which is of huge interest experimentally [30, 38] and will be analyzed in the next sections of this chapter. The macro spin is described by an on-site anisotropy, like shown in eq. (6.4) due to the C_{3v} symmetry of the trimer,

$$\mathcal{H}^{\mathsf{MS}}(\boldsymbol{e}) = K_{zz} e_z^2 \quad . \tag{6.50}$$

Note that we work here in the semi-classical representation to allow for a comparision with the results obtained in Chapter 4, which can straightforwardly be mapped to the quantum spin model used in the remainder of this Chapter. The full nanostructure, however, is described by a Heisenberg model, like discussed in Section 4.4.1. To map from the complex Heisenberg model, eventually even including higher-order interactions, to an effective on-site anisotropy of a single spin, an external magnetic field can be utilized. Minimizing the complete Heisenberg model for several different orientations of the magnetic field, e.g. based on the Lebedev mesh, one finds the ground state orientation of all spins of the nanostructure,

$$\frac{\mathrm{d}}{\mathrm{d}\boldsymbol{e}_i} \mathcal{H}^{\mathsf{Heisenberg}}(\{\boldsymbol{e}\}, \boldsymbol{B}) = 0 \quad \Rightarrow \quad \{\boldsymbol{e}^{\mathsf{GS}}(\boldsymbol{B})\} \quad , \tag{6.51}$$

which implicitly depend on the strength and the orientation of the magnetic field. In the case of the Fe trimer, the internal interactions yield an effective opening of the three magnetic moments. A weak magnetic field is able to rotate the magnetic moments keeping an effective opening angle between the three moments, which depending on the orientation may be affected. In contrast, a strong magnetic field (in comparison to the internal interactions) yields a collinear magnetic trimer, which can not be affected by the internal interactions. The ground state orientations can be averaged to obtain an effective direction of the macro spin, $\boldsymbol{e}^{\mathsf{MS}} = 1/N \sum_i \boldsymbol{e}_i$, which can be used to fit to an effective on-site anisotropy.

Figure 6.6 shows the magnetic anisotropy of an effective macro spin as function of the applied external magnetic field using the full parametrization of the Fe trimer deposited on Pt(111) up to the bilinear level shown in Table 4.4. The total anisotropy varies by more than 0.6 meV for the two different regimes of weak magnetic field and strong magnetic field. More importantly, the anisotropy changes sign favouring an out-of-plane configuration for weak magnetic fields, while in-plane configurations are favoured for strong magnetic fields. The internal interactions being responsible for non-collinearities are the on-site anisotropy, the DMI and the anisotropic exchange, which are of the order of 10 meV. Once the magnetic field can compete with the internal interactions ($\mu_{\mathrm{B}} = 0.058\,\mathrm{meV\,T^{-1}}$) a change in the anisotropy constant K of the macro spin can be seen.

In this section, we discussed the lifetime of a single spin seen in a telegraph noise experiment and its dependence on the on-site anisotropy. For a probed isolated nanostructure, we discussed the macro spin approximation, in which the internal building blocks and interactions

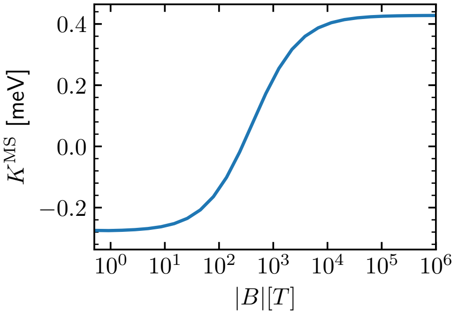

Figure 6.6.: Fitted magnetic anisotropy of the fcc-top-stacked Fe trimer on the Pt(111) surface in the macro spin approximation as function of the strength of the magnetic field. The self-consistent energy landscape of the non-collinear trimer exposed to different external magnetic fields is mapped to the energy landscape of a single spin in a C_{3v} symmetry with the anisotropy constant K^{MS}. All internal interaction up to the bilinear level are taken into account (see parametrization in Table 4.4).

are described by a single spin in an effective anisotropy. In the next section, we will extend this study and investigate the impact of interactions between nanostructures on the lifetime.

6.3. Magnetic stability of coupled nanostructures: The case of trimer and adatom

This section describes a collaborative work with the group of Dr. Jens Wiebe at the University of Hamburg. To set the ground, we first discuss the experimental findings and then use a combination of first principles and the master equation model to explain and disentangle the experimental findings.

6.3.1. Experimental findings

The experimentalists used lateral atom manipulation as illustrated in Fig. 6.7a to manipulate the position of an Fe adatom close to a central fcc-top-stacked Fe trimer. The lifetime of the trimer-adatom-complex can be probed from two different perspectives, either with the tip placed on the trimer or with the tip placed on the adatom, and therefore, with an electric current flowing through the timer or the adatom, respectively. The STM is operated in the so-called constant current mode, in which the distance to the surface is adjusted such that the current stays constant upon a change of the resistance either due to the topography or due to a change of the magnetization. An illustration of the measured telegraph noise is shown in Fig. 6.7b. Using the lateral atom manipulation several different positions of the adatom with respect to the trimer were investigated as illustrated in Fig. 6.7c. The magnetic orientation of the adatom with respect to the trimer was analyzed experimentally indicating an ferromagnetic

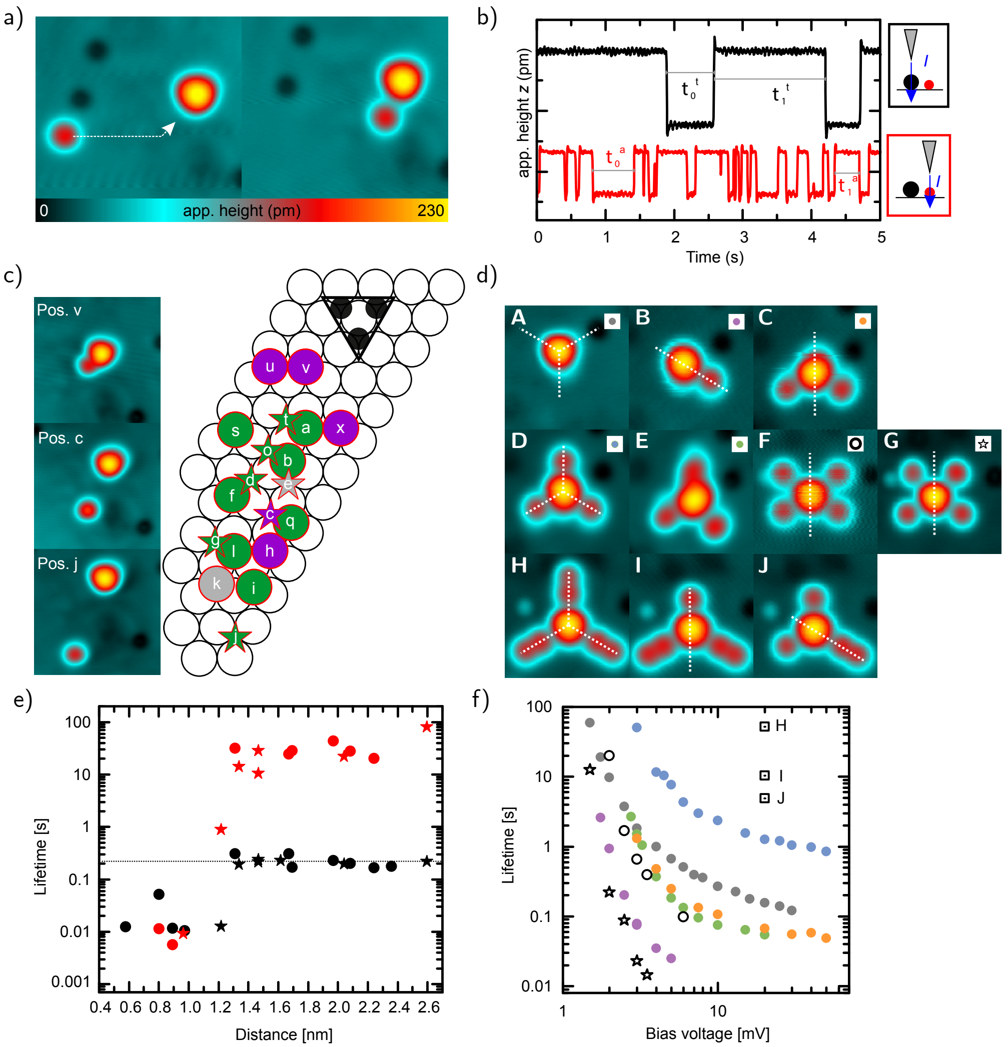

Figure 6.7.: Scanning tunneling microscopy measurements from different Fe-based structures on the Pt(111) surface. a) Illustration of the lateral atom manipulation of a single adatom close to a central Fe trimer. b) Example of a telegraph noise measurement of the trimer (black curve) and the adatom (red curve). c) Illustration of the different positions of the Fe adatom with respect to the fcc-top-stacked Fe trimer. Circles indicate a fcc-stacking position, while stars indicate a hcp-stacking positions. d) Illustration of several larger nanostructures composed out of a central fcc-top-stacked trimer and various adatoms surrounding it. The dotted lines indicate the present symmetries. e) Lifetimes of the trimer-adatom complex measured on the trimer (black) and on the adatom (red). The considered positions are shown in c). f) Voltage dependence of the lifetimes measured on the central trimer for the complexes shown in d). The Figures were taken from Reference [38].

alignment (purple) or an antiferromagnetic alignment (green). The lifetimes measured on the trimer and the adatom for all the positions are shown in Fig. 6.7e. The black data set is the measurement on the trimer, which indicates that the close-by adatom can have a strong impact on the lifetime of the trimer. The measurement can be separated into three regimes: The long-distance regime, an intermediate-distance regime and the close-distance regime. In the close-distance regime ($< 1.0\,\mathrm{nm}$) the lifetime of the trimer drops by more than one order of magnitude compared to the long-distance regime ($> 1.4\,\mathrm{nm}$). This finding contradicts with the well-known situation discussed in relation to Fig. 6.2c: Combining two spins enlarges the total spin, which should stabilize the structure. In the long-distance limit the lifetime of the isolated trimer is recovered (dashed black line). Another surprising finding appeared when the adatom is probed. In the close-distance regime the lifetimes of trimer and adatom coincide. However, in the long-distance regime the lifetime of the adatom surpasses the lifetime measured on the trimer, which is surprising for two reasons: First, the adatom being the smaller spin and having the smaller magnetic anisotropy should be less stable than the trimer, and second, the isolated adatom does not show any telegraph noise signature on its own. So far, an isolated adatom deposited on a metallic surface did not show any telegraph noise signal. Thus, from this measurement two questions arise: Why is the adatom destabilizing the trimer in the close-distance regime, and why is a long lifetime measured on the adatom in the long-distance regime?

In an additional measurement, the impact of the symmetry on the magnetic lifetime was investigated. Using multiple adatoms, which are placed in several different positions in the close-distance regime, more complex structures were built. The structures, which are depicted in Fig. 6.7d, obey different symmetries – namely no symmetry, C_s symmetry, C_{3v} symmetry. The lifetime of the central trimer is measured as function of the bias voltage, which is shown in Fig. 6.7f. The data set shows two trends: First, adding atoms does not necessarily stabilize the central trimer, and second, obeying the highest possible symmetry (C_{3v}) significantly enhances the lifetime of the central trimer. The first point can be seen by comparing the isolated trimer to the other systems. Adding one and two adatoms generally destabilizes the trimer, while adding three adatoms can still destabilize the trimer depending on the total symmetry of the system. The second point is noticeable, when comparing two systems having the same number of atoms, but different symmetries, e.g. the trimer with three additional adatoms obeying the C_{3v} symmetry (blue dot) and obeying no symmetry (green dot). The symmetric construction of the complex enhances the lifetime by almost two orders of magnitude. From this experiment we can raise one central question: Why does the symmetric placement of the nearby atoms drastically affect the lifetime of the central trimer?

In the next sections, we investigate these different findings from the theoretical point of view and answer the raised questions. We start with the magnetic configurations from first principles and continue with the description of the magnetic lifetimes from the master equation model.

6.3.2. Magnetic exchange interactions and simulated magnetic lifetimes

In a first step, the magnetic exchange interactions between a central fcc-top-stacked Fe trimer and an Fe adatom deposited on the Pt(111) surface are calculated for several positions of the Fe adatom. The computational details are similar to the ones discussed in Chapter 4. Each nanostructure is surrounded by its nearest-neighboring Pt cluster and calculated self-consistently. The magnetic exchange interactions are obtained by using the infinitesimal rotation method (Lichtenstein formula, see eq. (4.7)), which allows for an extraction of all interactions up the bilinear level. The magnetic anisotropy of the fcc-top-stacked Fe trimer in the macro spin approximation was discussed in Section 6.2.3 and found to be $K = -0.28\,\text{meV}$. However, this value differs drastically from the experimental finding of $D = -0.09\,\text{meV} \overset{\wedge}{=} K = -3.2\,\text{meV}$ [30], which will be used in the following. In the case of the isolated fcc-stacked adatom, the experimental anisotropy and the theoretical anisotropy obtained from band energy differences using the magnetic force theorem agree well with $K^{\text{exp}} = -1.66\,\text{meV} \overset{\wedge}{=} D = -0.19\,\text{meV}$ [34] and $K^{\text{theo}} = -1.92\,\text{meV}$.

The magnetic exchange interactions are shown in Fig. 6.8a-e. Shown are effective magnetic interactions between the three trimer atoms and the single adatom by summing the trimer degrees of freedom, e.g. (the site labelled i is the adatom)

$$J = \sum_{j\,\in\,\text{trimer}} J_{ij} \quad \text{and} \quad \boldsymbol{D} = \sum_{j\,\in\,\text{trimer}} \boldsymbol{D}_{ij} \quad , \tag{6.52}$$

which is the effective interaction between the adatom labeled i and the trimer. The maps of the isotropic exchange interaction J (a), the absolute value of the DMI $|\boldsymbol{D}|$ (b) and the largest absolute eigenvalue of the symmetric exchange (c) indicate oscillations, which are known for the RKKY interactions mediated by the surface electrons [62, 63]. All the interactions follow the C_{3v} symmetry of the system. Figures 6.8d and e show the magnetic interactions for the experimentally probed sites (see Fig. 6.7b). Apart from the present oscillations of the magnitudes, all interactions show a power-law decay as function of the distance. However, the power laws are different, which can be seen by comparing the close-range regime being dominated by the isotropic exchange and the long-range regime, for which the DMI and the anisotropic symmetric exchange are one order of magnitude larger than the isotropic exchange. To compare the magnetic interactions to the experimental findings, we use a classical Heisenberg model. Since the trimer has strong internal ferromagnetic interactions (see Section 4.4.1) and a strong experimental magnetic anisotropy, we approximate it by a single spin pointing out-of-plane. The remaining degree of freedom is the magnetic orientation of the adatom $\boldsymbol{e}_\text{a}$, which is obtained from minimizing the Heisenberg model,

$$\mathcal{H} = K_\text{a}(e^z_\text{a})^2 + Je^z_\text{a} + D^x e^y_\text{a} - D^y e^x_\text{a} + J^{xz}_\text{sym} e^x_\text{a} + J^{yz}_\text{sym} e^y_\text{a} + J^{zz}_\text{sym} e^z_\text{a} \quad . \tag{6.53}$$

The polar angle ϑ, which is the effective angle between the adatom and the trimer, is shown in Fig. 6.8f for all the possible positions of the adatom. In the close distance regime some noticeable non-collinearities are present, which for intermediate and long distances vanish due to the dominating out-of-plane magnetic anisotropy of the adatom. In total a complicated spatially anisotropic pattern of ferro- and antiferromagnetic alignments is present. Remarkably, comparing to the experimental measurements shown in Fig. 6.7c, the theoretical predictions are correct for all positions except position i, which is in long-distance regime and therefore exhibits only weak interactions resulting in a low contrast in experiment.

In a next step, the magnetic lifetimes were simulated using the master equation approach. As described in the introduction of this chapter, the trimer is modelled as a $S = 11/2$ spin, while the adatom is modelled as a $S = 5/2$ spin. The quantum Heisenberg model is constructed according to the classical Heisenberg model by replacing $\boldsymbol{e} \to \boldsymbol{S}/\sqrt{S(S+1)}$. The coupling ratio of the trimer are taken from Ref. [30], where detailed temperature- and voltage-dependent

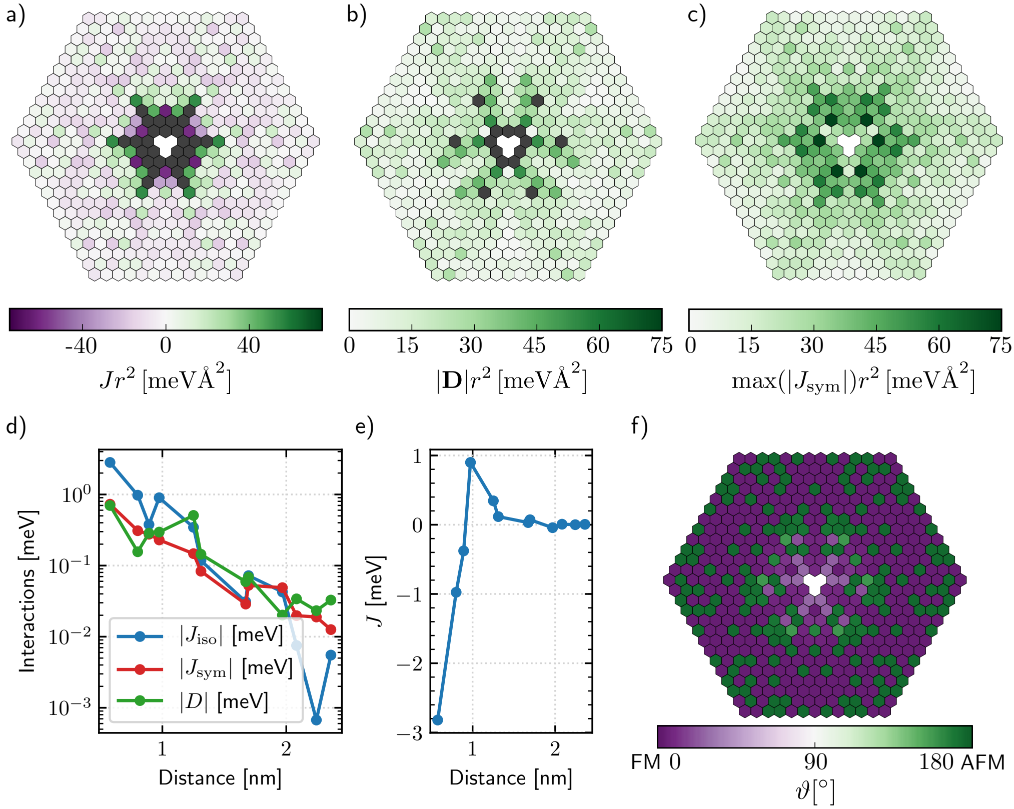

Figure 6.8.: Magnetic exchange interactions between a central fcc-top-stacked Fe trimer and an Fe adatom deposited on the Pt(111). The parameters are intended for a classical Heisenberg model with unit vectors and have to be scaled when used in a quantum Heisenberg model. a)-c) Maps of the isotropic exchange interaction (a), the DMI (b), and the anisotropic symmetric exchange interaction (c) for all possible positions of the adatom. The interactions are scaled by the square of the distance r^2. A grey color indicates that the value is out of the range of the colour scale. For the symmetric exchange the maximal absolute eigenvalue is shown. d) Logarithmic plot of the interactions for the experimental positions. e) Isotropic exchange interactions for the experimental positions. f) Magnetic ground state of the adatom trimer complex. Shown is the effective angle ϑ between the trimer and the adatom obtained from minimizing a classical Heisenberg model (see main text for a description of the method).

studies of the isolated trimer were performed. Since the isolated adatom shows no telegraph noise signal, similar studies cannot be performed for the adatom. Therefore, the coupling ratio of the adatom is a priori an unknown. Even though the coupling to the surface can be estimated using first principles, as will be shown in Section 6.4, the coupling to the tip cannot be determined. Hence, we assume that the adatom has the same coupling to the tip as the trimer, and the surface coupling differs by a factor of $v_\mathrm{S}^\mathrm{trimer}/v_\mathrm{S}^\mathrm{adatom} = 3.5$. The overall parameter k determining the scattering rates is fitted, such that the lifetime of the isolated trimer agrees with the experimental value of $\tau_\mathrm{trimer}^\mathrm{probed} = 0.48\,\mathrm{s}$. The simulated magnetic lifetimes are shown in Figure 6.9 for the case of the probed trimer (a) and the probed adatom (b). Similar to the experimental results, we separate the results into three regimes, which are discussed in the following.

Long-distance regime: Weak magnetic exchange as a sensor for magnetic stability

In the long-distance regime, where the trimer and the adatom are coupled weakly, the simulation of the probed trimer (Fig. 6.9a) recovers the lifetimes of the isolated trimer, which proves that the weakly-coupled adatom has no impact on the trimer. In contrast, an isolated probed adatom shows a lifetime of $\tau_\mathrm{adatom}^\mathrm{probed} = 13\,\mu\mathrm{s}$ in the simulation, but the longest lifetime seen when the adatom is probed while coupled to the trimer (Fig. 6.9) reaches up to $10^6\,\mathrm{s}$. The isolated unprobed trimer has a simulated lifetime of $\tau_\mathrm{trimer}^\mathrm{unprobed} = 8 \times 10^5\,\mathrm{s}$, while the unprobed adatom shows a lifetime of $\tau_\mathrm{adatom}^\mathrm{unprobed} = 0.4\,\mathrm{s}$.

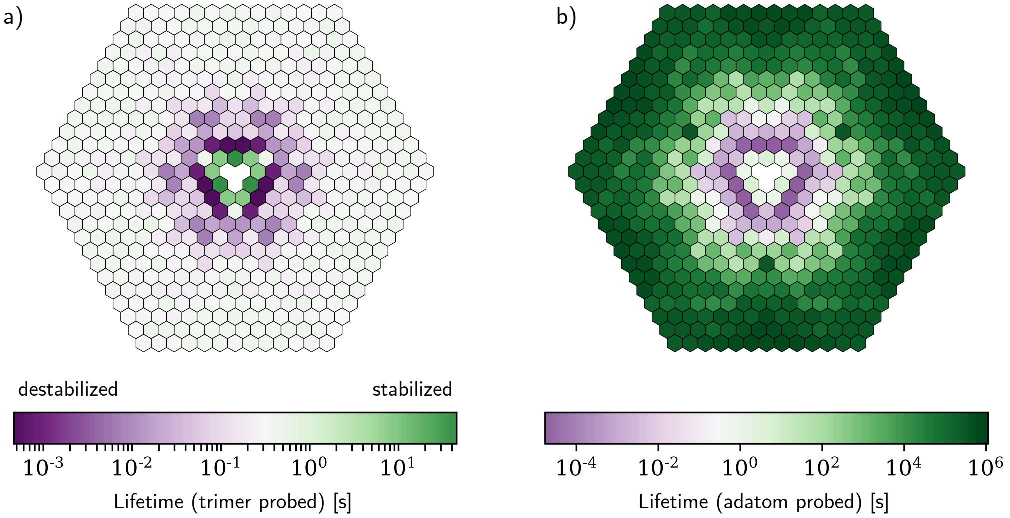

Figure 6.9.: Magnetic lifetimes simulated using the master equation approach for several positions of the adatom. Shown is the longest lifetime of the combined system. a) Trimer probed. b) Adatom probed. The spin model was constructed using the DFT parameters as described in the main text. The coupling ratio $v_\mathrm{T}/v_\mathrm{S} = 0.07$ of the trimer was taken from Ref. [30]. The overall parameter k was adjusted such that the lifetime of the isolated trimer fits the experimental finding of $\tau = 0.48\,\mathrm{s}$ (white color). The coupling ratio of the adatom was assumed to be the same as the one of the trimer.

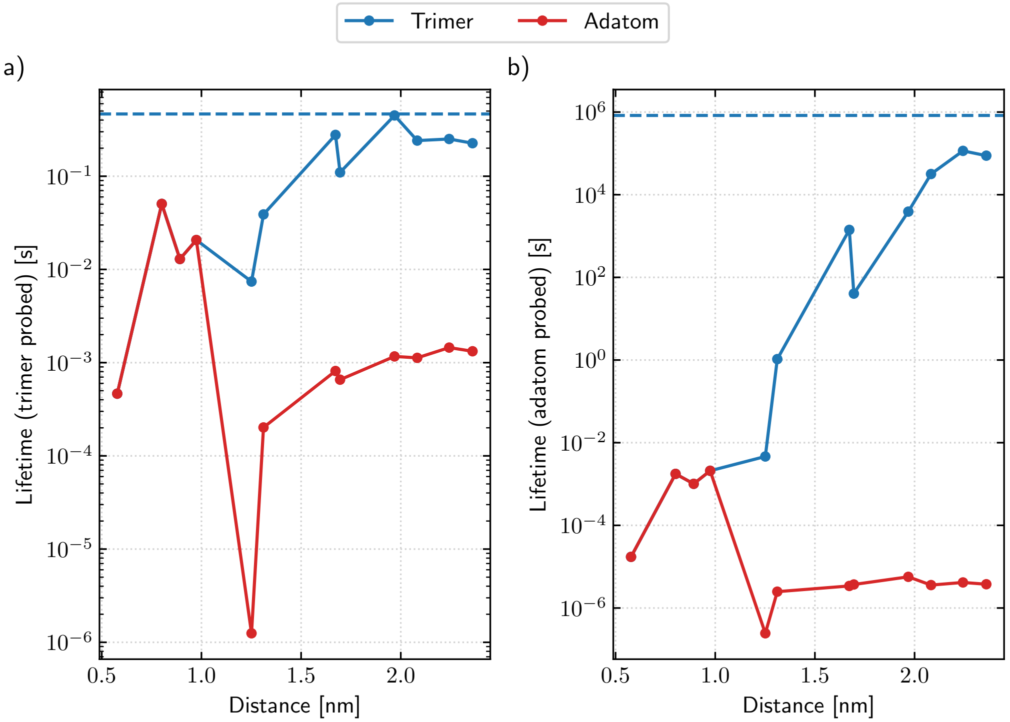

Figure 6.10.: Magnetic lifetimes of the trimer-adatom complex for the experimental positions. Shown are the lifetimes of the most important processes projected on the trimer (blue curves) and the adatom (red curves) obtained from eq. (6.48). a) Trimer probed. The dashed blue line indicates the lifetime of the isolated probed trimer $\tau = 0.48\,\mathrm{s}$. b) Adatom probed. The dashed blue line indicates the theoretical lifetime of the isolated unprobed trimer $8 \times 10^5\,\mathrm{s}$. The used model parameters are described in the main text.

To further investigate the simulated lifetimes, Fig. 6.10 shows the most important lifetimes projected on the subspace of the trimer and of the adatom as described in relation to eq. (6.48). In the close-distance regime, both projections yield the same lifetime showing that the strongly coupled trimer-adatom complex acts similar to a single unit. In the long-distance regime trimer and adatom show separate lifetimes. In the case of the probed trimer (a) the trimer approaches the experimentally measured lifetime with increasing separation to the adatom, while the adatom (unprobed by the tip) shows a lifetime in the order of $1\,\mathrm{ms}$ for the smallest separation, which is increasing as function of the distance. In the case of the probed adatom, the adatom shows a constant lifetime of the order of $10\,\mu\mathrm{s}$. In contrast, the trimer (unprobed by the tip) shows an increasing lifetime with increasing separation to the adatom, approaching the one of the unprobed trimer. Thus, the longest lifetime of the setup with the probed adatom is much larger than the longest lifetime of the probed trimer, similar to the experimental findings.

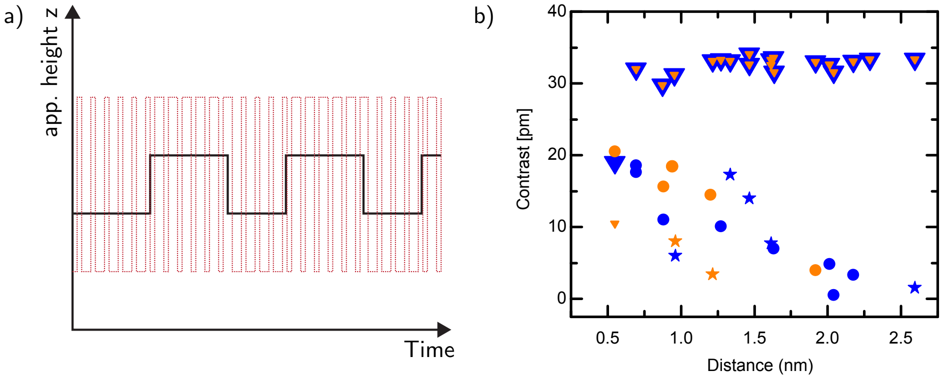

Figure 6.11.: Illustration of the asymmetry induced to the telegraph noise signal of the adatom by the unprobed trimer. a) The fast signal representing the actual switching of the adatom between its two ground states (red curve) can not be probed due to the slower temporal resolution of the STM. The slowly switching trimer induces an asymmetry to this signal via its weak coupling with the adatom (when the trimer and the adatom are aligned in a way that favours their magnetic coupling, the adatom remains a little longer in its magnetic state). This results in an average signal (black curve) corresponding to the magnetic state of the trimer, but probed via the weakly-coupled adatom. b) Experimental contrast (height difference between the two detected magnetic states) plotted as a function of the distance between trimer and adatom of the data sets used to determine the lifetimes shown in Fig. 6.7e. The triangles correspond to the probed trimer, while the circles and stars correspond to the measurement of the adatom. Figure b was taken from Ref. [38].

The main remaining question is: Why does the experiment detect the lifetime of the unprobed trimer in the telegraph noise signal of the adatom? We know that the isolated adatom cannot be detected by the telegraph noise experiments, since the time resolution in the experiments is of the order of $1\,\mathrm{ms}$, but the simulation indicates a lifetime of the probed adatom of the order of $10\,\mu\mathrm{s}$. However, it is known that a magnetic field induces an asymmetry in the telegraph noise signal. The magnetic field favours a certain direction of the spin resulting in a destabilization of one state over the other. Similarly, the weak magnetic coupling of the trimer to the adatom can induce an asymmetry in the telegraph noise favouring a certain orientation of the adatom, which is either ferro- or antiferromagnetic with respect to the trimer depending on the position of the adatom (see Fig. 6.8f). This asymmetry is indicated in Fig. 6.11a. Due to the time resolution of the experiment the asymmetry averages out resulting in an effective signal measured from the adatom and induced by the unprobed trimer. This hypothesis is strongly supported by the distance dependence of the experimental contrast shown in Fig. 6.11b. The contrast present in the measurement of the adatom decays towards no contrast as function of the distance between the trimer and the adatom due to the averaging process, while the contrast measured on the trimer is constant for all distances. Therefore, we can conclude that the adatom acts as a non-local sensor for the magnetic state of the unprobed trimer, which is drastically stabilized since it does not interact with the tip, but only with the surface.

Note that the lifetimes of the unprobed trimer presented in this section have two uncertainties: First, the used master equation approach in its current version does only include excitations arising from the temperature of the system and the external voltage and neglects quantum effects like e.g. zero-point spin fluctuations [39], which could be important for the surface-surface scattering. However, if a voltage is applied we do not expect those effects to be important, since the voltage excites the full spectrum of the magnetic anisotropy outweighing the effects of zero-point fluctuations. Second, in Section 6.2.2 we discussed the impact of higher-order magnetic anisotropies on the magnetic lifetime. Those anisotropies are also present in the trimer, but were neglected in this study. They might have a non-trivial impact on the lifetime of the probed and unprobed trimer. Combining those two uncertainties most probably results in the disagreement between the experimental measured lifetime of $100\,\mathrm{s}$ and the simulated one of 10^6 s.

Intermediate-distance regime: Destabilization via the Dzyaloshinskii-Moriya interaction

The next question we want to address is the source of the sudden decrease of the lifetime in the intermediate-distance regime starting at $1.4\,\mathrm{nm}$. In the experimental measurements the lifetimes of the probed trimer drop by more than one order or magnitude, while the probed adatom shows a drop by even more than three orders of magnitude (see Fig. 6.7e). On physical grounds, a magnetic interaction changing as function of the distance has to induce the sudden drop of the magnetic lifetime.

To examine the validity of this reasoning, we consider separately the impact on the magnetic lifetime of each kind of interaction. Fig. 6.12a shows the impact of the isotropic exchange interaction for the trimer-adatom complex neglecting all other magnetic interactions and considering only the local magnetic anisotropy of each of the constituents. A weak isotropic exchange induces a decrease of the longest lifetime of the system regardless of whether the interaction is ferromagnetic or antiferromagnetic. This might be related to a destabilization of the trimer by the adatom. For stronger isotropic interactions a clear separation between ferromagnetic and antiferromagnetic coupling is found. A strong ferromagnetic coupling of the trimer and the adatom results in a ground-state spin state with $S = 16/2$ stabilizing the total complex. When the ferromagnetic exchange dominates the on-site anisotropies ($J > 1\,\mathrm{meV}$) the lifetime converges to a constant level, which can be explained from the level diagram shown in Fig. 6.2 b and c. For weak ferromagnetic exchange the states of trimer and adatom are mixed, like illustrated in panel b. In the limit of a strong ferromagnetic isotropic exchange subspaces corresponding to the combined spin S_{tot}, which are energetically separated by $1/2\,S_{\text{tot}}(S_{\text{tot}} + 1)$, evolve. The internal structure of the subspace does only depend on the on-site anisotropies and therefore the lifetime saturates for strong isotropic exchanges. It is orders of magnitude larger, since the lowest energy subspace has a total spin of $S_{\text{tot}} = 16/2$ resulting in a significant stabilization (see Fig. 6.4a). Similarly, a strong antiferromagnetic isotropic coupling yields a saturating lifetime, which in contrast to the ferromagnetic interaction has a lower lifetime. In this specific example, a ground state spin of $S_{\text{tot}} = 6/2$ is formed, which results in the destabilization. These findings in combination with the nature of the coupling of the trimer and the adatom for the experimental positions shown in Fig. 6.8 shows that the isotropic interaction cannot be attributed to the sudden decrease of the lifetime at $1.4\,\mathrm{nm}$, since both, ferro- and

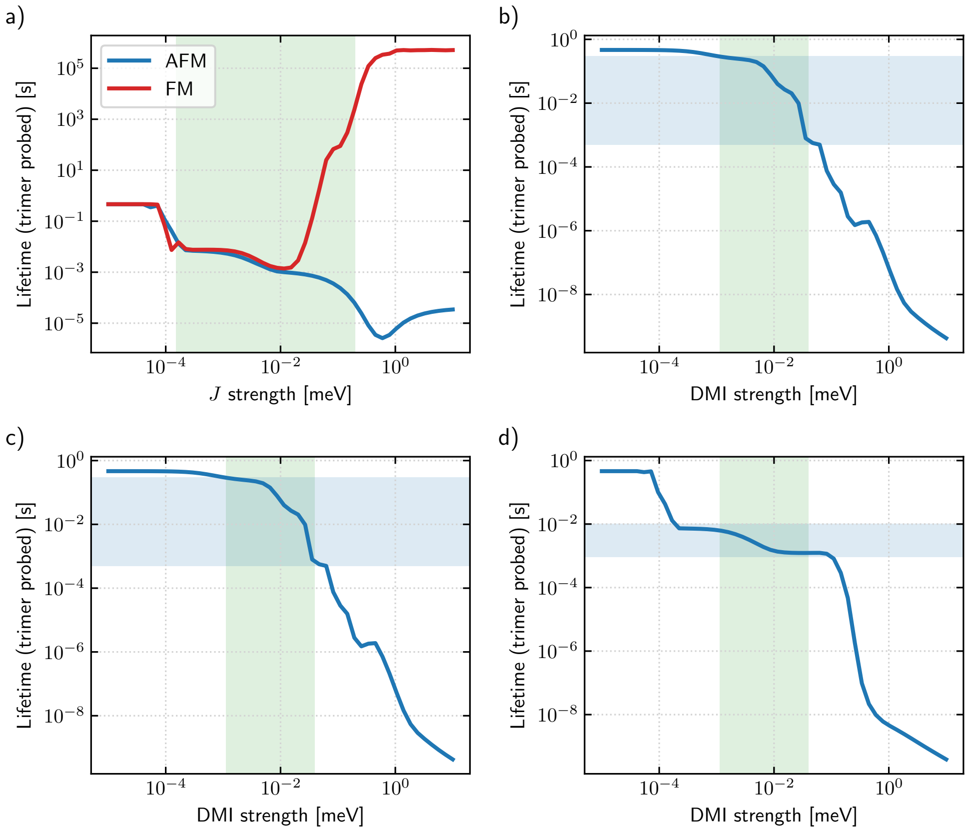

Figure 6.12.: Impact of the magnetic interactions on the longest magnetic lifetime of the adatom-trimer complex, when the trimer is probed. Initially both spins have only their on-site anisotropy without any interaction. a) Impact of the isotropic exchange interaction. The blue curve shows the lifetime for an antiferromagnetic coupling, while the red curve shows a ferromagnetic coupling. b), c), and d) show the impact of the DMI pointing in the x, y, and z direction, respectively. The green bars indicate the interaction range relevant for the experimental measurements, while the blue bars show the impact of the interactions in this range on the lifetime. Note that the strength of the magnetic interaction is intended for the quantum Heisenberg model. For a comparison with Fig. 6.8 the parameters have the be converted to the classical Heisenberg model.

antiferromagnetic couplings, are present below this threshold.

The impact of the DMI on the magnetic lifetimes is shown in Fig. 6.12b-d for the different component of the DM vector, which shows that an in-plane DMI induces a drastic destabilization of the magnetic lifetimes. While a weak DMI has no impact on the lifetimes, a DMI larger than 7×10^{-3} meV induces a drastic destabilization of the magnetic lifetime. Similar to an in-plane

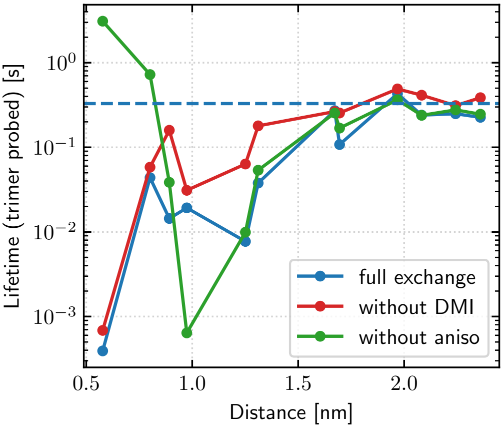

Figure 6.13.: Magnetic lifetimes of the trimer-adatom complex using subsets of the magnetic exchange interactions. The blue curve shows the lifetime using the full set of interactions, the red curve shows the lifetimes without considering the DMI, and the green curve shows the lifetimes without taking the anisotropic symmetric exchange into account. The lifetime of the isolated probed trimer is indicated as a dashed blue line.

anisotropy, the DMI mixes the eigenstates of the quantum spin model opening new transition channels and therefore drastically destabilizes the trimer-adatom complex. Comparing the threshold of 7×10^{-3} meV to the strength of the interactions for the experimental positions shown in Fig. 6.8d (note that a conversion factor of 17.7 between the quantum spin model and the classical Heisenberg model has to be applied) one finds that the DMI crosses the threshold for all positions closer than 1.4 nm. This strongly indicates that the DMI is the dominant mechanism destabilizing the trimer-adatom complex in the intermediate-distance regime.

To support this hypothesis, Fig. 6.13 shows the lifetime of the trimer-adatom complex without DMI and without anisotropic symmetric exchange. As can be seen the DMI is the main mechanism decreasing the lifetime for the positions between 0.8 nm and 1.4 nm, while it has no impact on the total lifetime for positions closer than 0.8 nm. Interestingly, the anisotropic symmetric exchange interaction has a significant effect on the lifetimes for distances closer than 0.8 nm, and therefore is the main mechanism lowering the lifetimes in the short-distance regime, which is discussed in the next section.

Short-distance regime: Effective in-plane anisotropies induced by the symmetric exchange interaction

The short-distance regime is of special importance for the complexes containing more than one additional adatom shown in Fig. 6.7d. All the additional atoms are placed in this regime. In contrast to the DMI, the anisotropic symmetric exchange can induce an effective anisotropy to the spin system. Assuming a collinear state, for which the DMI has no impact, the anisotropic symmetric exchange yields different energies for the magnetic states along x, y, and z. Being a symmetric matrix, the anisotropic exchange defines an easy-axis and an hard-axis similar to the magnetic on-site anisotropy or the moment of inertia known from classical mechanics. The easy-axis and the hard-axis are defined by the eigensystem of the symmetric tensor, $J^{\text{sym}}\boldsymbol{x}_i = \lambda_i \boldsymbol{x}_i$ with $i = \{1, 2, 3\}$, where the easy-axis is defined by the eigenvector corresponding to the smallest eigenvalue and the hard-axis corresponds to the largest eigenvalue. For collinear systems a configuration along the easy-axis is favoured. However, even without DMI there is a competition between the symmetric exchange and the on-site anisotropy resulting in non-collinear configurations, which tilts the constituents towards the easy-axis with the tilt depending on the strength of the on-site anisotropy.

Regarding the experimental setup, the question is: How is the symmetric exchange affecting the lifetime of the constituents and how can a symmetric arrangement of atoms enhance this lifetime? Considering only the onsite magnetic anisotropy and the isotropic exchange interaction, the eigenstates of the trimer and adatom combined system are spanned by the eigenstates of S_z. Similar to an in-plane anisotropy and the DMI, the symmetric exchange involves combinations of all three components of the spin operator $\boldsymbol{S}$. The x and y components mix the initial S_z eigenstates of the quantum Heisenberg hamiltonian and allow for new transition channels lowering the magnetic lifetime. To increase the stability of a spin, the main goal is to minimize the possible transition channels, which can be achieved by minimizing the impact of the in-plane components of the spin operators. Thus, the optimal configuration is achieved for a symmetric exchange, which is diagonal with an equal xx and yy-component resulting in a total exchange of the form,

$$J^{\text{iso}} + J^{\text{sym}} = \begin{pmatrix} J_\perp & 0 & 0 \\ 0 & J_\perp & 0 \\ 0 & 0 & J_\parallel \end{pmatrix} \quad , \tag{6.54}$$

involving only the zz-component apart from the isotropic component.

In the C_{3v} symmetry this goal can be achieved by arranging the atoms according to the present C_{3v} symmetry, which is the blue configuration of Fig. 6.7d. Labeling the central trimer as 0 and the surrounding atoms by $\{1, 2, 3\}$, the symmetric exchange tensors are related by,

$$J_{01} = \mathcal{R}(120°) J_{02} \mathcal{R}(120°)^{\mathrm{T}} = \mathcal{R}(240°) J_{03} \mathcal{R}(240°)^{\mathrm{T}} \quad . \tag{6.55}$$

If all surrounding adatoms contribute in the same way, this leads to a net effective anisotropy felt by the central trimer which is given by

$$J_{01} + J_{02} + J_{03} = \begin{pmatrix} \frac{3}{2}\left(J_{01}^{xx} + J_{01}^{yy}\right) & 0 & 0 \\ 0 & \frac{3}{2}\left(J_{01}^{xx} + J_{01}^{yy}\right) & 0 \\ 0 & 0 & 3J_{01}^{zz} \end{pmatrix} \quad . \tag{6.56}$$

Thus, retaining the original symmetry of the trimer eliminates the effective in-plane anisotropy felt by the trimer which is mediated by the symmetric exchange with the surrounding adatoms which is the dominating mechanism in the present regime.

The anisotropy induced by the symmetric exchange interaction for the complexes shown in Fig. 6.7d can be calculated using two different approaches: First, the anisotropy of the full

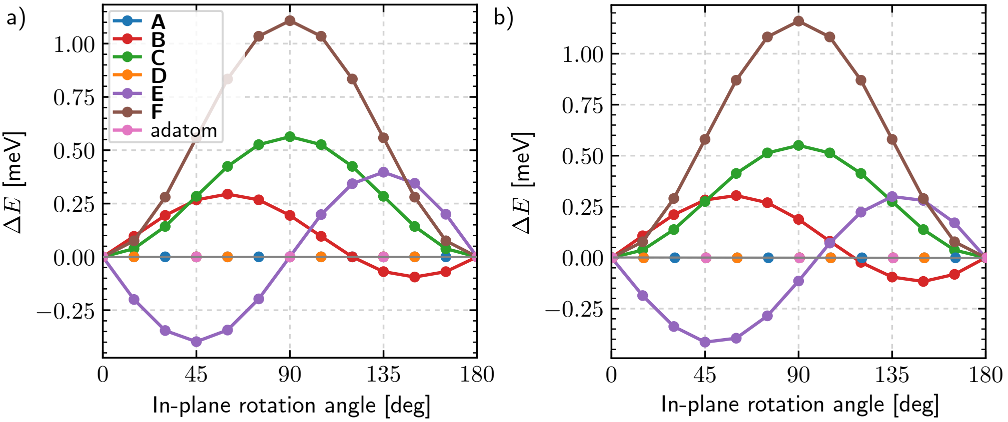

Figure 6.14.: Energy of the different systems upon rotating the magnetic moment collinearly in the x-y-plane ($\boldsymbol{e}_x \mathrel{\hat{=}} 0°$). The systems are labeled according to Fig. 6.7d. System A (isolated trimer), D (trimer plus three additional adatoms in a symmetric arrangement), and the isolated adatom show no effective in-plane anisotropy. a) Band energy difference of collinear rotations from first principles. b) Energy difference in the Heisenberg model using bilinear interactions.

complexes can be calculated from first principles using the magnetic force theorem and a collinear rotation of all the magnetic moments in the x-y plane, which is shown in Fig. 6.14a. Second, a Heisenberg model using bilinear interactions obtained from Lichtenstein's formula (see Chapter 4) can be used to calculate the energy upon collinear rotation of all moments as shown in Fig. 6.14b. Both methods agree very well showing that the anisotropic symmetric exchange interaction is in fact the only mechanism inducing an effective in-plane anisotropy to the complexes. All complexes, which do not retain the C_{3v} symmetry of the trimer and the surface, show a significant in-plane anisotropy, which is approximately one order of magnitude smaller than the out-of-plane on-site anisotropy of the trimer, $K^{\text{exp}} = -3.2\,\text{meV}$. As argued above, the systems retaining the C_{3v} symmetry do not show any effective in-plane anisotropy, which stabilizes the magnetic lifetimes of these complexes drastically, since no additional transition channels are opened.

To conclude, using the effective in-plane anisotropy it is possible to explain the experimental trends found for the different complexes shown in Fig. 6.7f. In total, the magnetic lifetime of interacting nanostructures is based on a complex interplay of the different exchange interactions. We found that the DMI in general destabilizes the systems, while the anisotropic symmetric exchange can stabilize and destabilize systems depending on its symmetry. The anisotropic symmetric exchange can be used to tune the magnetic stability and enhance the magnetic lifetime by orders of magnitude as shown in the experimental findings.

6.4. First-principles analysis of the surface coupling in Fe-based nanostructures on Pt(111)

In this section, we extend the previous study to different Fe-based nanostructures deposited on the Pt(111) surface, and focus on the surface coupling parameter v_S, which is among the magnetic anisotropy and the magnetic interactions the most important parameter for predicting magnetic stability. This procedure opens an avenue for a fully ab-initio modelling of the magnetic lifetime of magnetic complexes.

The surface coupling parameter v_S is related to the density of states of the d-states of the nanostructure, the density of states of the surface, and to the effective hybridization with the surface Γ, as discussed in relation to eq. (6.37). Using block matrix inversion we obtained an effective hamiltonian from first-principles, which can be mapped to eqs. (6.39) and (6.40), which is shown in Table 6.1 for the Fe adatom, Fe dimer and Fe trimer on the fcc-stacking position of the Pt(111) surface. Due to the formation of molecular-like bonding and antibonding states in the Fe dimer and Fe trimer, their electronic structure is influenced leading to modifications of the on-site tight-binding parameters. In fact, the modulations at the Fermi energy (which are relevant for the mapping procedure) result in an effective weakening of the hybridization Γ when increasing the nanostructure from an adatom to the trimer. Note that intuitively the trimer atoms should hybridize more since in addition to the surface states each trimer atom can hybridize with the other trimer atoms. The density of states at the Fermi level of the d-states of the nanostructure ρ_d is also shown in Table 6.1. Combining the effective hybridization Γ with the density of states of the d-states can be used to estimate the surface coupling v_S as discussed in relation to eq. (6.37), $v_\mathrm{S} \propto \sqrt{(\rho_d/\rho_\mathrm{S})\,\Gamma}$, where ρ_S is the density of states of the bare surface being indepenent of the nanostructure. For the three considered nanostructures the product $\rho_d\Gamma$ is close to the number of involved atom N. Thus, the surface coupling scales mostly with $v_\mathrm{S} \propto \sqrt{N}$. Note that the surface coupling ratio used in the Section 6.3 was found by fitting to the experimental data yielding, $v_\mathrm{S}^\mathrm{trimer}/v_\mathrm{S}^\mathrm{adatom} = \sqrt{3.5} = 1.87$, which agrees well with the previous finding.

	E_d [eV]	U [eV]	Γ [eV]	λ [eV]	ρ_d [#states/eV]	$v_\mathrm{S}/v_\mathrm{S}^\mathrm{adatom}$
Adatom	-1.038	1.777	-0.491	-0.027	1.502	1
Dimer	-0.936	1.728	-0.443	-0.026	3.780	1.507
Trimer	-0.874	1.686	-0.423	-0.021	5.736	1.814

Table 6.1.: Electronic properties of a fcc-stacked Fe adatom, a fcc-stacked Fe dimer and a fcc-top-stacked Fe trimer deposited on the Pt(111) surface. Shown is the on-site tight-binding parametrization obtained from first-principles as discussed in relation to eq. (6.39), the local density of states of the d-orbitals of the full nanostructure, and the surface coupling v_S, which is estimated by the relation given in eq. (6.37), $v_\mathrm{S} \propto \sqrt{\rho_d\Gamma}$.

6.5. Conclusions and outlook

In this chapter, we presented a systematic study of the magnetic lifetime as probed in telegraph noise STM experiments in coupled nanostructures. The combination of a quantum spin model parametrized from first-principles and a master equation approach enabled us to model and predict magnetic lifetimes based on only a couple of free parameters mainly related to the electronic properties of the STM tip, which are unknown. In collaboration with the experimental group of Dr. Jens Wiebe from the University of Hamburg, we investigated the impact of magnetic interactions between an fcc-top-stacked Fe trimer and an Fe adatom deposited on the Pt(111) surface on the magnetic stability measured on both constituents. With the model-based study we could identify three different regimes driven by different magnetic interactions. In the weak-coupling regime (large distances between the trimer and the adatom) the weak magnetic exchange interaction enables an indirect measurement of the magnetic state of the trimer by probing the adatom. While the adatom on its own does not show a magnetic signal in SP-STM since its lifetime is smaller than the time resolution of the measurement, we found that the trimer induces an asymmetry in the magnetic state of the adatom, which upon time-averaging is seen in the telegraph noise signal of the adatom. Via this asymmetry the magnetic state of the trimer can be probed without directly interacting with the trimer which increases its magnetic lifetime by orders of magnitude. In the intermediate-coupling regime, we found the DMI to significantly destabilize the trimer-adatom complex. Similar to an magnetic in-plane anisotropy, the DMI opens new transition channels and in general destabilizes a magnetic structure. In the strong-coupling regime (short distances between the trimer and the adatom), where intuitively the formation of a larger spin moment should enhance the magnetic stability, we found the symmetric anisotropic exchange interaction to significantly destabilize the trimer-adatom complex. The symmetric exchange induces an effective in-plane anisotropy to the trimer, which can be used to engineer magnetic stability using symmetry. We showed that placing multiple adatoms in the strong-coupling regime such that the C_{3v} symmetry of the trimer is preserved prevents the formation of an effective in-plane anisotropy, which can stabilize the magnetic stability of the trimer by orders of magnitude.

The combination of the master equation model, the spin model with parameters extracted from first-principles, and the estimation of the surface coupling from first-principles, might enable a new avenue for the quest of magnetic stability in small nanostructures. The methods presented in this Chapter can potentially be used to predict magnetic stability fully from ab-initio.

7

Boundary states in magnetic chains on Re(0001)

This chapter presents the emergence of zero-energy boundary states in magnetic Fe chains deposited on the superconducting Re(0001) surface. The boundary states are attributed to Majorana fermions, which are theoretically expected to emerge in superconducting one-dimensional chains with strong spin-orbit coupling or with a helical spin structure. Using first principles, we shed light on the magnetic properties of the Fe chain, extract parameters of an effective tight-binding hamiltonian, and show how a realistic description of the Fe chains leads to the formation of zero-energy boundary states. In collaboration with the experimental group of Dr. Jens Wiebe from the University of Hamburg, we investigate the impact of non-magnetic Co atoms on the Fe chain, which affects not only the magnetic structure of the chain, but also the boundary states. The Co termination of the Fe chain gives us a strong indication that the boundary states can be attributed to topologically non-trivial Majorana states. Since the main focus of this thesis is neither about superconductivity nor Majorana fermions, this chapter focuses on the magnetic properties of the chains and should be seen as a model application of the concepts described in the previous chapters. The complex topics of superconductivity, as well as Majorana fermions, will be only introduced briefly and we refer the reader to more comprehensive textbooks on the topics, e.g. [194, 195].

Parts of the presented work will be submitted for publication

L. Schneider†*, S. Brinker*† *et al., Nature Communications* ***11****, 4707 (2020)*
†*L. Schneider and S. Brinker contributed equally to this work.*

I have contributed to this publication in the following way: I performed the DFT calculation, the effective spin model calculations and the tight-binding simulations. I conceived the theoretical framework and analyzed the results of all calculations together with Dr. Manuel dos Santos Dias and Jun.-Prof. Samir Lounis. I contributed to the manuscript via discussions and corrections and I wrote the theoretical parts mainly published in the supplementary information.

7.1. Introduction

Superconductivity has been one of the most influential and fascinating fields of physics of the last century. Due to the lack of electron scattering, superconductors are ideal conductors without resistivity, which has important consequences like e.g. the repulsion of an external magnetic field (the Meissner effect) [196]. The conventional superconductors are well-described by the BCS theory formulated by Bardeen, Cooper and Schrieffer [197, 198], which were awarded the Nobel price in 1972. In the BCS theory the superconductivity is attributed to the formation of so-called Cooper pairs [199], which being of bosonic nature can form a Bose-Einstein condensate. The physical origin of the formation of Cooper pairs is the electron-phonon interaction. The BCS equations are often solved using the so-called Bogoliubov transformation [200] in the mean-field approximation. In addition to the above mentioned effects, the electronic structure of superconductors is gapped. The complex interplay of magnetism and superconductivity can lead to the emergence of so-called Yu-Shiba-Rusinov (YSR) states [201–203], which are in-gap states due to magnetic impurities in superconductors. Another type of in-gap and zero-energy state is related to the so-called Majorana fermions [204], which due to their non-abelian statistics are promising building blocks for qubits in topological quantum computing [78]. After the theoretical prediction of Majorana fermions at the interface of a superconductor and a topological insulator in 2008 by Fu and Kane [205], different theoretical proposals of Majorana fermions in helical magnetic chains on superconducting substrates [82, 206–210] have lead to the experimental observation of boundary states in magnetic chains on the Pb surface using real-space probing techniques [83, 85, 86, 211–213], which were attributed to the Majorana states. More recently, signatures of Majorana fermions have been observed in Fe chains deposited on the Re(0001) surface [84]. However, in all the experimental measurements it is not clear if the measured boundary states correspond to the theoretically predicted Majorana states or if they are topologically trivial Yu-Shiba-Rusinov states emerging due to changes in the magnetic structure at the boundary. Experimentally, the Re surface has one major advantage over the previously used Pb substrate: lateral atom manipulation is not possible on Pb but is possible on Re, allowing the precise construction of arbitrary magnetic nanostructures atom-by-atom. This opens a new avenue since these nanostructures can be designed in order to manipulate the emerging boundary states.

In collaboration with the experimental group of Dr. Jens Wiebe from the Universtity of Hamburg, we study in this Chapter magnetic Fe chains deposited on the Re(0001) surface. Using different first-principles techniques described in the previous chapters, we tackle the magnetic

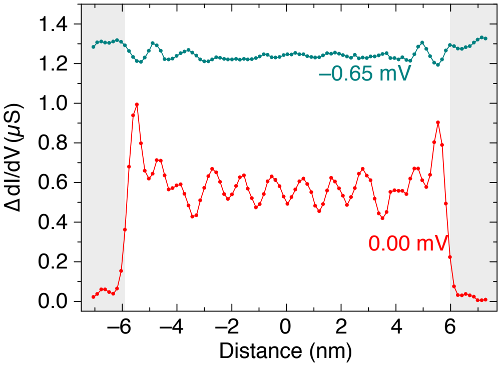

Figure 7.1.: Differential tunneling conductance ($\mathrm{d}I/\mathrm{d}V$) as experimentally observed in a 40-atomic Fe chain on Re(0001) by Kim *et al.* [84]. The differential tunneling conductance indicates two pronounced boundary in-gap states at $V = 0\,\mathrm{mV}$, while for voltages large than the superconducting gap (which was estimated to $0.28\,\mathrm{meV}$) the measurement shows only weak boundary effects. The figure was reproduced from Ref. [84].

structure of Fe chains on Re(0001). Experimental measurements using spin-resolved STM indicate a spin spiral with a wavelength of about four lattice constants [84], which could not be theoretically reproduced in Ref. [60], and pronounced boundary states as indicated in Fig. 7.1. In addition, we investigate the effect of additional Co atoms attached to the end of the Fe chain. Remarkably, while Co was found to be one of the most stable magnetic elements for the surfaces considered in Chapter 3, experimentally it was found to be non-magnetic on the Re(0001) surface and weakly magnetic using first-principles calculations [214]. Here, we first consider the magnetic properties of Co attached to the Fe chain and investigate its impacts on the magnetic structure of the Fe chain. We show how the Co termination eliminates boundary effects in the Fe chain making the emergence of trivial Yu-Shiba-Rusinov states less probable, and how it can be used to manipulate the lateral extend of the boundary states found in the Fe chain.

7.2. Tight-binding model for superconducting chains

In Section 6.1.2, we introduced the general form of a tight-binding model, $\mathcal{H}_{\text{TB}}$, which can be split into an on-site contribution, eq. (6.39), and an inter-site contribution corresponding to the hoppings between the atoms, eq. (6.40). In the spirit of the BCS model, superconductivity can be added to the general tight-binding model using an additional pairing potential in the mean-field approximation,

$$\mathcal{H}_{\text{pairing}} = \sum_{ij} \Delta_{im,jm'} \left(c^{\dagger}_{im\uparrow} c^{\dagger}_{jm'\downarrow} + c_{im\downarrow} c_{jm'\uparrow} \right) \quad , \tag{7.1}$$

which in its most general form can be non-local and orbital-dependent. The pairing term corresponds to the formation of pairs of electrons or holes of opposite spin – the so-called Cooper pairs. The pairing potential $\Delta_{im,jm'}$ can in principle be obtained from first principles, but it requires sophisticated methods to describe the electron-phonon coupling [215]. However in this Chapter, we treat the pairing as a model parameter, and assume it to be orbital-independent and local, $\Delta_{im,jm'} = \delta_{ij}\delta_{mm'}\Delta$ (consistent with s-wave superconductivity) similar to the model used by Li *et al.* [210]. Applying a Bogoliubov-de-Gennes (BdG) transformation (see e.g. [194, 195]) simplifies the total hamiltonian to,

$$\mathcal{H}_{\text{BdG}} = \begin{pmatrix} \mathcal{H}_{\text{TB}} & \Delta \otimes \mathrm{i}\,\sigma_y \\ -\Delta \otimes \mathrm{i}\,\sigma_y & -\mathcal{H}^*_{\text{TB}} \end{pmatrix} \quad , \tag{7.2}$$

where we used the basis

$$\Psi = \begin{pmatrix} u \\ v \end{pmatrix} \quad , \tag{7.3}$$

with the coefficients u and v corresponding to a particle and a hole, respectively, and the pairing Δ being off-diagonal in spin space indicated by the tensor product with the Pauli matrix. The BdG hamiltonian reflects the particle-hole symmetry of the superconducting state.

In this Chapter, we investigate the physics of one-dimensional finite magnetic chains deposited on superconducting surfaces. Previous studies of one-dimensional chains using a tight-binding model, e.g. [210], have mostly relied on the Slater-Koster parametrization [216] of the tight-binding parameters using tabulated bulk parameters (e.g. [217]), which might be unrealistic for the considered systems. Using the approach described in relation to eqs. (6.39) and (6.40), we use a first-principles scheme to obtain an effective tight-binding hamiltonian for the d-orbitals of the magnetic chains, which takes a renormalization due to the presence of the substrate into account. Therefore, the substrate does not explicitly enter the tight-binding model, but is considered via its impact on the tight-binding parameters. In contrast to Chapter 6, we restrict ourselves to hermitian hamiltonians, and therefore neglect the non-hermitian part of the hybridization with the surface. Furthermore, we assume the hoppings to be spin-independent and symmetric in the orbitals, $t_{ims,jm's'} = t_{jm's',ims} = t_{ims,jm's}\delta_{ss'} = t_{im's,jms}\delta_{ss'}$. In total, the considered tight-binding model takes the form,

$$\begin{aligned} \mathcal{H}_{\text{TB}} = &\sum_{i}\sum_{mm'}\sum_{ss'} \big(E_{d,i}\,\delta_{mm'}\delta_{ss'} + U_i\,\boldsymbol{e}_i\cdot\boldsymbol{\sigma}_{ss'}\delta_{mm'} + \lambda_i\,\boldsymbol{L}_{mm'}\cdot\boldsymbol{\sigma}_{ss'} + \Delta^{(\text{re})}_{i,mm'}\delta_{ss'}\big)c^\dagger_{ims}c_{im's'} \\ &+ \sum_{ij}\sum_{mm'}\sum_{s} t_{ims,jm's}c^\dagger_{ims}c_{jm's} \quad , \end{aligned} \tag{7.4}$$

where $E_{d,i}$ is the energy level of the d-orbitals, U_i is the spin splitting, $\boldsymbol{e}_i$ is the direction of the magnetic moment, λ_i is the spin-orbit coupling strength, $\boldsymbol{L}_{mm'}$ is the matrix element of the angular momentum, $\boldsymbol{\sigma}$ is the vector of Pauli matrices, $\Delta^{(\text{re})}_{i,mm'}$ is the crystal field splitting, and $t_{ims,jm's}$ is the orbital-dependent hopping between sites i and j.

Before starting with the description of realistic chains, we want to recap the state of the art, which goes mainly back to Ref. [210], where the Majorana physics in an Fe chain deposited on a Pb substrate were discussed. The pure Fe chain is described using the Slater-Koster parameters $V_{dd\sigma} = -0.67\,\text{eV}$, $V_{dd\pi} = 0.58\,\text{eV}$, and $V_{dd\delta} = -0.14\,\text{eV}$ restricted to nearest-neighbor hoppings, which results in the hopping matrix shown in Table 7.1. The band structure

	xy	yz	z^2	xz	x^2-y^2
xy	0.58	0.00	0.00	0.00	0.00
yz	0.00	−0.14	0.00	0.00	0.00
z^2	0.00	0.00	−0.28	0.00	0.23
xz	0.00	0.00	0.00	0.58	0.00
x^2-y^2	0.00	0.00	0.23	0.00	−0.54

Table 7.1.: Nearest-neighbor hopping matrix between the d-orbitals of an infinite Fe chain (oriented in the x-direction) using the Slater-Koster parametrization with $V_{dd\sigma} = -0.67$ eV, $V_{dd\pi} = 0.58$ eV, and $V_{dd\delta} = -0.14$ eV. All parameters are in units of [eV]. The parameters were taken from Ref. [210]

of an infinite one-dimensional Fe chain, which can be obtained by Fourier transforming the tight-binding or BdG hamiltonian, eq. (7.2), is shown in Fig. 7.2 for several different test cases. Fig. 7.2a shows the pure band structure of collinear Fe chain with a spin splitting of $U = 1.325$ eV and a constant energy of the d-levels of $E_d = -1.5$ eV (the Fermi energy is taken as the energy zero). Due to the symmetry of the one-dimensional chain and the Slater-Koster parametrization, there are two twofold-degenerate bands per spin channel. Adding spin-orbit (b) leads to a hybridization of the original bands and lifts some of the degeneracies. Note that the spin-orbit coupling strength is unrealistically large for the purpose of visualization. Fig. 7.2c shows the particle-hole symmetric band structure of the BdG hamiltonian without pairing potential, which leads to three band crossings at the Fermi level, as can be seen in Fig. 7.2d. Adding a finite proximity-induced pairing potential leads to a hybridization of two of the three band crossings, but can not open a gap in the full one-dimensional Brillouin zone, as shown in Fig. 7.2e. The superconductivity in the Fe chain is assumed to be induced by the superconducting substrate. To lift the last band crossing a non-collinear magnetic structure can be used, as shown in Fig. 7.2f, where an in-plane spin spiral with four lattice constants wavelength is considered. Due to the used supercell containing four atoms the number of bands is increased by a factor of four. Thus, from this simple example we see the most important ingredients for a band gap to occur in the superconducting Fe chain: Magnetism, superconductivity, spin-orbit coupling and a non-collinear magnetic structure.

7.2.1. Infinite chains and the Majorana number

Majorana bound states can occur at the boundaries of finite one-dimensional chains being zero-energy in-gap states. In order to predict their appearance, Kitaev introduced a topological invariant, the so-called Majorana number $\mathcal{M}$ [218], which is defined for the infinite chain and is a necessary but not sufficient condition for Majorana bound states to emerge in finite chains. The Majorana number can be defined using BdG hamiltonian obtained by Fourier-transforming, eq. (7.2), once it is represented in the basis of the so-called Majorana operators,

$$A_k = -\mathrm{i} U \mathcal{H}_{\mathsf{BdG}}(k) U^\dagger \quad , \tag{7.5}$$

where U defines the transformation to the Majorana operator basis. The Majorana number is the sign of the product of the so-called Pfaffian (Pf) of this matrix at the Γ-point, $k = 0$, and at

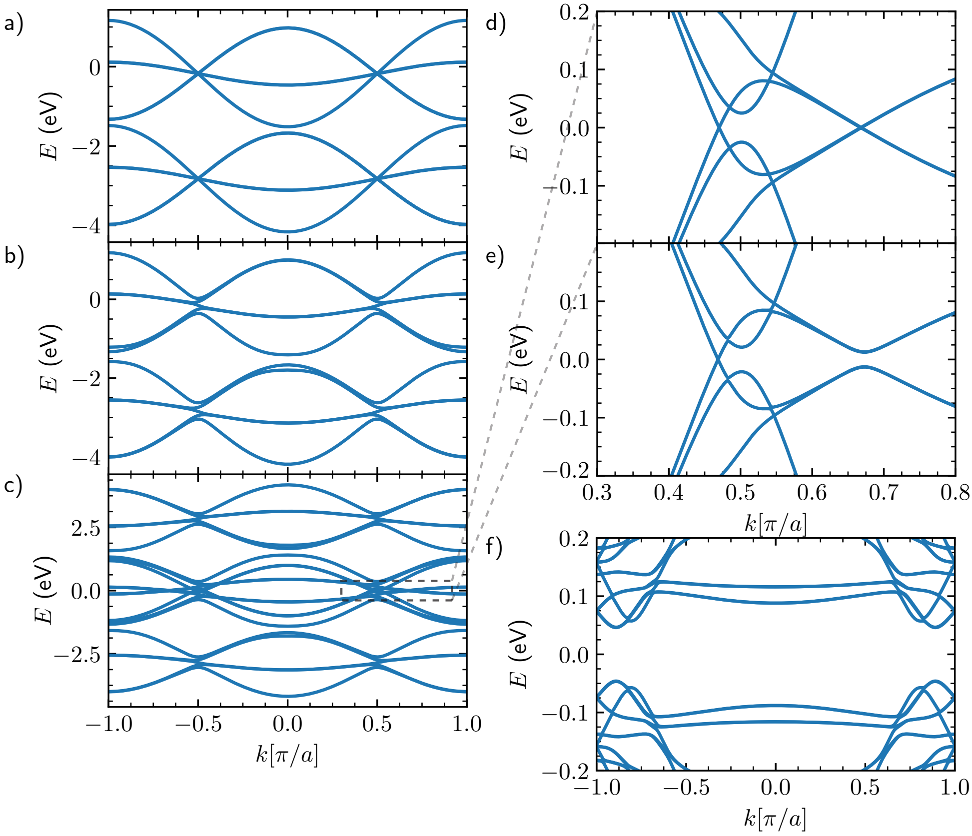

Figure 7.2.: Band structure of an one-dimensional infinite Fe chain in the tight-binding model. The hopping is described using the Slater-Koster parametrization with bulk Fe parameters. The on-site average d-level energy is $E_d = -1.5\,\text{eV}$ and the spin splitting $U = 1.325\,\text{eV}$. a) Collinear chain without spin-orbit coupling and superconducting pairing. b) Collinear chain with spin-orbit coupling and without superconducting pairing. c) Collinear chain with spin-orbit coupling and with particle-hole symmetry but no superconducting gap. d) Enlarged view of the band structure in c) around the Fermi energy. e) Collinear chain with spin-orbit coupling and with a superconducting pairing. f) Now the magnetic structure is changed from ferromagnetic to a spin-spiral rotation with a wavelength of four lattice constants and with spin-orbit coupling as well as a superconducting pairing. The unit cell contains four Fe atoms. Spin-orbit coupling is described locally with a strength of $\lambda = 0.1\,\text{eV}$. The proximity-induced superconducting pairing potential is $\Delta = 0.1\,\text{eV}$. Panel a-e reproduce the results from Ref. [210].

the Brillouin zone boundary, $k = \pi/a$, where a is either the lattice constant or the size of the supercell in case of a non-collinear state,

$$\mathcal{M} = \text{sgn}\big[\text{Pf}(A_{k=0})\text{Pf}(A_{k=\pi/a})\big] \quad . \tag{7.6}$$

For negative Majorana numbers, the Pfaffian of the hamiltonian takes opposite values between the Γ-point and the zone boundary, which indicates that the chain is topologically non-trivial.

The Majorana number of the pure Fe chain using the SK parametrization with bulk parameters as function of the center of the d-bands E_d and the spin splitting U is shown in Fig. 7.3. The phase diagram shown in Fig. 7.3a is obtained from a collinear Fe chain without spin-orbit coupling and without proximity-induced superconducting pairing, $\Delta = 0$. Thus, it is obvious that in a finite chain with these parameters no Majorana bound states could emerge. However, the Majorana number indicates a non-trivial state for nearly all realistic parameters, since typically U is of the order of $1\,\text{eV}$, which highlights that the Majorana number is a necessary but not sufficient condition.

Fig. 7.3b shows the phase diagram including a large superconducting pairing of $\Delta = 0.9\,\text{eV}$. The superconducting pairing clearly modifies the phase diagram shifting the non-trivial phase to larger spin splittings, which basically shows that magnetism has to dominate the superconductivity for Majorana bound states to emerge.

As a last remark of this section, we want to mention that treating the proximity-induced superconductivity in the Fe chains by using a superconducting pairing in the Fe without treating the source of the superconductivity – the substrate – has some known problems, see e.g. [210]. The finite chains need large pairing potentials Δ, which lead to unrealistically large band gaps, in order to find zero-energy boundary states with a realistic localization corresponding to the correlation length of the Majorana states. To improve this drawback more sophisticated methods would have to be employed, for instance based on embedding techniques.

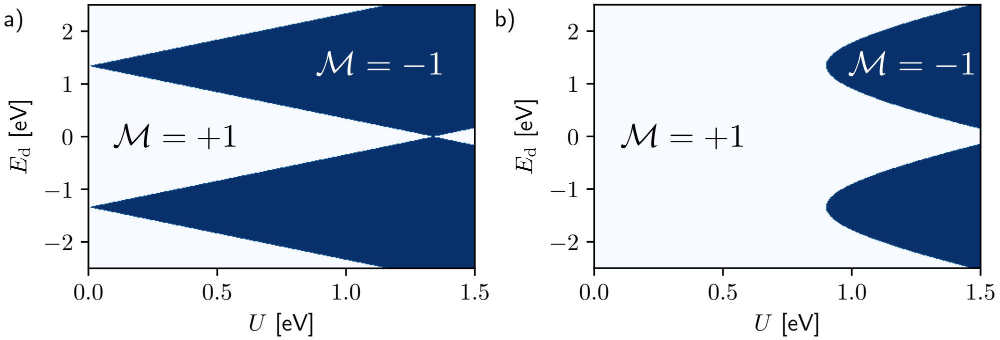

Figure 7.3.: Majorana number $\mathcal{M} = \text{sgn}\left(\text{Pf}(A_{k=0})\text{Pf}(A_{k=\pi/a})\right)$ as function of the average d-level energy E_d and the spin splitting U. The collinear Fe chain is described by the Slater-Koster parametrization using bulk Fe parameters. The topological trivial states are white, while the topological non-trivial regions are blue. a) Chain without proximity-induced super conducting pairing, $\Delta = 0\,\text{eV}$. b) Chain with proximity-induced super conducting parining of $\Delta = 0.9\,\text{eV}$.

7.3. Chains deposited on Re(0001)

We focus on three different one-dimensional $3d$ transition metal chains deposited on the Re(0001) surface, a 20-atomic Fe chain and the same chain with 5 Co atoms attached to one end of the chain and to both ends of the chain. First, the magnetic ground state properties obtained from first principles are presented. Second, an effective tight-binding model for the chains is set up using those first-principles calculations, and last, the proximity-induced superconductivity is added as a parameter and the emerging boundary states are investigated.

7.3.1. Magnetic properties

The chains are constructed similar to the systems presented in Chapter 4 with the computational details explained in Section 3.3.1, but using the full potential instead of the atomic sphere approximation. For the real space cluster of the three chains used in the embedding scheme, we consider nearest-neighbor clusters containing 146, 181, and 216 sites (including vacuum sites) and the chain atoms are placed in the hcp-stacking position. The relaxations of the chains are assumed to be $20\,\%$ of the inter-layer distance towards the Re substrate, which is based on a Quantum Espresso calculation of a single Fe atom, which relaxed by $18\,\%$ towards the surface (the computational details of this calculation are similar to the one presented in Section 3.3.1). The geometry of the cluster containing the 20-atomic Fe chain and 5 Co atoms at each end is shown in Fig. 7.4b.

The first important properties being addressed are the magnetic moments of the Fe and Co atoms. The spin magnetic moments are shown in the upper panel of Fig. 7.4a. In the center the Fe chain shows a magnetic moment of $2.12\,\mu_\mathrm{B}$ per atom for all three chains. At the boundary of the 20-atomic Fe chain, the magnetic moment of the boundary Fe atom increases to $2.26\,\mu_\mathrm{B}$, which is related to the lower coordination number of the boundary Fe atom. Interestingly, adding five Co atoms to the end of the Fe chain increases the coordination number of the interfacial Fe atom and leads to a bulk-like magnetic moment of $2.11\,\mu_\mathrm{B}$. Astonishingly, the Co atoms do not show magnetism on their own, which is explained by the Co chain not satisfying the Stoner criterion on the Re(0001) substrate (see Ref. [214] for the case of a Co adatom). This is an interesting result for two reasons: First, in Chapter 3 we saw that Co is one of the most stable magnetic elements favouring a magnetic state for all considered surfaces. Second, previous studies of single Co adatoms in the hcp-stacking positions on the Re(0001) substrate [214] found a contradiction between the experimentally observed non-magnetic state and the theoretically predicted moment of $1.5\,\mu_\mathrm{B}$. Here, we showed that five Co atoms in the vicinity of Fe do not show magnetism on their own, which agrees with the experimental finding. However, Fig. 7.4a also shows that the Co atom next to the Fe atom is strongly polarized by its neighbor, resulting in a magnetic moment of $0.86\,\mu_\mathrm{B}$.

To investigate the magnetic structure of the different chains, we extracted the magnetic exchange interactions using the infinitesimal rotation method, eq. (4.7). The isotropic bilinear exchange is shown in Fig. 7.5 for the nearest and next-nearest neighbors. In the center of the 20-atomic Fe chain the nearest neighbor exchange is $J_1 = 29\,\mathrm{meV}$, while the next-nearest neighbor exchange is $J_2 = 16\,\mathrm{meV}$, which with the used sign convention correspond to antiferromagnetic interactions. Thus, there is a strong frustration between the nearest and next-

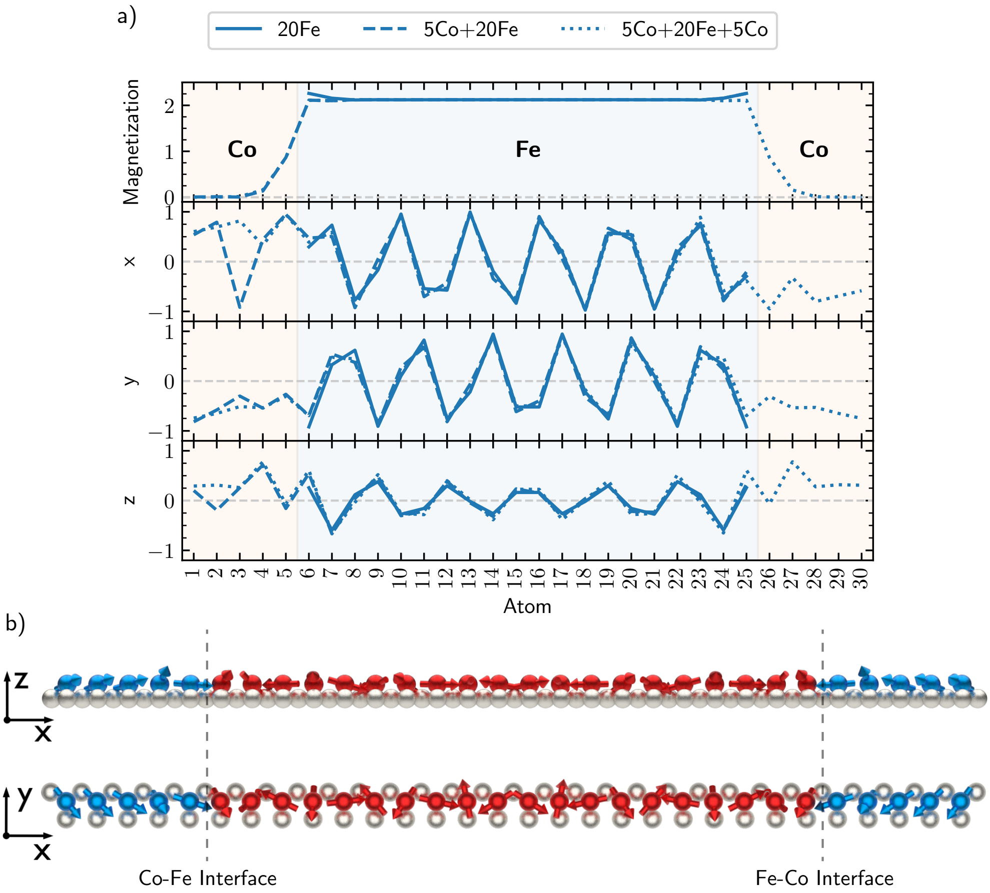

Figure 7.4.: a) Magnetic ground state configuration of the 20-atomic Fe chain without Co, and with Co attached to one and both sides. The upper panel shows the spin magnetic moment per atom in units of μ_B. The three lower three panels show the components of the direction of the magnetic moment (unit vector). A magnetic anisotropy of $1\,\mathrm{meV}$ in the y-direction is assumed to break the ground state degeneracy. b) Illustration of the 20-atomic Fe chain (red) with Co (blue) attached to both sides. A top view and a side view of the magnetic structure are shown.

nearest neighbor interactions. To see which state these interaction would favour, consider for the sake of simplicity a spin spiral with a rotation angle of α between the sites. The energy of an N-atomic chain is given by,

$$E(\alpha) = 2NJ_1\cos(\alpha) + 2NJ_2\cos(2\alpha) \quad , \tag{7.7}$$

which for the exchange interactions of the Fe chain results in a spin spiral with $\alpha = 117°$, or in terms of the wavelength $\lambda = 3.1a$, where a is the nearest-neighbor distance.

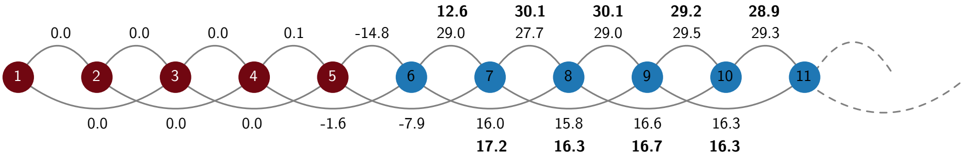

Figure 7.5.: Isotropic bilinear exchange interaction of the chains deposited on the Re(0001) surface. The interactions are obtained using the infinitesimal rotation method (see Chapter 4). The parameters for the 20-atomic Fe chain (blue circles) are shown in bold, while the parameters that show the effect of the five Co atoms (red circles) attached to one side of the Fe chain are shown in a regular font.

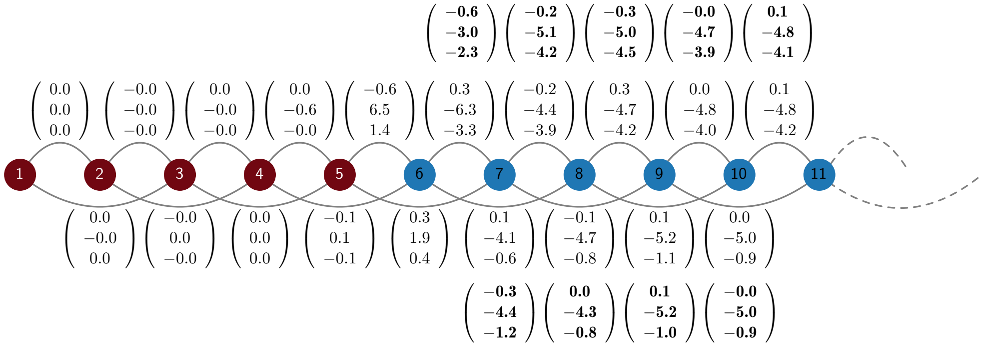

Figure 7.6.: Dzyaloshinskii-Moriya vector of the chains deposited on the Re(0001) surface. The parameters of the 20-atomic Fe chain (blue circles) are shown in bold, while the effect of the five Co atoms (red circles) attached to one side of the Fe chain are shown in a regular font. The (x, y, z) components of the DMI vectors refer to the coordinate frame of Fig. 7.4.

At the boundary of the Fe chain, the nearest neighbor interaction decreases significantly to $12.6\,\mathrm{meV}$. Similar to the magnetic moment, attaching Co to the end of the chain results in a more bulk-like interfacial Fe with the Fe-Fe interaction increasing to $29\,\mathrm{meV}$, which is shown in Fig. 7.5. The interfacial Co atom shows a large ferromagnetic interaction with the interfacial Fe atom of $-14.8\,\mathrm{meV}$, which is remarkable since the induced magnetic moment of the Co atom is much smaller than the one of the Fe atom.

The Dzyaloshinkskii-Moriya vectors for the nearest and next-nearest neighbors are shown in Fig. 7.6. In the center of the chain the nearest neighbor DMI has a strength of $|\boldsymbol{D}_1| = 6.3\,\mathrm{meV}$ and lies in the y-z plane forming an angle of about 45° with the y-axis. The next-nearest neighbor DMI points mainly in the y-direction with a magnitude of $|\boldsymbol{D}_2| = 5.2\,\mathrm{meV}$. Both, nearest and next-nearest neighbor DMI have the same chirality. Since the DMI is significantly smaller than the isotropic exchange interaction it mainly impacts the plane and the sense of rotation, the latter being defined by the vector chirality, $\boldsymbol{e}_n \times \boldsymbol{e}_{n+1}$, but not the opening angle between the magnetic moments of the neighboring sites. Furthermore, there is a competition between the

y-components of the nearest neighbor DMI and the y-component of the next-nearest neighbor DMI. Since the isotropic exchange fixes the angle between neighboring sites to approximately $110\,°$, the vector chirality between nearest neighbors has the opposite orientation to the one between next-nearest neighbors. However, the y-component of the DMI favours the same chirality for nearest and next-nearest neighbors. The energy gain or loss from the nearest neighbor DMI is counteracted by the one of the next-nearest neighbor DMI. In contrast, the z-component of the DMI is only large for the nearest neighbor bond. Thus, an energy gain can be achieved with the proper vector chirality. Therefore, energetically the x-z-plane is disfavoured as plane of rotation, resulting in a mainly in-plane (x-y) spin spiral. As was already shown for the isotropic exchange interaction, adding Co to the end of the Fe chain, see Fig. 7.6, results in a more bulk-like DMI between the nearest-neighbor Fe atoms next to the Co and a large DMI between the interfacial Co and Fe atom is found.

In addition to the complex anisotropic symmetric exchange, which is of the order of $1\,\mathrm{meV}$ for the considered Fe chain, we also investigate the magnetic on-site anisotropy of the three different chains. Since this former interaction has a matrix structure similar to the on-site anisotropy, we concentrate on the latter. We use the torque method to extract the magnetic anisotropy energy, similar to the method presented in Section 4.1.1. However, here we restrict ourselves to a collinear rotation of the ferromagnetic Fe chain on the closed path $z \to x \to y \to z$. We use magnetic constraining fields to self-consistently obtain the torque on each Fe atom. As the magnetic moment of the Co atoms is induced by the Fe atoms, they are not considered as independent degrees of freedom, so we do not apply the magnetic constraint to them, and we neglect their on-site anisotropy in the following. For each atom i the on-site anisotropy in the Heisenberg model is fitted to the torques,

$$\frac{\partial E}{\partial \boldsymbol{e}_i} = 2K_i\boldsymbol{e}_i + \sum_j J_{ij}\boldsymbol{e}_j \quad , \tag{7.8}$$

using the procedure described in Section 4.1.1 and using the exchange interactions obtained from the infinitesimal rotation method as input. In general, the on-site anisotropy of each atom in the chain has no symmetry constraints, since no local symmetry applies to the chain atoms. However, the central mirror symmetry of the chain relates the on-site anisotropy of an atom i to its mirrored atom j,

$$K_i = \mathcal{M}_x K_j \mathcal{M}_x^{\mathsf{T}} = \begin{pmatrix} K_j^{xx} & -K_j^{xy} & -K_j^{xz} \\ -K_j^{xy} & K_j^{yy} & K_j^{yz} \\ -K_j^{xz} & K_j^{yz} & -K_j^{xx} - K_j^{yy} \end{pmatrix} \quad , \tag{7.9}$$

where $\mathcal{M}_x$ is the mirror operator for a mirror along the x-direction. For an infinite chain the xy and xz elements of the on-site anisotropy vanish due to this symmetry (as all atoms are identical in this case, $K_i = K_j$).

The on-site anisotropy of the central Fe atoms is found to be

$$K_{15} = \begin{pmatrix} 0.13 & 0.00 & 0.00 \\ 0.00 & 0.21 & -0.65 \\ 0.00 & -0.65 & -0.34 \end{pmatrix} \text{meV} \quad , \tag{7.10}$$

whose eigensystem is given by

$$\lambda = \{-0.77, 0.13, 0.64\} \quad \text{with} \quad \boldsymbol{x} = \left\{ \begin{pmatrix} 0.0 \\ 0.54 \\ 0.84 \end{pmatrix}, \begin{pmatrix} 1.0 \\ 0.0 \\ 0.0 \end{pmatrix}, \begin{pmatrix} 0.0 \\ -0.84 \\ 0.54 \end{pmatrix} \right\} \quad . \tag{7.11}$$

Thus, the on-site anisotropy has the easy axis in the y-z plane at an angle of $32°$ with the z-axis towards the positive y-direction. The hard-axis is perpendicular to the easy-axis, also in the y-z plane, while the x-axis defines energetically an intermediate axis. Similarly to the DMI, the on-site anisotropy can determine the plane of rotation of a spin spiral. However, the energy scales of the on-site anisotropy are nearly one order or magnitude smaller than the DMI. Therefore, the plane of rotation is weakly affected by the on-site anisotropy.

The magnetic structures of the three different chains obtained by minimizing a Heisenberg hamiltonian containing all the bilinear magnetic exchange interactions and the on-site anisotropies is shown in Fig. 7.4. The magnetic structures follow the central spatial mirror symmetry. Adding Co atoms to one side of the system breaks the mirror symmetry of the Fe chain, while adding Co to both side preserves the mirror symmetry of the Fe chain. A spin spiral with a wavelength of approximately $3.1a$ is found, which has a plane of rotation forming an angle of approximately 30° with the x-y plane.

When comparing the magnetic structure to the structure observed by Kim *et al.* using spin-polarized STM [84], the wavelength is close to the experimentally found wavelength of $4a$. The experiment showed indications for a plane of rotation, which favours the out-of-plane component, while the spin spiral we found is mainly in-plane. However, since it is experimentally difficult to distinguish between out-of-plane tip polarization and in-plane tip polarization, there might be an error in the assignment from the experimental side. We also want to note that our results are vastly different from the results obtained by Lászlóffy *et al.* [60] on a similar Fe chain deposited on Re(0001). In contrast to our results, they did not find a large next-nearest neighbor antiferromagnetic isotropic exchange interaction, which is the main driving mechanism for the spin spiral wavelength close to $4a$. This might be related to additional computational approximations employed by those authors, such as the atomic sphere approximation and the angular momentum cutoff of $\ell_{\mathsf{max}} = 2$. In addition to the calculation of the exchange interactions, they also performed a so-called ab-initio spin dynamics calculation to obtain the spin structure of the Fe chain directly from first principles without considering a Heisenberg model. With this alternative approach the authors found a spin spiral which is quite similar to the one we have previously described.

7.3.2. Effective tight-binding models

In this section, we set up a realistic tight-binding model for the different chains using first-principles input paramters and the magnetic structures determined in the previous section. The model is used to analyze the emergence of zero-energy boundary states in the presence of proximity-induced superconductivity.

Tight-binding parameters

Using the KKR Green functions and block matrix inversion (see discussion around eqs. (6.39) and (6.40)), we extract an effective tight-binding hamiltonian. The on-site parameters of the 20-atomic Fe chain without Co and with Co attached to each side is shown in Table 7.2. The parameters of the 20-atomic Fe chain are hardly influenced at the boundary of the chain. The spin splitting, which is proportional to the spin moment of the atoms, and the average d-level energy are slightly increasing at the boundary of the chain, but the spin-orbit strength is not affected. A very important difference of the first-principles parametrization of the Fe chain

	E_d [eV]	U [eV]	Γ [eV]	λ [eV]		E_d [eV]	U [eV]	Γ [eV]	λ [eV]
					Co 1	-0.874	0.020	-0.625	0.038
					Co 2	-0.933	0.049	-0.648	0.039
					Co 3	-0.935	0.192	-0.649	0.039
					Co 4	-0.939	0.246	-0.650	0.039
					Co 5	-1.001	0.416	-0.654	0.039
Fe 1	-0.884	1.090	-0.750	0.041	Fe 6	-0.882	1.019	-0.769	0.042
Fe 2	-0.931	1.057	-0.776	0.042	Fe 7	-0.893	1.029	-0.771	0.042
Fe 3	-0.901	1.034	-0.775	0.042	Fe 8	-0.911	1.039	-0.775	0.042
Fe 4	-0.909	1.040	-0.774	0.041	Fe 9	-0.912	1.039	-0.774	0.041
Fe 5	-0.908	1.038	-0.773	0.042	Fe 10	-0.908	1.037	-0.774	0.042
Fe 6	-0.911	1.040	-0.773	0.041	Fe 11	-0.911	1.039	-0.774	0.041
Fe 7	-0.911	1.039	-0.774	0.042	Fe 12	-0.910	1.040	-0.774	0.042
Fe 8	-0.910	1.039	-0.775	0.042	Fe 13	-0.910	1.039	-0.774	0.042
Fe 9	-0.910	1.039	-0.774	0.042	Fe 14	-0.910	1.039	-0.774	0.041
Fe 10	-0.910	1.039	-0.774	0.042	Fe 15	-0.910	1.039	-0.774	0.041
Fe 11	-0.910	1.039	-0.774	0.042	Fe 16	-0.910	1.039	-0.774	0.041
Fe 12	-0.910	1.039	-0.774	0.042	Fe 17	-0.910	1.039	-0.774	0.041
Fe 13	-0.910	1.039	-0.775	0.042	Fe 18	-0.910	1.039	-0.774	0.042
Fe 14	-0.911	1.039	-0.774	0.042	Fe 19	-0.910	1.040	-0.774	0.042
Fe 15	-0.911	1.040	-0.773	0.041	Fe 20	-0.911	1.039	-0.774	0.041
Fe 16	-0.908	1.038	-0.773	0.042	Fe 21	-0.908	1.037	-0.774	0.042
Fe 17	-0.909	1.040	-0.774	0.041	Fe 22	-0.912	1.039	-0.774	0.041
Fe 18	-0.901	1.034	-0.775	0.042	Fe 23	-0.911	1.039	-0.775	0.042
Fe 19	-0.931	1.057	-0.776	0.042	Fe 24	-0.893	1.029	-0.771	0.042
Fe 20	-0.884	1.090	-0.750	0.041	Fe 25	-0.882	1.019	-0.769	0.042
					Co 26	-1.001	0.416	-0.654	0.039
					Co 27	-0.939	0.247	-0.650	0.039
					Co 28	-0.935	0.192	-0.649	0.039
					Co 29	-0.933	0.050	-0.648	0.039
					Co 30	-0.874	0.020	-0.625	0.038

Table 7.2.: On-site parameters of the 20-atomic Fe chain witout Co (left) and with 5 Co atoms attached to each side (right) obtained from first principles. All parameters are in units of [eV].

$\Delta_{10}^{\text{(re)}}$	xy	yz	z^2	xz	x^2-y^2
xy	-0.287	-0.000	0.000	0.564	-0.000
yz	-0.000	-0.207	-0.004	0.000	0.551
z^2	0.000	-0.004	1.024	0.000	-0.020
xz	0.564	0.000	0.000	-0.277	0.000
x^2-y^2	-0.000	0.551	-0.020	0.000	-0.253

Table 7.3.: Crystal field splitting $\Delta^{\text{(re)}}$ of the 10-th Fe atom of the 20-atomic Fe chain. All parameters are in units of [eV].

$t_{10,11}$	xy	yz	z^2	xz	x^2-y^2
xy	0.35	0.00	0.00	-0.08	0.00
yz	0.00	0.00	0.00	0.00	0.12
z^2	0.00	0.00	-0.13	0.00	0.31
xz	-0.08	0.00	0.00	0.05	0.00
x^2-y^2	0.00	0.12	0.31	0.00	-0.38

Table 7.4.: Hopping matrix between the d-orbitals of the two central Fe atoms of the 20-atomic Fe chain deposited on Re(0001) obtained from first principles. All parameters are in units of [eV].

$t_{1,2}$	xy	yz	z^2	xz	x^2-y^2
xy	0.29	0.01	-0.01	-0.07	0.00
yz	0.01	0.02	0.00	0.01	0.09
z^2	-0.01	0.00	-0.05	-0.01	0.25
xz	-0.07	0.01	-0.01	0.03	0.01
x^2-y^2	0.00	0.09	0.25	0.01	-0.33

Table 7.5.: Hopping matrix between the d-orbitals of the first two neighboring Co atoms at the border of the 20-atomic Fe chain with 5 Co atoms attached to each side obtained from first principles. All parameters are in units of [eV].

compared to the widely used SK parametrization is that crystal field effects are taken into account. The matrix $\Delta^{\text{(re)}}$ (see eq. 7.4) for one of the central Fe atom is shown in Table 7.3. There is a significant hybridization between the xy and xz orbitals, and between the yz and x^2-y^2 orbitals, which is related to the symmetry of the one-dimensional chain deposited on the hexagonal Re(0001) surface, which leads to an orbital-dependent energy shift.

Interestingly, the 20-atomic Fe chain with Co attached to both sides not only indicates that the 20-atomic Fe chain is more homogeneous (see Table 7.2), but also shows that the Co atoms behave similar to the Fe but with decreasing spin moment. All on-site parameters except the spin splitting deviate less than $20\,\%$ from the corresponding ones of the central Fe atom.

The hopping matrix between the central Fe atoms of the 20-atomic Fe chain is shown in Table 7.4, while the hopping matrix between the first two Co atoms of the 20-atomic Fe chain with 5 Co atoms attached to each side is shown in Table 7.5. Both hopping matrices show a similar structure and are quantitatively similar. Note that the hopping Fe atoms vastly differs from the Slater-Koster parametrization using bulk Fe parameters shown in Table 7.1. In addition to the shown nearest-neighbor hoppings, our first-principles results indicate large hoppings beyond the nearest-neighbor bond. Even for atoms separated by four lattice constants a z^2 to z^2 hopping of $t_{8,12}^{z^2,z^2} = 0.12\,\mathrm{eV}$ is found. These hoppings are most probably related to a renormalization from the Re substrate, which is indirectly taken into account in our approach. The z^2 orbitals have a significant overlap with the substrate orbitals, which can mediated an effective hopping between two far-away Fe atoms.

Band structure and Majorana number

To analyze the possibility for Majorana bound states to emerge from our realistic tight-binding model, we construct an one-dimensional Fe chain using the tight-binding parameters from the center of the 20-atomic Fe chain. We include hoppings up to the 4th-nearest neighbor and assume a spin spiral state with four lattice constants wavelength (similar to the experimentally found one) with the plane of rotation tilted by 30° with respect the the x-y plane. The band structure of the superconducting state with a pairing potential of $\Delta = 0.83\,\mathrm{eV}$ is shown in Fig. 7.7. The combination of the superconductivity and the non-collinear magnetic structure opens a band gap of $\Delta E_{\text{gap}} = 0.09\,\mathrm{eV}$. The Majorana number calculated for this set of parameters indicates that the Fe chain is in the non-trivial phase with $\mathcal{M} = -1$.

To investigate the impact of the average d-level energy and the spin splitting on the Majorana number, similar to the well-known results shown in Fig. 7.3, Fig. 7.8a shows the phase diagram

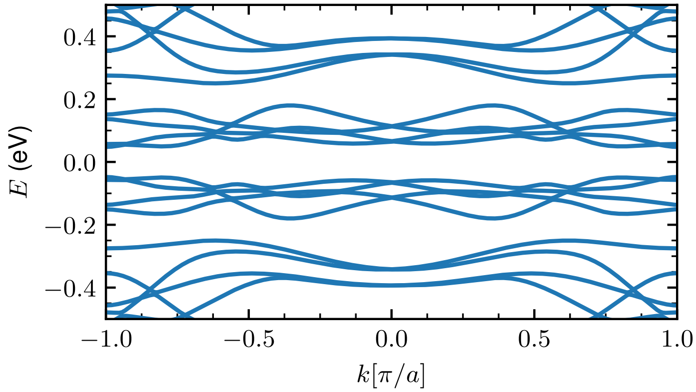

Figure 7.7.: Band structure of the pure Fe chain using an effective Hamiltonian from first principles (see eqs. (7.2) and (7.4)). The pairing potential is set to $\Delta = 0.83\,\mathrm{eV}$. Hoppings are included up to the fourth neighbor. The magnetic moments are assumed to rotate in the plane that makes an angle of 30° with the xy-plane with a wavelength of four lattice constants. A super cell with four Fe atoms is used. The parameters are taken from the center of the 20-atomic Fe chain. The Majorana number of $\mathcal{M} = -1$ indicates that the chain is in the non-trivial phase.

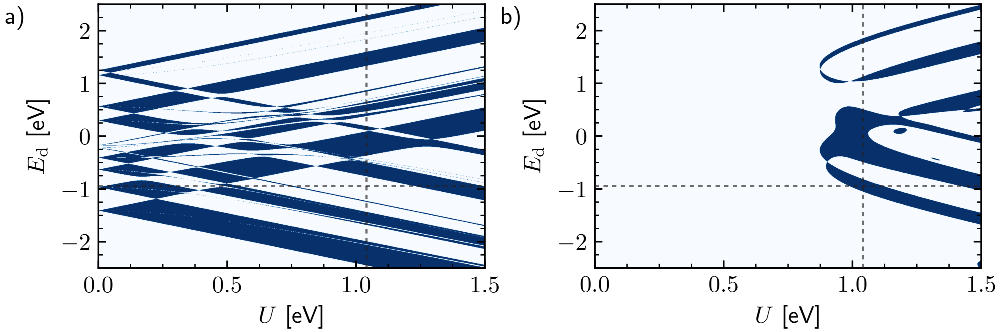

Figure 7.8.: Majorana number $\mathcal{M} = \text{sgn}\left(\text{Pf}(A_{k=0})\text{Pf}(A_{k=\pi/a})\right)$ as function of the average d-level energy E_d and the spin splitting U. The remaining parameters are taken from the center of the 20-atomic Fe chain as shown in Tables 7.2 and 7.3 and hoppings are included up the fourth neighbor. The magnetic moments are assumed to rotate in the plane that makes an angle of 30 ° with the xy-plane with a wavelength of four lattice constants. The topological trivial states are white, while the topological non-trivial regions are blue. a) Pairing potential of $\Delta = 0.0$ eV. b) Pairing potential of $\Delta = 0.83$ eV. The dashed lines indicate the values obtained from the first-principles calculations.

of the Majorana number using the realistic hoppings, and the realistic crystal field splitting. The phase diagram shows a complex landscape of trivial and non-trivial regions, which results from the complex combination of orbital-dependent hoppings and the crystal field splitting. Note that the phase diagram is very sensitive to most of the ingredients, namely the chosen magnetic structure, the number of shells considered for the hoppings, and the crystal field splitting. Without superconducting pairing, the phase diagram indicates that the Fe chain is in the trivial phase. However, for the simple one-dimensional models it is known that large pairings have to reproduce a lateral extent of the boundary states that resembles the experimental observations (see e.g. [210]). Fig. 7.8b shows a phase diagram for a large pairing of $\Delta = 0.83$ eV. For the first-principles parameters the phase diagram now indicates that the Fe chain is in the topologically non-trivial region, which is a necessary condition for Majorana bound states to emerge.

Overall, our analysis shows that the commonly-used phase diagram shown in Fig. 7.3 does not apply to realistic one-dimensional chains and that without the precise knowledge of the proximity-induced pairing potential, e.g. from first principles, a prediction of Majorana bound states based solely on the Majorana number is unreliable.

Boundary states in real space

Using the realistic tight-binding hamiltonian with the parameters obtained from first-principles and the magnetic structure described in Section 7.3.1 for the three different considered chains, we can investigate the formation of boundary states in real space. Fig. 7.9a shows the probability density of the lowest-energy wavefunction for the three chains. Depending on the precise

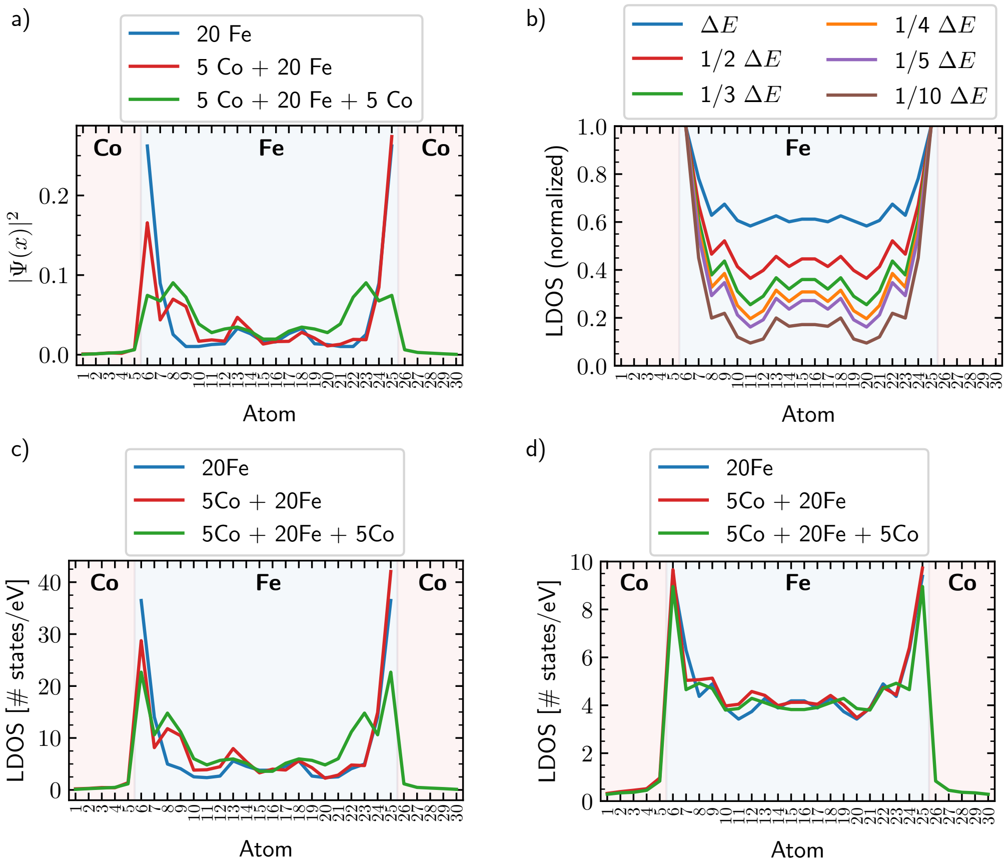

Figure 7.9.: Spatial localization of the boundary states. a) Probability density of the lowest-energy boundary state for the three different chains. b)-d) Local density of states at the Fermi level. An artificial broadening is used to account for temperature effects. The dependence of the LDOS of the 20-atomic Fe chain on the broadening is shown in panel b. ΔE is the bandgap induced by superconductivity, which is found to be $\Delta = 0.09\,\mathrm{eV}$ within the model. The LDOS of all three chains is shown for two different broadenings in c and d. A broadening of $1/20\Delta E$ is used in c, while a broadening of $1/2\Delta E$ is used in d. The parametrizations and magnetic structures are obtained from first-principles as described in the main text.

value of the pairing potential Δ, the energy of the lowest-energy state varies, but there is always a clear separation between the lowest-energy state and other in-gap states. For example for the 20-atomic Fe chain with Co attached to both sides and a pairing potential of $0.83\,\mathrm{eV}$, the lowest-energy state is at $0.7\,\mathrm{meV}$, while the second lowest-energy state is at $7.4\,\mathrm{meV}$. Keep in mind that the energy scales are corrupted due to the large pairing potential, which is needed in the one-dimensional models for boundary states to emerge. In principle, the pairing potential can be tuned in order to minimize the energy of the lowest-energy state, which yields energies less than $1\,\mu\text{eV}$. However, the real space distribution does not depend on the precise value of the pairing, which is why we restrict ourselves to a common pairing of $\Delta = 0.83\,\text{eV}$ for all three chains. The lowest-energy state of the 20-atomic Fe chain shown in Fig. 7.9a shows a high probability density at the boundaries of the chains with only small probability in the center of the chain. The boundary states are localized to the two boundary Fe atoms. Attaching five Co atoms to one end of the chain influences the boundary states at the end of the Fe chain, while the other boundary is nearly unaffected. The state at the Fe-Co interface remains confined to the Fe chain with a negligible probability distribution spreading to the Co atoms, which indicates that the magnetism in the Fe chain is important for the boundary state. However, its localization at the end of the Fe chain is strongly modified, with a high probability density now extending up to the fourth Fe atom counting from the Fe-Co interface. This effect becomes even more visible when attaching Co to both sides of the 20-atomic Fe chain. In both interface regions clear boundary states emerge, which are spread to four Fe atoms. Thus, attaching Co does not impact the formation of boundary states in the Fe chain, but it does impact their spatial localization.

To estimate the impact of temperature and other experimental inaccuracies, which are reflected by an energy broadening, Fig. 7.9b shows the local density of states at the Fermi level ($E = 0$) for the 20-atomic Fe chain as function of an artificial broadening Γ normalized to the boundary states, which is defined by

$$\rho_i(E = 0) = \frac{1}{\pi} \sum_n \langle n|\mathcal{P}_i|n\rangle \, \frac{\Gamma}{E_n^2 + \Gamma^2} \quad , \tag{7.12}$$

where n sums the eigenstates with eigenenergy E_n of the BdG hamiltonian, eq. (7.2), and $\mathcal{P}_i$ is the projector on the i-th atom. The broadening is given as function of the estimated band gap of $\Delta E = 0.09\,\text{eV}$ (see Fig. 7.7). When the broadening is increased, in addition to the lowest-energy state other states contribute to the local density of states. Increasing the broadening reduces the difference in the local density of states between the boundary and the center of the chain. For the chosen broadening of up to ΔE, a clear signature of the boundary state remains. The broadening basically introduces a constant background, which is similar to the states known from the simple particle in a box picture.

For a small broadening of $1/20\,\Delta E$ the local density of states is shown in Fig. 7.9c. This broadening mainly involves the lowest-energy state and signatures of the first excited states. The main features are identical to the lowest-energy probability distribution: There are clear boundary states for all three chains, and attaching Co influences the localization of these states. With increasing broadening these features are washed out, as can be seen in Fig. 7.9d for a broadening of $1/2\,\Delta E$. While all chains show clear boundary states, there are only minor differences in their effective spatial localization as perceived from the spectra, due to the high energy broadening.

STM experiments show that the superconducting Re(0001) surface has an energy gap of $0.28\,\text{meV}$, which is also seen when probing the Fe chain [84]. For typical experimental temperatures, the temperature broadening is approximately $T = 350\,\text{mK}$, so $k_\text{B}T = 0.03\,\text{meV}$, but additional experimental inaccuracies yield energy resolutions of the order of $\sim 0.1\,\text{meV}$. Thus, it remains unclear if the theoretical predicted delocalization effects can be experimentally observed, or to be precise if the experiment would resolve a local density of states which is closer either to Fig. 7.9 c or d.

7.4. Conclusions and outlook

In this Chapter, we showed how the interplay of superconductivity and a complex magnetic structure gives rise to boundary states in one-dimensional Fe chains deposited on the Re(0001) surface, and how an Fe-Co interface can influence these boundary states. First, we investigated the magnetic properties of the three considered chains and found how the frustrated isotropic interaction between nearest and next-nearest neighbors yields a spin spiral with a wavelength of approximately $\lambda = 3a$. The plane of rotation is fixed by the strong Dzyaloshinskii-Moriya interaction favouring an in-plane spiral over the out-of-plane spiral, while the magnetic anisotropy (both on-site and pairwise) was found to have a negligible impact on the magnetic state of the chain. An experimental study of this system found a spin spiral with wavelength $\lambda = 4a$ [84], in fair agreement with our results. A previous theoretical work also based on KKR calculations found quite different magnetic interactions from the ones we obtained [60], which we assume is due to the additional numerical approximations used by those authors.

Special attention was also given to the impact of Co atoms on the Fe chain. We found the 5-atomic Co chain to be non-magnetic on the Re(0001) substrate with proximity-induced magnetism only in the vicinity of the magnetic Fe chain. The additional interface with Co increases the coordination number the boundary Fe atom resulting in a bulk-like (i.e., similar to those of the Fe atoms in the middle of the chain) magnetic moment at the interface. In the terms of the magnetic interactions, the interfacial Co atom showed significant isotropic exchange and DMI, and the interactions in the interfacial Fe region approached the interactions in the center of the chain. In total, the Co acts like a non-magnetic extension of the Fe chain, smearing out the boundary effects in the Fe chain.

To analyze the impact of superconductivity, a tight-binding model was used. Parameters for a realistic one-dimensional tight-binding model of the Fe chain accounting indirectly for the effects of the Re substrate were extracted using first-principles calculations. Similar to the magnetic structure, we showed that Co acts like a non-magnetic extension of the Fe chain with comparable tight-binding parameters. Using the realistic model parameters, we analyzed the Majorana number as function of the average d-level energy and the spin splitting. We found a complex phase space, which is sensitive to a variety of parameters contradicting the commonly used phase diagram, which predicts a topologically non-trivial state for most magnetic chains [210]. From our analysis it remains unclear, whether a prediction of Majorana bound states in finite chains using the Majorana number of an infinite chain is meaningful. Boundary effects in the finite chain influence the tight-binding parameters and the magnetic structure in a non-trivial way, but the Majorana number of the infinite chain is very sensitive to exactly those small changes.

In a last step, the formation of boundary states in the three different finite chains was analyzed. The lowest-energy eigenstates of the BdG hamiltonian show clear boundary states for the 20-atomic Fe chain. These states are modulated in the vicinity of Co, which is reflected in their spatial delocalization. However, the states do not spread to the Co atoms indicating a strong dependence on the magnetism in the Fe chain. Combined with the knowledge of the Majorana number for this particular chain, the boundary states might correspond to a Majorana bound state. In that case, the localization of the boundary state would correspond to the coherence length of the Majorana state, and we showed that the candidate Majorana state can be engineered using the Fe-Co interface.

Our results are in particular important for the interpretation of experimentally found boundary states, since it is not clear if these states are trivial Yu-Shiba-Rusinov states or non-trivial Majorana states. From our analysis it turned out that the Co termination of the Fe chain minimizes magnetic and electronic boundary effects in the Fe chain. However, for trivial boundary states to emerge these boundary effects, like e.g. an increase in the magnetization at the boundary, are necessary. Thus, we have a strong motivation to attribute the boundary states to the topologically non-trivial Majorana states, a finding which has important implications for the field of topological quantum computing.

8

Conclusions

In this thesis, we have presented a comprehensive analysis of various effects in magnetic nanostructures deposited on non-magnetic surfaces based on first-principles calculations assisted by simplified models. In order to describe magnetic properties like the orbital magnetic moment, higher-order magnetic exchange interactions, and spin dynamics in non-collinear systems, different developments have lead to extensions and improvements in the DFT codes developed in Jülich using the Korringa-Kohn-Rostoker Green function method.

The ground state charge current density and its classical connection to the orbital magnetic moment uncovered a so far neglected contribution to the orbital magnetism – the inter-atomic orbital moment, which was discussed in Chapter 3. Among the well-known magnetic contributions relevant for the induced magnetism, namely the induced spin moment and the induced atomic orbital moment, we identified the inter-atomic orbital moment as a third contribution to the induced magnetism and found important implications. Using a unique computational scheme that handled up to 3000 substrate atoms, we were able to shed light on its properties, in particular on its long range, its anisotropy, its relevance in terms of its magnitude, and its distinct physical origin. The Pt(111) surface was identified to offer the ideal combination of strong spin-orbit coupling and large spin polarizability resulting in tremendous corrections arising from the inter-atomic orbital moment, which for some cases even exceeds its atomic counterpart. With a range of more than $20\,\text{Å}$ the inter-atomic orbital moment significantly extends beyond the other magnetic contributions, which reach approximately $7.5\,\text{Å}$, and therefore it might open an avenue for new long ranged effects and interactions based on the orbital degrees of freedom. Using magnetic stray fields, we proposed how the range of the induced magnetism could be probed using experimental techniques being sensitive to the magnetic field like scanning nitrogen-vacancy microscopy. Our results show unambiguously that the inter-atomic orbital moment being part of the total magnetic moment has to be addressed both from the fundamental theoretical point of view, but also for the interpretation of experiments.

After addressing the ground-state spin and orbital magnetic moments, we focused on the spin degrees of freedom and in particular on higher-order magnetic exchange interactions, which were discussed in Chapter 4. A microscopic model based on a separation of spin-orbit coupling sites and magnetic sites shed light on the general functional form of higher-order interactions and enabled the derivation of symmetry rules. We identified the chiral biquadratic interaction as the biquadratic equivalent to the bilinear Dzyaloshinskii-Moriya interaction and analyzed its importance in realistic systems, namely magnetic dimers on $4d$ transition metal surfaces, based on the method of constraining fields, which has been implemented in the local KKR codes as part of this thesis work. We found this new interaction to have non-trivial implications for the non-collinear state of dimers, one-dimensional chains, and complex non-collinear structures like a nanoskyrmion lattice, which was favoured over e.g. single $\boldsymbol{Q}$-states.

The spin dynamics in non-collinear nanostructures were addressed in Chapter 5 with particular focus on the Gilbert damping. Using an Anderson model, we were able to identify and catalogue the most important dependencies of the Gilbert damping on the non-collinear magnetic state in an atomistic representation. Depending on the magnetic moment, we found significant isotropic and chiral dependencies, where the latter ones originate from spin-orbit coupling and give rise to the so-called chiral damping. The functional forms were used to explain first-principles calculations of magnetic dimers deposited on the Au(111) surface. Our atomistic representation is especially valuable for the field of atomistic spin dynamics, since it allows for a realistic study of the spin dynamics in non-collinear structures. Our findings might help for the design of future devices like racetrack memories utilizing domain walls or skyrmions, for which we expect a non-trivial impact.

Spin dynamics were also approached from another angle by describing the magnetic stability as probed in telegraph noise STM experiments in Chapter 6. Special focus was given to the impact of interactions and especially long-ranged interactions on the magnetic stability of an Fe trimer coupled to an Fe adatom on the Pt(111) surface. We identified three different regimes, each driven by a distinct bilinear interaction. In the weak-coupling regime, we found the weak interaction to enable an indirect measurement of the magnetic state of the trimer by probing the adatom. In the intermediate-coupling regime, the Dzyaloshinskii-Moriya interaction was found to destabilize the trimer-adatom complex, which was shown to be a general implication of this interaction. In the strong-coupling regime, in which intuitively the strong isotropic coupling should enhance the magnetic stability, we found the symmetric anisotropic interaction to substantially destabilize the trimer-adatom complex due to an effective induced in-plane anisotropy. The last finding allowed for a systematic engineering of magnetic stability by utilizing a symmetric arrangement of surrounding adatoms. Therefore in the strong-coupling regime, placing adatoms in a way that preserves the C_{3v} symmetry of the trimer significantly enhances the lifetime of the trimer by orders of magnitude, since the effective in-plane anisotropy is suppressed.

The results part of this thesis was concluded with Chapter 7, where we focused on the complex interplay of magnetism and superconductivity in magnetic chains deposited on the superconducting Re(0001) substrate. We solved the puzzling magnetic ground state of Fe chains, which was found to be based on the interplay of strong antiferromagnetic nearest and next-nearest neighbor interactions resulting in a spin spiral of close to four lattice constants wavelength agreeing well with the experimental findings. By using a mapping from first-principles to an effective tight-binding model including only the d-states of the magnetic chain, but accounting indirectly for the impact of the Re substrate, we were able to include superconductivity (as a parameter) and describe the emergence of boundary states in real space, which were previously observed in STM experiments. The realistic tight-binding parametrization shed light on the complex phase diagram of the topological Majorana phase in realistic one-dimensional chains. Using non-magnetic Co termination, we were able to minimize boundary effects in the electronic and magnetic structure of the Fe chain strengthening the assumption that the found boundary states originate from Majorana states and not from Yu-Shiba-Rusinov states.

Future perspectives

For most of the effects discussed in this thesis finite nanostructures on surfaces are perfect prototypical test systems since they allow for an easy understanding of the basic mechanisms in real space and they are potentially useful for spintronics devices. Another maybe even more studied direction in the field of spintronics are two-dimensional systems. Especially the study of higher-order magnetic exchange interactions and the study of the full angular dependencies of the Gilbert damping could have a strong impact in two-dimensional and bulk structures. However, systematic studies like presented in this thesis are computationally not feasible for extended systems, for which only a subset of higher-order interactions or a subset of angular dependencies of the Gilbert damping can be used. Our work can help to identify these subsets and to solve some of the puzzling magnetic ground states and to broaden the understanding of spin dynamics especially in non-collinear structures.

With respect to the magnetic stability, our work set the ground for a model study which is solely based on first-principles parameters. Further systematic studies with respect to the chemical nature of the nanostructure and the substrate could help predicting new stable magnets. Our general findings on the dependence of the magnetic stability on the interactions between nanostructures can also help to design future spintronics devices, for example a grid of stable nanomagnets which uses the knowledge of the impact of magnetic interactions to maximize the magnetic stability of each nanomagnet, while minimizing the interactions between the nanomagnet.

A

Rydberg atomic units

If not explicitly mentioned throughout this thesis Rydberg atomic units are used, for which the fundamental physical constants are defined by,

Definition	Quantity
$\hbar = 1$	Planck constant
$a_B = 1$	Bohr radius
Ry $= 1$	Rydberg energy
$4\pi\epsilon_0 = 1$	Coulomb constant

leading to the following important quantities:

	Quantity
$e = \sqrt{2}$	elementary charge
$m_e = \frac{1}{2}$	electron mass
$\mu_B = \sqrt{2}$	Bohr magneton

B

Magnetic susceptibility using Matsubara Green functions

An introduction to the Matsubara formalism can be found in standard textbooks, e.g. Ref. [118, 119, 219].

A generic correlation function of a non-interacting system is defined in real time as

$$C_{AB}(\boldsymbol{r},\boldsymbol{r}';t-t') = -\mathrm{i}\,\Theta(t-t')\left\langle\left[\hat{A}(\boldsymbol{r},t),\hat{B}(\boldsymbol{r}',t')\right]_{\pm}\right\rangle \quad , \tag{B.1}$$

where $\langle A\rangle$ is the ground-state expectation value, and $[A,B]_{\pm} = AB \pm BA$ is the (anti-)commutator for bosonic and fermionic operators A and B, respectively. For imaginary times the time-ordered correlation function is defined by

$$C_{AB}(\boldsymbol{r},\boldsymbol{r}';\tau) = -\left\langle T_\tau\left[\hat{A}(\boldsymbol{r},\tau)\hat{B}(\boldsymbol{r}',0)\right]\right\rangle \quad , \tag{B.2}$$

with the time ordering symbol T_τ,

$$T_\tau\left[A(\tau)B(\tau')\right] = \begin{cases} A(\tau)B(\tau'), & \text{for } \tau > \tau' \\ \pm B(\tau')A(\tau), & \text{for } \tau < \tau' \end{cases} \quad . \tag{B.3}$$

For the spin–spin correlation function the operators are

$$\hat{A} = \mathcal{S}^\alpha_i(\boldsymbol{r},\tau) \quad , \quad \hat{B} = \mathcal{S}^\beta(\boldsymbol{r},\tau) \quad \text{with} \quad \mathcal{S}^\alpha(\boldsymbol{r},\tau) = \psi^\dagger(\boldsymbol{r},\tau)\boldsymbol{\sigma}^\alpha\psi(\boldsymbol{r},\tau) \quad , \tag{B.4}$$

which yields for the correlation function,

$$\chi^{\alpha\beta}_{mm}(\boldsymbol{r},\boldsymbol{r}';\tau) = -\left\langle T_\tau\left[\mathcal{S}^\alpha(\boldsymbol{r},\tau)\mathcal{S}^\beta(\boldsymbol{r}',0)\right]\right\rangle \tag{B.5}$$

$$= -\sum_{s_1\ldots s_4}\left\langle T_\tau\psi^\dagger_{s_1}(\boldsymbol{r},\tau)\sigma^\alpha_{s_1s_2}\psi_{s_2}(\boldsymbol{r},\tau)\psi^\dagger_{s_3}(\boldsymbol{r}',0)\sigma^\beta_{s_3s_4}\psi_{s_4}(\boldsymbol{r}',0)\right\rangle \tag{B.6}$$

$$= -\sum_{s_1\ldots s_4}\sigma^\alpha_{s_1s_2}\sigma^\beta_{s_3s_4}\left\langle T_\tau\psi^\dagger_{s_1}(\boldsymbol{r},\tau)\psi_{s_2}(\boldsymbol{r},\tau)\psi^\dagger_{s_3}(\boldsymbol{r}',0)\psi_{s_4}(\boldsymbol{r}',0)\right\rangle \tag{B.7}$$

Calling $1 = (s_1,\boldsymbol{r},\tau)$, $2 = (s_2,\ldots)$ and applying Wick's theorem one finds:

$$\left\langle T_\tau\psi^\dagger_{s_1}(\boldsymbol{r},\tau)\psi_{s_2}(\boldsymbol{r},\tau)\psi^\dagger_{s_3}(\boldsymbol{r}',0)\psi_{s_4}(\boldsymbol{r}',0)\right\rangle$$

$$
\begin{aligned}
&= \left\langle T_\tau \left[\delta_{12}\delta_{34} - \delta_{12}\psi(4)\psi^\dagger(3) - \delta_{34}\psi(2)\psi^\dagger(1) - \psi(2)\psi(4)\psi^\dagger(1)\psi^\dagger(3)\right]\right\rangle \\
&= \ldots - G^{(2)}(2,4;1,3) = \ldots - \begin{vmatrix} G(2,1) & G(2,3) \\ G(4,1) & G(4,3) \end{vmatrix} = \ldots - G(2,1)G(4,3) + G(2,3)G(4,1) \quad ,
\end{aligned}
\tag{B.8}
$$

where we first used the fermionic anti-commutation relations, $G^{(2)}$ is the two-particle Green function and G is the single-particle Green function. We focus on the transverse spin susceptibility, $\alpha, \beta = x, y$, for which the Pauli matrices are off-diagonal in spin so that there are no additional terms rising from the commutation relations in eq. (B.8). The previous formula yields

$$
\begin{aligned}
\chi^{\alpha\beta}_{mm}(\boldsymbol{r}, \boldsymbol{r}'; \tau) = \sum_{s_1 \ldots s_4} \sigma^\alpha_{s_1 s_2} \sigma^\beta_{s_3 s_4} \Big[& G(\boldsymbol{r}, \tau, s_2; \boldsymbol{r}, \tau, s_1) G(\boldsymbol{r}', 0, s_4; \boldsymbol{r}', 0, s_3) \\
& - G(\boldsymbol{r}, \tau, s_2; \boldsymbol{r}', 0, s_3) G(\boldsymbol{r}', 0, s_4; \boldsymbol{r}, \tau, s_1) \Big] \quad .
\end{aligned}
\tag{B.9}
$$

Without SOC the first term in the bracket vanishes since the Green function is spin-diagonal for a ferromagnetic system with the magnetization along the z-direction resulting in

$$
\chi^{\alpha\beta}_{mm}(\boldsymbol{r}, \boldsymbol{r}'; \tau) = - \sum_{s_1 \ldots s_4} \sigma^\alpha_{s_1 s_2} \sigma^\beta_{s_3 s_4} G(\boldsymbol{r} s_2, \boldsymbol{r}' s_3; \tau) G(\boldsymbol{r}' s_4, \boldsymbol{r} s_1; -\tau) \quad . \tag{B.10}
$$

The Fourier transformation of this expression is a convolution,

$$
c(\tau) = a(\tau) b(-\tau) = \left(\frac{1}{\beta} \sum_{\mathrm{i}\omega_n} a(\mathrm{i}\omega_n) e^{-\mathrm{i}\omega_n \tau} \right) \left(\frac{1}{\beta} \sum_{\mathrm{i}\omega_m} b(\mathrm{i}\omega_m) e^{\mathrm{i}\omega_m \tau} \right) \tag{B.11}
$$

$$
= \frac{1}{\beta^2} \sum_{\mathrm{i}\omega_n, \mathrm{i}\omega_m} a(\mathrm{i}\omega_n) b(\mathrm{i}\omega_m) e^{\mathrm{i}(\omega_m - \omega_n)\tau} \tag{B.12}
$$

$$
= \frac{1}{\beta} \sum_{\mathrm{i}\omega_n} \left(\frac{1}{\beta} \sum_{\mathrm{i}\omega_m} a(\mathrm{i}\omega_n + \mathrm{i}\omega_m) b(\mathrm{i}\omega_m) \right) e^{-\mathrm{i}\omega_n \tau} \tag{B.13}
$$

$$
= \frac{1}{\beta} \sum_{\mathrm{i}\omega_n} c(\mathrm{i}\omega_n) e^{-\mathrm{i}\omega_n \tau} \quad , \tag{B.14}
$$

which yields for the correlation function

$$
\chi^{\alpha\beta}_{mm}(\boldsymbol{r}, \boldsymbol{r}'; \mathrm{i}\omega_n) = \frac{1}{\beta} \sum_{\mathrm{i}\omega_m} \sum_{s_1 \ldots s_4} \sigma^\alpha_{s_1 s_2} \sigma^\beta_{s_3 s_4} G(\boldsymbol{r} s_2, \boldsymbol{r}' s_3; \mathrm{i}\omega_n + \mathrm{i}\omega_m) G(\boldsymbol{r}' s_4, \boldsymbol{r} s_1; \mathrm{i}\omega_m) \tag{B.15}
$$

$$
= \frac{1}{\beta} \sum_{\mathrm{i}\omega_m} \mathrm{Tr} \left[\boldsymbol{\sigma}^\alpha G(\boldsymbol{r}, \boldsymbol{r}'; \mathrm{i}\omega_n + \mathrm{i}\omega_m) \boldsymbol{\sigma}^\beta G(\boldsymbol{r}', \boldsymbol{r}; \mathrm{i}\omega_m) \right] \quad , \tag{B.16}
$$

where $\mathrm{i}\omega_n$ are bosonic Matsubara frequencies and $\mathrm{i}\omega_m$ are fermionic Matsubara frequencies. The sum over the fermionic Matsubara frequencies can be performed by using Cauchy's integral formula and the Fermi distribution function, which has poles at fermionic Matsubara frequencies as can be seen as follows: The residue of the Fermi distribution, $n_F(z) = (e^{\beta z} + 1)^{-1}$, is given by

$$
\mathrm{Res}\,(n_F(z))\big|_{z = \mathrm{i}\omega_m} = -\frac{1}{\beta} \quad . \tag{B.17}
$$

Assume $g(z)$ to be an analytic function inside an area enclosed by a path γ yields by using the Cauchy's integral formula,

$$\oint_\gamma \frac{\mathrm{d}z}{2\pi\mathrm{i}} n_F(z) g(z) = -\frac{1}{\beta} \sum_{\mathrm{i}\omega_n} g(\mathrm{i}\omega_n) \quad . \tag{B.18}$$

The Green function in eq. (B.16) has a branch cut at the real axis. However, the energy argument of one of the Green functions is shifted by $\mathrm{i}\omega_n$. Therefore the expression has two branch cuts at Im$(z) = 0$ and at Im$(z) = -\mathrm{i}\omega_n$. For $\mathrm{i}\omega_n > 0$ (which is needed for the analytic continuation), a proper contour γ consists of three paths:

- A half circle (Im$(z) > 0$) with a connection at $z = \mathrm{i}0^+$
- A half circle (Im$(z) < 0$) with a connection at $z = -\mathrm{i}\omega_n - \mathrm{i}0^+$
- A rectangle with connections $z = -\mathrm{i}0^+$ and $z = -\mathrm{i}\omega_n + \mathrm{i}0^+$

Applying this to (B.16) one finds:

$$\begin{aligned} \chi^{\alpha\beta}_{mm}(\boldsymbol{r}, \boldsymbol{r}'; \mathrm{i}\omega_n) = \int & \frac{\mathrm{d}\epsilon}{2\pi i} n_F(\epsilon) \\ & \times \left\{ -\text{Tr}\left[\boldsymbol{\sigma}^\alpha G(\boldsymbol{r}, \boldsymbol{r}'; \mathrm{i}\omega_n + \epsilon + \mathrm{i}0^+) \boldsymbol{\sigma}^\beta G(\boldsymbol{r}', \boldsymbol{r}; \epsilon + \mathrm{i}0^+)\right] \right. \\ & \quad + \text{Tr}\left[\boldsymbol{\sigma}^\alpha G(\boldsymbol{r}, \boldsymbol{r}'; \mathrm{i}\omega_n + \epsilon - \mathrm{i}0^+) \boldsymbol{\sigma}^\beta G(\boldsymbol{r}', \boldsymbol{r}; \epsilon - \mathrm{i}0^+)\right] \\ & \quad - \text{Tr}\left[\boldsymbol{\sigma}^\alpha G(\boldsymbol{r}, \boldsymbol{r}'; \epsilon + \mathrm{i}0^+) \boldsymbol{\sigma}^\beta G(\boldsymbol{r}', \boldsymbol{r}; \epsilon - \mathrm{i}\omega_n + \mathrm{i}0^+)\right] \\ & \quad \left. + \text{Tr}\left[\boldsymbol{\sigma}^\alpha G(\boldsymbol{r}, \boldsymbol{r}'; \epsilon - \mathrm{i}0^+) \boldsymbol{\sigma}^\beta G(\boldsymbol{r}', \boldsymbol{r}; \epsilon - \mathrm{i}\omega_n - \mathrm{i}0^+)\right] \right\} \quad . \end{aligned} \tag{B.19}$$

Doing the analytic continuation $\mathrm{i}\omega_n \to \omega + \mathrm{i}\eta$ with $\eta \to 0^+$ one obtains the final result:

$$\begin{aligned} \chi^{\alpha\beta}_{mm}(\boldsymbol{r}, \boldsymbol{r}'; \omega) = \int & \frac{\mathrm{d}\epsilon}{2\pi\mathrm{i}} n_F(\epsilon) \\ & \times \left\{ -\text{Tr}\left[\boldsymbol{\sigma}^\alpha G(\boldsymbol{r}, \boldsymbol{r}'; \omega + \epsilon + \mathrm{i}\eta) \boldsymbol{\sigma}^\beta G(\boldsymbol{r}', \boldsymbol{r}; \epsilon + \mathrm{i}0^+)\right] \right. \\ & \quad + \text{Tr}\left[\boldsymbol{\sigma}^\alpha G(\boldsymbol{r}, \boldsymbol{r}'; \omega + \epsilon + \mathrm{i}\eta) \boldsymbol{\sigma}^\beta G(\boldsymbol{r}', \boldsymbol{r}; \epsilon - \mathrm{i}0^+)\right] \\ & \quad - \text{Tr}\left[\boldsymbol{\sigma}^\alpha G(\boldsymbol{r}, \boldsymbol{r}'; \epsilon + \mathrm{i}0^+) \boldsymbol{\sigma}^\beta G(\boldsymbol{r}', \boldsymbol{r}; \epsilon - \omega - \mathrm{i}\eta)\right] \\ & \quad \left. + \text{Tr}\left[\boldsymbol{\sigma}^\alpha G(\boldsymbol{r}, \boldsymbol{r}'; \epsilon - \mathrm{i}0^+) \boldsymbol{\sigma}^\beta G(\boldsymbol{r}', \boldsymbol{r}; \epsilon - \omega - \mathrm{i}\eta)\right] \right\} \quad . \end{aligned} \tag{B.20}$$

This formula can be applied for the calculation of the Kohn-Sham susceptibility discussed in eq. (2.107).

C

Table of real spherical harmonics

Throughout this thesis real spherical harmonics are used. The real spherical harmonics $Y_{(\ell,m)}$ up to $\ell = 2$ are given by,

$$Y_{(0,0)}(\boldsymbol{e}) = \sqrt{\frac{1}{4\pi}} \qquad \big(= s\text{-orbital}\big) \qquad \text{(C.1)}$$

$$Y_{(1,-1)}(\boldsymbol{e}) = \sqrt{\frac{3}{4\pi}}\,\frac{y}{r} \qquad \big(= p_y\text{-orbital}\big) \qquad \text{(C.2)}$$

$$Y_{(1,0)}(\boldsymbol{e}) = \sqrt{\frac{3}{4\pi}}\,\frac{z}{r} \qquad \big(= p_z\text{-orbital}\big) \qquad \text{(C.3)}$$

$$Y_{(1,1)}(\boldsymbol{e}) = \sqrt{\frac{3}{4\pi}}\,\frac{x}{r} \qquad \big(= p_x\text{-orbital}\big) \qquad \text{(C.4)}$$

$$Y_{(2,-2)}(\boldsymbol{e}) = \sqrt{\frac{15}{4\pi}}\,\frac{xy}{r^2} \qquad \big(= d_{xy}\text{-orbital}\big) \qquad \text{(C.5)}$$

$$Y_{(2,-1)}(\boldsymbol{e}) = \sqrt{\frac{15}{4\pi}}\,\frac{yz}{r^2} \qquad \big(= d_{yz}\text{-orbital}\big) \qquad \text{(C.6)}$$

$$Y_{(2,0)}(\boldsymbol{e}) = \frac{1}{2}\sqrt{\frac{5}{4\pi}}\,\frac{2z^2 - x^2 - y^2}{r^2} \qquad \big(= d_{z^2}\text{-orbital}\big) \qquad \text{(C.7)}$$

$$Y_{(2,1)}(\boldsymbol{e}) = \sqrt{\frac{15}{4\pi}}\,\frac{xz}{r^2} \qquad \big(= d_{xz}\text{-orbital}\big) \qquad \text{(C.8)}$$

$$Y_{(2,2)}(\boldsymbol{e}) = \frac{1}{2}\sqrt{\frac{15}{4\pi}}\,\frac{x^2 - y^2}{r^2} \qquad \big(= d_{x^2-y^2}\text{-orbital}\big) \quad , \qquad \text{(C.9)}$$

where $\boldsymbol{e}$ is a unit vector with $\boldsymbol{e} = (x, y, z)/r$ and $r = \sqrt{x^2 + y^2 + z^2}$.

D

Relations for the product of Pauli matrices

In the following some useful relations for the trace of the product of Pauli matrices are given,

$$\frac{1}{2}\,\mathrm{Tr}\ \sigma^\alpha\sigma^\beta = \delta_{\alpha\beta} \quad , \tag{D.1}$$

$$\frac{1}{2}\,\mathrm{Tr}\ \sigma^\alpha\sigma^\beta\sigma^\gamma = \mathrm{i}\,\epsilon_{\alpha\beta\gamma} \quad , \tag{D.2}$$

$$\frac{1}{2}\,\mathrm{Tr}\ \sigma^\alpha\sigma^\beta\sigma^\gamma\sigma^\delta = \delta_{\alpha\beta}\delta_{\gamma\delta} - \delta_{\alpha\gamma}\delta_{\beta\delta} + \delta_{\beta\gamma}\delta_{\alpha\delta} \quad , \tag{D.3}$$

$$\frac{1}{2}\,\mathrm{Tr}\ \sigma^\alpha\sigma^\beta\sigma^\gamma\sigma^\delta\sigma^\eta = \mathrm{i}\,(\delta_{\delta\eta}\epsilon_{\alpha\beta\gamma} + \delta_{\alpha\beta}\epsilon_{\gamma\delta\eta} - \delta_{\alpha\gamma}\epsilon_{\beta\delta\eta} + \delta_{\beta\gamma}\epsilon_{\alpha\delta\eta}) \quad , \tag{D.4}$$

$$\begin{aligned}\frac{1}{2}\,\mathrm{Tr}\ \sigma^\alpha\sigma^\beta\sigma^\gamma\sigma^\delta\sigma^\eta\sigma^\zeta = {}& -\epsilon_{\alpha\beta\gamma}\epsilon_{\delta\eta\zeta} + \delta_{\alpha\beta}\delta_{\gamma\delta}\delta_{\eta\zeta} - \delta_{\alpha\gamma}\delta_{\beta\delta}\delta_{\eta\zeta} + \delta_{\alpha\delta}\delta_{\beta\gamma}\delta_{\eta\zeta} - \delta_{\alpha\beta}\delta_{\gamma\eta}\delta_{\delta\zeta} \quad , \\ & + \delta_{\alpha\beta}\delta_{\delta\eta}\delta_{\gamma\zeta} + \delta_{\alpha\gamma}\delta_{\beta\eta}\delta_{\delta\zeta} - \delta_{\alpha\gamma}\delta_{\delta\eta}\delta_{\beta\zeta} - \delta_{\beta\gamma}\delta_{\alpha\eta}\delta_{\delta\zeta} + \delta_{\beta\gamma}\delta_{\delta\eta}\delta_{\alpha\zeta} \quad .\end{aligned} \tag{D.5}$$

In the last equation the product of two Levi-Civita symbols can be related to a sum of Kronecker deltas,

$$\epsilon_{\alpha\beta\gamma}\epsilon_{\delta\eta\zeta} = \begin{vmatrix} \delta_{\alpha\delta} & \delta_{\alpha\eta} & \delta_{\alpha\zeta} \\ \delta_{\beta\delta} & \delta_{\beta\eta} & \delta_{\beta\zeta} \\ \delta_{\gamma\delta} & \delta_{\gamma\eta} & \delta_{\gamma\zeta} \end{vmatrix} \tag{D.6}$$

$$= \delta_{\alpha\delta}\delta_{\beta\eta}\delta_{\gamma\zeta} + \delta_{\alpha\eta}\delta_{\beta\zeta}\delta_{\gamma\delta} + \delta_{\alpha\zeta}\delta_{\beta\delta}\delta_{\gamma\eta} - \delta_{\gamma\delta}\delta_{\beta\eta}\delta_{\alpha\zeta} - \delta_{\gamma\eta}\delta_{\beta\zeta}\delta_{\alpha\delta} - \delta_{\beta\delta}\delta_{\alpha\eta}\delta_{\gamma\zeta} \quad , \tag{D.7}$$

which would then express eq. (D.5) as a sum of 15 terms involving only Kronecker deltas. In general the trace over an even number of arbitrary Pauli matrices can always be brought to this form, while for an odd number there is always one Levi-Civita symbol remaining in every term.

E

Derivation of the master equation

In this Appendix we show how the transition rates $W_{MM'}^{\eta\rightarrow\eta'}$ used in the master equation approach in Chapter 6 can be derived following the steps of Delgado and Fernández-Rossier [191]. We first define

$$S^{\alpha}_{MM',\eta\eta'} = \frac{1}{\chi}\sum_{i} v_i^{\eta} v_i^{\eta'} \langle M|S_i^{\alpha}|M'\rangle \quad , \tag{E.1}$$

with

$$\chi = \sum_{i} v_i^T v_i^S \quad , \tag{E.2}$$

which quantifies the tip-surface transmission through the quantum spins (either single atoms or a nanostructure described by a macro spin), which are probed by the tip. If only the i-th atom is interacting with the tip and therefore couples to the tip it simplifies to $\chi = v_i^S v_i^T$. This is the case, which we consider in the following. The spin operators simplify to

$$S^{\alpha}_{MM',TS} = S^{\alpha}_{i,MM'} = \langle M|S_i^{\alpha}|M'\rangle \quad , \tag{E.3}$$

$$S^{\alpha}_{MM',TT} = \frac{v_i^T}{v_i^S} S^{\alpha}_{i,MM'} = \frac{v_i^T}{v_i^S}\langle M|S_i^{\alpha}|M'\rangle \quad , \tag{E.4}$$

$$S^{\alpha}_{MM',SS} = \frac{1}{\chi}\sum_{j} \left(v_j^S\right)^2 \langle M|S_j^{\alpha}|M'\rangle \quad . \tag{E.5}$$

Combining eq. (E.1) and eqs. (6.16) and (6.17) the transmission rates are given by,

$$W_{MM'}^{\eta\rightarrow\eta'} = \frac{2\pi T_0^2 \chi^2}{\hbar}\mathcal{G}(\Delta_{MM'} + \mu_{\eta} - \mu_{\eta'})\Sigma_{MM'}^{\eta\rightarrow\eta'} \quad , \tag{E.6}$$

with

$$\begin{aligned}\Sigma_{MM'}^{\eta\rightarrow\eta'} =& \frac{1}{4}\delta_{MM'}\left[\mathcal{R}^{+}(\eta\eta') + 2\zeta\mathcal{R}^{-}(\eta\eta')\sum_{\alpha} S^{\alpha}_{MM',\eta\eta'}\right] \\ &+ \zeta^2\left[|S^{+}_{MM',\eta\eta'}|^2\rho_{\eta\downarrow}\rho_{\eta'\uparrow} + |S^{-}_{MM',\eta\eta'}|^2\rho_{\eta\uparrow}\rho_{\eta'\downarrow} + \mathcal{R}^{+}(\eta\eta')|S^{z}_{MM',\eta\eta'}|^2\right]\end{aligned} \quad , \tag{E.7}$$

with $\mathcal{R}^{\pm}(\eta\eta') = \rho_{\eta\uparrow}\rho_{\eta'\uparrow} \pm \rho_{\eta\downarrow}\rho_{\eta'\downarrow}$ and

$$\zeta = \frac{\mathcal{T}}{T_0} \quad , \tag{E.8}$$

being the ratio of spin-flip-assisted and elastic tunnel matrix elements ζ. Note that the we only assume a spin polarization in the tip, which means that the surface is unpolarized, $\rho_{S\downarrow} = \rho_{S\uparrow} = \frac{1}{2}\rho_S$. Thus, one finds for $\mathcal{R}$,

$$\mathcal{R}^{+} = \begin{pmatrix} \frac{1}{2}\rho_S^2 & \frac{1}{2}\rho_S\rho_T \\ \frac{1}{2}\rho_S\rho_T & \rho_T^2\frac{1+\mathcal{P}_T}{2} \end{pmatrix} \quad , \quad \mathcal{R}^{-} = \begin{pmatrix} 0 & \frac{1}{2}\rho_S\rho_T\mathcal{P}_T \\ \frac{1}{2}\rho_S\rho_T\mathcal{P}_T & \rho_T^2\mathcal{P}_T \end{pmatrix} \quad , \tag{E.9}$$

where the polarization of the tip was defined as (tip polarized along z, normal to the surface plane)

$$\mathcal{P}_T = \frac{\rho_{T\uparrow} - \rho_{T\downarrow}}{\rho_{T\uparrow} + \rho_{T\downarrow}} \quad . \tag{E.10}$$

It directly follows from the definition of the polarization

$$\rho_{T\uparrow} = \frac{\rho_T}{2}\left(1 + \mathcal{P}_T\right) \quad , \quad \rho_{T\downarrow} = \frac{\rho_T}{2}\left(1 - \mathcal{P}_T\right) \quad , \tag{E.11}$$

and

$$\rho_{T\uparrow}\rho_{T\downarrow} = \frac{\rho_T^2}{4}\left(1 - \mathcal{P}_T^2\right) \quad . \tag{E.12}$$

The different contributions to the transition rates are therefore given by:

$$\Sigma^{S\to S}_{MM'} = \frac{\rho_S^2}{4}\left\{\frac{1}{2}\delta_{MM'} + \zeta^2\left[|S^{+}_{MM',SS}|^2 + |S^{-}_{MM',SS}|^2 + 2|S^{z}_{MM',SS}|^2\right]\right\} \quad , \tag{E.13}$$

$$\begin{aligned} \Sigma^{T\to T}_{MM'} = &\frac{\rho_T^2}{4}\left\{\delta_{MM'}\left[\frac{1+\mathcal{P}_T}{2} + 2\zeta\mathcal{P}_T\sum_\alpha S^{\alpha}_{MM',TT}\right]\right. \\ &\left. + \zeta^2\left[|S^{+}_{MM',TT}|^2\left(1 - \mathcal{P}_T^2\right) + |S^{-}_{MM',TT}|^2\left(1 - \mathcal{P}_T^2\right) + 2\left(1 + \mathcal{P}_T\right)|S^{z}_{MM',TT}|^2\right]\right\} \end{aligned} \quad , \tag{E.14}$$

$$\begin{aligned} \Sigma^{T\to S}_{MM'} = &\frac{\rho_T\rho_S}{4}\left\{\frac{1}{2}\delta_{MM'}\left[1 + 2\zeta\mathcal{P}_T\sum_\alpha S^{\alpha}_{MM',TS}\right]\right. \\ &\left. + \zeta^2\left[|S^{+}_{MM',TS}|^2\left(1 - \mathcal{P}_T\right) + |S^{-}_{MM',TS}|^2\left(1 + \mathcal{P}_T\right) + 2|S^{z}_{MM',TS}|^2\right]\right\} \end{aligned} \quad , \tag{E.15}$$

$$\begin{aligned} \Sigma^{S\to T}_{MM'} = &\frac{\rho_T\rho_S}{4}\left\{\frac{1}{2}\delta_{MM'}\left[1 + 2\zeta\mathcal{P}_T\sum_\alpha S^{\alpha}_{MM',TS}\right]\right. \\ &\left. + \zeta^2\left[|S^{+}_{MM',TS}|^2\left(1 + \mathcal{P}_T\right) + |S^{-}_{MM',TS}|^2\left(1 - \mathcal{P}_T\right) + 2|S^{z}_{MM',TS}|^2\right]\right\} \end{aligned} \quad , \tag{E.16}$$

Due to the coupling to the tip and the surface (v_i^η), all processes involving the tip will only play a role for the spins which are probed by the tip. The unprobed spins will only contribute to the $S \to S$ transition rate, which describes the spin relaxation and thermal excitation due to surface electrons.

Rewriting eqs. (E.13)-(E.16) yields a set of different transition rates, which all depend on common parameters,

$$\begin{aligned} W_{MM'}^{S\to S} =& \mathcal{G}_{MM'}^{SS} k_i \Bigg\{ \frac{1}{2}\delta_{MM'} (r_i^{\mathsf{TS}})^2 + \zeta^2 \Bigg[\Bigg| \sum_j r_{ij}^{\mathsf{S}} S_{j,MM'}^{+} \Bigg|^2 \\ & + \Bigg| \sum_j r_{ij}^{\mathsf{S}} S_{j,MM'}^{-} \Bigg|^2 + 2 \Bigg| \sum_j r_{ij}^{\mathsf{S}} S_{j,MM'}^{z} \Bigg|^2 \Bigg] \Bigg\} \end{aligned} , \tag{E.17}$$

$$\begin{aligned} W_{MM'}^{T\to T} =& \mathcal{G}_{MM'}^{TT} k_i \left(r^{\mathsf{rho}} (r_i^{\mathsf{TS}})^2 \right)^2 \Bigg\{ \delta_{MM'} \left[\frac{1}{(r_i^{\mathsf{TS}})^2} \frac{1+\mathcal{P}_T}{2} + \frac{1}{r_i^{\mathsf{TS}}} 2\zeta \mathcal{P}_T \sum_\alpha S_{i,MM'}^{\alpha} \right] \\ & + \zeta^2 \left[|S_{i,MM'}^{+}|^2 \left(1 - \mathcal{P}_T^2\right) + |S_{i,MM'}^{-}|^2 \left(1 - \mathcal{P}_T^2\right) + 2\left(1 + \mathcal{P}_T\right) |S_{i,MM'}^{z}|^2 \right] \Bigg\} \end{aligned} , \tag{E.18}$$

$$\begin{aligned} W_{MM'}^{T\to S} =& \mathcal{G}_{MM'}^{TS} k_i r^{\mathsf{rho}} (r_i^{\mathsf{TS}})^2 \Bigg\{ \frac{1}{2}\delta_{MM'} \left[1 + 2\zeta \mathcal{P}_T \sum_\alpha S_{i,MM'}^{\alpha} \right] \\ & + \zeta^2 \left[|S_{i,MM'}^{+}|^2 (1 - \mathcal{P}_T) + |S_{i,MM'}^{-}|^2 (1 + \mathcal{P}_T) + 2 |S_{i,MM'}^{z}|^2 \right] \Bigg\} \end{aligned} , \tag{E.19}$$

$$\begin{aligned} W_{MM'}^{S\to T} =& \mathcal{G}_{MM'}^{ST} k_i r^{\mathsf{rho}} (r_i^{\mathsf{TS}})^2 \Bigg\{ \frac{1}{2}\delta_{MM'} \left[1 + 2\zeta \mathcal{P}_T \sum_\alpha S_{i,MM'}^{\alpha} \right] \\ & + \zeta^2 \left[|S_{i,MM'}^{+}|^2 (1 + \mathcal{P}_T) + |S_{i,MM'}^{-}|^2 (1 - \mathcal{P}_T) + 2 |S_{i,MM'}^{z}|^2 \right] \Bigg\} \end{aligned} , \tag{E.20}$$

where we used the ratio parameters,

$$r_i^{\mathsf{TS}} = \frac{v_i^T}{v_i^S} \quad \text{and} \quad r^{\mathsf{rho}} = \frac{\rho_T}{\rho_S} \tag{E.21}$$

an total prefactor,

$$k_i = \frac{2\pi T_0^2 \chi^2}{\hbar} \frac{\rho_S^2}{4} \left(\frac{v_i^S}{v_i^T} \right)^2 = \frac{2\pi T_0^2 (v_i^S)^4}{\hbar} \frac{\rho_S^2}{4} \quad , \tag{E.22}$$

and the ratio of the surface coupling $r_{ij}^{\mathsf{S}} = (v_i^{\mathsf{S}} / v_j^{\mathsf{S}})^2$.

For a multi-spin system the prefactor can be described by a common prefactor and the surface coupling ratio r_{ij}^{S}. For example for a two spin system one finds

$$k_1 = \frac{2\pi T_0^2 (v_1^S)^4}{\hbar} \frac{\rho_S^2}{4} \tag{E.23}$$

$$k_2 = \frac{2\pi T_0^2 (v_2^S)^4}{\hbar} \frac{\rho_S^2}{4} = \frac{2\pi T_0^2 (v_1^S)^4}{\hbar} \frac{\rho_S^2}{4} \left(r_{12}^{\mathsf{S}} \right)^2 = k_1 \left(r_{12}^{\mathsf{S}} \right)^2 \quad . \tag{E.24}$$

As a last assumption, we focus only on the elastic contributions, which gives rise to eqs. (6.18)-(6.21).

List of Figures

List of Tables

List of abbreviations

Abbreviation	Explanation
ASA	atomic sphere approximation
BCS	Bardeen-Cooper-Schrieffer theory for superconductivity
BdG	Bogoliubov-de-Gennes transformation
DFT	density functional theory
DMI	Dzyaloshinskii-Moriya interaction
FP	full potential
GGA	generalized gradient approximation
KKR	Korringa-Kohn-Rostoker method
L(S)DA	local (spin) density approximation
PBE	common exchange-correlation functional
SOC	spin-orbit coupling
(SP-)STM	(spin-polarized) scanning tunneling microscopy
YSR	Yu-Shiba-Rusinov states

Convention	Explanation
$\boldsymbol{r}$	Three-dimensional vector
$\epsilon_{\alpha\beta\gamma}$	Levi-Civita symbol
$\delta_{\alpha\beta}$	Kronecker delta
$\delta(\boldsymbol{r})$	Dirac delta function
$\boldsymbol{\sigma}$	Vector of Pauli matrices
$\boldsymbol{L}$	Angular momentum operator/vector
$Y_L(\hat{r})$	Real spherical harmonic

In this thesis the Einstein sum convention is used, repeated indices are summed implicitly.

Bibliography

[1] A. S. G. Andrae and T. Edler. On Global Electricity Usage of Communication Technology: Trends to 2030. *Challenges* **6**, 117–157 (2015).

[2] N. Jones. How to Stop Data Centres from Gobbling up the World's Electricity. *Nature* **561**, 163–166 (2018).

[3] L. Eeckhout. Is Moore's Law Slowing Down? What's Next? *IEEE Micro* **37**, 4–5 (2017).

[4] G. Binasch, P. Grünberg, F. Saurenbach, and W. Zinn. Enhanced Magnetoresistance in Layered Magnetic Structures with Antiferromagnetic Interlayer Exchange. *Physical Review B* **39**, 4828–4830 (1989).

[5] M. N. Baibich, J. M. Broto, A. Fert, F. N. Van Dau, F. Petroff, P. Etienne, G. Creuzet, A. Friederich, and J. Chazelas. Giant Magnetoresistance of (001)Fe/(001)Cr Magnetic Superlattices. *Physical Review Letters* **61**, 2472–2475 (1988).

[6] M. Julliere. Tunneling between Ferromagnetic Films. *Physics Letters A* **54**, 225–226 (1975).

[7] T. Miyazaki and N. Tezuka. Giant Magnetic Tunneling Effect in Fe/Al$_2$O$_3$/Fe Junction. *Journal of Magnetism and Magnetic Materials* **139**, L231–L234 (1995).

[8] J. S. Moodera, L. R. Kinder, T. M. Wong, and R. Meservey. Large Magnetoresistance at Room Temperature in Ferromagnetic Thin Film Tunnel Junctions. *Physical Review Letters* **74**, 3273–3276 (1995).

[9] T. Jungwirth, X. Marti, P. Wadley, and J. Wunderlich. Antiferromagnetic Spintronics. *Nature Nanotechnology* **11**, 231–241 (2016).

[10] A. Fert, N. Reyren, and V. Cros. Magnetic Skyrmions: Advances in Physics and Potential Applications. *Nature Reviews Materials* **2**, 17031 (2017).

[11] F. Zheng, F. N. Rybakov, A. B. Borisov, D. Song, S. Wang, Z.-A. Li, H. Du, N. S. Kiselev, J. Caron, A. Kovács, M. Tian, Y. Zhang, S. Blügel, and R. E. Dunin-Borkowski. Experimental Observation of Chiral Magnetic Bobbers in B20-Type FeGe. *Nature Nanotechnology* **13**, 451–455 (2018).

[12] Y. Liu, R. K. Lake, and J. Zang. Binding a Hopfion in a Chiral Magnet Nanodisk. *Physical Review B* **98**, 174437 (2018).

[13] A. Fert, V. Cros, and J. Sampaio. Skyrmions on the Track. *Nature Nanotechnology* **8**, 152–156 (2013).

[14] R. Tomasello, E. Martinez, R. Zivieri, L. Torres, M. Carpentieri, and G. Finocchio. A Strategy for the Design of Skyrmion Racetrack Memories. *Scientific Reports* **4**, 1–7 (2014).

[15] S. S. P. Parkin, M. Hayashi, and L. Thomas. Magnetic Domain-Wall Racetrack Memory. *Science* **320**, 190–194 (2008).

[16] G. Binnig, H. Rohrer, C. Gerber, and E. Weibel. Tunneling through a Controllable Vacuum Gap. *Applied Physics Letters* **40**, 178–180 (1982).

[17] G. Binnig, H. Rohrer, C. Gerber, and E. Weibel. Surface Studies by Scanning Tunneling Microscopy. *Physical Review Letters* **49**, 57–61 (1982).

[18] G. Binnig, H. Rohrer, C. Gerber, and E. Weibel. 7x7 Reconstruction on Si(111) Resolved in Real Space. *Physical Review Letters* **50**, 120–123 (1983).

[19] D. M. Eigler and E. K. Schweizer. Positioning Single Atoms with a Scanning Tunnelling Microscope. *Nature* **344**, 524–526 (1990).

[20] R. Wiesendanger, H.-J. Güntherodt, G. Güntherodt, R. J. Gambino, and R. Ruf. Observation of Vacuum Tunneling of Spin-Polarized Electrons with the Scanning Tunneling Microscope. *Physical Review Letters* **65**, 247–250 (1990).

[21] S. Heinze, M. Bode, A. Kubetzka, O. Pietzsch, X. Nie, S. Blügel, and R. Wiesendanger. Real-Space Imaging of Two-Dimensional Antiferromagnetism on the Atomic Scale. *Science* **288**, 1805–1808 (2000).

[22] S. Blügel, M. Weinert, and P. H. Dederichs. Ferromagnetism and Antiferromagnetism of 3d-Metal Overlayers on Metals. *Physical Review Letters* **60**, 1077–1080 (1988).

[23] S. Heinze, K. von Bergmann, M. Menzel, J. Brede, A. Kubetzka, R. Wiesendanger, G. Bihlmayer, and S. Blügel. Spontaneous atomic-scale magnetic skyrmion lattice in two dimensions. *Nat. Phys.* **7**, 713–718 (2011).

[24] J. Tersoff and D. R. Hamann. Theory and Application for the Scanning Tunneling Microscope. *Physical Review Letters* **50**, 1998–2001 (1983).

[25] J. Tersoff and D. R. Hamann. Theory of the Scanning Tunneling Microscope. *Physical Review B* **31**, 805–813 (1985).

[26] B. C. Stipe, M. A. Rezaei, and W. Ho. Single-Molecule Vibrational Spectroscopy and Microscopy. *Science* **280**, 1732–1735 (1998).

[27] A. J. Heinrich, J. A. Gupta, C. P. Lutz, and D. M. Eigler. Single-Atom Spin-Flip Spectroscopy. *Science* **306**, 466–469 (2004).

[28] N. Tsukahara, K.-i. Noto, M. Ohara, S. Shiraki, N. Takagi, Y. Takata, J. Miyawaki, M. Taguchi, A. Chainani, S. Shin, and M. Kawai. Adsorption-Induced Switching of Magnetic Anisotropy in a Single Iron(II) Phthalocyanine Molecule on an Oxidized Cu(110) Surface. *Physical Review Letters* **102**, 167203 (2009).

[29] A. Spinelli, B. Bryant, F. Delgado, J. Fernández-Rossier, and A. F. Otte. Imaging of Spin Waves in Atomically Designed Nanomagnets. *Nature Materials* **13**, 782–785 (2014).

[30] J. Hermenau, J. Ibañez-Azpiroz, C. Hübner, A. Sonntag, B. Baxevanis, K. T. Ton, M. Steinbrecher, A. A. Khajetoorians, M. d. S. Dias, S. Blügel, R. Wiesendanger, S. Lounis, and J. Wiebe. A Gateway towards Non-Collinear Spin Processing Using Three-Atom Magnets with Strong Substrate Coupling. *Nature Communications* **8**, 642 (2017).

[31] C. F. Hirjibehedin, C.-Y. Lin, A. F. Otte, M. Ternes, C. P. Lutz, B. A. Jones, and A. J. Heinrich. Large Magnetic Anisotropy of a Single Atomic Spin Embedded in a Surface Molecular Network. *Science* **317**, 1199–1203 (2007).

[32] T. Balashov, T. Schuh, A. F. Takács, A. Ernst, S. Ostanin, J. Henk, I. Mertig, P. Bruno, T. Miyamachi, S. Suga, and W. Wulfhekel. Magnetic Anisotropy and Magnetization Dynamics of Individual Atoms and Clusters of Fe and Co on Pt(111). *Physical Review Letters* **102**, 257203 (2009).

[33] A. A. Khajetoorians, S. Lounis, B. Chilian, A. T. Costa, L. Zhou, D. L. Mills, J. Wiebe, and R. Wiesendanger. Itinerant Nature of Atom-Magnetization Excitation by Tunneling Electrons. *Physical Review Letters* **106**, 037205 (2011).

[34] A. A. Khajetoorians, B. Baxevanis, C. Hübner, T. Schlenk, S. Krause, T. O. Wehling, S. Lounis, A. Lichtenstein, D. Pfannkuche, J. Wiebe, and R. Wiesendanger. Current-Driven Spin Dynamics of Artificially Constructed Quantum Magnets. *Science* **339**, 55–59 (2013).

[35] S. Loth, M. Etzkorn, C. P. Lutz, D. M. Eigler, and A. J. Heinrich. Measurement of Fast Electron Spin Relaxation Times with Atomic Resolution. *Science* **329**, 1628–1630 (2010).

[36] F. D. Natterer, K. Yang, W. Paul, P. Willke, T. Choi, T. Greber, A. J. Heinrich, and C. P. Lutz. Reading and Writing Single-Atom Magnets. *Nature* **543**, 226–228 (2017).

[37] T. Miyamachi, T. Schuh, T. Märkl, C. Bresch, T. Balashov, A. Stöhr, C. Karlewski, S. André, M. Marthaler, M. Hoffmann, M. Geilhufe, S. Ostanin, W. Hergert, I. Mertig, G. Schön, A. Ernst, and W. Wulfhekel. Stabilizing the Magnetic Moment of Single Holmium Atoms by Symmetry. *Nature* **503**, 242 (2013).

[38] J. Hermenau, S. Brinker, M. Marciani, M. Steinbrecher, M. dos Santos Dias, R. Wiesendanger, S. Lounis, and J. Wiebe. Stabilizing spin systems via symmetrically tailored RKKY interactions. *Nature Communications* **10**, 2565 (2019).

[39] J. Ibañez-Azpiroz, M. dos Santos Dias, S. Blügel, and S. Lounis. Zero-Point Spin-Fluctuations of Single Adatoms. *Nano Letters* **16**, 4305–4311 (2016).

[40] F. Donati, S. Rusponi, S. Stepanow, C. Wäckerlin, A. Singha, L. Persichetti, R. Baltic, K. Diller, F. Patthey, E. Fernandes, J. Dreiser, Ž. Šljivančanin, K. Kummer, C. Nistor, P. Gambardella, and H. Brune. Magnetic remanence in single atoms. *Science* **352**, 318–321 (2016).

[41] S. Loth, S. Baumann, C. P. Lutz, D. M. Eigler, and A. J. Heinrich. Bistability in Atomic-Scale Antiferromagnets. *Science* **335**, 196–199 (2012).

[42] P. Gambardella, S. Rusponi, M. Veronese, S. S. Dhesi, C. Grazioli, A. Dallmeyer, I. Cabria, R. Zeller, P. H. Dederichs, K. Kern, C. Carbone, and H. Brune. Giant Magnetic Anisotropy of Single Cobalt Atoms and Nanoparticles. *Science* **300**, 1130–1133 (2003).

[43] I. G. Rau, S. Baumann, S. Rusponi, F. Donati, S. Stepanow, L. Gragnaniello, J. Dreiser, C. Piamonteze, F. Nolting, S. Gangopadhyay, O. R. Albertini, R. M. Macfarlane, C. P. Lutz, B. A. Jones, P. Gambardella, A. J. Heinrich, and H. Brune. Reaching the Magnetic Anisotropy Limit of a 3d Metal Atom. *Science* **344**, 988–992 (2014).

[44] S. Baumann, F. Donati, S. Stepanow, S. Rusponi, W. Paul, S. Gangopadhyay, I. G. Rau, G. E. Pacchioni, L. Gragnaniello, M. Pivetta, J. Dreiser, C. Piamonteze, C. P. Lutz, R. M. Macfarlane, B. A. Jones, P. Gambardella, A. J. Heinrich, and H. Brune. Origin of Perpendicular Magnetic Anisotropy and Large Orbital Moment in Fe Atoms on MgO. *Physical Review Letters* **115**, 237202 (2015).

[45] P. Hohenberg and W. Kohn. Inhomogeneous Electron Gas. *Physical Review* **136**, B864–B871 (1964).

[46] W. Kohn and L. J. Sham. Self-Consistent Equations Including Exchange and Correlation Effects. *Physical Review* **140**, A1133–A1138 (1965).

[47] R. M. Martin. Electronic Structure Basic Theory and Practical Methods. Cambridge University Press, 2004.

[48] N. Papanikolaou, R. Zeller, and P. H. Dederichs. Conceptual Improvements of the KKR Method. *Journal of Physics: Condensed Matter* **14**, 2799–2823 (2002).

[49] W. Heisenberg. Zur Theorie des Ferromagnetismus. *Z. Phys.* **49**, 619–636 (1928).

[50] L. D. Landau and E. Lifshitz. On the theory of the dispersion of magnetic permeability in ferromagnetic bodies. *Phys. Z. Sowjet.* **8**, 153 (1935).

[51] T. L. Gilbert. A phenomenological theory of damping in ferromagnetic materials. *IEEE Transactions on Magnetics* **40**, 3443 (2004).

[52] P. Kurz, G. Bihlmayer, K. Hirai, and S. Blügel. Three-Dimensional Spin Structure on a Two-Dimensional Lattice: Mn /Cu(111). *Physical Review Letters* **86**, 1106–1109 (2001).

[53] D. Hobbs, J. Hafner, and D. Spišák. Understanding the Complex Metallic Element Mn. I. Crystalline and Noncollinear Magnetic Structure of α-Mn. *Physical Review B* **68**, 014407 (2003).

[54] I. Dzyaloshinsky. A Thermodynamic Theory of Weak Ferromagnetism of Antiferromagnetics. *Journal of Physics and Chemistry of Solids* **4**, 241–255 (1958).

[55] T. Moriya. Anisotropic Superexchange Interaction and Weak Ferromagnetism. *Physical Review* **120**, 91 (1960).

[56] M. Bode, M. Heide, K. von Bergmann, P. Ferriani, S. Heinze, G. Bihlmayer, A. Kubetzka, O. Pietzsch, S. Blügel, and R. Wiesendanger. Chiral Magnetic Order at Surfaces Driven by Inversion Asymmetry. *Nature* **447**, 190–193 (2007).

[57] A. Al-Zubi, G. Bihlmayer, and S. Blügel. Modeling magnetism of hexagonal Fe monolayers on 4d substrates. *Phys. Status Solidi B* **248**, 2242–2247 (2011).

[58] A. Krönlein, M. Schmitt, M. Hoffmann, J. Kemmer, N. Seubert, M. Vogt, J. Küspert, M. Böhme, B. Alonazi, J. Kügel, H. A. Albrithen, M. Bode, G. Bihlmayer, and S. Blügel. Magnetic Ground State Stabilized by Three-Site Interactions: Fe/Rh(111). *Phys. Rev. Lett.* **120**, 207202 (2018).

[59] S. Brinker, M. d. S. Dias, and S. Lounis. The Chiral Biquadratic Pair Interaction. *New Journal of Physics* **21**, 083015 (2019).

[60] A. Lászlóffy, L. Rózsa, K. Palotás, L. Udvardi, and L. Szunyogh. Magnetic structure of monatomic Fe chains on Re(0001): Emergence of chiral multispin interactions. *Phys. Rev. B* **99**, 184430 (2019).

[61] S. Grytsiuk, J.-P. Hanke, M. Hoffmann, J. Bouaziz, O. Gomonay, G. Bihlmayer, S. Lounis, Y. Mokrousov, and S. Blügel. Topological–Chiral Magnetic Interactions Driven by Emergent Orbital Magnetism. *Nature Communications* **11**, 1–7 (2020).

[62] A. A. Khajetoorians, J. Wiebe, B. Chilian, S. Lounis, S. Blügel, and R. Wiesendanger. Atom-by-Atom Engineering and Magnetometry of Tailored Nanomagnets. *Nature Physics* **8**, 497–503 (2012).

[63] A. A. Khajetoorians, M. Steinbrecher, M. Ternes, M. Bouhassoune, M. d. S. Dias, S. Lounis, J. Wiebe, and R. Wiesendanger. Tailoring the Chiral Magnetic Interaction between Two Individual Atoms. *Nature Communications* **7**, 10620 (2016).

[64] J. Friedel. Metallic Alloys. *Il Nuovo Cimento (1955-1965)* **7**, 287–311 (1958).

[65] M. F. Crommie, C. P. Lutz, and D. M. Eigler. Imaging standing waves in a two-dimensional electron gas. *Nature* **363**, 524–527 (1993).

[66] S. Lounis, A. Bringer, and S. Blügel. Magnetic Adatom Induced Skyrmion-Like Spin Texture in Surface Electron Waves. *Physical Review Letters* **108**, 207202 (2012).

[67] A. A. Khajetoorians, T. Schlenk, B. Schweflinghaus, M. dos Santos Dias, M. Steinbrecher, M. Bouhassoune, S. Lounis, J. Wiebe, and R. Wiesendanger. Spin Excitations of Individual Fe Atoms on Pt(111): Impact of the Site-Dependent Giant Substrate Polarization. *Physical Review Letters* **111**, 157204 (2013).

[68] M. Bouhassoune, M. d. S. Dias, B. Zimmermann, P. H. Dederichs, and S. Lounis. RKKY-like Contributions to the Magnetic Anisotropy Energy: $3d$ Adatoms on Pt(111) Surface. *Physical Review B* **94**, 125402 (2016).

[69] G. G. Low and T. M. Holden. Distribution of the Ferromagnetic Polarization Induced by Iron and Cobalt Atoms in Palladium. *Proceedings of the Physical Society* **89**, 119 (1966).

[70] G. J. Nieuwenhuys. Magnetic Behaviour of Cobalt, Iron and Manganese Dissolved in Palladium. *Advances in Physics* **24**, 515–591 (1975).

[71] T. Herrmannsdörfer, S. Rehmann, W. Wendler, and F. Pobell. *J. Low Temp. Phys.* **104**, 49–65 (1996).

[72] J.-P. Hanke, F. Freimuth, A. K. Nandy, H. Zhang, S. Blügel, and Y. Mokrousov. *Phys. Rev. B* **94**, 121114 (2016).

[73] J.-P. Hanke, F. Freimuth, S. Blügel, and Y. Mokrousov. Prototypical Topological Orbital Ferromagnet γ-FeMn. *Scientific Reports* **7**, 41078 (2017).

[74] M. Serlin, C. L. Tschirhart, H. Polshyn, Y. Zhang, J. Zhu, K. Watanabe, T. Taniguchi, L. Balents, and A. F. Young. Intrinsic Quantized Anomalous Hall Effect in a Moiré Heterostructure. *Science* **367**, 900–903 (2020).

[75] J. D. Jackson. Classical Electrodynamics. John Wiley & Sons, Inc., 1999.

[76] T. Thonhauser. Theory of orbital magnetization in solids. *Int. J. Mod. Phys. B* **25**, 1429–1458 (2011).

[77] S. Brinker. First-principles investigation of charge and spin currents in magnetic nanostructures. MA thesis. Fachgruppe Physik, 2016.

[78] C. Nayak, S. H. Simon, A. Stern, M. Freedman, and S. Das Sarma. Non-Abelian Anyons and Topological Quantum Computation. *Reviews of Modern Physics* **80**, 1083–1159 (2008).

[79] S. D. Sarma, M. Freedman, and C. Nayak. Majorana Zero Modes and Topological Quantum Computation. *npj Quantum Information* **1**, 1–13 (2015).

[80] T.-P. Choy, J. M. Edge, A. R. Akhmerov, and C. W. J. Beenakker. Majorana Fermions Emerging from Magnetic Nanoparticles on a Superconductor without Spin-Orbit Coupling. *Physical Review B* **84**, 195442 (2011).

[81] I. Martin and A. F. Morpurgo. Majorana Fermions in Superconducting Helical Magnets. *Physical Review B* **85**, 144505 (2012).

[82] S. Nadj-Perge, I. K. Drozdov, B. A. Bernevig, and A. Yazdani. Proposal for Realizing Majorana Fermions in Chains of Magnetic Atoms on a Superconductor. *Physical Review B* **88**, 020407 (2013).

[83] S. Nadj-Perge, I. K. Drozdov, J. Li, H. Chen, S. Jeon, J. Seo, A. H. MacDonald, B. A. Bernevig, and A. Yazdani. Observation of Majorana Fermions in Ferromagnetic Atomic Chains on a Superconductor. *Science* **346**, 602–607 (2014).

[84] H. Kim, A. Palacio-Morales, T. Posske, L. Rózsa, K. Palotás, L. Szunyogh, M. Thorwart, and R. Wiesendanger. Toward Tailoring Majorana Bound States in Artificially Constructed Magnetic Atom Chains on Elemental Superconductors. *Science Advances* **4**, eaar5251 (2018).

[85] M. Ruby, F. Pientka, Y. Peng, F. von Oppen, B. W. Heinrich, and K. J. Franke. End States and Subgap Structure in Proximity-Coupled Chains of Magnetic Adatoms. *Physical Review Letters* **115**, 197204 (2015).

[86] M. Ruby, B. W. Heinrich, Y. Peng, F. von Oppen, and K. J. Franke. Exploring a Proximity-Coupled Co Chain on Pb(110) as a Possible Majorana Platform. *Nano Letters* **17**, 4473–4477 (2017).

[87] A. Fert and P. M. Levy. Role of Anisotropic Exchange Interactions in Determining the Properties of Spin-Glasses. *Phys. Rev. Lett.* **44**, 1538–1541 (1980).

[88] P. M. Levy and A. Fert. Anisotropy Induced by Nonmagnetic Impurities in CuMn Spin-Glass Alloys. *Phys. Rev. B* **23**, 4667–4690 (1981).

[89] M. A. L. Marques, C. A. Ulrich, F. Nogueira, A. Rubio, K. Burke, and E. K. U. Gross. Time-Dependent Density Functional Theory. Springer-Verlag Berlin Heidelberg, 2006.

[90] E. Engel and R. M. Dreizler. Density Functional Theory: An Advanced Course. Springer-Verlag Berlin Heidelberg, 2011.

[91] N. Helbig and M. Lezaic. lecture notes in density functional theory, RWTH Aachen University. 2015.

[92] J. Zabloudil. Electron Scattering in Solid Matter: A Theoretical and Computational Treatise. Springer, 2005.

[93] B. H. Drittler. KKR-Greensche Funktionsmethode für das volle Zellpotential. PhD thesis. RWTH Aachen, 1991.

[94] D. S. G. Bauer. Development of a relativistic full-potential first-principles multiple scattering Green function method applied to complex magnetic textures of nano structures at surfaces. PhD thesis. RWTH Aachen, 2014.

[95] U. von Barth and L. Hedin. A local exchange-correlation potential for the spin polarized case: I. *Journal of Physics C: Solid State Physics* **5**, 1629–1642 (1972).

[96] D. M. Ceperley and B. J. Alder. Ground State of the Electron Gas by a Stochastic Method. *Physical Review Letters* **45**, 566–569 (1980).

[97] S. H. Vosko, L. Wilk, and M. Nusair. Accurate Spin-Dependent Electron Liquid Correlation Energies for Local Spin Density Calculations: A Critical Analysis. *Canadian Journal of physics* **58**, 1200–1211 (1980).

[98] O. Gunnarsson, M. Jonson, and B. I. Lundqvist. Descriptions of Exchange and Correlation Effects in Inhomogeneous Electron Systems. *Physical Review B* **20**, 3136–3164 (1979).

[99] R. Q. Hood, M. Y. Chou, A. J. Williamson, G. Rajagopal, and R. J. Needs. Exchange and Correlation in Silicon. *Physical Review B* **57**, 8972–8982 (1998).

[100] J. P. Perdew, K. Burke, and M. Ernzerhof. Generalized Gradient Approximation Made Simple. *Physical Review Letters* **77**, 3865–3868 (1996).

[101] J. P. Perdew, A. Ruzsinszky, G. I. Csonka, O. A. Vydrov, G. E. Scuseria, L. A. Constantin, X. Zhou, and K. Burke. Restoring the Density-Gradient Expansion for Exchange in Solids and Surfaces. *Physical Review Letters* **100**, 136406 (2008).

[102] P. Strange. Relativistic Quantum Mechanics. Cambridge University Press, 1998.

[103] D. J. Singh and L. Nordstrom. Planewaves, Pseudopotentials, and the LAPW Method. Springer US, 2006.

[104] J. Korringa. On the Calculation of the Energy of a Bloch Wave in a Metal. *Physica* **13**, 392–400 (1947).

[105] W. Kohn and N. Rostoker. Solution of the Schrödinger Equation in Periodic Lattices with an Application to Metallic Lithium. *Physical Review* **94**, 1111–1120 (1954).

[106] K. Wildberger, P. Lang, R. Zeller, and P. H. Dederichs. Fermi-Dirac Distribution in Ab Initio Green's-Function Calculations. *Physical Review B* **52**, 11502 (1995).

[107] M. dos Santos Dias, B. Schweflinghaus, S. Blügel, and S. Lounis. Relativistic Dynamical Spin Excitations of Magnetic Adatoms. *Physical Review B* **91**, 075405 (2015).

[108] H. Skriver. The LMTO Method. Springer, 1984.

[109] juKKR – DFT made in Jülich. `https://jukkr.fz-juelich.de`. Accessed: 2019-11-20.

[110] A. S. Davydov. Quantum Mechanics. Oxford: Pergamon, 1965.

[111] M. dos Santos Dias, J. Bouaziz, M. Bouhassoune, S. Blügel, and S. Lounis. Chirality-Driven Orbital Magnetic Moments as a New Probe for Topological Magnetic Structures. *Nature Communications* **7**, 13613 (2016).

[112] W. Nolting. Grundkurs Theoretische Physik 3 – Elektrodynamik. Springer-Verlag Berlin Heidelberg , 2011.

[113] G. M. Stocks, B. Ujfalussy, X. Wang, D. M. C. Nicholson, W. A. Shelton, Y. Wang, A. Canning, and B. L. Györffy. Towards a Constrained Local Moment Model for First Principles Spin Dynamics. *Philosophical Magazine B* **78**, 665–673 (1998).

[114] B. Újfalussy, X.-D. Wang, D. M. C. Nicholson, W. A. Shelton, G. M. Stocks, Y. Wang, and B. L. Gyorffy. Constrained Density Functional Theory for First Principles Spin Dynamics. *Journal of Applied Physics* **85**, 4824–4826 (1999).

[115] P. Kurz, F. Förster, L. Nordström, G. Bihlmayer, and S. Blügel. Ab Initio Treatment of Noncollinear Magnets with the Full-Potential Linearized Augmented Plane Wave Method. *Physical Review B* **69**, 024415 (2004).

[116] S. Mankovsky, S. Bornemann, J. Minár, S. Polesya, H. Ebert, J. B. Staunton, and A. I. Lichtenstein. Effects of spin-orbit coupling on the spin structure of deposited transition-metal clusters. *Phys. Rev. B* **80**, 014422 (2009).

[117] E. Runge and E. K. U. Gross. Density-Functional Theory for Time-Dependent Systems. *Physical Review Letters* **52**, 997 (1984).

[118] A. Fetter and J. Walecka. Quantum Theory of Many-Particle Systems. Dover Publications, 2003.

[119] H. Bruus and K. Flensberg. Many-Body Quantum Theory in Condensed Matter Physics. Oxford University Press, 2004.

[120] G. Giuliani and G. Vignale. Quantum Theory of the Electron Liquid. Cambridge University Press, 2005.

[121] S. Brinker, M. dos Santos Dias, and S. Lounis. Interatomic orbital magnetism: The case of $3d$ adatoms deposited on the Pt(111) surface. *Phys. Rev. B* **98**, 094428 (2018).

[122] F. Meier, L. Zhou, J. Wiebe, and R. Wiesendanger. Revealing Magnetic Interactions from Single-Atom Magnetization Curves. *Science* **320**, 82–86 (2008).

[123] L. Zhou, J. Wiebe, S. Lounis, E. Vedmedenko, F. Meier, S. Blügel, P. H. Dederichs, and R. Wiesendanger. Strength and directionality of surface Ruderman–Kittel–Kasuya–Yosida interaction mapped on the atomic scale. *Nature Physics* **6**, 187–191 (2010).

[124] A. Oswald, R. Zeller, and P. H. Dederichs. Giant Moments in Palladium. *Physical Review Letters* **56**, 1419–1422 (1986).

[125] R. Zeller. Large-Scale Electronic-Structure Calculations for Isolated Transition-Metal Impurities in Palladium. *Modelling and Simulation in Materials Science and Engineering* **1**, 553 (1993).

[126] D. Xiao, J. Shi, and Q. Niu. Berry Phase Correction to Electron Density of States in Solids. *Physical Review Letters* **95**, 137204 (2005).

[127] T. Thonhauser, D. Ceresoli, D. Vanderbilt, and R. Resta. Orbital Magnetization in Periodic Insulators. *Physical Review Letters* **95**, 137205 (2005).

[128] I. Souza and D. Vanderbilt. Dichroic f-Sum Rule and the Orbital Magnetization of Crystals. *Physical Review B* **77**, 054438 (2008).

[129] R. Bianco and R. Resta. Mapping Topological Order in Coordinate Space. *Physical Review B* **84**, 241106 (2011).

[130] R. Bianco and R. Resta. Orbital Magnetization as a Local Property. *Physical Review Letters* **110**, 087202 (2013).

[131] A. Marrazzo and R. Resta. Irrelevance of the Boundary on the Magnetization of Metals. *Physical Review Letters* **116**, 137201 (2016).

[132] G. Bihlmayer, Y. M. Koroteev, P. M. Echenique, E. V. Chulkov, and S. Blügel. The Rashba-Effect at Metallic Surfaces. *Surface Science* **600**, 3888–3891 (2006).

[133] P. Hao, Y. Fang, J. Sun, G. I. Csonka, P. H. T. Philipsen, and J. P. Perdew. Lattice constants from semilocal density functionals with zero-point phonon correction. *Phys. Rev. B* **85**, 014111 (2012).

[134] P. Błoński and J. Hafner. Density-Functional Theory of the Magnetic Anisotropy of Nanostructures: An Assessment of Different Approximations. *Journal of Physics: Condensed Matter* **21**, 426001 (2009).

[135] P. Giannozzi, O. Andreussi, T. Brumme, O. Bunau, M. B. Nardelli, M. Calandra, R. Car, C. Cavazzoni, D. Ceresoli, M. Cococcioni, N. Colonna, I. Carnimeo, A. D. Corso, S. de Gironcoli, P. Delugas, R. A. DiStasio, A. Ferretti, A. Floris, G. Fratesi, G. Fugallo, R. Gebauer, U. Gerstmann, F. Giustino, T. Gorni, J. Jia, M. Kawamura, H.-Y. Ko, A. Kokalj, E. Küçükbenli, M. Lazzeri, M. Marsili, N. Marzari, F. Mauri, N. L. Nguyen, H.-V. Nguyen, A. Otero-de-la-Roza, L. Paulatto, S. Poncé, D. Rocca, R. Sabatini, B. Santra, M. Schlipf, A. P. Seitsonen, A. Smogunov, I. Timrov, T. Thonhauser, P. Umari, N. Vast, X. Wu, and S. Baroni. Advanced capabilities for materials modelling with QUANTUM ESPRESSO. *Journal of Physics: Condensed Matter* **29**, 465901 (2017).

[136] A. D. Corso. Pseudopotentials periodic table: From H to Pu. *Computational Materials Science* **95**, 337–350 (2014).

[137] A. I. Liechtenstein, M. I. Katsnelson, V. P. Antropov, and V. A. Gubanov. Local Spin Density Functional Approach to the Theory of Exchange Interactions in Ferromagnetic Metals and Alloys. *Journal of Magnetism and Magnetic Materials* **67**, 65–74 (1987).

[138] Š. Pick, V. S. Stepanyuk, A. N. Baranov, W. Hergert, and P. Bruno. Effect of Atomic Relaxations on Magnetic Properties of Adatoms and Small Clusters. *Physical Review B* **68**, 104410 (2003).

[139] J. Bouaziz, M. d. S. Dias, F. S. M. Guimarães, S. Blügel, and S. Lounis. Impurity-induced orbital magnetization in a Rashba electron gas. *Phys. Rev. B* **98**, 125420 (2018).

[140] F. Reinert, G. Nicolay, S. Schmidt, D. Ehm, and S. Hüfner. Direct measurements of the L-gap surface states on the (111) face of noble metals by photoelectron spectroscopy. *Phys. Rev. B* **63**, 115415 (2001).

[141] A. Weismann, M. Wenderoth, S. Lounis, P. Zahn, N. Quaas, R. G. Ulbrich, P. H. Dederichs, and S. Blügel. Seeing the Fermi Surface in Real Space by Nanoscale Electron Focusing. *Science* **323**, 1190–1193 (2009).

[142] L. Rondin, J.-P. Tetienne, T. Hingant, J.-F. Roch, P. Maletinsky, and V. Jacques. Magnetometry with nitrogen-vacancy defects in diamond. *Rep. Prog. Phys.* **77**, 056503 (2014).

[143] M. dos Santos Dias, J. Bouaziz, M. Bouhassoune, S. Blügel, and S. Lounis. Chirality-Driven Orbital Magnetic Moments as a New Probe for Topological Magnetic Structures. *Nature Communications* **7**, 13613 (2016).

[144] E. Koch. Exchange Mechanisms, Lecture Notes, Correlated Electrons: From Models to Materials Modeling and Simulation Vol. 2. Forschungszentrum Jülich, 2012.

[145] M. A. Ruderman and C. Kittel. Indirect Exchange Coupling of Nuclear Magnetic Moments by Conduction Electrons. *Physical Review* **96**, 99–102 (1954).

[146] T. Kasuya. A Theory of Metallic Ferro- and Antiferromagnetism on Zener's Model. *Progress of Theoretical Physics* **16**, 45–57 (1956).

[147] K. Yosida. Magnetic Properties of Cu-Mn Alloys. *Physical Review* **106**, 893–898 (1957).

[148] M. Heide, G. Bihlmayer, and S. Blügel. Dzyaloshinskii-Moriya Interaction Accounting for the Orientation of Magnetic Domains in Ultrathin Films: Fe/W(110). *Physical Review B* **78**, 140403 (2008).

[149] S. Meckler, N. Mikuszeit, A. Preßler, E. Y. Vedmedenko, O. Pietzsch, and R. Wiesendanger. Real-Space Observation of a Right-Rotating Inhomogeneous Cycloidal Spin Spiral by Spin-Polarized Scanning Tunneling Microscopy in a Triple Axes Vector Magnet. *Physical Review Letters* **103**, 157201 (2009).

[150] L. Udvardi, L. Szunyogh, K. Palotás, and P. Weinberger. First-Principles Relativistic Study of Spin Waves in Thin Magnetic Films. *Physical Review B* **68**, 104436 (2003).

[151] A. Kitaev. Anyons in an Exactly Solved Model and Beyond. *Annals of Physics* **321**, 2–111 (2006).

[152] G. Jackeli and G. Khaliullin. Mott Insulators in the Strong Spin-Orbit Coupling Limit: From Heisenberg to a Quantum Compass and Kitaev Models. *Physical Review Letters* **102**, 017205 (2009).

[153] J. Chaloupka, G. Jackeli, and G. Khaliullin. Kitaev-Heisenberg Model on a Honeycomb Lattice: Possible Exotic Phases in Iridium Oxides $\mathrm{A_2IrO_3}$. *Physical Review Letters* **105**, 027204 (2010).

[154] M. Roger, J. H. Hetherington, and J. M. Delrieu. Magnetism in solid ^{3}He. *Rev. Mod. Phys.* **55**, 1–64 (1983).

[155] M. Takahashi. Half-filled Hubbard model at low temperature. *Journal of Physics C: Solid State Physics* **10**, 1289–7301 (1977).

[156] A. H. MacDonald, S. M. Girvin, and D. Yoshioka. t/U expansion for the Hubbard model. *Phys. Rev. B* **37**, 9753–9756 (1988).

[157] F. Michaud, F. Vernay, S. R. Manmana, and F. Mila. Antiferromagnetic Spin-S Chains with Exactly Dimerized Ground States. *Phys. Rev. Lett.* **108**, 127202 (2012).

[158] M. Hoffmann and S. Blügel. Systematic Derivation of Realistic Spin Models for Beyond-Heisenberg Solids. *Physical Review B* **101**, 024418 (2020).

[159] C. D. Batista, S.-Z. Lin, S. Hayami, and Y. Kamiya. Frustration and chiral orderings in correlated electron systems. *Rep. Prog. Phys.* **79**, 084504 (2016).

[160] R. Ozawa, S. Hayami, and Y. Motome. Zero-Field Skyrmions with a High Topological Number in Itinerant Magnets. *Phys. Rev. Lett.* **118**, 147205 (2017).

[161] S. Hayami, R. Ozawa, and Y. Motome. Effective bilinear-biquadratic model for noncoplanar ordering in itinerant magnets. *Phys. Rev. B* **95**, 224424 (2017).

[162] H. Ebert and S. Mankovsky. Anisotropic Exchange Coupling in Diluted Magnetic Semiconductors: Ab Initio Spin-Density Functional Theory. *Physical Review B* **79**, 045209 (2009).

[163] S. Polesya, S. Mankovsky, O. Sipr, W. Meindl, C. Strunk, and H. Ebert. Finite-Temperature Magnetism of Fe$_x$Pd$_{1-x}$ and Co$_x$Pt$_{1-x}$ Alloys**. 82**, 214409 (2010).

[164] S. Mankovsky, S. Polesya, and H. Ebert. Extension of the standard Heisenberg Hamiltonian to multispin exchange interactions. *arXiv e-prints* , arXiv:1909.11361 (2019).

[165] R. Drautz and M. Fähnle. Spin-cluster expansion: parametrization of the general adiabatic magnetic energy surface with ab initio accuracy. *Phys. Rev. B* **69**, 104404 (2004).

[166] R. Drautz and M. Fähnle. Parametrization of the magnetic energy at the atomic level. *Phys. Rev. B* **72**, 212405 (2005).

[167] V. I. Lebedev and D. Laikov. A quadrature formula for the sphere of the 131st algebraic order of accuracy. *Doklady Mathematics* **59**, 477–481 (1999).

[168] A. Crépieux and C. Lacroix. Dzyaloshinsky–Moriya Interactions Induced by Symmetry Breaking at a Surface. *J. Magn. Magn. Mater.* **182**, 341–349 (1998).

[169] C. F. Hirjibehedin, C. P. Lutz, and A. J. Heinrich. Spin Coupling in Engineered Atomic Structures. *Science* **312**, 1021–1024 (2006).

[170] O. Eriksson, A. Bergman, L. Bergqvist, and J. Hellsvik. Atomistic Spin Dynamics: Foundations and Applications. Oxford University Press, 2017.

[171] S. Bhattacharjee, L. Nordström, and J. Fransson. Atomistic Spin Dynamic Method with both Damping and Moment of Inertia Effects Included from First Principles. *Phys. Rev. Lett.* **108**, 057204 (2012).

[172] L. Chen, S. Mankovsky, S. Wimmer, M. A. W. Schoen, H. S. Körner, M. Kronseder, D. Schuh, D. Bougeard, H. Ebert, D. Weiss, and C. H. Back. Emergence of anisotropic Gilbert damping in ultrathin Fe layers on GaAs(001). *Nature Physics* **14**, 490–494 (2018).

[173] Y. Li, F. Zeng, S. S.-L. Zhang, H. Shin, H. Saglam, V. Karakas, O. Ozatay, J. E. Pearson, O. G. Heinonen, Y. Wu, A. Hoffmann, and W. Zhang. Giant Anisotropy of Gilbert Damping in Epitaxial CoFe Films. *Phys. Rev. Lett.* **122**, 117203 (2019).

[174] E. Jué, C. K. Safeer, M. Drouard, A. Lopez, P. Balint, L. Buda-Prejbeanu, O. Boulle, S. Auffret, A. Schuhl, A. Manchon, I. M. Miron, and G. Gaudin. Chiral damping of magnetic domain walls. *Nature Materials* **15**, 272 (2015).

[175] C. A. Akosa, I. M. Miron, G. Gaudin, and A. Manchon. Phenomenology of chiral damping in noncentrosymmetric magnets. *Phys. Rev. B* **93**, 214429 (2016).

[176] F. Freimuth, S. Blügel, and Y. Mokrousov. Chiral damping, chiral gyromagnetism, and current-induced torques in textured one-dimensional Rashba ferromagnets. *Phys. Rev. B* **96**, 104418 (2017).

[177] C. A. Akosa, A. Takeuchi, Z. Yuan, and G. Tatara. Theory of chiral effects in magnetic textures with spin-orbit coupling. *Phys. Rev. B* **98**, 184424 (2018).

[178] K.-W. Kim, H.-W. Lee, K.-J. Lee, K. Everschor-Sitte, O. Gomonay, and J. Sinova. Roles of chiral renormalization on magnetization dynamics in chiral magnets. *Phys. Rev. B* **97**, 100402 (2018).

[179] K. M. D. Hals and A. Brataas. Spin-Orbit Torques and Anisotropic Magnetization Damping in Skyrmion Crystals. *Physical Review B* **89**, 064426 (2014).

[180] F. S. M. Guimarães, M. dos Santos Dias, B. Schweflinghaus, and S. Lounis. Engineering Elliptical Spin-Excitations by Complex Anisotropy Fields in Fe Adatoms and Dimers on Cu(111). *Physical Review B* **96**, 144401 (2017).

[181] F. S. M. Guimarães, J. R. Suckert, J. Chico, J. Bouaziz, M. d. S. Dias, and S. Lounis. Comparative Study of Methodologies to Compute the Intrinsic Gilbert Damping: Interrelations, Validity and Physical Consequences. *Journal of Physics: Condensed Matter* **31**, 255802 (2019).

[182] P. W. Anderson. Localized Magnetic States in Metals. *Physical Review* **124**, 41 (1961).

[183] G. Chaudhary, M. d. S. Dias, A. H. MacDonald, and S. Lounis. Anatomy of magnetic anisotropy induced by Rashba spin-orbit interactions. *Phys. Rev. B* **98**, 134404 (2018).

[184] S. Lounis, A. T. Costa, R. B. Muniz, and D. L. Mills. Dynamical Magnetic Excitations of Nanostructures from First Principles. *Physical Review Letters* **105**, 187205 (2010).

[185] R. Wood. Future Hard Disk Drive Systems. *Journal of Magnetism and Magnetic Materials* **321**, 555–561 (2009).

[186] B. T. Thole, P. Carra, F. Sette, and G. van der Laan. X-ray circular dichroism as a probe of orbital magnetization. *Phys. Rev. Lett.* **68**, 1943–1946 (1992).

[187] D. Wortmann, S. Heinze, P. Kurz, G. Bihlmayer, and S. Blügel. Resolving Complex Atomic-Scale Spin Structures by Spin-Polarized Scanning Tunneling Microscopy. *Phys. Rev. Lett.* **86**, 4132–4135 (2001).

[188] F. Delgado and J. Fernández-Rossier. Spin Decoherence of Magnetic Atoms on Surfaces. *Progress in Surface Science* **92**, 40–82 (2017).

[189] K. W. H. Stevens. Matrix Elements and Operator Equivalents Connected with the Magnetic Properties of Rare Earth Ions. *Proceedings of the Physical Society. Section A* **65**, 209 (1952).

[190] B. Wybourne. Spectroscopic properties of rare earths. Wiley, 1965.

[191] F. Delgado and J. Fernández-Rossier. Spin Dynamics of Current-Driven Single Magnetic Adatoms and Molecules. *Physical Review B* **82**, 134414 (2010).

[192] H. Schoeller. Dynamics of open quantum systems, Lecture Notes of the 45th IFF Spring School “Computing Solids - Models, ab initio methods and supercomputing”. Forschungszentrum Jülich, 2014.

[193] J. Appelbaum. $s-d$ Exchange Model of Zero-Bias Tunneling Anomalies. *Physical Review Letters* **17**, 91–95 (1966).

[194] J. B. Ketterson and S. N. Song. Superconductivity. Cambridge University Press, 1999.

[195] J.-X. Zhu. Bogoliubov-de Gennes Method and Its Applications. Springer International Publishing Switzerland, 2016.

[196] W. Meissner and R. Ochsenfeld. Ein neuer Effekt bei Eintritt der Supraleitfähigkeit. *Naturwissenschaften* **21**, 787–788 (1933).

[197] J. Bardeen, L. N. Cooper, and J. R. Schrieffer. Microscopic Theory of Superconductivity. *Physical Review* **106**, 162–164 (1957).

[198] J. Bardeen, L. N. Cooper, and J. R. Schrieffer. Theory of Superconductivity. *Physical Review* **108**, 1175–1204 (1957).

[199] L. N. Cooper. Bound Electron Pairs in a Degenerate Fermi Gas. *Physical Review* **104**, 1189–1190 (1956).

[200] N. N. Bogoljubov. On a New Method in the Theory of Superconductivity. *Il Nuovo Cimento (1955-1965)* **7**, 794–805 (1958).

[201] Y. Luh. Bound state in superconductors with paramagnetic impurities. *Acta Physica Sinica* **21**, 75 (1965).

[202] H. Shiba. Classical Spins in Superconductors. *Progress of Theoretical Physics* **40**, 435–451 (1968).

[203] A. I. Rusinov. Superconductivity near a Paramagnetic Impurity. *Soviet Journal of Experimental and Theoretical Physics Letters* **9**, 85 (1969).

[204] E. Majorana. Teoria simmetrica dell'elettrone e del positrone. *Il Nuovo Cimento (1924-1942)* **14**, 171 (1937).

[205] L. Fu and C. L. Kane. Superconducting Proximity Effect and Majorana Fermions at the Surface of a Topological Insulator. *Physical Review Letters* **100**, 096407 (2008).

[206] F. Pientka, L. I. Glazman, and F. von Oppen. Topological Superconducting Phase in Helical Shiba Chains. *Physical Review B* **88**, 155420 (2013).

[207] M. M. Vazifeh and M. Franz. Self-Organized Topological State with Majorana Fermions. *Physical Review Letters* **111**, 206802 (2013).

[208] J. Klinovaja, P. Stano, A. Yazdani, and D. Loss. Topological Superconductivity and Majorana Fermions in RKKY Systems. *Physical Review Letters* **111**, 186805 (2013).

[209] B. Braunecker and P. Simon. Interplay between Classical Magnetic Moments and Superconductivity in Quantum One-Dimensional Conductors: Toward a Self-Sustained Topological Majorana Phase. *Physical Review Letters* **111**, 147202 (2013).

[210] J. Li, H. Chen, I. K. Drozdov, A. Yazdani, B. A. Bernevig, and A. H. MacDonald. Topological Superconductivity Induced by Ferromagnetic Metal Chains. *Physical Review B* **90**, 235433 (2014).

[211] R. Pawlak, M. Kisiel, J. Klinovaja, T. Meier, S. Kawai, T. Glatzel, D. Loss, and E. Meyer. Probing Atomic Structure and Majorana Wavefunctions in Mono-Atomic Fe Chains on Superconducting Pb Surface. *npj Quantum Information* **2**, 1–5 (2016).

[212] B. E. Feldman, M. T. Randeria, J. Li, S. Jeon, Y. Xie, Z. Wang, I. K. Drozdov, B. A. Bernevig, and A. Yazdani. High-Resolution Studies of the Majorana Atomic Chain Platform. *Nature Physics* **13**, 286–291 (2017).

[213] S. Jeon, Y. Xie, J. Li, Z. Wang, B. A. Bernevig, and A. Yazdani. Distinguishing a Majorana Zero Mode Using Spin-Resolved Measurements. *Science* **358**, 772–776 (2017).

[214] L. Schneider, M. Steinbrecher, L. Rózsa, J. Bouaziz, K. Palotás, M. d. S. Dias, S. Lounis, J. Wiebe, and R. Wiesendanger. Magnetism and In-Gap States of $3d$ Transition Metal Atoms on Superconducting Re. *npj Quantum Materials* **4**, 1–8 (2019).

[215] I. Errea, M. Calandra, C. J. Pickard, J. Nelson, R. J. Needs, Y. Li, H. Liu, Y. Zhang, Y. Ma, and F. Mauri. High-Pressure Hydrogen Sulfide from First Principles: A Strongly Anharmonic Phonon-Mediated Superconductor. *Physical Review Letters* **114**, 157004 (2015).

[216] J. C. Slater and G. F. Koster. Simplified LCAO Method for the Periodic Potential Problem. *Physical Review* **94**, 1498–1524 (1954).

[217] D. A. Papaconstantopoulos. Handbook of the Band Structure of Elemental Solids: From Z = 1 To Z = 112. Springer US, 2015.

[218] A. Y. Kitaev. Unpaired Majorana Fermions in Quantum Wires. *Physics-Uspekhi* **44**, 131–136 (2001).

[219] G. D. Mahan. Many-Particle Physics. Springer US, 2000.

List of publications

First author publication in chronological order

1. *Interatomic orbital magnetism: The case of 3d adatoms deposited on the Pt(111) surface*,
   Sascha Brinker, Manuel dos Santos Dias, and Samir Lounis,
   Physical Review B **98**, 094428 (2018)
2. *Stabilizing spin systems via symmetrically tailored RKKY interactions*,
   Jan Hermenau†, **Sascha Brinker**†, Marco Marciani, Manuel Steinbrecher, Manuel dos Santos Dias, Roland Wiesendanger, Samir Lounis, and Jens Wiebe,
   Nature Communications **10**, 2565 (2019)
   †Jan Hermenau and **Sascha Brinker** contributed equally to this work.
3. *The chiral biquadratic interaction*,
   Sascha Brinker, Manuel dos Santos Dias, and Samir Lounis,
   New Journal of Physics **21**, 083015 (2019)
4. *Spin, atomic and interatomic orbital magnetism induced by 3d nanostructures deposited on transition metal surfaces*,
   Sascha Brinker, Manuel dos Santos Dias, and Samir Lounis,
   Physical Review Materials **4**, 024404 (2020)
5. *Controlling in-gap end states by linking nonmagnetic atoms and artificially-constructed spin chains on superconductors*,
   Lucas Schneider†, **Sascha Brinker**†, Manuel Steinbrecher, Thore Posske, Manuel dos Santos Dias, Samir Lounis, Roland Wiesendanger, and Jens Wiebe,
   Nature Communications **11**, 4707 (2020)
   †Lucas Schneider and **Sascha Brinker** contributed equally to this work.
6. *Prospecting chiral multisite interactions in prototypical magnetic systems*,
   Sascha Brinker, Manuel dos Santos Dias, and Samir Lounis,
   Physical Review Research **2**, 033240 (2020)

7. *Non-collinear Gilbert damping from a real space approach*,
   Sascha Brinker, Manuel dos Santos Dias, and Samir Lounis,
   To be submitted (2020).
8. *First-principles investigation of magnetic lifetimes of coupled nanostructures*,
   Sascha Brinker, Manuel dos Santos Dias, and Samir Lounis,
   In preparation.

Further publications unrelated to this thesis

9. *Uniformity of the pseudomagnetic field in strained graphene*,
   Gerard J. Verbiest, **Sascha Brinker**, and Christoph Stampfer,
   Physical Review B **92**, 075417 (2015)
10. *Correlating Josephson supercurrents, Shiba states and unconventional spin-excitations in quantum spins coupled to superconductors*,
    Felix Küster, Ana M. Montero, Filipe S. M. Guimarães, **Sascha Brinker**, Samir Lounis, Paolo Sessi, and Stuart S. P. Parkin,
    Under consideration in Nature Communications (2020).

Acknowledgements

A doctoral thesis is a long-term project that requires interaction and collaboration with various people, whom I would like to thank for their support. In recent years, I have had the privilege of working out the basics of this work in an intercultural group in Jülich. The people in this group not only made this work possible, but also made working enjoyable.

First of all, I would like to thank my supervisor Prof. Dr. Samir Lounis for not only giving me the opportunity to work in his group, but also for finding the right way with his almost infinite ideas and for permanently motivating me and all his group members.

Equally, I would like to thank Dr. Manuel dos Santos Dias, whose contribution to this work goes far beyond his formal association, which is being my scientific advisor. He is the experienced theoretical physicist who helped me approaching the fundamental and complex physical topics I had to deal with during my PhD from the right angle. With his open-door policy, he always shared his astonishing wisdom and helped me whenever I got stuck. I cannot thank him enough for his contribution to this work.

I also thank Prof. Dr. Stefan Blügel for giving me the opportunity to write my PhD thesis at his institute and Prof. Dr. Stefan Wessel for agreeing to by my second corrector. During my work as a PhD student I had the opportunity to collaborate with the experimental group of Dr. Jens Wiebe from the University of Hamburg, whom I would like to thank for giving me insights in the experimental environment and mindset, and for initiating interesting works.

Since theoretical physics involves not only the work with pen, paper and computer, but also interpersonal relations, I would like to thank the friends I found in the time of my PhD, in particular Manuel, Filipe, Flaviano, Markus, Imara, Julen, and all the other members of our institute with whom I shared a nice time during social events.

Furthermore, I gratefully acknowledge the computing time granted through JARA-HPC on the supercomputer JURECA at the Forschungszentrum Jülich.

Last but not least, I would like to thank my family for their permanent support and my girlfriend Helen, who accompanies me through life's journeys since almost a decade, and fully supported me even during the toughest times.

Band / Volume 216
Development of a surface acoustic wave sensor for in situ detection of molecules
D. Finck (2020), 63 pp
ISBN: 978-3-95806-464-5

Band / Volume 217
Detection and Statistical Evaluation of Spike Patterns in Parallel Electrophysiological Recordings
P. Quaglio (2020), 128 pp
ISBN: 978-3-95806-468-3

Band / Volume 218
Automatic Analysis of Cortical Areas in Whole Brain Histological Sections using Convolutional Neural Networks
H. Spitzer (2020), xii, 162 pp
ISBN: 978-3-95806-469-0

Band / Volume 219
Postnatale Ontogenesestudie (Altersstudie) hinsichtlich der Zyto- und Rezeptorarchitektonik im visuellen Kortex bei der grünen Meerkatze
D. Stibane (2020), 135 pp
ISBN: 978-3-95806-473-7

Band / Volume 220
Inspection Games over Time: Fundamental Models and Approaches
R. Avenhaus und T. Krieger (2020), VIII, 455 pp
ISBN: 978-3-95806-475-1

Band / Volume 221
High spatial resolution and three-dimensional measurement of charge density and electric field in nanoscale materials using off-axis electron holography
F. Zheng (2020), xix, 182 pp
ISBN: 978-3-95806-476-8

Band / Volume 222
Tools and Workflows for Data & Metadata Management of Complex Experiments
Building a Foundation for Reproducible & Collaborative Analysis in the Neurosciences
J. Sprenger (2020), X, 168 pp
ISBN: 978-3-95806-478-2

Band / Volume 223
Engineering of *Corynebacterium glutamicum* towards increased malonyl-CoA availability for polyketide synthesis
L. Milke (2020), IX, 117 pp
ISBN: 978-3-95806-480-5

Band / Volume 224
Morphology and electronic structure of graphene supported by metallic thin films
M. Jugovac (2020), xi, 151 pp
ISBN: 978-3-95806-498-0

Band / Volume 225
Single-Molecule Characterization of FRET-based Biosensors and Development of Two-Color Coincidence Detection
H. Höfig (2020), XVIII, 160 pp
ISBN: 978-3-95806-502-4

Band / Volume 226
Development of a transcriptional biosensor and reengineering of its ligand specificity using fluorescence-activated cell sorting
L. K. Flachbart (2020), VIII, 102 pp
ISBN: 978-3-95806-515-4

Band / Volume 227
Strain and Tool Development for the Production of Industrially Relevant Compounds with *Corynebacterium glutamicum*
M. Kortmann (2021), II, 138 pp
ISBN: 978-3-95806-522-2

Band / Volume 228
Complex magnetism of nanostructures on surfaces: from orbital magnetism to spin excitations
S. Brinker (2021), III, 208 pp
ISBN: 978-3-95806-525-3

Weitere ***Schriften des Verlags im Forschungszentrum Jülich*** unter
http://wwwzb1.fz-juelich.de/verlagextern1/index.asp

Schlüsseltechnologien / Key Technologies
Band / Volume 228
ISBN 978-3-95806-525-3

Mitglied der Helmholtz-Gemeinschaft

JÜLICH
Forschungszentrum